Scale-Up of Miscible Flood Processes

Annual Report

F.M. Orr, Jr., Principal Investigator

January 1991

SCALE-UP OF MISCIBLE FLOOD PROCESSES

ANNUAL REPORT

Franklin M. Orr, Jr., Principal Investigator

Department of Petroleum Engineering
Stanford University
Stanford, California 94305

Prepared for the U.S. Department of Energy
Under Grant No. DE-FG21-89MC26253

January 1991

Table of Contents

Page

List of Tables ii
List of Figures iv
Acknowledgements xiii
Abstract xiv

1. Introduction 1

2. Phase Behavior, Fluid Properties, and Characterization of Crude Oils 3

   2.1 Phase Behavior of CO_2/Means Crude Oil Mixture 3
   (Aaron Stessman)

   2.2 GC-MS Analyses of Permian Basin Crude Oils 12
   (K. D. Hagedorn and Mustafa Yilmaz)

   2.3 Supercritical Fluid Chromatography for Crude Oil Characterization 26
   (M. P. Stadler)

   2.4 Summary 40

3. Interaction of Phase Behavior and Flow 41

   3.1 Effect of Volume Change on Mixing in Vaporizing and Condensing Gas Drives 41
   (Birol Dindoruk)

   3.2 Theory of Three-Component, Two-Phase Flow in Radial Systems 87
   (Russell Johns and Birol Dindoruk)

   3.3 Interfering Shocks in Slug Injection Processes 96
   (Russell Johns)

   3.4 Capillary Imbibition and Gravity Segregation: Interactions with Phase Equilibrium in Oil/Brine/Alcohol System 127
   (D. S. Schechter and Dengen Zhou)

   3.5 Summary 156

4. Viscous Fingering and Reservoir Heterogeneity 157

   4.1 Experimental Investigation of Viscous Fingering in Heterogeneous Porous Media 157
   (D. C. Brock)

   4.2 Simulation of Viscous Fingering in Heterogeneous Porous Media 192
   (Hamdi Tchelepi)

   4.3 Summary 215

5. Summary 219

References 221

List of Tables

Page

Table 2.3-1. Results of regression. The binary interaction parameters are taken from Deo et al. (1989). The $\overline{V}_1^{\infty,s}$ values are calculated. The exception is $C_{12}H_{26}$ for which $\overline{V}_1^{\infty,s}$ was taken from Fig. 2.3-6 and δ_{12} was calculated. 34

Table 3.1-1. Parameters for the Example Problems. 48

Table 3.1-2. MOC Solution of Binary Case with Volume Change on Mixing at 160°F and 1250 PSIA. 50

Table 3.1-3. MOC Solution of Binary Case with No Volume Change on Mixing at 160°F and 1250 PSIA. 50

Table 3.1-4. Initial and Injection Data for the Ternary Example Cases. 56

Table 3.1-5. MOC Solution of Ternary Case with Volume Change on Mixing at 160°F and 1250 PSIA, (CASE 1). 57

Table 3.1-6. MOC Solution of Ternary Case with No Volume Change on Mixing at 160°F and 1250 PSIA, (CASE 1). 58

Table 3.1-7. MOC Solution of Ternary Case with Volume Change on Mixing at 160°F and 1675 PSIA, (CASE 2). 65

Table 3.1-8. MOC Solution of Ternary Case with No Volume Change on Mixing at 160°F and 1675 PSIA, (CASE 2). 66

Table 3.1-9. MOC Solution of Ternary Case with Volume Change on Mixing at 160°F and 800 PSIA, (CASE 3). 67

Table 3.1-10. MOC Solution of Ternary Case with No Volume Change on Mixing at 160°F and 800 PSIA, (CASE 3). 68

Table 3.1-11. MOC Solution of Ternary Case with Volume Change on Mixing at 160°F and 1250 PSIA, (CASE 4). 80

Table 3.1-12. MOC Solution of Ternary Case with No Volume Change on Mixing at 160°F and 1250 PSIA, (CASE 4). 81

Table 3.2-1. Buckley-Leverett Immiscible Displacement. 89

Table 3.2-2. Miscible Displacement, No Volume Change on Mixing. 91

Table 3.2-3. Miscible Displacement with Volume Change on Mixing. 94

Table 3.3-1. Densities and Viscosities of H_2O-NBA System. 102

Table 3.3-2. Detailed Analytic Solution for Arbitrary Slug Size Injection. 122

Table 3.4-1. Properties of Equilibrated Phases (Morrow et al. 1985). 129

Table 3.4-2. Compositions of Equilibrated Phases. 129

Table 3.4-3. Chalk Core Data from Cuiec et al. (1990). 145

Table 3.4-4. Core Properties for Calculated Recovery Curves Shown in Fig. 3.4-14..... 145

Table 3.4-5. Inverse Bond Numbers for Core Displacements. 150

Table 3.4-6. Parameters for Nonequilibrium Analysis. 150

Table 4.1-1. Densities and Viscosities of the Fluids Used in the Experiments..... 158

Table 4.2-1. Data Sets Statistics. 202

List of Figures

		Page
Fig. 2.1-1	Bubblepoint pressure determination by expansion of the sample at a constant rate of 0.1 cm^3/min.	5
Fig. 2.1-2	Pressure-composition phase diagram for mixtures of CO_2 with Means crude oil at 90°F.	6
Fig. 2.1-3	Pressure-composition phase diagram for mixtures of CO_2 with Means crude oil at 105°F.	7
Fig. 2.1-4	Pressure-composition phase diagram for mixtures of CO_2 with Means crude oil at 120°F.	8
Fig. 2.1-5	Pseudoternary phase compositions for samples taken at 2000 psia and 105°F.	9
Fig. 2.1-6	Composition distribution of hydrocarbons present in the CO_2-rich phase, the original oil, and the oil-rich phase for samples taken at 2000 psia and 105°F.	10
Fig. 2.2-1	Distribution of molecular types present in Maljamar crude oil.	14
Fig. 2.2-2	Distribution of molecular types present in Wasson crude oil.	14
Fig. 2.2-3	Distribution of molecular types present in crude oil C.	15
Fig. 2.2-4	Distribution of molecular types present in crude oil D.	15
Fig. 2.2-5	Distribution of molecular types present in Means crude oil.	16
Fig. 2.2-6	Carbon number distribution for Maljamar crude oil.	17
Fig. 2.2-7	Carbon number distribution for Wasson crude oil.	17
Fig. 2.2-8	Carbon number distribution for crude oil C.	18
Fig. 2.2-9	Carbon number distribution for crude oil D.	18
Fig. 2.2-10	Carbon number distribution for Means crude oil.	19
Fig. 2.2-11	Elution times for hydrocarbons with a given carbon number.	20
Fig. 2.2-12	Average molecular weights of carbon number cuts for Maljamar crude oil.	21
Fig. 2.2-13	Normalized partition coefficients as a function of elution time for hydrocarbons identified from samples of equilibrium CO_2-rich and oil-rich phases for an 85 mole percent mixture of CO_2 with Means crude oil at 2000 psia and 105°F.	23

Fig. 2.2-14 Normalized partition coefficients as a function of carbon number..... 24

Fig. 2.2-15 Partition coefficients for hydrocarbons with eleven carbon atoms..... 25

Fig. 2.2-16 Compositions of CO_2-rich (upper) and oil-rich (lower) phases measured by GC-MS..... 27

Fig. 2.3-1 SFC apparatus (plumbing)..... 29

Fig. 2.3-2 SFC apparatus (networking)..... 30

Fig. 2.3-3 Example chromatogram of methane and n-docosane at 131°C..... 35

Fig. 2.3-4 Fit of Eq. (2.3-19) to experimental results for n-docosane at 131°C..... 36

Fig. 2.3-5 Plot illustrating the high statistical correlation between $\overline{V}_1^{\infty,s}$ and δ_{ij}. These results are for n-docosane at 131°C..... 37

Fig. 2.3-6 $\overline{V}_1^{\infty,s}$ correlation using δ_{ij}'s from Deo et al. (1989)..... 38

Fig. 2.3-7 Phase behavior of CO_2/n-dodecane binary system at 90°F. The solid line is the predicted phase behavior using the Peng-Robinson EOS with the binary interaction parameter determined from Fig. 2.3-6. The stars are actual experimental data from Stewart and Nielsen (1954)..... 39

Fig. 3.1-1 Recovery of Maljamar separator oil from slim tubes by continuous displacement with CO_2 at 90°F. Arrows indicate CO_2 breakthrough..... 42

Fig. 3.1-2 Oil recovery curves for displacement of C_{10} by CO_2 at 1250 psia and 160°F: a) Volume change on mixing b) No volume change on mixing..... 51

Fig. 3.1-3 Composition profiles for displacement of C_{10} by CO_2 at 1250 psia and 160°F: a) Volume change on mixing b) No volume change on mixing..... 52

Fig. 3.1-4 Saturation profiles for displacement of C_{10} by CO_2 at 1250 psia and 160°F: a) Volume change on mixing b) No volume change on mixing..... 53

Fig. 3.1-5 Total velocity profile for displacement of C_{10} by CO_2 at 1250 psia and 160°F: a) Volume change on mixing b) No volume change on mixing..... 54

Fig. 3.1-6 Composition routes for displacement of a C_4-C_{10} mixture by pure CO_2 at 1250 psia and 160°F: a) Volume change on mixing b) No volume change on mixing..... 59

Fig. 3.1-7 Composition profiles for displacement of a C_4-C_{10} mixture by pure CO_2 at 1250 psia and 160°F: a) Volume change on mixing b) No volume change on mixing..... 60

Fig. 3.1-8 Saturation and total velocity profiles for displacement of a C_4-C_{10} mixture by pure CO_2 at 1250 psia and 160°F: a) Volume change on mixing b) No volume change on mixing. 61

Fig. 3.1-9 Effluent mole fractions for displacement of a C_4-C_{10} mixture by pure CO_2 at 1250 psia and 160°F: a) Volume change on mixing b) No volume change on mixing. 62

Fig. 3.1-10 Recovery curves for displacement of a C_4-C_{10} mixture by pure CO_2 at 1250 psia and 160°F: a) Volume change on mixing b) No volume change on mixing. 63

Fig. 3.1-11 Composition routes for ternary C_1-C_4-C_{10} system at 1675 psia and 160°F: a) Volume change on mixing b) No volume change on mixing. 69

Fig. 3.1-12 Composition profiles for displacement of C_4-C_{10} mixture by pure C_1 at 1675 psia and 160°F: a) Volume change on mixing b) No volume change on mixing. 70

Fig. 3.1-13 Saturation and total velocity profiles for displacement of a C_4-C_{10} mixture by C_1 at 1675 psia and 160°F: a) Volume change on mixing b) No volume change on mixing. 71

Fig. 3.1-14 Effluent mole fractions for displacement of a C_4-C_{10} mixture by pure C_1 at 1675 psia and 160°F: a) Volume change on mixing b) No volume change on mixing. 72

Fig. 3.1-15 Recovery curves for displacement of a C_1-C_{10} mixture by pure C_1 at 1675 psia and 160°F: a) Volume change on mixing b) No volume change on mixing. 73

Fig. 3.1-16 Composition routes for displacement of a C_4-C_{10} mixture by pure CO_2 at 800 psia and 160°F: a) Volume change on mixing b) No volume change on mixing. 74

Fig. 3.1-17 Composition profiles for displacement of a C_4-C_{10} mixture by pure CO_2 at 800 psia and 160°F: a) Volume change on mixing b) No volume change on mixing. 75

Fig. 3.1-18 Saturation and total velocity profiles for displacement of a C_4-C_{10} mixture by pure CO_2 at 800 psia and 160°F: a) Volume change on mixing b) No volume change on mixing. 76

Fig. 3.1-19 Effluent mole fractions for displacement of a C_4-C_{10} mixture by pure CO_2 at 800 psia and 160°F: a) Volume change on mixing b) No volume change on mixing. 77

Fig. 3.1-20 Recovery curves for displacement of a C_4-C_{10} mixture by pure CO_2 at 800 psia and 160°F: a) Volume change on mixing b) No volume change on mixing. 78

Fig. 3.1-21 Composition routes for displacement of a C_4-C_{10} mixture by a CO_2-C_4 mixture (condensing gas drive) at 1250 psia and 160°F: a) Volume change on mixing b) No volume change on mixing. 82

Fig. 3.1-22 Composition profiles for displacement of a C_4-C_{10} mixture by a CO_2-C_4 mixture (condensing gas drive) at 1250 psia and 160°F a) Volume change on mixing b) No volume change on mixing. 83

Fig. 3.1-23 Saturation and total velocity profiles for displacement of a C_4-C_{10} mixture by a CO_2-C_4 mixture (condensing gas drive) at 1250 psia and 160°F: a) Volume change on mixing b) No volume change on mixing. 84

Fig. 3.1-24 Effluent mole fractions for displacement of a C_4-C_{10} mixture by a CO_2-C_4 mixture (condensing gas drive) at 1250 psia and 160°F: a) Volume change on mixing b) No volume change on mixing. 85

Fig. 3.1-25 Recovery curves for displacement of a C_4-C_{10} mixture by a CO_2-C_4 mixture (condensing gas drive) at 1250 psia and 160°F: a) Volume change on mixing b) No volume change on mixing. 86

Fig. 3.2-1 Comparison of linear and radial solutions at 0.5 PV injected for displacement of a 20 mole % C_4/80 mole % C_{10}. 95

Fig. 3.2-2 CO_2-C_4-C_{10} system, linear vs. radial solution at 1.0 pore volumes injected, concentration profile. 97

Fig. 3.2-3 Comparison of linear and radial flow velocities at 1.0 PV injected. 98

Fig. 3.3-1 Measured relative permeabilities for H_2O-NBA system and best fits to data. 103

Fig. 3.3-2 Overall fractional flow function and shock trajectories. 105

Fig. 3.3-3 Hypothetical time-distance diagram showing the idea of a Reimann equivalent. 106

Fig. 3.3-4 Complex time-distance diagram with multiple Reimann equivalents. 108

Fig. 3.3-5 Time-distance diagram showing the long term solution and the resolution of the interference region. 109

Fig. 3.3-6 Analytical solution for constant injection of water. 110

Fig. 3.3-7 Analytical and numerical composition and saturation profiles at 0.5 PVI for continuous H_2O injection into pure NBA. 111

Fig. 3.3-8 Interference of shocks and waves for 0.5 PV water slug injection, accurate solution up to first intersection point. 112

Fig. 3.3-9 Analytical and numerical composition and saturation profiles at 0.6 PVI for injection of a 0.5 PV H_2O slug into pure NBA. 113

Fig. 3.3-10 Enlargement of the interference region on the time-distance diagram 114

Fig. 3.3-11 Complete analytical solution for injection of a 0.5 PV water slug. 116

Fig. 3.3-12 Analytical and numerical composition and saturation profiles at 0.7 PVI for injection at a 0.5 PV H_2O slug into pure NBA. 117

Fig. 3.3-13 Analytical and numerical composition and saturation profiles at 0.9 PVI for injection of a 0.5 PV H_2O slug into pure NBA. 118

Fig. 3.3-14 Interference of shocks at a second intersection point for injection of a 0.1 PV water slug. The solution shown applies only up to the time of the second intersection. 119

Fig. 3.3-15 Analytical and numerical composition and saturation profiles at 0.2 PVI for injection of a 0.1 PV H_2O slug into pure NBA. 120

Fig. 3.3-16 Complete analytical solution for injection of a 0.1 PV water slug 123

Fig. 3.3-17 Analytical and numerical composition and saturation profiles at 0.5 PVI for injection of a 0.1 PV H_2O slug into pure NBA. 124

Fig. 3.3-18 Analytical and numerical composition and saturation profiles at a 1.0 PVI for injection of a 0.1 PV H_2O slug into pure NBA. 125

Fig. 3.3-19 Complete analytical solution for arbitrary water slug size. 126

Fig. 3.4-1 Phase diagram for IPA, 2% $CaCl_2$ and isooctane (Morrow et al. 1985). 130

Fig. 3.4-2 Schematic of imbibition apparatus. 132

Fig. 3.4-3 Schematic of plexiglass core holder. 133

Fig. 3.4-4 Oil production during imbibition experiments with equilibrated fluids in a Berea sandstone core with permeability k = 100 md. In these experiments produced oil phase collected in the fracture, reducing the area available for imbibition 134

Fig. 3.4-5 Oil production during imbibition experiments with equilibrated fluids in a Berea sandstone core with permeability k = 500 md. In these experiments produced oil phase collected in the fracture, reducing the area available for imbibition. 135

Fig. 3.4-6 Oil production during imbibition experiments with equilibrated fluids in the 500 md Berea core. In these experiments produced oil collected above the top face of the core, allowing the core to be immersed continuously in the wetting phase. 136

Fig. 3.4-7 Oil production in a brown sandstone core from the Masalan formation with a permeability of k = 700 md. In these experiments, produced oil collected above the top face of the core, allowing the core to be immersed continuously in the wetting phase. 137

Fig. 3.4-8 Scaled imbibition rates for the oil production curves in Fig. 3.4-7. 138

Fig. 3.4-9 Comparison of equilibrium and nonequilibrium imbibition for the 500 md core. 140

Fig. 3.4-10 Comparison of equilibrium and nonequilibrium recovery data for the 100 md core. 141

Fig. 3.4-11 Limiting case analysis of capillary dominated imbibition. 143

Fig. 3.4-12 Comparison of theory with data of Cuiec et al. (1990) 146

Fig. 3.4-13 Comparison of Eq. (3.4-15) with data of Cuiec et al. (1990). 148

Fig. 3.4-14 Effect of reduction in IFT on recovery rate according to Eq. (3.4-23). 151

Fig. 3.4-15 Imbibition for fluids not in equilibrium. 153

Fig. 3.4-16 Dimensionless time required for recovery of half the movable oil. BC 1 refers to cases in which the core was completely immersed in wetting phase. BC 2 refers to cores that were partially immersed. 155

Fig. 4.1-1 Dimensions of two-dimensional bead packs. 159

Fig. 4.1-2 Schematic of equipment for flow visualization experiments. 161

Fig. 4.1-3 Measured front positions during displacement of undyed oil by dyed oil with the same viscosity and density. 162

Fig. 4.1-4 Permeability distribution estimated from the front position of Fig. 4.1-3 for the two-layer model of Fig. 4.1-1. 164

Fig. 4.1-5 The four models used in experiments. 165

Fig. 4.1-6(a-c) Injected fluid concentrations in an experimental displacement at M=40 and q=6 ml/min in the homogeneous model. 166

Fig. 4.1-6(d-f) Injected fluid concentrations in an experimental displacement at M=40 and q=6 ml/min in the homogeneous model. 167

Fig. 4.1-7(a-c) Simulated concentration distributions for a displacement at M=40 in the homogeneous model. 168

Fig. 4.1-7(d-f) Simulated concentration distributions for a displacement at M=40 in the homogeneous model. 169

Fig. 4.1-8 Comparison of the appearance of fingers in the simulation (a) and experiment (b) for a displacement at M=40 and q=6 ml/min in the homogeneous model. 171

Fig. 4.1-9 Comparison of cross-sectional averaged compositions in experiment and simulation of a displacement at M=40 and q=6 ml/min in the homogeneous model. 172

Fig. 4.1-10 Comparison of the 0.2 concentration contour in experiment (a) and simulation (b) at M=40 and q=6 ml/min in the homogeneous model. 173

Fig. 4.1-11 Comparison of the effluent composition curves in experiment and simulation at M=40 and q=6 ml/min in the homogeneous model. 174

Fig. 4.1-12(a-c) Injected fluid concentration in an experimental displacement at M=40 and q=6 ml/min in the two-layer model. 175

Fig. 4.1-12(d-f) Injected fluid concentration in an experimental displacement at M=40 and q=6 ml/min in the two-layer model. 176

Fig. 4.1-13(a-c) Simulated concentration distributions for displacement at M=40 in the two-layer model. 177

Fig. 4.1-13(d-f) Simulated concentration distributions for displacement at M=40 in the two-layer model. 178

Fig. 4.1-14(a-c) Injected fluid concentration in an experimental displacement at M=40 and q=6 ml/min in the streak model. 180

Fig. 4.1-14(d-f) Injected fluid concentration in an experimental displacement at M=40 and q=6 ml/min in the streak model. 181

Fig. 4.1-15(a-c) Simulated concentration distributions for displacement at M=40 in the streak model. 182

Fig. 4.1-15(d-f) Simulated concentration distributions for displacement at M=40 in the streak model. 183

Fig. 4.1-16(a-c) Injected fluid concentration in an experimental displacement at M=1 and q=6 ml/min in the checkered model. 184

Fig. 4.1-16(d-f) Injected fluid concentration in an experimental displacement at M=1 and q=6 ml/min in the checkered model. 185

Fig. 4.1-17(a-c) Injected fluid concentration in an experimental displacement at M=40 and q=6 ml/min in the checkered model. 186

Fig. 4.1-17(d-f) Injected fluid concentration in an experimental displacement at M=40 and q=6 ml/min in the checkered model. 188

Fig. 4.1-17(g-i) Injected fluid concentration in an experimental displacement at M=40 and q=6 ml/min in the checkered model. 189

Fig. 4.1-18(a-c) Simulated concentration distributions for displacement at M=40 in the checkered model. 190

Fig. 4.1-18(d-f) Simulated concentration distributions for displacement at M=40 in the checkered model. 191

Fig. 4.2-1 Permeability map for the checkerboard model. 196

Fig. 4.2-2 Concentration gray-scale maps for the experiment, new and old boundary condition at M = 80, PVI = 0.10. 197

Fig. 4.2-3 Concentration gray-scale maps for the experiment, new and old boundary condition at M = 80, PVI = 0.15. 198

Fig. 4.2-4 Concentration gray-scale maps for the experiment, new and old boundary condition at M = 80, PVI = 0.20. 199

Fig. 4.2-5 Concentration gray-scale maps for the experiment, new and old boundary condition at M = 80, PVI = 0.25. The four models used in experiments. 200

Fig. 4.2-6 Gray-scale map of the permeability distribution for the original Berea data set (C.V. = 0.284). 203

Fig. 4.2-7 Gray-scale map of the permeability distribution for the first modified data set (C.V. = 0.56). 204

Fig. 4.2-8 Gray-scale map of the permeability distribution for the second modified data set (C.V. = 0.86). 205

Fig. 4.2-9 X-direction variograms for the three data sets. 207

Fig. 4.2-10 Y-direction variograms for the three data sets. 208

Fig. 4.2-11 The 50% concentration contour at 0.4, 0.5, 0.7 and 0.9 PVI at M=1 for the original Berea data set. 209

Fig. 4.2-12 The 50% cvoncentration contour at 0,4 0.5, 0.7 and 0.9 PVI at M=1 for the first modified data set. 210

Fig. 4.2-13 The 50% concentration contour at 0.4, 0.5, 0.7 and 0.9 PVI at M=1 for the second modified data set. 211

Fig. 4.2-14 The 50% concentration contour at 0.4, 0.5, 0.7 and 0.9 PVI at M=7.5 for the original Berea data set. 212

Fig. 4.2-15 The 50% concentration contour at 0.4, 0.5, 0.7 and 0.9 PVI at M=7.5 for the first modified data set. 213

Fig. 4.2-16 The 50% concentration contour at 0.4, 0.5, 0.7 and 0.9 PVI at M=7.5 for the second modified data set. 214

Fig. 4.2-17 The 50% concentration contour at 0.4, 0.5, 0.7 and 0.9 PVI at M=100 for the original Berea data set. 216

Fig. 4.2-18 The 50% concentration contour at 0.4, 0.5, 0.7 and 0.9 PVI at M=100 for the first modified data set. 217

Fig. 4.2-19 The 50% concentration contour at 0.4, 0.5, 0.7 and 0.9 PVI at M=100 for the second modified data set. 218

Acknowledgements

The research program described in this report was supported by the U. S. Department of Energy under Grant DE-FG21-89-26253 and by the Stanford University Miscible Flooding Industrial Affiliates: Arco Oil and Gas Company, BP Exploration Inc., Chevron Oil Field Research Company, Conoco Inc., Exxon Production Research Company, Intevep, S.A., Japan National Oil Corporation, Marathon Oil Company, Mobil Research and Development Corporation, Shell Development Company, Texaco Inc., Unocal Corporation and Western Atlas International. Fellowship funds for graduate students whose work is described here were provided by the National Science Foundation, the Steel Fund, the Littlefield Fund, the Whiteford Fund and the Terry Fund. We gratefully acknowledge all those sources of support.

Many of our fellow students and faculty in the School of Earth Sciences contributed to the ideas presented here. In the Petroleum Engineering Department, Khalid Aziz, Bill Brigham, Roland Horne and Hank Ramey along with their graduate students helped us grapple with a host of experimental and theoretical problems too numerous to mention. Our links with faculty and students in other Earth Sciences departments also paid off. We are indebted to Amos Nur's Rock Physics group (Geophysics) for use of their image processing equipment in Dave Brock's viscous fingering experiments. Ideas from Andre Journel's Geostatistics group (Applied Earth Sciences) are to be found in many places in this report. Our collaboration with Simon Brassell's Organic Geochemistry group (Geology) has made us much more productive users of our shared GC/MS. Our future work will no doubt continue to be much influenced by our Earth Sciences colleagues, who insist that we deal with petrophysical reality from time to time. We are also grateful to our colleagues at the U.S. Department of Energy (especially Royal Watts, our Technical Project Officer) and at the companies who support this research effort. We thank them for their interest, for taking time to listen to and talk to our students, and for offering many thoughtful comments and suggestions.

This report was assembled by Pat Ota, Jeanne Mankinen and Yolanda Williams from scraps of paper, fragments of text, cryptic notes in margins and computer files beyond counting. Ted Sumida demonstrated yet again his commitment to eradication of typographical and grammatical indiscretions. If it looks like a finished product, they deserve the credit. Those of us who are listed as authors give special thanks for their careful attention to detail, for their patience with all of us, and especially for the fact that their senses of humor have remained intact throughout the extended period of preparation of the report.

F. M. Orr, Jr.
Stanford, California
January 1991

Disclaimer

Any opinions, findings, conclusions, or recommendations expressed herein are those of the authors and do not necessarily reflect the views of DOE.

Abstract

This report describes recent progress in a research effort to quantify the scaling of interactions of phase behavior of multicomponent mixtures with unstable flow in heterogeneous porous media. New results are presented in three areas:

(1) Phase behavior, fluid properties and characterization of crude oils

(2) Interactions of phase behavior and flow

(3) Viscous fingering and reservoir heterogeneity.

In the first area, results of phase behavior experiments are reported for mixtures of CO_2 with crude oil from the Means field. Detailed analyses of phase compositions are also reported for samples taken during the PVT experiments. Also reported are results of an investigation of crude oil compositions and phase compositions by gas chromatography combined with mass spectrometry. Those analyses show that molecular weights calculated for single carbon number cuts agree well with the n-alkane molecular weight despite the fact that there is considerable variation in actual carbon number within a cut. The experimental results also show that efficiency with which a given molecule is extracted by dense CO_2 correlates better with chromatographic elution time than it does with carbon number. Finally, a new method for characterization of crude oils by supercritical fluid chromatography is demonstrated.

In the second area, the first detailed comparison is reported for displacements with and without volume change as components change phase. The solutions described were obtained by the method of characteristics. They show that volume change alters composition paths only slightly, but it changes flow velocity dramatically. They also show that breakthrough recoveries calculated without volume change are generally higher than those obtained when volume is not conserved. Also described is a transformation that allows radial flow solutions to be obtained from the linear solutions presented previously. Problems that must be solved if MOC solutions are to be obtained for slug injections processes are outlined in an analysis of binary displacements with interfering shocks. The examples presented indicate how more complex problems such as injection of a CO_2 slug followed by methane or nitrogen chase gas can be analyzed. Results of experiments to investigate the interactions of phase behavior, interfacial tension variations, and gravity segregation are also reported, as is an analysis of associated scaling issues.

Results of experiments and numerical computations that describe the growth of viscous fingers are described in the third area. Both results and simulations show clearly that even mild permeability heterogeneity can have a dramatic effect on the form and location of viscous fingers. They also show that the simulations reproduce with good accuracy the transition from flow dominated by viscous forces to flow dominated by the permeability distribution. The agreement between simulation and experiment is good enough that the particle-tracking simulation approach can be used with confidence to explore scaling questions.

1. Introduction

An important constraint on the implementation of field-scale miscible flood processes is the accuracy of predictions of process performance. Because the uncertainty in predictions of the amount and timing of oil recovery can be large, the risk associated with investments in miscible flood projects can also be high, especially in an uncertain price environment. No amount of research like that described here will reduce price uncertainty, but substantial reductions in the uncertainties associated with performance predictions at field scale can be achieved. The key issue is scaling: How do we translate measures of displacement performance from laboratory scale, where they are experimentally accessible, to field scale, where accurate predictions of oil recovery rate are needed?

This report is an account of recent progress in a research effort that attacks question of scaling from several directions. The multifaceted approach is dictated by the complexity of the process itself. When carbon dioxide (CO_2), nitrogen (N_2), methane (C_1), or some other "miscible" fluid is injected into an oil reservoir, a complex web of interactions begins. It is by now well established that phase behavior is responsible for high local displacement efficiency, as abundantly available evidence from nearly one-dimensional slim tube displacements and corresponding mathematical analyses of the chromatographic separations that occur in one-dimensional flow indicate. Flow in reservoir rocks is anything but one-dimensional, however. Instead, heterogeneities in permeability and porosity cause nonuniform displacement. Viscous instabilities, which occur when low viscosity solvent displaces higher viscosity oil, also lead to nonuniform flow. In addition, crossflow between zones of fast and slow flow can be driven by viscous forces, gravity segregation, and capillary forces in addition to the slower processes of diffusion and dispersion. That crossflow, in turn, can cause mixing of fluids with very different compositions. The result is that some oil is moved into zones of fast flow and some solvent reaches zones of slow flow before it would do so by longitudinal flow alone. In addition, the chromatographic separations that arise from the interaction of phase behavior and multiphase flow are also altered by transverse mixing due to crossflow. Thus, the fundamental scaling question is: How do phase behavior, nonuniform flow, and crossflow act and interact to determine displacement performance at field scale?

In principle, that question could be answered by performing detailed, fine-grid, compositional reservoir simulations—simulations that include accurate representations of all the relevant physical mechanisms as well as "adequate" resolution of reservoir heterogeneities and viscous fingers. In practice, however, field-scale simulations of that sort are not currently feasible. Hence, we have divided the research effort into investigations of individual and pairs of mechanisms—representation of phase behavior and efficient laboratory characterization of crude oils, phase behavior and multiphase flow, crossflow and phase behavior, viscous fingering and heterogeneity. The objective is to understand which mechanisms are most important at field scale and to use that understanding to guide development of field-scale simulation tools that represent the most important physical mechanisms and are no more complex than need be. Throughout the research, we use a combination of analytical mathematics, numerical simulation and experimental verification. The experimental component is an essential part of the research. Only if the analytical and numerical models can be shown to represent with reasonable accuracy the relevant physical mechanisms, can they be used with confidence to explore complex questions of scale.

In chapter 2, we consider three questions:

(1) How much do we need to know about the composition of a crude oil predictions of phase behavior with an equation of state (EOS)?

(2) Can we use supercritical fluid chromatography to obtain composition and other crude oil characterization data efficiently?

(3) How do variations in the structure of molecules present in a crude oil influence how they partition in high pressure phase separations?

The motivation for this area of work is the need for adequate EOS representation of phase behavior with a relatively small number of pseudocomponents, so that interactions of phase behavior and nonuniform flow can be explored efficiently for displacements of crude oils.

In Chapter 3, we consider the interactions of phase behavior and flow. The first three sections of Chapter 3 apply the method of characteristics to obtain analytical solutions for one-dimensional follow in the absence of dispersion. While such analyses apply only to limiting cases, they provide a very useful framework for understanding the behavior of numerical simulations, and they permit detailed assessment of the accuracy of numerical simulations, a task that is often difficult for the nonlinear problems considered here. The last section of Chapter 3 reports surprising results of experiments to investigate combined effects of capillary imbibition and gravity segregation in systems in which phase behavior creates low and high interfacial tensions.

Interactions of viscous instability and permeability heterogeneity are examined in Chapter 4. Additional development of a particle-tracking technique for simulation of the growth of viscous fingers is described. In addition, results of a detailed comparison of simulation predictions with experimental observations of finger dimensions is reported. The good agreement obtained, without resorting to history matching, suggests that the particle-tracking technique represents with reasonable accuracy the physical mechanisms that control unstable displacements in both homogeneous and heterogeneous porous media.

The complexity of the physical mechanisms that come into play during a miscible flood guarantees this to be a progress report, not a statement of problem solution. Though much remains to be done, the research described here represents a step toward the goal of detailed understanding of the scaling behavior of miscible flood processes.

2. Phase Behavior, Fluid Properties, and Characterization of Crude Oils

Phase behavior is of fundamental importance to miscible flood processes. The transfer of components between phases, when coupled to multiphase flow, causes chromatographic separations that determine local displacement efficiency, as the theory presented in Chapter 3 indicates. Fluid properties (density, viscosity, interfacial tensions, and so on) are also controlled by the compositions of the phases that form during a displacement. Thus, accurate quantitative description of phase behavior is of central importance to understanding of the impact of heterogeneity, viscous fingering, crossflow, and the mixing they induce.

Detailed description of phase behavior requires, of course, some specification of the composition of the crude oil for use in an equation of state (EOS), for example. In this chapter we describe a set of experiments to determine the level of detail required for adequate description of a crude oil, and we examine how compositional information can be acquired efficiently. In Section 2.1, we report results of phase equilibrium experiments for mixtures of CO_2 with Means crude oil. Samples taken during those experiments were analyzed by simulated distillation, a gas chromatography (GC) technique with relatively low resolution, and by mass spectroscopy (GC-MS), which permits identification of specific molecules present in a mixture. Results of those experiments are reported in Section 2.2. In Section 2.3 we turn to the question of characterization of components in an oil for calculations with an EOS, and examine whether constraints on the parameters used in an EOS can be set from supercritical fluid chromatography (SFC) data using high-pressure CO_2 as a carrier.

2.1 Phase Behavior of CO_2/Means Crude Oil Mixtures

Aaron Stessman

Experimental measurements of the phase behavior of a system of west Texas stock tank oil (Means) and CO_2 are currently in progress. Measurements of phase volumes for three overall CO_2 concentrations have been made at temperatures of 90°, 105° and 120°F and over a range of pressures. In addition, samples of the equilibrated CO_2-rich and oil-rich phases were taken at one set of conditions in the neighborhood of the minimum miscibility pressure (MMP) reported by Magruder et al. (1990) for this crude oil. The densities, viscosities and compositions of both phases were measured. The experimental equipment used in this study has been described in detail previously by Orr (1989).

2.1.1 Experimental Procedures

Overall CO_2 concentrations of 23.0, 49.6 and 85.5 mole percent were created by adding the appropriate mass of CO_2 to a known mass of Means stock tank oil held in a windowed PVT cell. The molecular weight of the Means oil, 241 g/gmole, used to compute overall molar composition, was determined from simulated distillation compositional analysis using gas chromatography. Oil density was measured with a Mettler-Paar densitometer over a range of temperatures.

At each temperature phase volumes in the two- and, where present, three-phase regions were measured after equilibration, and the pressure was recorded. Phase volumes were measured from the position of the phase interfaces as seen through the window of the PVT cell. Bubblepoint pressures were measured by slow expansion of the volume of the system initially in the single-phase region with simultaneous observations of the decline in pressure. With the appearance of a vapor phase, the system compressibility is dominated by the vapor and an abrupt deviation in the slope of declining pressure is seen. A typical plot of the system

pressure decline during volume expansion is shown in Fig. 2.1-1. This technique was also used to determine the pressure at which the vapor phase first appeared in the three-phase region.

Samples of the CO_2-rich and oil-rich liquid phases were taken at 105°F and 2000 psia, which is near the reported MMP for this oil (Magruder et al. 1990). The densities of the two phases were measured at these conditions by a Mettler-Paar densitometer mounted in the sampling line. Viscosities of the phases were calculated from the pressure drop experienced across a calibrated capillary tube while sampling at a constant rate. Each phase was then flashed to near atmospheric conditions. The low-pressure separation resulted in vapor and liquid phases, which were then sampled and analyzed for composition using gas chromatography techniques. The hydrocarbon liquid was analyzed by simulated distillation on an OV-101 column using a flame ionization detector (FID). Vapor samples were separated on a Porapak Q column with a thermal conductivity detector (TCD). The compositions of the original phases were calculated by recombination of the flashed liquid, whose weight was measured, with the flashed vapor. The moles of flashed vapor were calculated from the pressure of the vapor in a cell of known volume. Because the pressure in that cell was in the neighborhood of one atmosphere, the ideal gas law was used to calculate the amount of gas evolved from the sample.

2.1.2 Results

Figs. 2.1-2 to 2.1-4 show pressure-composition phase diagrams for the mixtures of Means stock tank oil with CO_2 at three temperatures: 90, 105 and 120°F. The phase boundaries shown in the 60 to 80 mole percent range were estimated from the behavior of similar Permian Basin oils when mixed with CO_2 (Orr and Jensen 1984). This region is currently being explored in more detail in continuing experiments with this system. For each of the temperatures and at low mole fraction CO_2, two phases: liquid and vapor were observed below the bubblepoint pressure. At a high mole fraction of CO_2, however, three phases: a CO_2-rich vapor, a CO_2-rich liquid and an oil-rich liquid were observed for the two lower temperatures. The three-phase region is near the extrapolated vapor pressure of CO_2, as expected (Orr and Jensen 1984, Larsen et al. 1989). At higher pressures, two phase liquid-liquid behavior was observed. In that region of the phase diagram large changes in pressure resulted in small changes in the volume fractions of each phase. For example, at 105°F, as the system was compressed from 1500 to 3900 psia, the volume fraction of oil-rich liquid increased only slightly from 61.3% to 66.7%.

At 120°F, the 85 mole percent CO_2 mixture changed gradually from what appeared to be two-phase liquid-vapor to a less compressible two-phase system similar to the liquid-liquid systems observed at lower temperature, but no three-phase region was observed. Thus, the maximum temperature for three-phase behavior with the Means crude is evidently somewhere between 105° and 120°F. The disappearance of the three-phase region was investigated further by setting the pressure to produce three phases. There the temperature was increased with the overall sample volume held constant. As the temperature increased, the three-phase region disappeared at about 114°F.

Samples were taken of each of the two liquid phases present at 2000 psia, 105°F and an overall mole fraction CO_2 of 0.855. These phases were found to have densities of 0.8148 gm/cc and 0.9014 gm/cc for the CO_2-rich and oil-rich liquids, respectively. Their corresponding viscosities were 0.144 cp and 1.542 cp.

The compositional analysis of each phase as well as the overall mixture is summarized in Fig. 2.1-5. A more detailed representation of the phase compositions is given in Fig. 2.1-6. For the purpose of comparing the relative proportion of hydrocarbons found in each phase, the mole fraction of each hydrocarbon component was normalized to remove the CO_2, so that the mole fraction presented is of the total hydrocarbons in each sample. The CO_2-rich phase

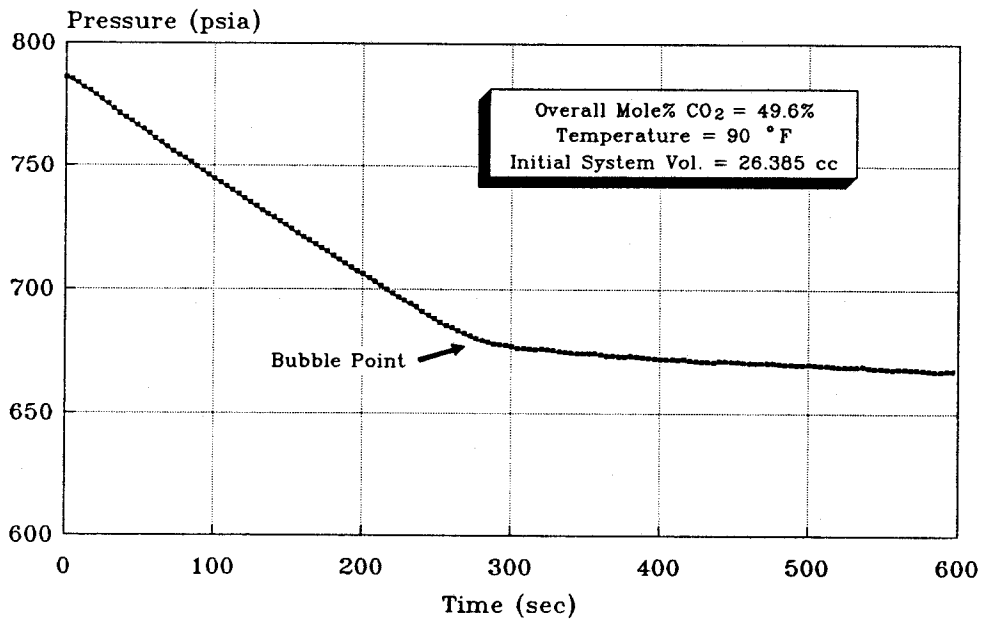

Figure 2.1-1. Bubblepoint pressure determination by expansion of the sample at a constant rate of 0.1 cm^3/min.

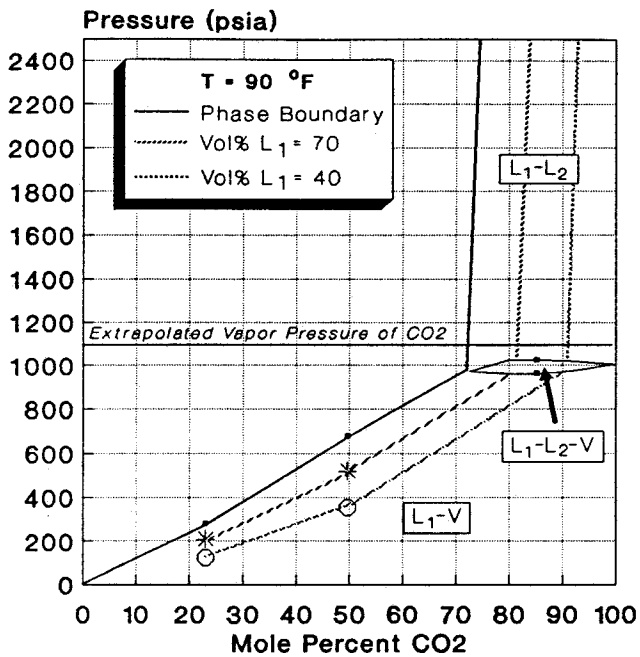

Figure 2.1-2. Pressure-composition phase diagram for mixtures of CO_2 with Means crude oil at 90°F.

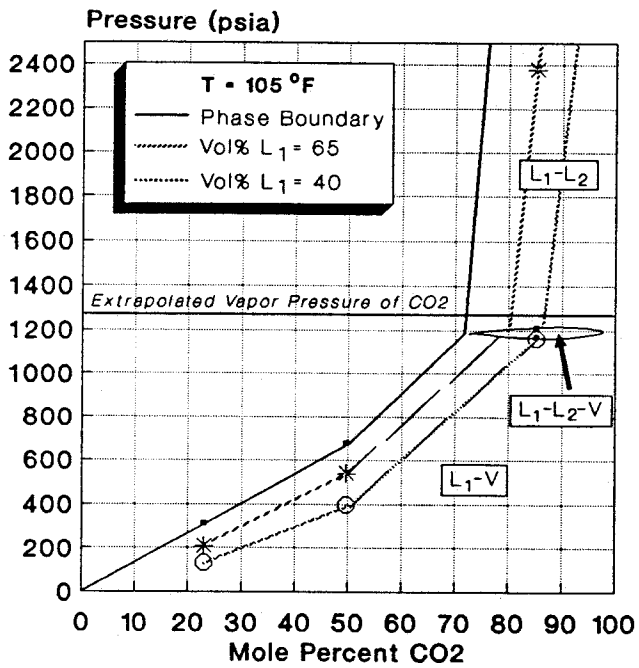

Figure 2.1-3. Pressure-composition phase diagram for mixtures of CO_2 with Means crude oil at 105°F.

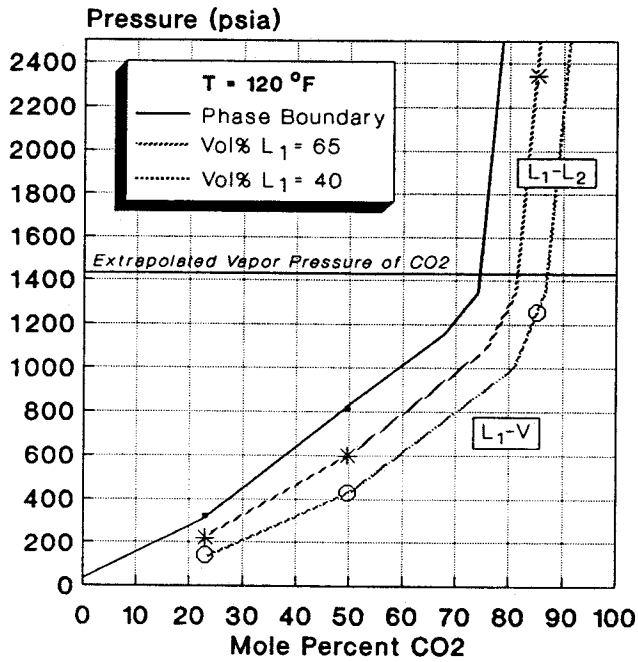

Figure 2.1-4. Pressure-composition phase diagram for mixtures of CO_2 with Means crude oil at 120°F.

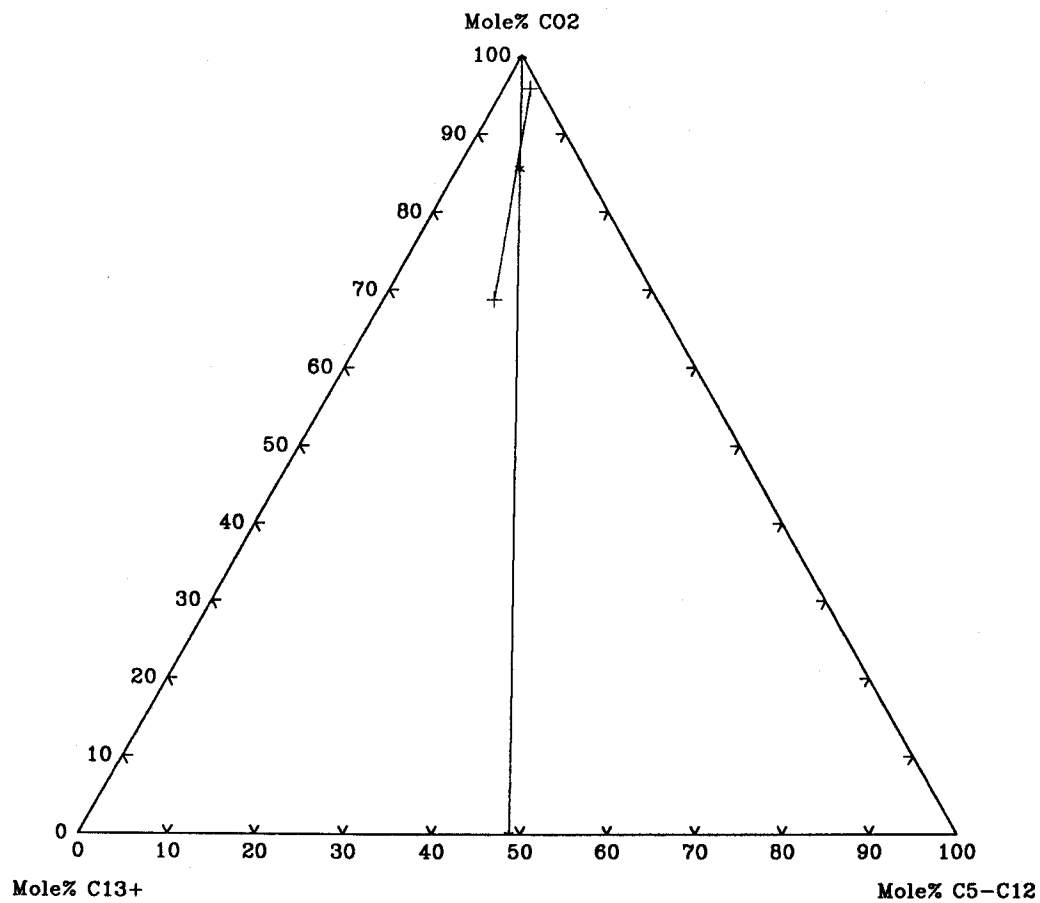

Figure 2.1-5. Pseudoternary phase compositions for samples taken at 2000 psia and 105°F.

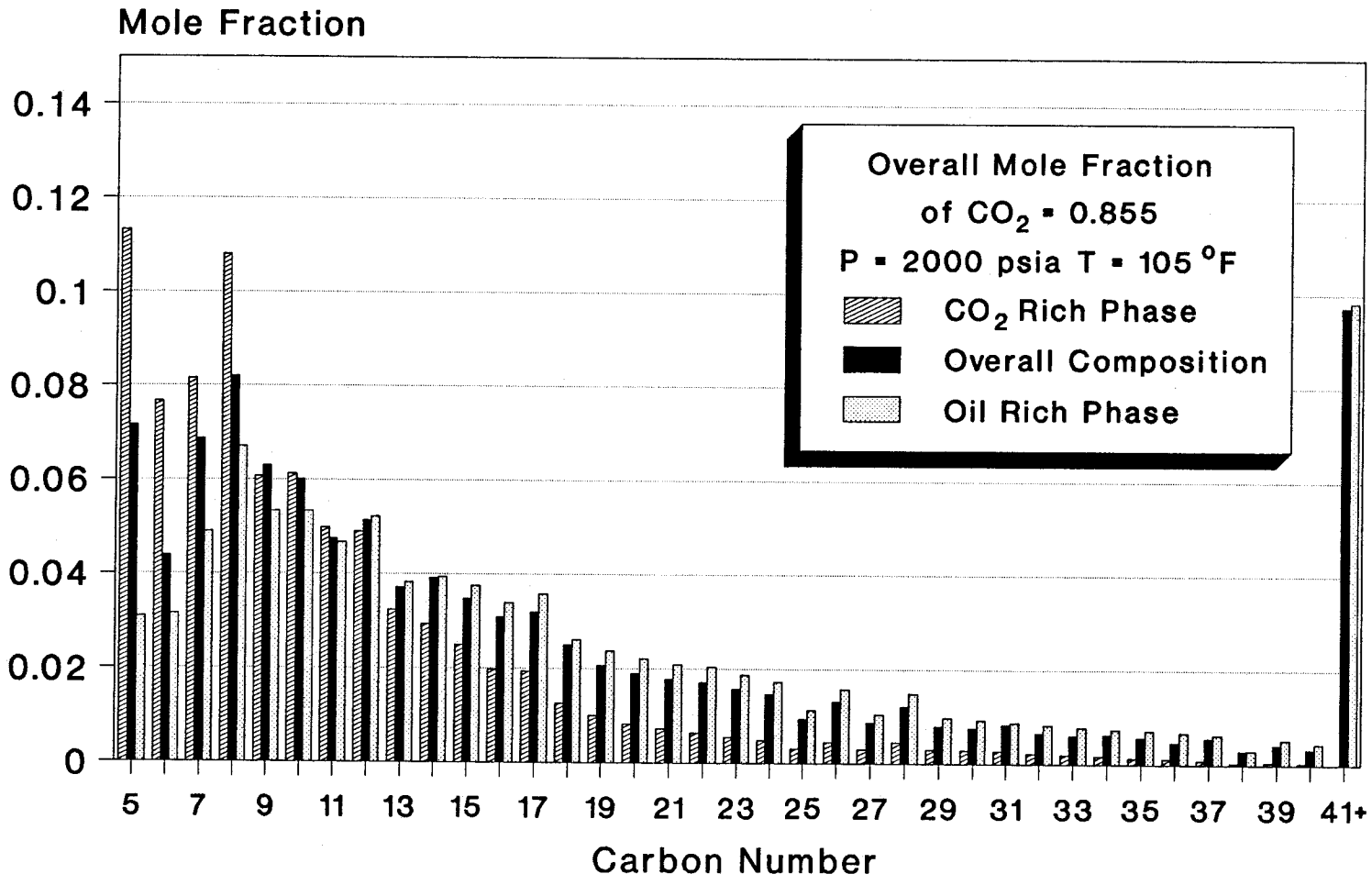

Figure 2.1-6. Composition distribution of hydrocarbons present in the CO_2-rich phase, the original oil, and the oil-rich phase for samples taken at 2000 psia and 105°F.

contained 95.8 mole percent CO_2 and the oil-rich phase, 68.7 mole percent CO_2. Fig. 2.1-6 illustrates clearly that CO_2 extracts the lighter hydrocarbons most efficiently. Below C_{12} the mole fraction of hydrocarbons in the CO_2-rich phase was larger than the overall mole fraction, and the mole fraction present in the oil-rich liquid was lower than the overall value. For hydrocarbons C_{13} and heavier, mole fractions in the oil-rich phase were higher than those of the original oil or the CO_2-rich phase. Thus, C_{11}-C_{12} and smaller hydrocarbons were extracted preferentially by the CO_2, while C_{13+} hydrocarbons remained in larger quantities in the oil-rich phase. It is interesting to note, however, that significant amounts of the hydrocarbons up to about C_{20} partitioned into the CO_2-rich phase, and that trace amounts of those as high as C_{40} were extracted from the crude oil.

2.1.3 Discussion

The general features of the phase behavior shown in Figs. 2.1-2 to 2.1-4 are quite similar to those reported previously for other Permian basin oils (Orr et al. 1981, Orr and Jensen 1984), despite the fact that the Means crude oil is somewhat heavier than oils examined previously (see Section 2.2 for a detailed comparison of the composition of several Permian basin oils). That result is consistent with the idea that a three-phase region will appear at temperatures above the critical temperature of CO_2 only if sufficient quantities of extractable hydrocarbons are present in the oil. The results shown in Fig. 2.1-5 indicate that dense CO_2 was able to extract significant amounts of hydrocarbons up to C_{20} or so. Thus, the experimental evidence for extraction is consistent with the appearance of three phases as long as the temperature is not too far above 88°F (31°C), the critical temperature of CO_2. The results shown here are also consistent with the analyses of Orr and Jensen (1984) and Larsen et al. (1989), who showed that if three phases appear, they will do so in the neighborhood of the extrapolated vapor pressure of CO_2. It is interesting to note, however, that the MMP for this oil, reported by Magruder et al. (1990) to be between 1850 and 2300 psia, is significantly higher than that of the oil examined by Orr and Jensen. Thus, while the phase diagrams are similar, the MMP's are not. The reasons for the differences must lie in the composition of the oil. Therefore, more detailed composition data are needed for further analysis of the MMP differences.

Additional experimental evidence concerning the specific hydrocarbons extracted by CO_2 is presented in Section 2.2, where results of analyses by mass spectrometry are described. Additional experiments to investigate the behavior of mixtures containing 75 mole percent CO_2 are underway now, and additional samples of CO_2-rich and oil-rich phases will be obtained. Those samples will permit an assessment of the effect of changes in pressure (and, hence, changes in density of the CO_2-rich phase) on the amounts and types of hydrocarbon molecules extracted.

2.1.4 Conclusions

Phase volume and phase composition measurements obtained for mixtures of CO_2 with Means crude oil at several temperatures indicate that:

(1) Phase behavior of the Means oil system is qualitatively and quantitatively similar to that observed for other Permian basin oils, despite the fact that the Means oil is heavier than oils from other fields investigated to date.

(2) Hydrocarbons lighter than C_{12} are extracted preferentially by dense CO_2, while C_{13+} hydrocarbons remain in greater quantities in the oil-rich phase.

(3) Despite the fact that smaller molecules are extracted more efficiently, significant amounts of hydrocarbons up to C_{20} and detectable amounts of hydrocarbons as heavy as C_{40} are extracted by a dense CO_2-rich phase.

2.2 GC-MS Analyses of Permian Basin Crude Oils

Karen D. Hagedorn and Mustafa Yilmaz

The composition of a crude oil must be known if predictions of miscible flood phase behavior are to be made. The methods most commonly used to determine crude oil compositions are true boiling-point distillation and simulated distillation (SIMDIS) by gas chromatography. While these methods give information about the distribution of hydrocarbons present, they do not provide any information as to what chemical structures make up these distributions. Mass spectrometry (GC-MS), however, can be used to determine the composition of a crude oil in terms of the structures of individual components. In this section, we report results of GC-MS analyses of samples taken in the PVT experiments described in Section 2.1. In addition, we report and compare analyses of five crude oils from the Permian Basin. Overall distributions of various chemical types and their distributions with respect to carbon number are reported. The effect of chemical structure on elution order from the GC is also discussed.

2.2.1 Experimental Equipment and Procedures

The experimental equipment used for these analyses consisted of a Finnigan MAT TSQ 70 mass spectrometer connected in series with a Varian 3400 gas chromatograph. A 30m x 0.32mm ID fused silica capillary column with a nonpolar dimethylpolysiloxane stationary phase of 0.5μm thickness was used to separate the components in roughly boiling point order for analysis in the mass spectrometer. Straight crude oil samples of 0.35μl were introduced into the column using a split injection technique. The column was temperature programmed from -10°C to 300°C at 3°C per minute, with isothermal periods at -10° and 300°. Electron impact (EI) was used as the ionization technique because it provides a wide array of fragment ions and because the characteristic EI spectra of many compounds are well documented. Each experiment required approximately 2 hours to complete.

2.2.2 Data Analysis

Once the raw data were collected, individual peaks were quantified and identified. An automatic quantitation program calculated peak areas based on user supplied baseline and noise level parameters. For each peak that was assigned an area, the mass spectrum was called up for identification. Identification was accomplished mainly through library searches, pattern interpretation by the user, comparison of elution order with published data or, more likely, a combination of all of these techniques.

Because crude oil is such a complex mixture, complete separation of all components by gas chromatography, especially within a reasonable time period, is nearly impossible. Thus, many of the calculated peaks actually consisted of two or more components coeluting. This occurrence is usually apparent from the mass spectrum. In some cases, spectral subtraction can "clean up" a spectrum enough for it to be identified in a library search. In most cases, however, it is up to the user to assign portions of the fragment pattern (i.e. certain ions) to individual components. Quantitative separation of coeluting components is done by assigning a percentage of the total peak area to each compound believed to be present, based on the summation of the intensities of the ions assigned to that compound.

The result of the quantitation and identification procedures was a list of components and their individual peak areas. Those areas were then converted to area fractions, which are roughly equivalent to weight fractions. True weight fraction calculations require the knowledge of a response factor for each component. For this study, response factors have been assumed to be equal to 1.0 for all components.

2.2.3 Analyses of Permian Basin Oils

Five crude oils were analyzed by the GC/MS technique. It should be noted that the fifth oil, Means, was analyzed under slightly different conditions than the other four.

The data presented here include compounds that elute before n–C_{30}. The column temperature limit prevented heavier compounds from being eluted from the column. In addition, the split injection technique requires that the sample be vaporized before it is flushed into the column. This technique may prevent some heavier components from getting into the column because the sample may not be completely vaporized. Because the intent of this investigation is to identify molecules extracted by dense CO_2, the limitation to molecules smaller than n–C_{30} is not a serious one.

Figs. 2.2-1 to 2.2-5 show the breakdown of the five oils by chemical type. The first two oils, Maljamar and Wasson, appear to be very similar. Oil C shows a much higher concentration of naphthenes than the first two. Oil D has much higher aromatic concentrations and also has higher sulfur content than any of the other oils. These four oils are quite similar, however, especially in terms of the n-alkane distribution. Fig. 2.2-5 shows the chemical type distribution for the Means oil. Like Oil C, Means has a relatively high concentration of naphthenes for this group of oils. The most significant deviation from the other four oils is in the n-alkane content. Means has a much higher area (weight) fraction of n-alkanes than the others.

Plots of the carbon number distributions of several chemical types, including n-alkanes, are given in Figs. 2.2-6 to 2.2-10. Those plots give a better indication of composition than do overall groupings by type because small molecules are extracted better than large ones by dense CO_2 regardless of type. Again, the Maljamar and Wasson compositions are very much alike. The graphs for Oil C and Oil D show that the heavy concentrations of naphthenes or aromatics occur primarily in the carbon number range of C_7 to C_{10}. The n-alkane difference between the Means oil and the other four oils is again depicted in Fig. 2.2-10. Means contains a significantly larger amount of higher carbon number n-alkanes than any of the others. While the differences in experimental conditions may make the difference difficult to interpret, other data, as well as simple visual inspection, confirm that Means is indeed the heavier oil.

In addition to very detailed compositional analyses, the use of mass spectrometry can provide information on the effect of chemical type on elution order from the GC. A major assumption in SIMDIS analyses is that any component eluting between C_{n-1} and C_n is a C_n compound. Fig. 2.2-11 shows the cumulative amount of C_n eluted versus elution time for several carbon numbers. The overlap of multiple curves at a given elution time shows that this assumption is not strictly justified, especially at higher carbon numbers. Since many pseudocomponent properties are based on the SIMDIS single carbon number assumption, knowledge of the true composition of each of these cuts is valuable.

Fig. 2.2-12 shows the calculated molecular weight for each single carbon number cut for Maljamar oil and the corresponding n-alkane molecular weights. Similar plots for the other oils show much the same results. The plots indicate that, for these oils, at least, the n-alkane molecular weight is a very good approximation for the cut molecular weight. Thus, despite the fact that hydrocarbons in a single carbon number cut do not necessarily have the carbon number of the associated n-alkane, the average molecular weight is still quite close to that of the n-alkane.

2.2.4 Analysis of Samples from PVT Experiments

Phase samples were collected from a PVT analysis of a Means-CO_2 mixture with a CO_2 concentration of 85 mole percent. The samples were taken at 2000 psia and 105°F (see Section 2.1). The samples from the PVT cell were flashed to standard conditions. Each of the

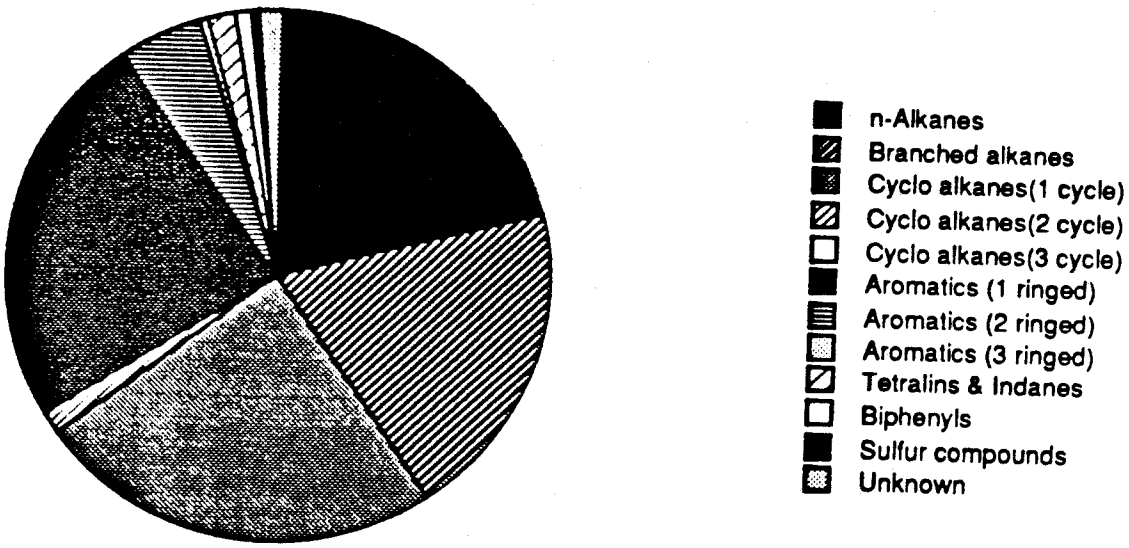

Figure 2.2-1. Distribution of molecular types present in Maljamar crude oil.

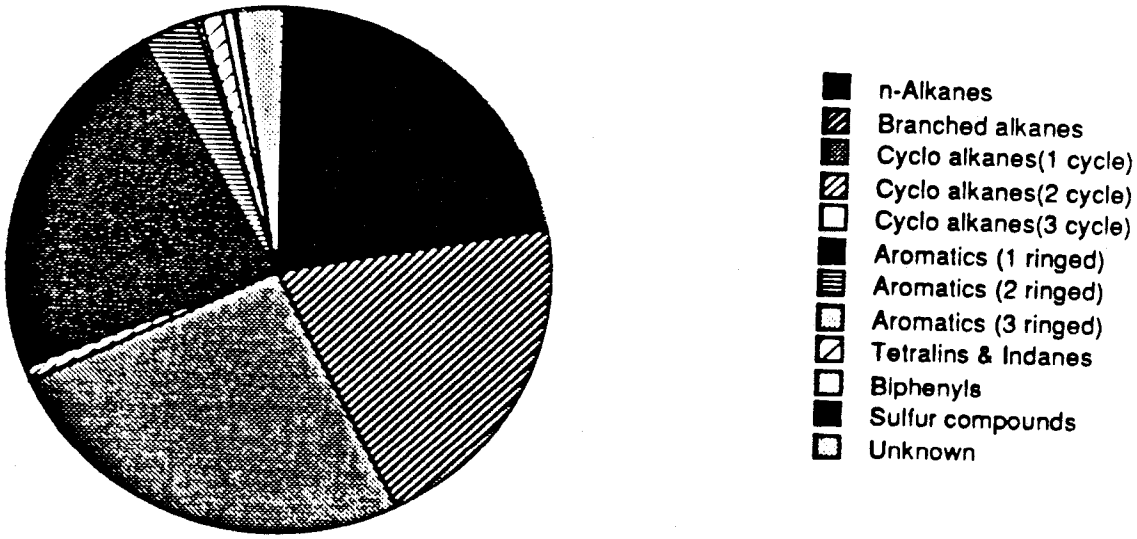

Figure 2.2-2. Distribution of molecular types present in Wasson crude oil.

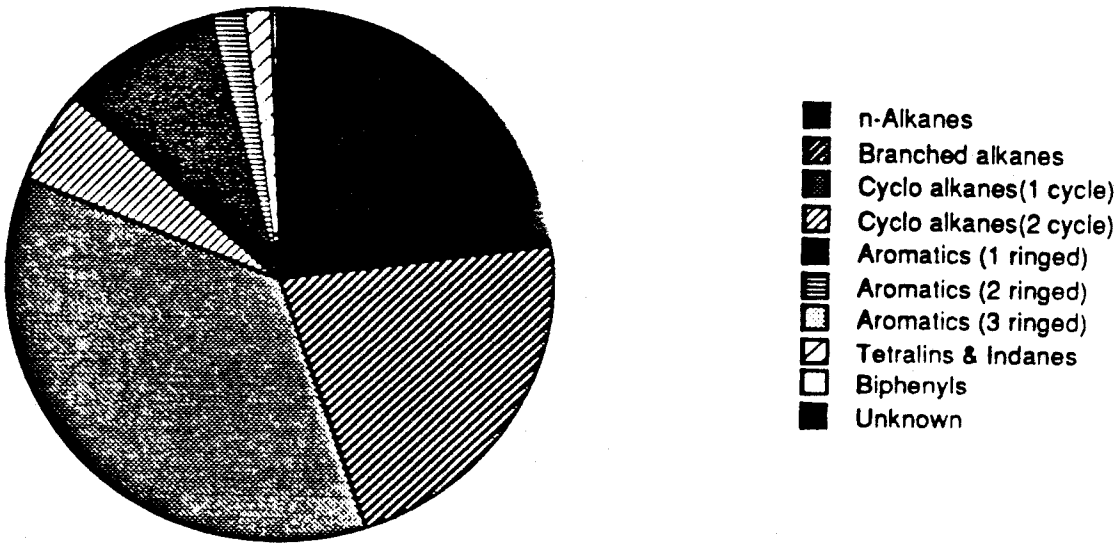

Figure 2.2-3. Distribution of molecular types present in crude oil C.

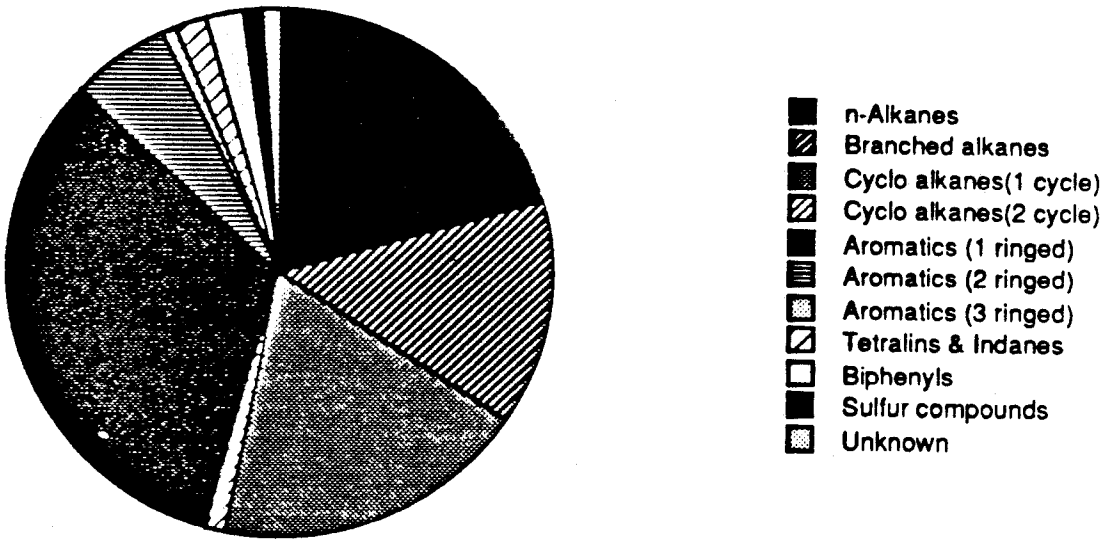

Figure 2.2-4. Distribution of molecular types present in crude oil D.

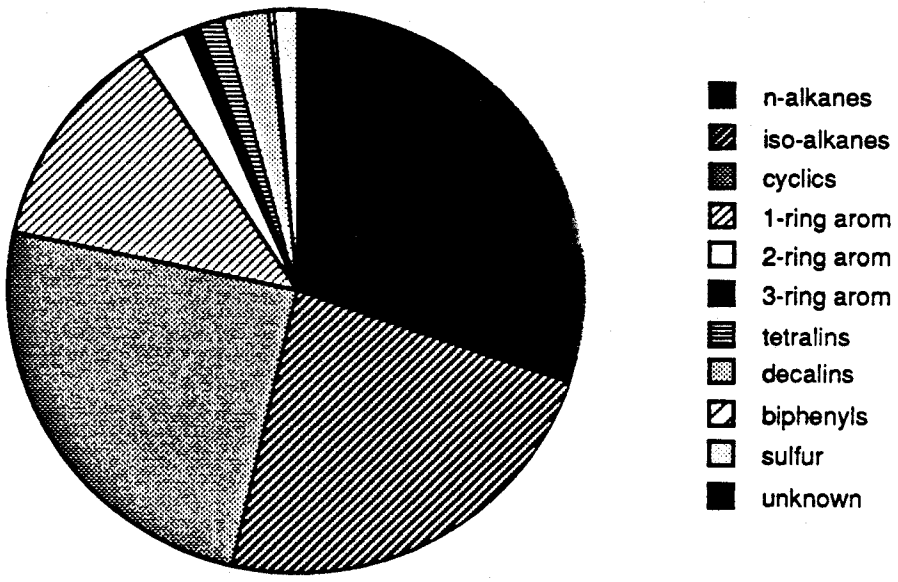

Figure 2.2-5. Distribution of molecular types present in Means crude oil.

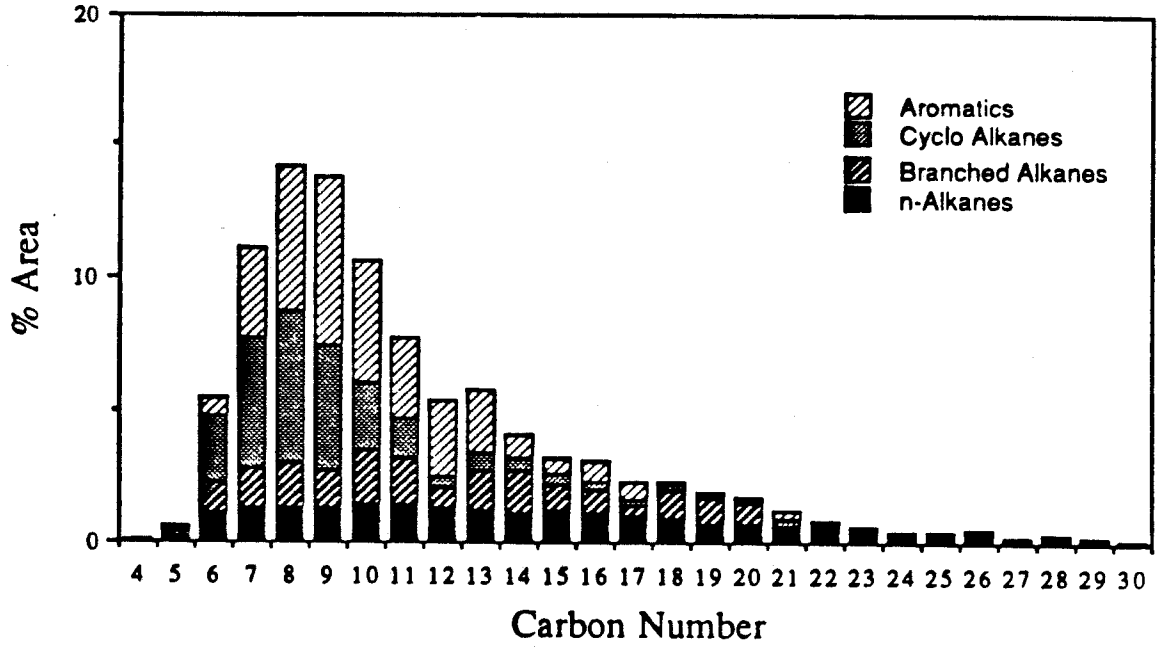

Figure 2.2-6. Carbon number distribution for Maljamar crude oil.

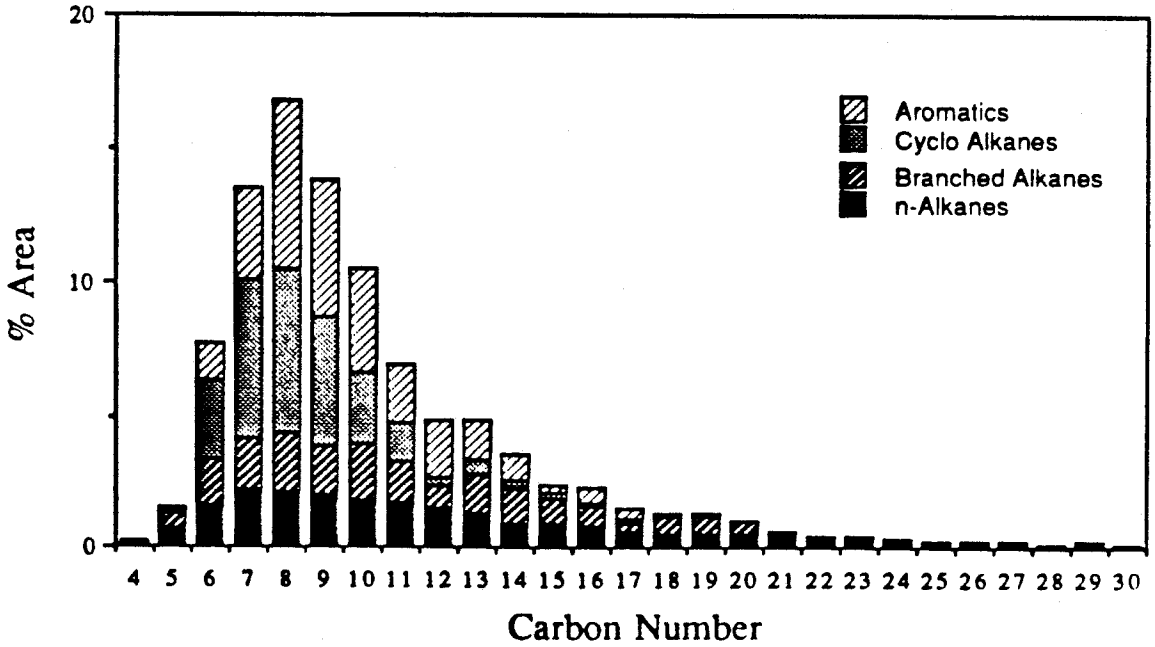

Figure 2.2-7. Carbon number distribution for Wasson crude oil.

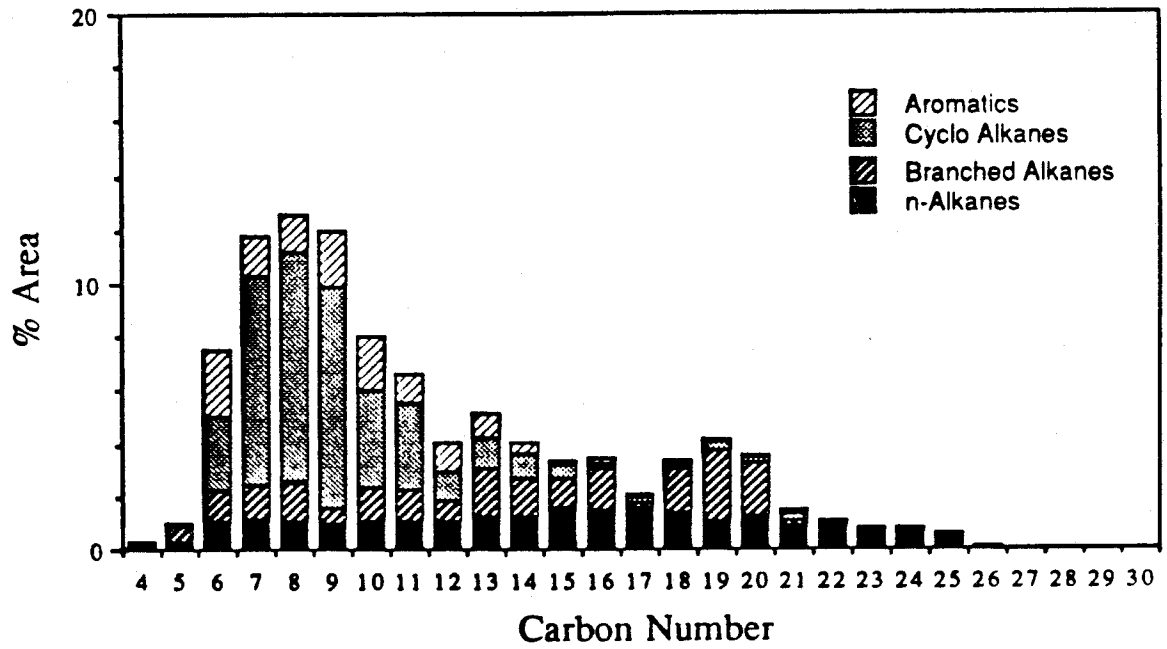

Figure 2.2-8. Carbon number distribution for crude oil C.

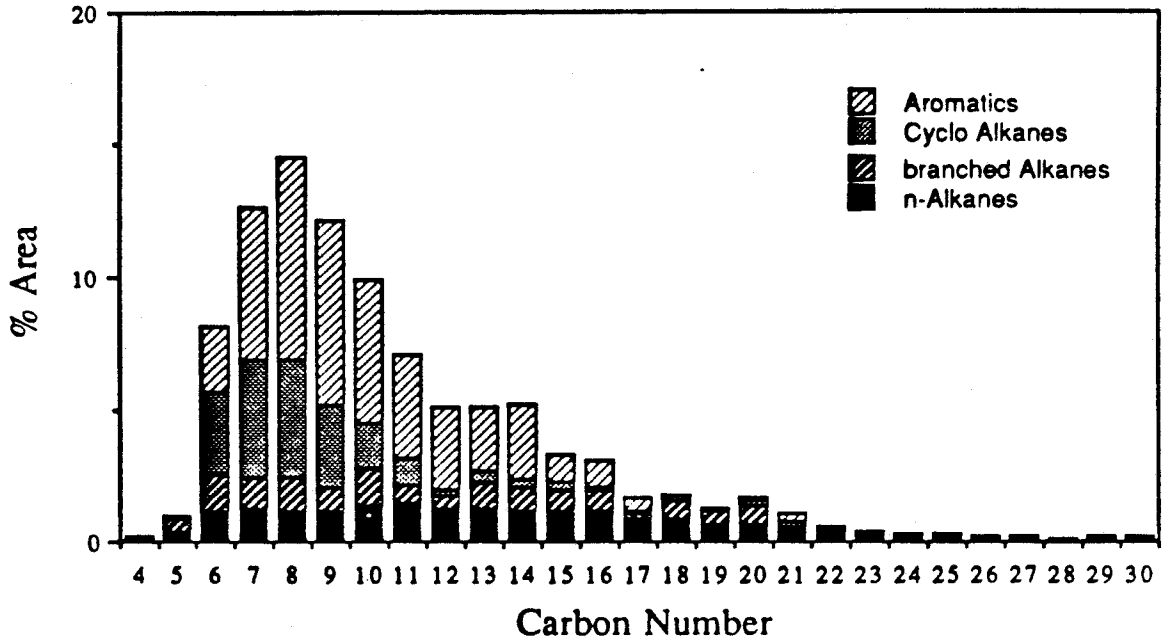

Figure 2.2-9. Carbon number distribution for crude oil D.

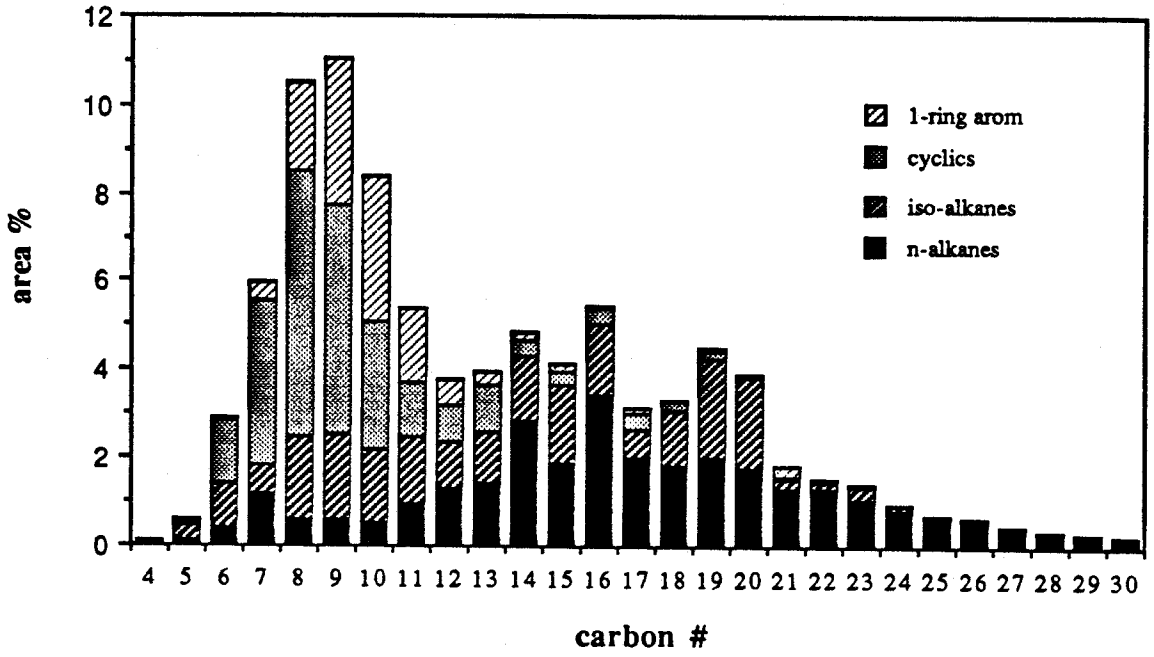

Figure 2.2-10. Carbon number distribution for Means crude oil.

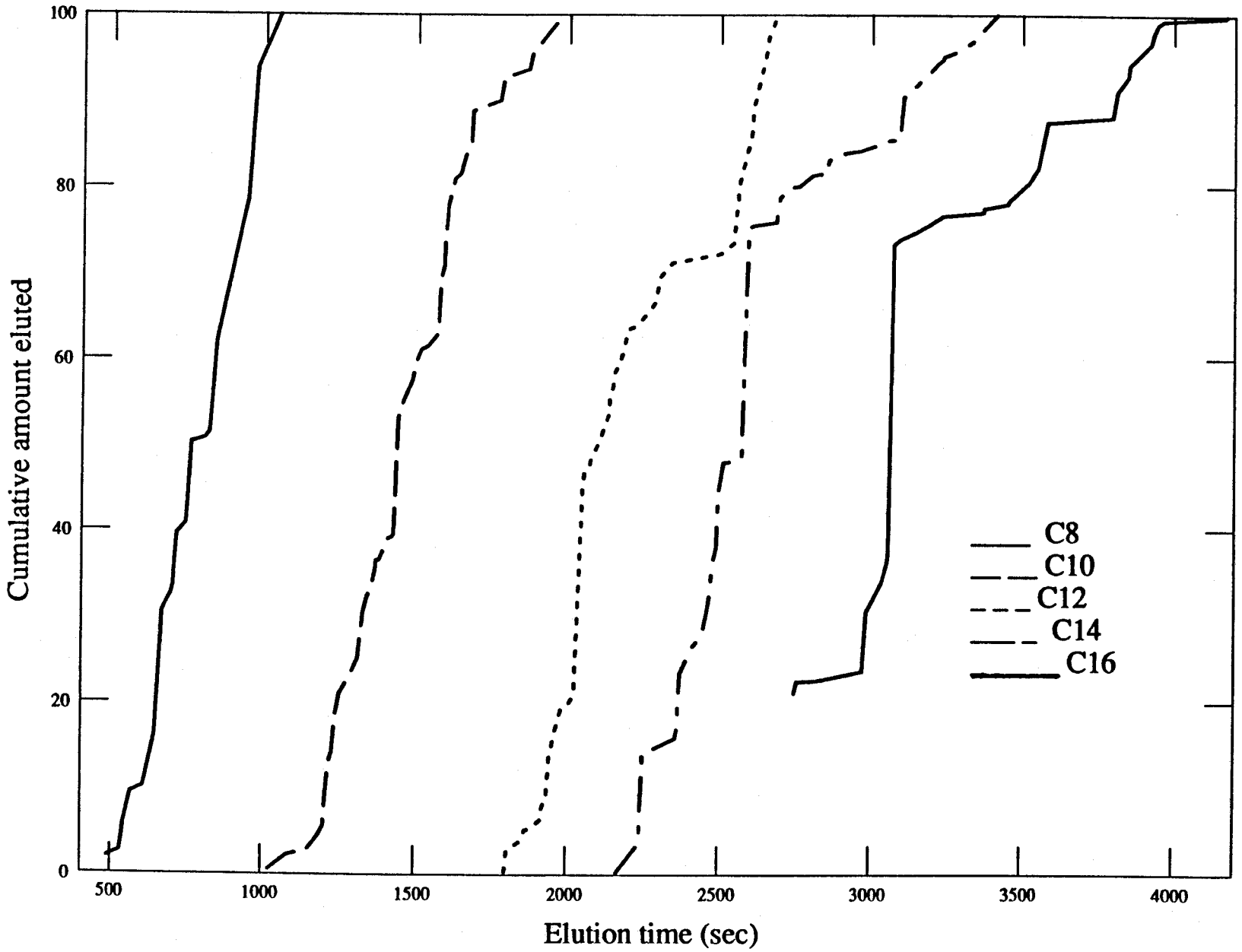

Figure 2.2-11. Elution times for hydrocarbons with a given carbon number.

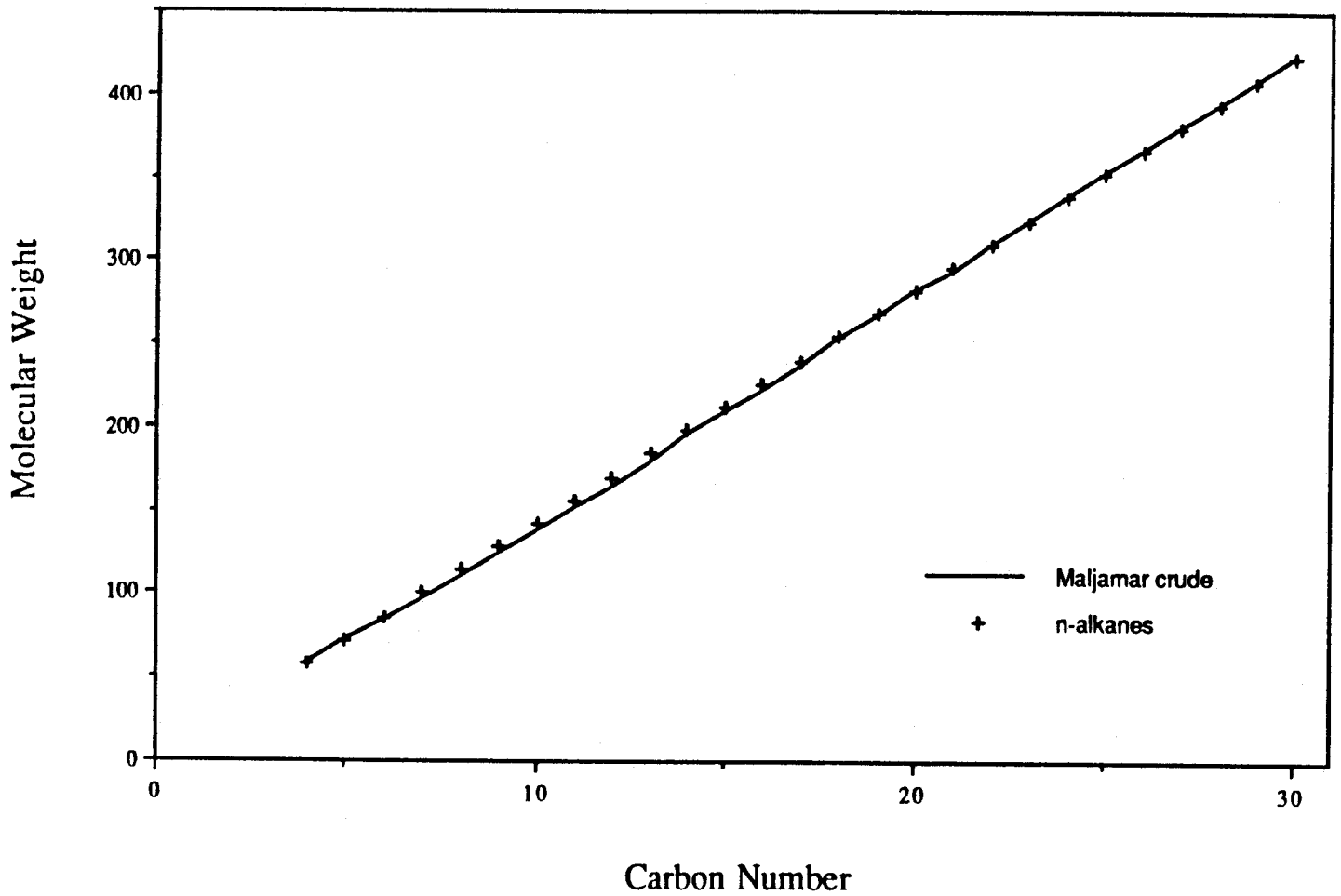

Figure 2.2-12. Average molecular weights of carbon number cuts for Maljamar crude oil.

two phases from the cell then produced a vapor sample and a liquid sample at standard conditions, resulting in a total of four samples. The vapor samples were analyzed using a gas chromatograph equipped with a TCD detector. The liquid samples were run on the GC/MS under conditions identical to those used for the straight crude oils. The vapor and liquid compositions for each phase sampled from the PVT cell were then recombined by material balance to yield an overall composition for each phase in the cell.

Because the GC analyses yielded only single carbon number compositions and the GC/MS analyses yielded much more detailed information, an assumption had to be made in order to recombine the two sets of data. For the hydrocarbons present in the vapor, which included only carbon numbers up to C_8, the assumption was made that all components in a given carbon number cut partition equally into the upper phase. The single carbon number GC data could then be divided up based on the GC/MS compositions for the liquid phase. In this manner, the two data sets could be recombined without losing the detailed GC/MS data.

Once the overall compositions for the phases in the cell were determined, components that were present in identifiable amounts in both phases and that could be indisputably matched to each other were selected for further analysis. K-values were calculated for each of these components on both mass fraction and mole fraction bases. The K-value is defined as the fraction of a given component in the upper phase divided by the fraction of that same component in the lower phase.

Results of the analyses are shown in Figs. 2.2-13 and 2.2-14. Fig. 2.2-13 shows K-values based on mole fractions versus MS scan number. (For these experiments, MS scan number corresponds directly to elution time in seconds.) Eleven different chemical type groups are represented by the different symbols. The data up to a scan number of about 2000 s (corresponding to a carbon number of about 10) are quite scattered, probably due to the difficulties in maintaining a material balance. However, the data after 2000 s show a fairly good correlation between K-value and elution time. (Note that elution time is column dependent, so these results hold only for this type of column.) When Fig. 2.2-13 is compared to Fig. 2.2-14, which shows mole fraction based K-values versus carbon number, it is apparent that K-values for carbon numbers greater than 10 correlate better with scan time than with carbon number. This is largely due to the presence of intermediate carbon number multi-ring compounds, especially the aromatics, which elute much later than alkanes having the same carbon number. Fig. 2.2-14 shows clearly that two and three ring aromatics tend to have the lowest K-values for a given carbon number. However, Fig. 2.2-13 shows that the K-values for these compounds are similar to those of the compounds that elute at the same time. That result suggests that pseudocomponents, mixtures of components lumped together for EOS computations, can be chosen conveniently from chromatography data. The ideal pseudocomponent is a set of hydrocarbons that partitions together. The results shown indicate that, on average, hydrocarbons that elute together also partition similarly.

Fig. 2.2-15 shows the effect of chemical type on K-value for a given carbon number. Note that the chemical types shown in Fig. 2.5-15 describe only the basic structure. Any of these may have one or more alkyl chains of any length. Fig. 2.2-15 confirms the idea that the multi-ring compounds with aromatic character partition into the upper phase much less effectively than other compounds of the same carbon number. Fig. 2.2-15 also shows that branched alkanes are the most effectively extracted by CO_2 (i.e., they have the highest K-values). The variation in K-values for compounds with the same chemical type and the same carbon number may be due to isomeric differences. For example, ring compounds with several short or branched side chains are probably extracted more efficiently by dense CO_2 than are molecules with a single long, unbranched side chain. More experimental evidence will be required, however, to sort out the reasons for the differences.

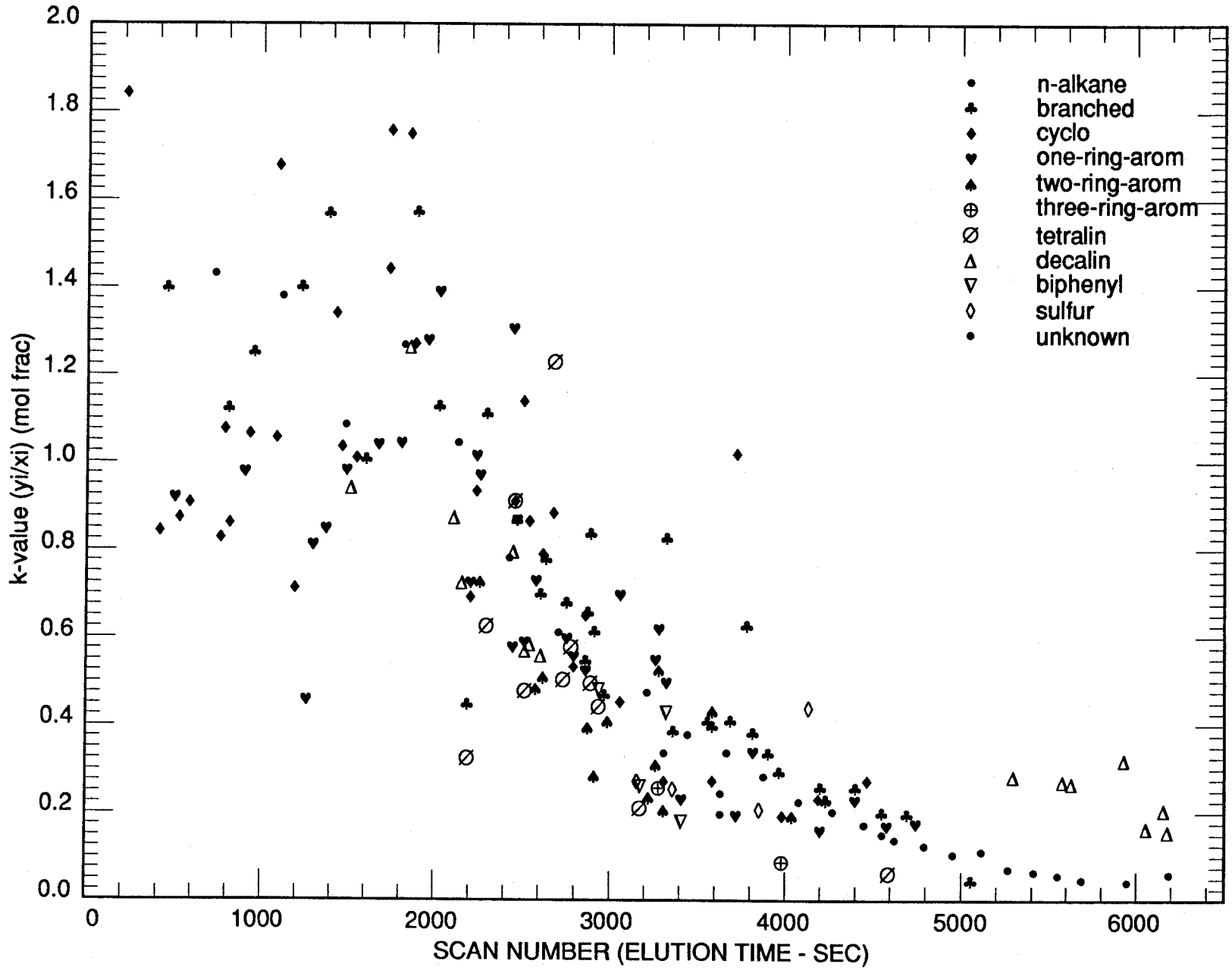

Figure 2.2-13. Normalized partition coefficients as a function of elution time for hydrocarbons identified from samples of equilibrium CO_2-rich and oil-rich phases for an 85 mole percent mixture of CO_2 with Means crude oil at 2000 psia and 105°F.

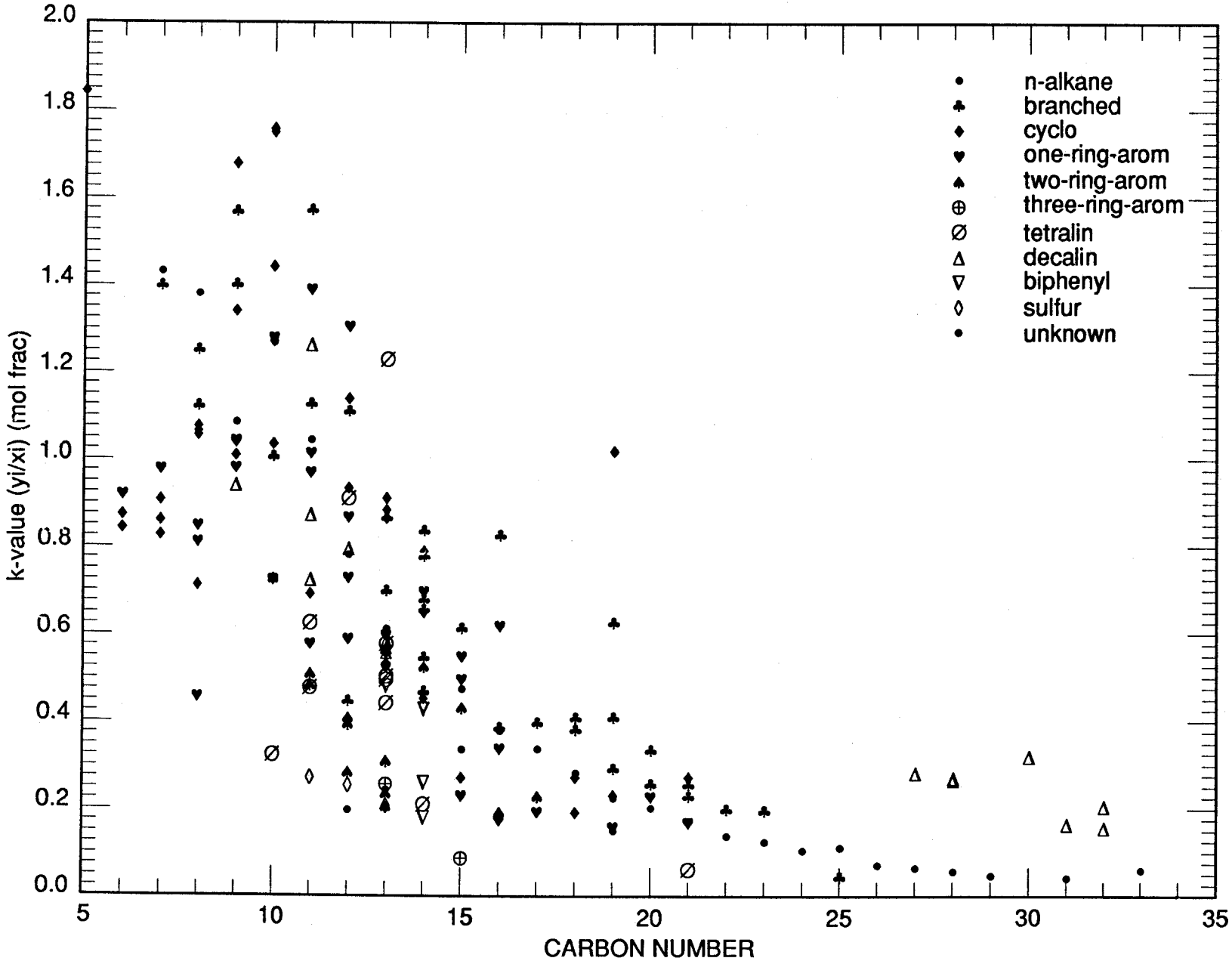

Figure 2.2-14. Normalized partition coefficients as a function of carbon number.

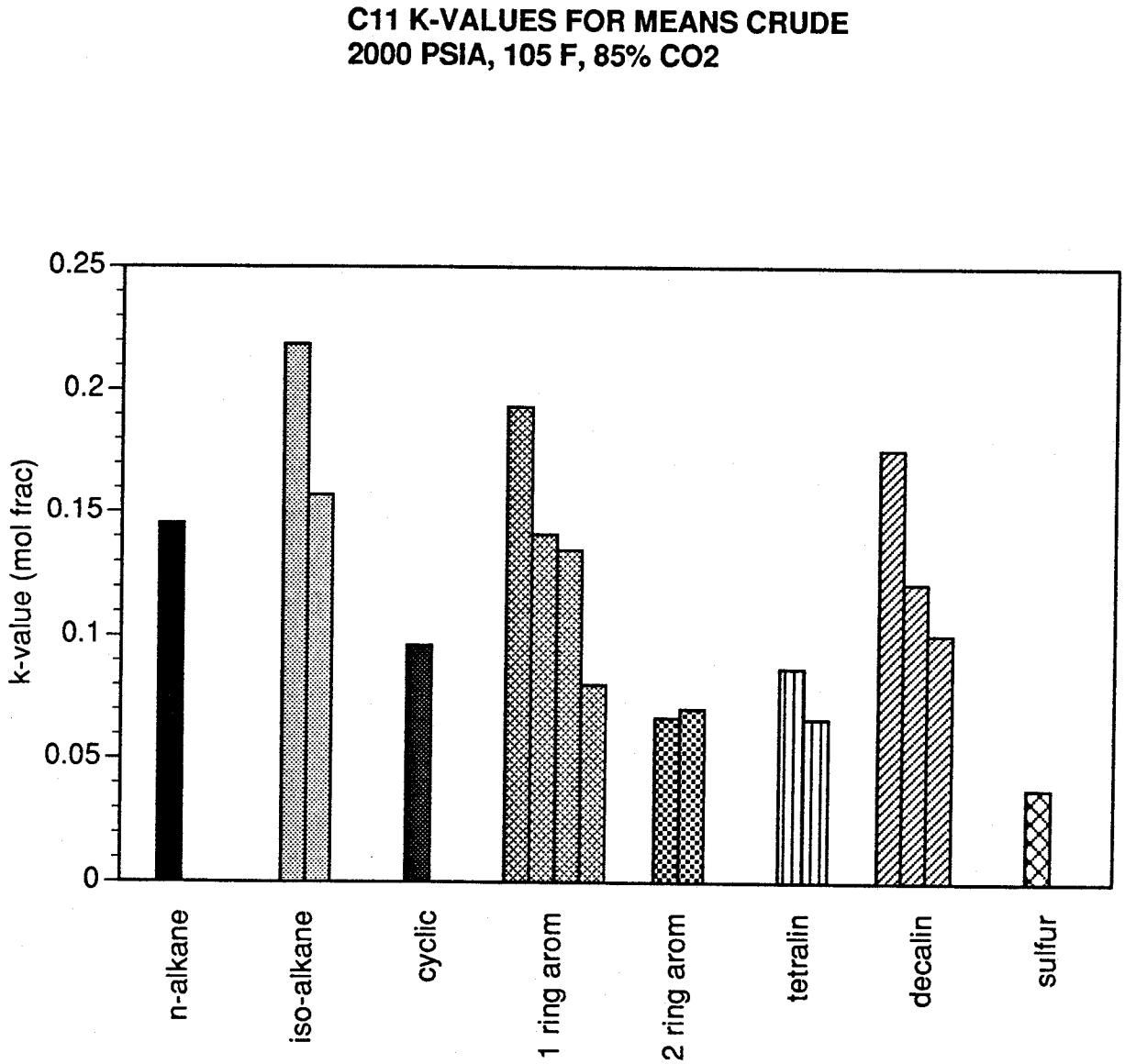

Figure 2.2-15. Partition coefficients for hydrocarbons with eleven carbon atoms.

Another comparison of the phase composition data, again normalized to remove the CO_2 present in each phase, is shown in Fig. 2.2-16. It reports the mole fractions of hydrocarbons of each carbon number determined for the components identified by GC-MS. It is similar therefore to Fig. 2.1-6, for which the data were obtained by simulated distillation. Clearly, the CO_2-rich phase contained lighter hydrocarbons than did the oil-rich phase. In Fig. 2.2-16, hydrocarbons carbon numbers were identified directly, so there are some quantitative differences from the estimated carbon numbers of Fig. 2.1-6. In addition, difficulties in identification compounds heavier than C_{20} limited the accuracy of that portion of the GC-MS analysis. Even so, both analyses indicate that substantial quantities of hydrocarbons up to C_{20} were extracted by CO_2 and both show that hydrocarbons lighter than about C_{12} are extracted preferentially over heavier hydrocarbons.

2.2.4 Conclusions

The detailed analyses of crude oils and of hydrocarbon samples taken from high-pressure phase equilibrium experiments lead to the following conclusions:

(1) Three oils, Wasson, Maljamar, and Oil D showed quite similar distributions of alkanes, naphthenes, and aromatics. Oil C showed larger naphthene and smaller aromatic concentrations than the others. Means crude oil was richer in heavy alkanes than other oils.

(2) Molecular weights calculated for single carbon number cuts agree well with the molecular weight of the corresponding n-alkane.

(3) Efficiency with which a given molecule is extracted by CO_2 correlates better with elution time than with carbon number. Thus, grouping of actual components into pseudocomponents by elution time from a nonpolar column is a reasonable approach for EOS calculations.

(4) Branched and normal alkanes are extracted more efficiently by dense CO_2 than are compounds containing rings, particularly those with multiple fused aromatic rings.

2.3 Supercritical Fluid Chromatography for Crude Oil Characterization

Maurice P. Stadler

The traditional method of studying phase behavior is by pressure-volume-temperature (PVT) experiments of the type described in Section 2.1. A typical experiment requires loading a vessel with the mixture to be studied, controlling the pressure and temperature in the vessel, and sampling and analyzing the phases that result. The data are used to tune an equation-of-state representation of phase behavior, which can then be used to interpolate between known results and also predict the phase behavior of new systems. The tuning procedure frequently requires the determination of binary interaction parameters between each hydrocarbon component or pseudocomponent and CO_2 if the application is to CO_2 miscible flooding. Binary interaction parameters are used to improve the accuracy of the EOS. However, PVT experiments are time consuming, and sampling operations are difficult. Thus, the development of techniques to obtain appropriate PVT information more efficiently would reduce the cost of experiments for crude oil characterization.

A more straightforward experimental technique is supercritical fluid chromatography (SFC). The SFC apparatus is similar to a gas chromatograph, except that the carrier fluid is high-pressure CO_2. Hydrocarbons, such as crude oils or pure hydrocarbon compounds, can be injected into the chromatograph. In this section we show that thermodynamic theory can be used to relate the time needed for a given compound to pass through the chromatograph to its

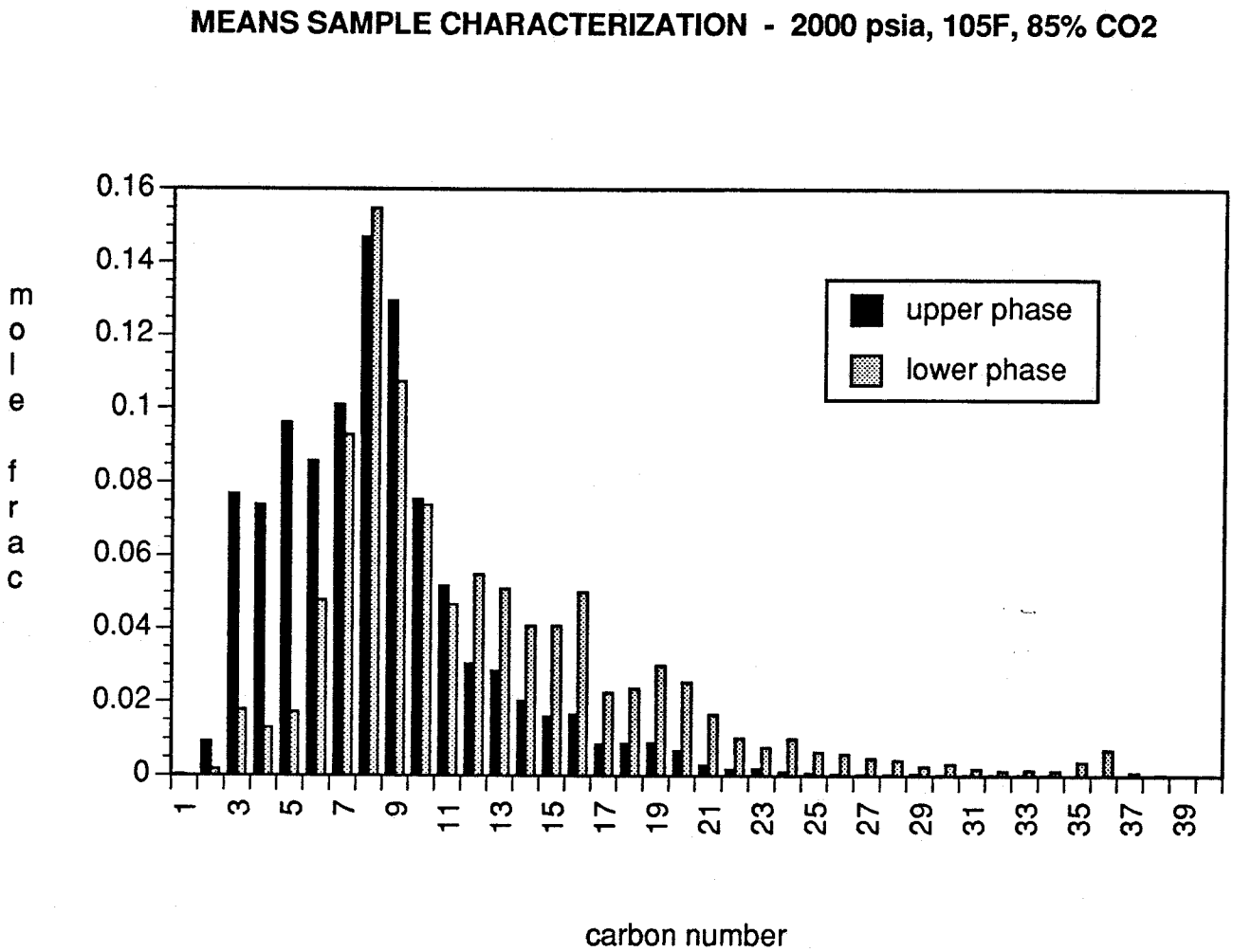

Figure 2.2-16. Compositions of CO_2-rich (upper) and oil-rich (lower) phases measured by GC-MS.

interaction with the CO_2 carrier fluid. In other words, the SFC retention times of the various hydrocarbon compounds can be used to determine some of the constants needed in the EOS.

2.3.1 SFC Apparatus

The apparatus, supplied by Applied Biosystems, is basically a GC which has been modified to accept supercritical CO_2 as the carrier fluid. This is done by placing a pump between the CO_2 supply vessel and the injection port. A schematic diagram of the entire apparatus is shown in Fig. 2.3-1.

The gas chromatograph used is a Hewlett-Packard (HP) Model 5890. A flame ionization detector is used to detect the material eluted from the column. This type of detector is ideal for analysis of hydrocarbons with a CO_2 carrier fluid because hydrocarbons burn easily whereas CO_2 does not.

An SFC MicroGradient System pump (Applied Biosystems) delivers the CO_2 at high pressures. This pump is designed to deliver fluids accurately at low flow rates. The pump consists of two 10 ml syringe pump cylinders. An important feature of the pump is that it can be programmed to deliver fluid at fixed or steadily changing pressures. That feature is similar to temperature programming in gas chromatography. The maximum allowable pressure is 5500 psig.

The injector is a Valco Model C14W manual injection valve. The column (Polysiloxane PM, 20 cm x 1.0 mm) was also supplied by Applied Biosystems. This type of column was chosen due to its ability to separate hydrocarbons. The column is connected to the detector through a restrictor, which is a 40 cm x .050 mm ID fused silica capillary. For this study, a Hewlett-Packard 3396A Integrator was used.

In order to facilitate the lab work, the experiments and data acquisition are partially automated by linking the components electronically. A schematic of the network is shown in Fig. 2.3-2. The HP 3396A Integrator and the HP 5890 GC are linked via the Instrument Network (INET). INET digitally transfers the raw detector data to the integrator. Also, the integrator can control all of the set points (oven temperature, detector temperature, etc.) of the GC.

The pump also has features for networking. The rear panel of the pump has relays for activating four external devices. Two of these event actuators are used in this study, one to activate the injector and one to start the integrator. These two events are included in the pump pressure program and start at exactly the same time.

Finally, the integrator is linked to an IBM Personal Computer AT through an RS232C port. This is done in order to store the chromatographic runs on the hard drive of the PC since the memory of the integrator is limited. In other words, the PC is simply used as an external disc drive. A file server program was acquired from HP, so that files can be transferred from the integrator to the PC and vice versa.

2.3.2 Thermodynamic Model of SFC

In this section, equations necessary to determine binary interaction parameters from SFC are derived. This derivation follows that of van Wassen and Schneider (1975).

The chromatographic column through which the CO_2 and injected material flow consists of two phases: a mobile phase (m), and a stationary phase (s). The solute of interest (component 1) is distributed between these two phases. The mobile phase consists almost entirely of CO_2 (component 2).

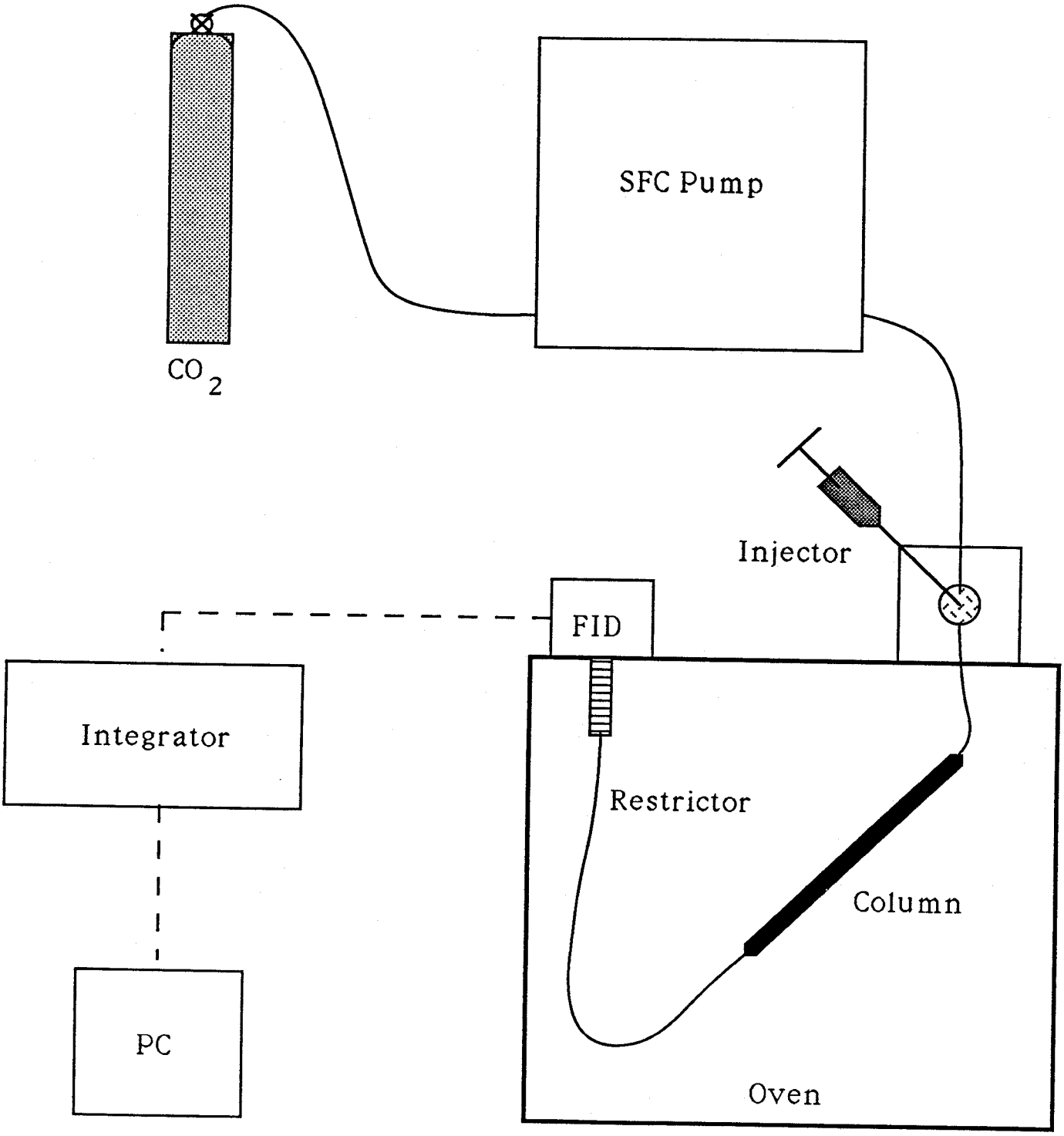

Figure 2.3-1. SFC apparatus (plumbing).

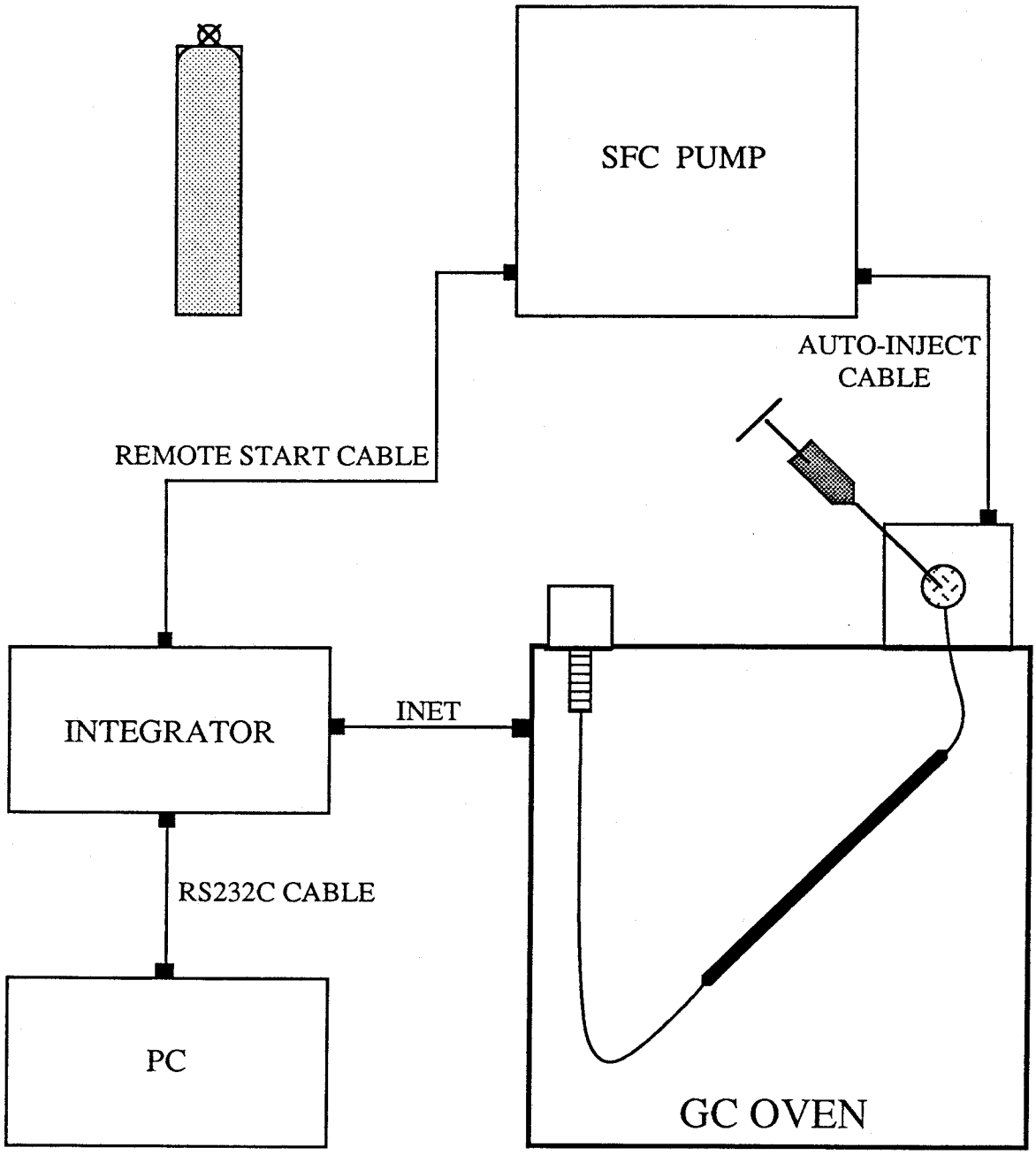

Figure 2.3-2. SFC apparatus (networking).

The chemical potential of the solute can be determined as follows.

$$d\overline{G}_1 = RT\, d\ln \hat{f}_1 \qquad \text{(const T)} \tag{2.3-1}$$

where $\overline{G}_1$ is the partial molar Gibbs function of the solute, R is the universal gas constant, T is the temperature, and $\hat{f}_1$ is the partial fugacity of the solute. Integration from the ideal state, indicated by a superscript o, yields

$$\overline{G}_1 - G_1^o = RT \ln\frac{\hat{f}_1}{f_1^o} \tag{2.3-2}$$

Addition and subtraction of RT ln x_1 to the right hand side of this equation, where x_1 is the mole fraction of component 1, gives

$$\overline{G}_1 - G_1^o = RT \ln\frac{\hat{f}_1}{x_1 f_1^o} + RT \ln x_1 \tag{2.3-3}$$

From the definition of the activity coefficient, $\gamma_i = \hat{f}_i/x_i f_1^o$,

$$\overline{G}_1 = G_1^o + RT \ln \gamma_1 x_1 \tag{2.3-4}$$

Since the partial molar Gibbs function is equivalent to the chemical potential,

$$\mu_1 = G_1^o + RT \ln \gamma_1 x_1 \tag{2.3-5}$$

If the solute is at local equilibrium in the column, then its chemical potential will be equal in both the mobile (m) and stationary (s) phases.

$$G_1^{o,m} + RT \ln \gamma_1^m x_1^m = G_1^{o,s} + RT \ln \gamma_1^s x_1^s \tag{2.3-6}$$

If the solute is at infinite dilution, then Henry's law is a reasonable choice for the ideal solution reference state, and $\gamma_1^m = \gamma_1^s = 1$. Eq. (2.3-6) now becomes

$$G_1^{o,m} + RT \ln x_1^m = G_1^{o,s} + RT \ln x_1^s \tag{2.3-7}$$

$$\ln\frac{x_1^s}{x_1^m} = \frac{1}{RT}(G_1^{o,m} - G_1^{o,s}) \tag{2.3-8}$$

From chromatography theory, the capacity ratio, k_1', (which is directly proportional to the partition coefficient) is given by

$$k_1' \equiv \frac{x_1^s}{x_1^m}\frac{V^m}{V^s}\frac{V^{t,s}}{V^{t,m}} = \frac{t_r}{t_o} - 1 \tag{2.3-9}$$

where V is the molar volume, V^t is the total volume, t_r is the chromatographic retention time of the solute, and t_o is the time it takes the carrier gas to pass through the column. The units of k_1' are (moles of solute 1 in the stationary phase)/(moles of solute 1 in the mobile phase). These units become clear upon including the units in the definition in Eq. (2.3-9).

$$x \;[=]\; \frac{\text{moles of solute}}{\text{moles of phase}},\; V \;[=]\; \frac{\text{volume of phase}}{\text{moles of phase}},\text{ and } V^t \;[=]\; \text{volume of phase} \tag{2.3-10}$$

The equality in Eq. (2.3-9) is used to calculate the capacity factor experimentally. Combination of Eqs. (2.3-8) and (2.3-9) gives

$$\ln\left[k_1'\frac{V^s}{V^m}\frac{V^{t,m}}{V^{t,s}}\right] = \frac{1}{RT}(G_1^{o,m} - G_1^{o,s}) \tag{2.3-11}$$

Next we take the partial derivative of Eq. (2.3-11) with respect to pressure. In addition we assume that

$$\left[\frac{\partial}{\partial P}\left(\frac{V^s V^{t,m}}{V^{t,s}}\right)\right]_T = 0 \tag{2.3-12}$$

Also, recall that

$$\left(\frac{\partial G_1^o}{\partial P}\right)_{T,x} = V_1^o \tag{2.3-13}$$

Eq. (2.3-11) now becomes

$$\left(\frac{\partial \ln k_1'}{\partial P}\right)_T = \frac{1}{RT}(V_1^{o,m} - V_1^{o,s}) + \left(\frac{\partial \ln V_1^m}{\partial P}\right)_T \tag{2.3-14}$$

Recall that for Henry's law, $V_1^o = \overline{V}_1^\infty$, where $\overline{V}_1^\infty$ is the partial molar volume of component 1 at infinite dilution. Also, $V^m = V_2$ since the mobile phase is essentially pure CO_2. Making these substitutions, Eq. (2.3-14) becomes

$$\left(\frac{\partial \ln k_1'}{\partial P}\right)_T = \frac{1}{RT}(\overline{V}_1^{\infty,m} - \overline{V}_1^{\infty,s}) + \frac{1}{V_2}\left(\frac{\partial \ln V_2}{\partial P}\right)_T \tag{2.3-15}$$

Now, $\overline{V}_1^{\infty,m}$ can be calculated from the expression

$$\overline{V}_1^{\infty,m} = \lim_{n_1\to 0}\left\{\left[\frac{\partial(nV^m)}{\partial n_1}\right]_P\right\}_{T,n_2} \tag{2.3-16}$$

$$= \lim_{n_1\to 0}\left[-n\left(\frac{\partial V^m}{\partial P}\right)_{n_1}\left(\frac{\partial P}{\partial n_1}\right)_{V^m}\right]_{T,n_2} \tag{2.3-17}$$

Substitution of this expression into Eq. (2.3-15) yields

$$\left(\frac{\partial \ln k_1'}{\partial P}\right)_T = -\frac{1}{RT}\left\{n\lim_{n_1\to 0}\left[\left(\frac{\partial V^m}{\partial P}\right)_{n_1}\left(\frac{\partial P}{\partial n_1}\right)_{V^m} + \overline{V}_1^{\infty,s}\right\} + \frac{1}{V_2}\left(\frac{\partial V_2}{\partial P}\right)_T \tag{2.3-18}$$

or

$$\left(\frac{\partial \ln k_1'}{\partial P}\right)_T = -\frac{n}{RT}\lim_{n_1\to 0}\left(\frac{\partial P}{\partial n_1}\right)_{V,T,n_2}\left(\frac{\partial V_2}{\partial P}\right)_T - \frac{\overline{V}_1^{\infty,s}}{RT} + \frac{1}{V_2}\left(\frac{\partial V_2}{\partial P}\right)_T \tag{2.3-19}$$

This is the equation that is used to predict the elution time of a solute through the SFC.

2.3.3 Procedure

The Peng-Robinson EOS is used to calculate the terms in Eq. (2.3-19) (Yonker et al. 1987). The only unknowns during a chromatographic experiment are $\overline{V}_1^{\infty,s}$ and δ_{12}, the Peng-Robinson binary interaction coefficient between the solute and CO_2, as long as the critical properties, P_c and T_c, and the acentric factor, ω, are known. $\overline{V}_1^{\infty,s}$ and δ_{12} can be determined by measuring the elution times of the solute at several pressures and fitting Eq. (2.3-19) to the data.

The typical experimental procedure includes making several chromatographic runs for a selected hydrocarbon at different pressures. In each constant pressure run, the retention time of the solute and the residence time of the carrier fluid (as measured with methane) is taken directly from the chromatograph. (Fig. 2.3-3 is an example of one such constant pressure run.) With these retention times and pressures, the first term of Eq. (2.3-19) can be determined. The second and fourth terms in Eq. (2.3-19) are calculated with the Peng-Robinson EOS, which includes the unknown binary interaction parameter, δ_{12}. The third term in Eq. (2.3-19) is also unknown. The two unknowns are calculated by regression using the retention times vs. pressure as input. An example fit of Eq. (2.3-19) to actual experimental data is given in Fig. 2.3-4.

2.3.4 Results and Discussion

Although the procedure described in Subsection 2.3.3 should allow determination of the binary interaction parameter between the solute of interest and CO_2, this is not the case in practice. The reason is that $\overline{V}_1^{\infty,s}$ and δ_{12} have a very high statistical correlation. Fig. 2.3-5 illustrates this high statistical correlation. Fig. 2.3-5 was constructed by calculating $\overline{V}_1^{\infty,s}$ using Eq. (2.3-19) for δ_{12} ranging from 0.5 to 1.5. The n-docosane experiment was chosen for this figure. It is evident that $\overline{V}_1^{\infty,s}$ and δ_{12} are not independent parameters. This means that these two values can not be determined simultaneously with high precision from a single set of data.

One possible solution to this problem is to create a correlation to determine $\overline{V}_1^{\infty,s}$ independently. This is done by fitting Eq. (2.3-19) to SFC experiments involving hydrocarbons for which the CO_2 binary interaction parameters are reported in the literature. For this case, the regression involves only one unknown, $\overline{V}_1^{\infty,s}$. The correlation shown in Fig. 2.3-6 presents the results of these experiments. This correlation plots the value of $\overline{V}_1^{\infty,s}$ obtained from chromatographic experiments at several pressures for normal alkanes ranging from octane (n-C_8) to dotriacontane (n-C_{32}). The experimental values of $\overline{V}_1^{\infty,s}$ are listed in Table 2.3-1. The EOS terms in Eq. (2.3-19) were calculated using binary interaction parameters taken from Deo et al. (1989). These binary interaction parameters are also listed in Table 2.3-1.

We will now illustrate the use of this correlation. Suppose we wish to know the phase behavior of a CO_2–n-dodecane binary system. Entering the x-axis of Fig. 2.3-6 at 12 (for the number of carbon atoms in dodecane) yields 590 cm^3/mol for $\overline{V}_1^{\infty,s}$. From a set of chromatographic experiments for dodecane at varying pressures and this value of $\overline{V}_1^{\infty,s}$, regression of Eq. (2.3-19) yields a binary interaction parameter of 0.094 between CO_2 and n-dodecane. With this binary interaction parameter, the Peng-Robinson EOS is used to calculate the phase behavior of a CO_2–n-dodecane binary system. This calculated phase behavior is shown in a P-x diagram in Fig. 2.3-7. Also shown is actual phase behavior data determined experimentally by Stewart and Neilsen (1954). The calculated phase behavior agrees fairly well with the experimental data except in the critical region. [Deo et al. (1989) have shown that the Peng-Robinson EOS with a binary interaction parameter of 0.1035 accurately matches the experimental data of Stewart and Neilsen (1954).]

Table 2.3-1. Results of regression. The binary interaction parameters are taken from Deo et al. (1989). The $\overline{V}_1^{\infty,s}$ values are calculated. The exception is $C_{12}H_{26}$ for which $\overline{V}_1^{\infty,s}$ was taken from Fig. 2.3-6 and δ_{12} was calculated.

n-Alkane	Binary Interaction Parameter	$\overline{V}_1^{\infty,s}$ ($cm^3\ mol^{-1}$)
C_8H_{18}	.109	470.
C_8H_{18}	.109	473.
C_8H_{18}	.109	409.
$C_{10}H_{22}$	.100	495.
$C_{10}H_{22}$	.100	570.
$C_{10}H_{22}$	.100	544.
$C_{11}H_{24}$	.100	545.
$C_{12}H_{26}$	.094	590.
$C_{14}H_{30}$	.110	580.
$C_{14}H_{30}$	.110	589.
$C_{15}H_{32}$	.093	670.
$C_{16}H_{34}$	.098	682.
$C_{16}H_{34}$	.098	604.
$C_{16}H_{34}$	.098	711.
$C_{18}H_{38}$	.104	742.
$C_{22}H_{46}$	.093	883.
$C_{22}H_{46}$	.093	910.
$C_{32}H_{66}$	.063	1349.
$C_{32}H_{66}$	.063	1347.
$C_{32}H_{66}$	.063	1345.
$C_{32}H_{66}$	.063	1330.
$C_{32}H_{66}$	.063	1338.

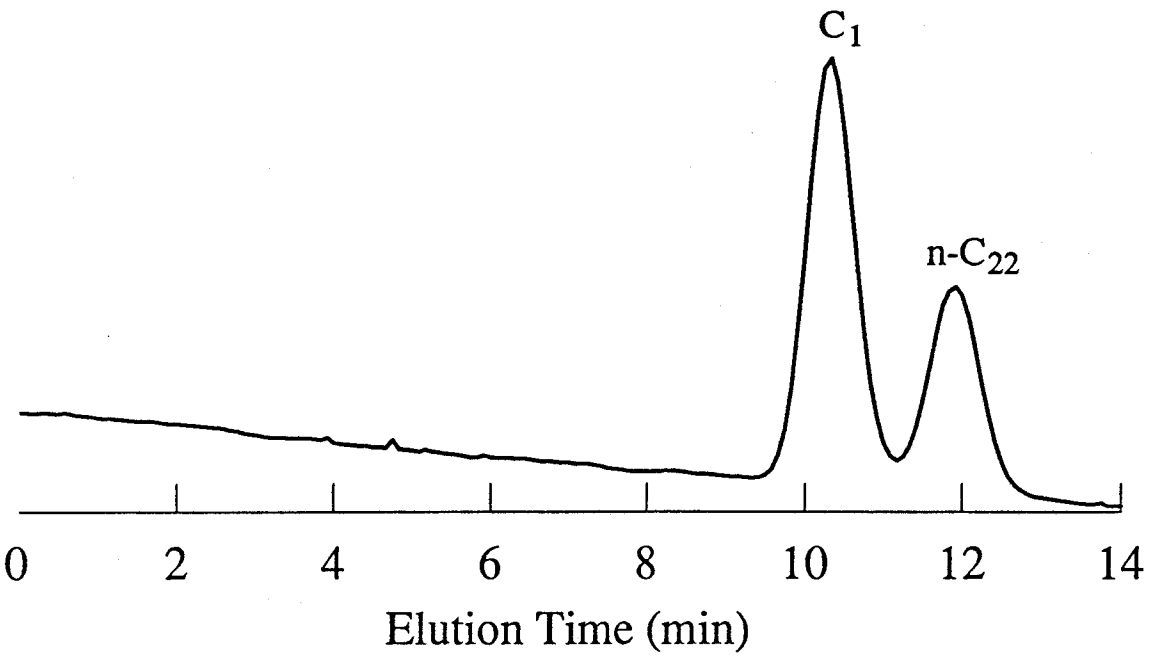

Figure 2.3-3. Example chromatogram of methane and n-docosane at 131°C.

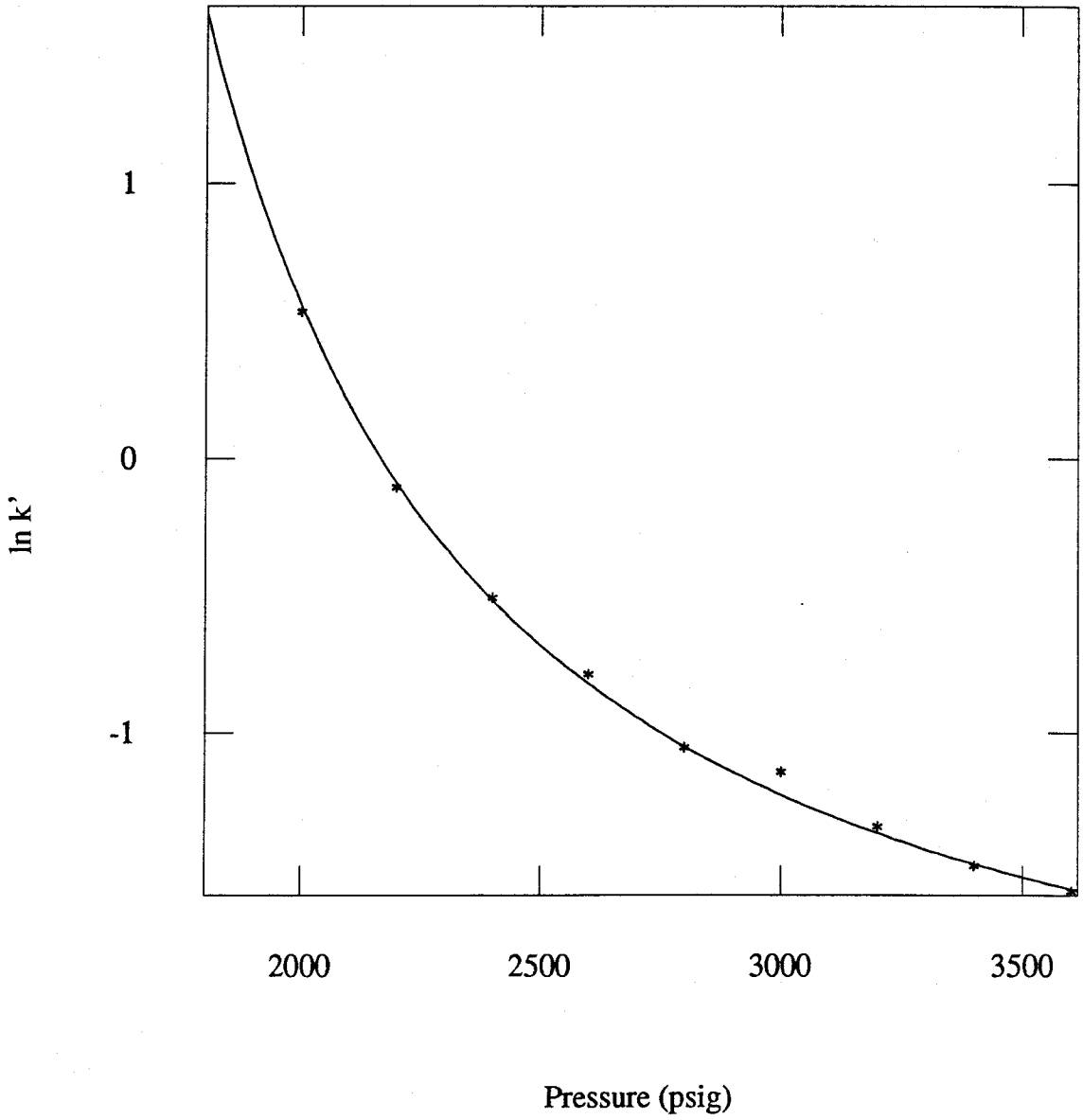

Figure 2.3-4. Fit of Eq. (2.3-19) to experimental results for n-docosane at 131°C.

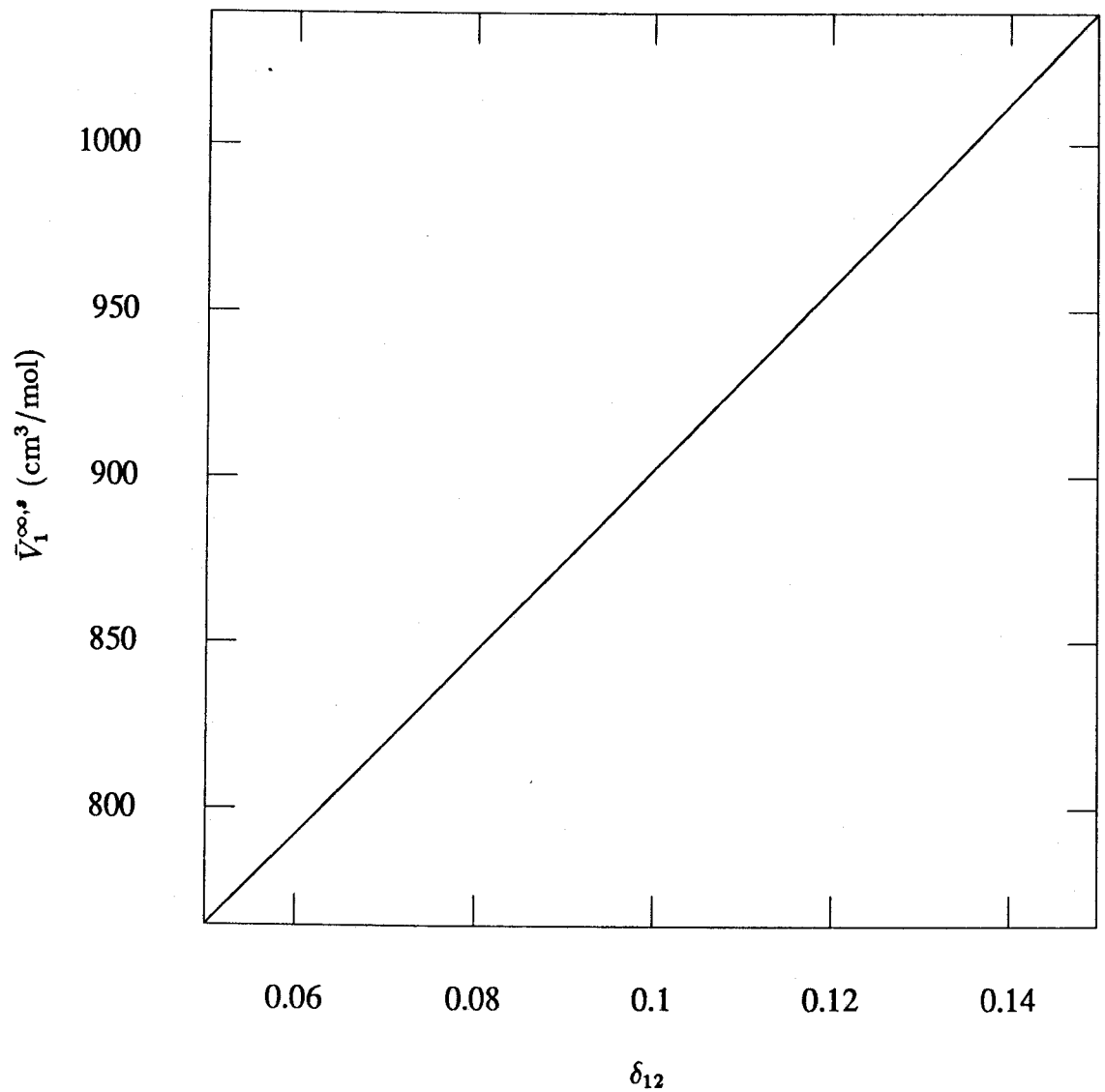

Figure 2.3-5. Plot illustrating the high statistical correlation between $\bar{V}_1^{\infty,s}$ and δ_{ij}. These results are for n-docosane at 131°C.

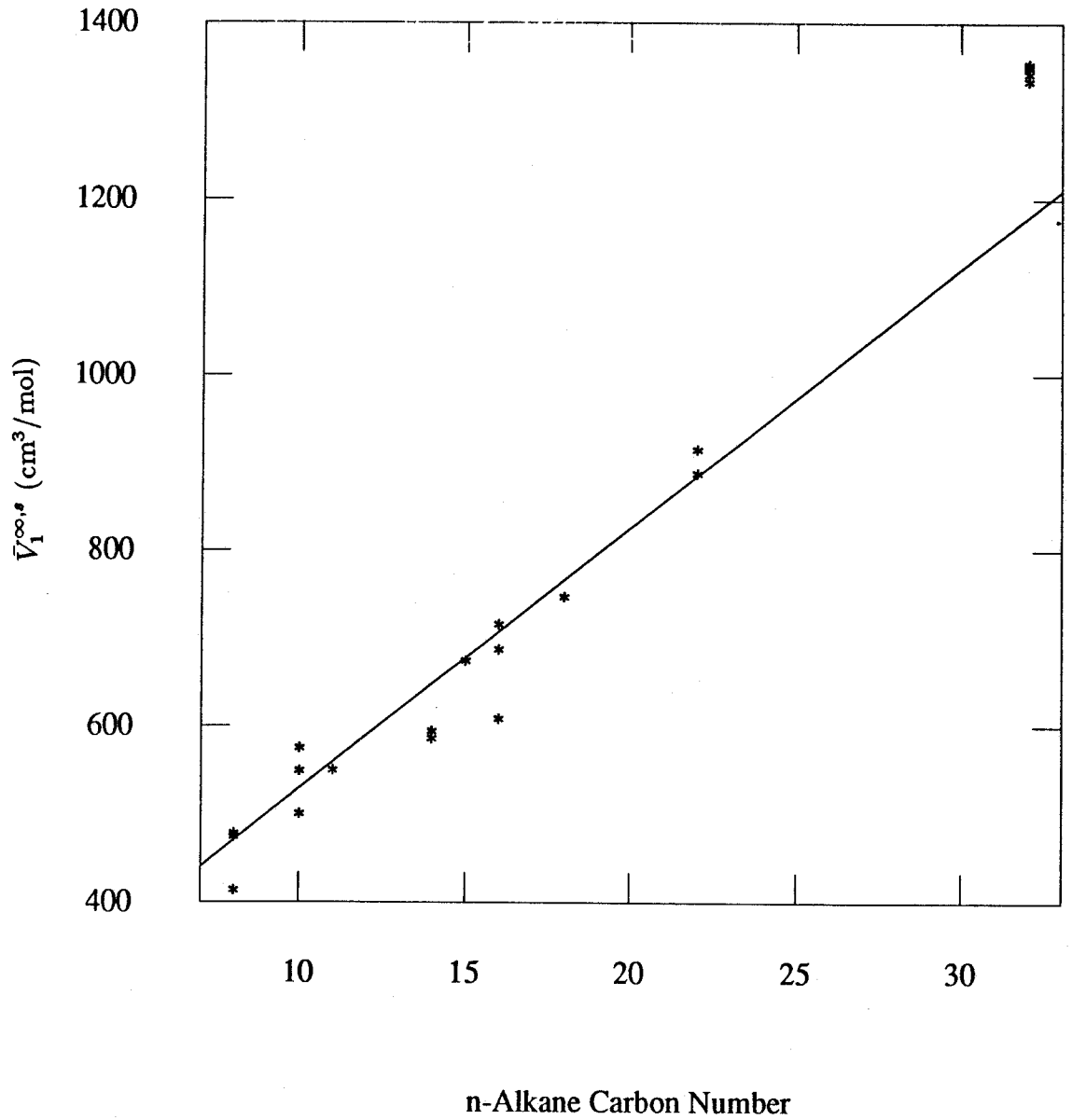

Figure 2.3-6. $\bar{V}_1^{\infty,s}$ correlation using δ_{ij}'s from Deo et al. (1989).

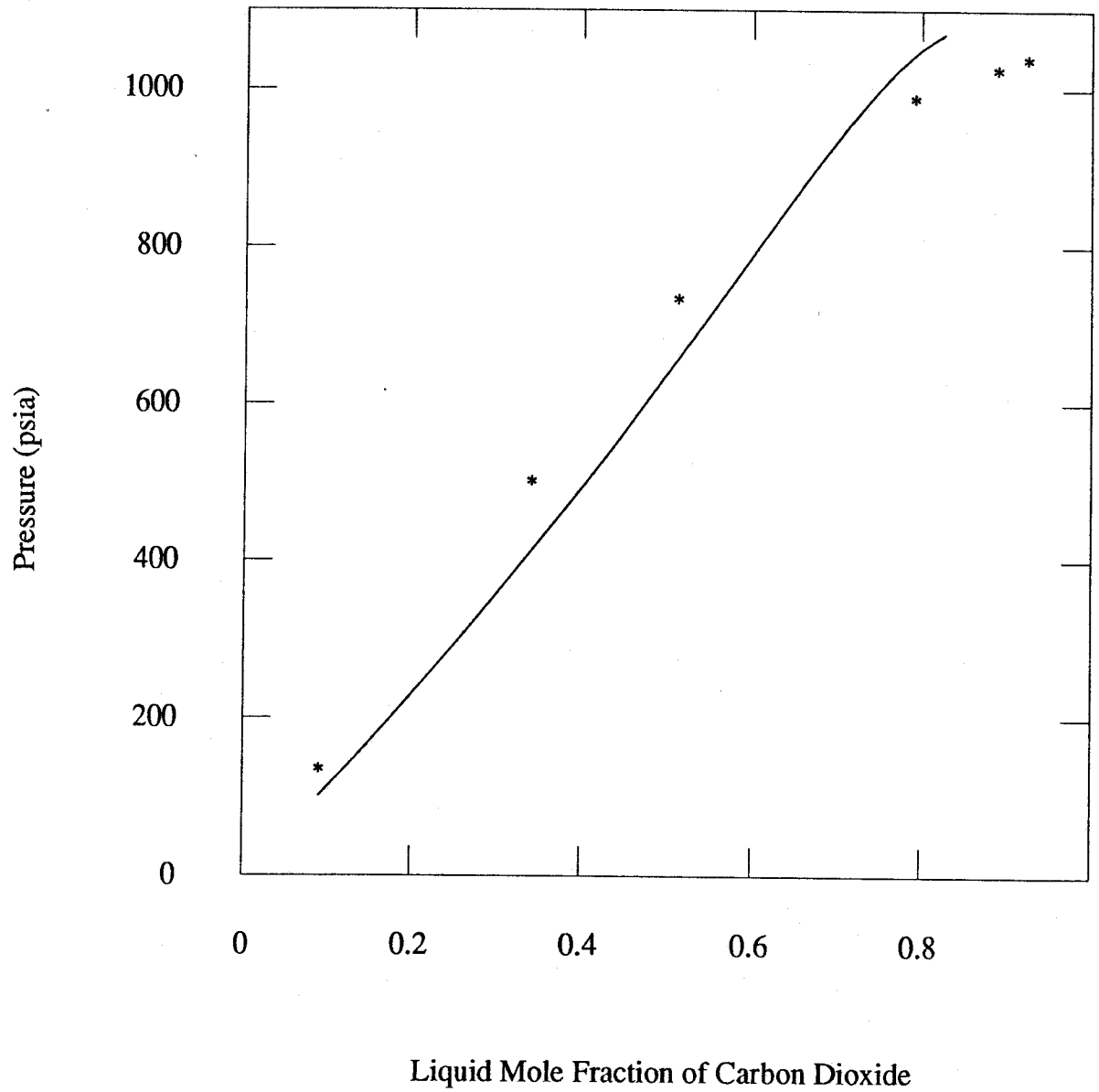

Figure 2.3-7. Phase behavior of CO_2/n-dodecane binary system at 90°F. The solid line is the predicted phase behavior using the Peng-Robinson EOS with the binary interaction parameter determined from Fig. 2.3-6. The stars are actual experimental data from Stewart and Nielsen (1954).

Application of the correlation of Fig. 2.3-6 to other hydrocarbons is currently being studied. If appropriate values of V_1^{∞}, can be estimated for a large enough set of hydrocarbons, then SFC, then the technique demonstrated here can be applied to hydrocarbon components (or pseudocomponents), for which there are virtually no binary experimental data in existence. SFC data would then provide additional experimental constraints for the characterization of an oil for EOS calculations. Thus, it may be possible to use SFC measurements to augment or even replace some PVT measurements for crude oil characterization.

2.3.5 Conclusions

(1) A method for determining binary interaction parameters using SFC has been demonstrated. Additional experimental verification of the technique is needed to determine the potential accuracy of the method.

(2) Binary interaction parameters of some normal alkanes can be determined using the correlation presented in Fig. 2.3-6.

2.4 Summary

The results of PVT experiments reported in Section 2.1 indicate that the overall appearance of pressure-composition phase diagrams is not terribly sensitive to differences in composition of the crude oil in question. Solubility of CO_2 in the oil is similar for oil from the Wasson field, for example, and for oil from the Means field despite the fact that the Means oil is somewhat heavier and contains more heavy normal alkanes, while the Wasson oil is generally lighter, as the analyses reported in Section 2.2 show. Furthermore, the three-phase region observed for Means/CO_2 mixtures appeared at temperatures and pressures quite similar to those of Wasson (Orr and Jensen 1984). That result is consistent with previous analyses of the phase diagrams that show that three-phase behavior appears at temperatures above the critical temperature of CO_2 when the oil contains enough extractable hydrocarbons. The fact that the MMP for Means is higher than that of lighter oils with similar phase diagrams, however, suggests that additional information is needed about effects of oil composition on development of miscibility.

Detailed analyses by GC-MS of samples of CO_2-rich and oil-rich phases taken during the PVT experiments of Section 2.1 were reported in Section 2.2. Those measurements show that extraction of hydrocarbons by dense CO_2 correlates better with elution time than with carbon number. Hydrocarbons such as those containing multiple condensed aromatic rings are extracted less efficiently than branched alkanes with the same carbon number, for example, and also elute later in chromatographic separations on the nonpolar columns used. That result suggests that it is quite reasonable to define pseudocomponents based on simulated distillation by gas chromatography. The analyses also indicate that it is reasonable to estimate the molecular weight for a given carbon number cut in simulated distillations as that of the corresponding normal alkane.

Finally, in Section 2.3, a new method for determination of binary interaction parameters for CO_2-hydrocarbon pairs was demonstrated. It makes use of a thermodynamic analysis of supercritical fluid chromatography with CO_2 as a carrier. In that procedure, an equation of a state is used to calculate properties of the mobile CO_2 phase, and experiments are used to characterize the interactions of the hydrocarbons with the stationary phase. Phase behavior for CO_2-C_{12} mixtures calculated with the binary interaction parameter determined from SFC experiments showed good agreement with experimental data. The agreement obtained suggests that it may be possible to use SFC analyses to obtain crude oil characterizations for equation-of-state calculations.

3. Interactions of Phase Behavior and Flow

Phase behavior makes possible the high displacement efficiency that is observed in successful miscible floods. It does so, however, it does because there is a chromatographic separation of components present in the oil and injected fluid due to the fact that phases present flow at different rates. In this chapter, we consider several aspects of the interaction of two-phase flow with component partitioning between the flowing phases.

In Section 3.1, analytical solutions for condensing and vaporizing gas drives are obtained by the method of characteristics (MOC), and the impact of volume change as components move between phases is illustrated. In Section 3.2, a simple transformation is used to obtain solutions for flow in radial systems from those developed previously for linear flow. In Section 3.3, we consider the analytical theory of interfering shocks. Such situations occur when a slug of fluid of some composition is injected, followed by fluid of some other composition.

The final section of this chapter is devoted to experimental observations of the combined effects of phase behavior, capillary imbibition, and gravity segregation. The experimental results indicate clearly that there is still much to be learned about the interplay of phase behavior with the mixing that results from crossflow, whether due to capillary or gravity forces.

3.1 Effect of Volume Change on Mixing in Vaporizing and Condensing Gas Drives

Birol Dindoruk

The analytical theory of one-dimensional displacement of multicomponent, multiphase mixtures was formulated in a systematic way by Helfferich (1981) for systems in which a given mass of a component occupied the same volume no matter what phase that component happened to be in. For the liquid-liquid surfactant-oil-water systems considered, that assumption was perfectly reasonable. For gas injection, however, the assumption of no volume change as a component moves from one phase to the other is less satisfactory. Fig. 3.1-1, for example, shows results of a slim tube displacement (Orr and Taber 1984) in which CO_2 breakthrough occurred after one pore volume had been injected. That can only occur if volume is not conserved during the displacement. Dumoré et al. (1984) extended Helfferich's theory to ternary systems with volume change, and Monroe et al. (1990) obtained the first solutions for flow of four component systems. Some investigators have assumed that volume change on mixing influences the propagation velocity of fluids of given composition but that the compositions of fluids that form during a displacement are not strongly affected (Pande and Orr 1989). In this section, we describe a detailed test of that assumption.

3.1.1 Model Formulation.

The governing mass balance equation for one-dimensional flow of multiphase, multicomponent mixtures is (Helfferich 1981, Dumoré et al. 1984, Monroe et al. 1990):

$$\frac{\partial}{\partial t}\sum_{j=1}^{n_p} x_{ij}\rho_j S_j + \frac{\partial}{\partial x}\frac{v}{\phi}\sum_{j=1}^{n_p} x_{ij}\rho_j f_j = 0 \quad i = 1, n_c. \tag{3.1-1}$$

where

t = time
x = distance

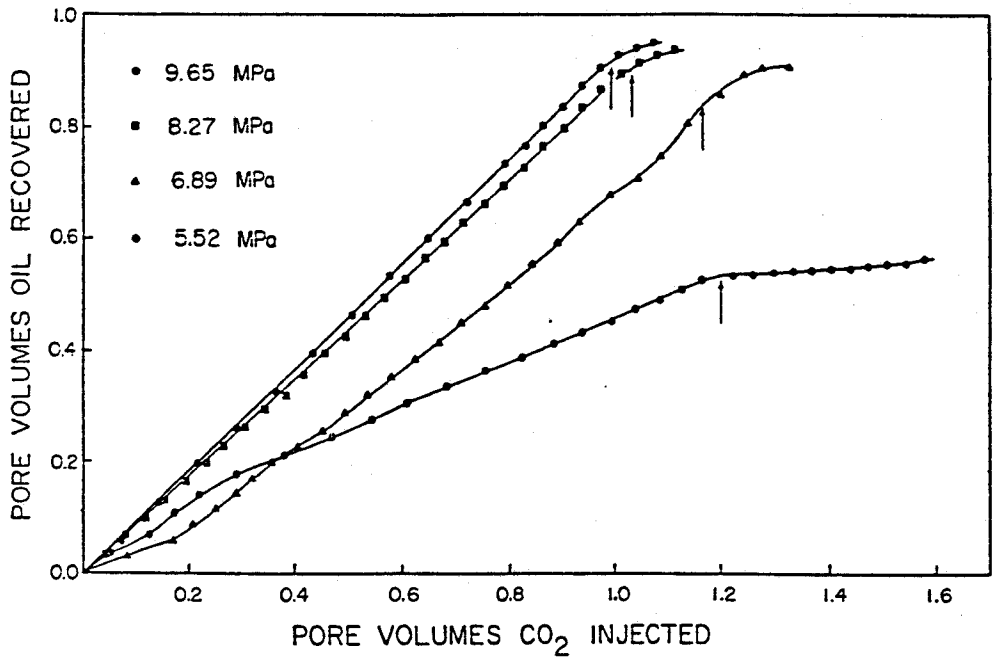

Figure 3.1-1. Recovery of Maljamar separator oil from slim tubes by continuous displacement with CO_2 at 90°F. Arrows indicate CO_2 breakthrough.

n_p = number of phases
n_c = number of components
x_{ij} = mole fraction of component i in phase j
ρ_j = density of phase j
S_j = saturation of phase j
f_j = fractional flow of phase j
v = total velocity
ϕ = porosity

The derivation of equation is based on the following

1. Any phases present reach chemical equilibrium instantaneously.
2. Pressure changes over the displacement length have negligible effect on the phase behavior.
3. The displacement process is isothermal.
4. The fractional flow functions are unique functions of composition.
5. The porous medium is homogeneous.
6. Effects of dispersive mixing are neglected.
7. The flow is one-dimensional.

The material balance equations can be written more simply in terms of the local overall mole fraction of component i, G_i^*, and the overall flux of component i, F_i^*.

$$G_i^* = G_i^*(z_i) = \sum_{j=1}^{n_p} x_{ij}\rho_j S_j \quad i = 1, n_c. \tag{3.1-2}$$

$$F_i^* = F^*(z_i, v) = \frac{v}{\phi}\sum_{j=1}^{n_p} x_{ij}\rho_j f_j = 0 \quad i = 1, n_c. \tag{3.1-3}$$

where z_i is the overall mole fraction of component i. The resulting form of the material balance is

$$\frac{\partial G_i^*}{\partial t} + \frac{\partial F_i^*}{\partial x} = 0 \quad i = 1, n_c. \tag{3.1-4}$$

In the discussion that follows, we will make use of the dimensionless form of the material balance equations

$$\frac{\partial G_i}{\partial \tau} + \frac{\partial F_i}{\partial \xi} = 0 \quad i = 1, n_c. \tag{3.1-5}$$

with the following definitions for distance, time, density and velocity, respectively:

$$\xi = \frac{x}{L}$$

$$\tau = \frac{q_{inj}t}{\phi AL}$$

$$\rho_{jD} = \frac{\rho_j}{\rho_{ini}}$$

$$v_D = \frac{v}{v_{inj}},$$

where

A	=	flow area
L	=	system length
v_{inj}	=	injection velocity
ρ_{ini}	=	density of the original fluid in the system
q_{inj}	=	injection rate

and

$$G_i = \sum_{j=1}^{n_p} x_{ij}\rho_{jD}S_j$$

$$F_i = v_D \sum_{j=1}^{n_p} x_{ij}\rho_{jD}f_j$$

Eq. (3.1-5) was solved by the method of characteristics. In this section only Riemann problems are considered, those in which the initial composition is constant and fluid of fixed composition is injected. Those initial conditions can be written

$$z_i(\xi,0) = \begin{cases} z_{i_{inj}}, & \xi<0 \\ z_{i_{ini}}, & \xi>0 \end{cases} \tag{3.1-6}$$

To construct the solution we rewrite Eq. (3.1-5) in terms of a characteristic variable, $\eta = \xi/\tau$.

$$\frac{dG_i}{d\eta}\frac{\partial\eta}{\partial\tau} + \frac{dF_i}{d\eta}\frac{\partial\eta}{\partial\xi} = 0 \qquad i=1,\ n_c \tag{3.1-7}$$

Here, the derivatives with respect to η are ordinary derivatives since the solution is mapped onto a single variable. The method of characteristics seeks solutions along characteristic lines; that is, where the value of the characteristic variable, η, is constant

$$d\eta = d\tau\frac{\partial\eta}{\partial\tau} + d\xi\frac{\partial\eta}{\partial\xi} = 0 \tag{3.1-8}$$

or

$$\frac{d\xi}{d\tau} = -\frac{\frac{\partial\eta}{\partial\tau}}{\frac{\partial\eta}{\partial\xi}} = \lambda \tag{3.1-9}$$

where λ is the characteristic composition (wave) velocity.

If Eq. (3.1-9) is substituted into Eq. (3.1-7), the resulting system of equations is

$$-\lambda \frac{dG_i}{d\eta} + \frac{dF_i}{d\eta} = 0 \quad i = 1, n_c. \tag{3.1-10}$$

The final step in the formulation of the eigenvalue problem is to note that F_i and G_i are functions of η only through the compositions, z_i, and the local flow velocity, v_D. Hence we can write

$$\frac{dF_i}{d\eta} = \frac{\partial F_i}{\partial v_D}\frac{\partial v_D}{\partial \eta} + \sum_{i=1}^{n_c-1} \frac{\partial F_i}{\partial z_i}\frac{\partial z_i}{\partial \eta} \tag{3.1-11}$$

$$\frac{dG_i}{d\eta} = \sum_{i=1}^{n_c-1} \frac{\partial G_i}{\partial z_i}\frac{\partial z_i}{\partial \eta} \tag{3.1-12}$$

The sums in Eqs. (3.1-11) and (3.1-12) extend only to n_c-1, because the mole fractions must always sum to one, and, hence, the last mole fraction cannot be varied independently. Substitution of Eqs. (3.1-11) and (3.1-12) into (3.1-10) yields

$$\begin{bmatrix} \frac{\partial F_1}{\partial z_1} & \frac{\partial F_1}{\partial z_2} & \cdots & \frac{\partial F_1}{\partial z_{n_c-1}} & \frac{\partial F_1}{\partial v_D} \\ \vdots & \vdots & & \vdots & \vdots \\ \frac{\partial F_{n_c}}{\partial z_1} & \frac{\partial F_{n_c}}{\partial z_2} & \cdots & \frac{\partial F_{n_c}}{\partial z_{n_c-1}} & \frac{\partial F_{n_c}}{\partial v_D} \end{bmatrix} \begin{bmatrix} \frac{dz_1}{d\eta} \\ \vdots \\ \frac{dv_D}{d\eta} \end{bmatrix} =$$

$$\lambda \begin{bmatrix} \frac{\partial G_1}{\partial z_1} & \frac{\partial G_1}{\partial z_2} & \cdots & \frac{\partial G_1}{\partial z_{n_c-1}} & 0 \\ \vdots & \vdots & & \vdots & \vdots \\ \frac{\partial G_{n_c}}{\partial z_1} & \frac{\partial G_{n_c}}{\partial z_2} & \cdots & \frac{\partial G_{n_c}}{\partial z_{n_c-1}} & 0 \end{bmatrix} \begin{bmatrix} \frac{dz_1}{d\eta} \\ \vdots \\ \frac{dv_D}{d\eta} \end{bmatrix} \tag{3.1-13}$$

which can be written

$$\bar{\bar{F}}\bar{x} = \lambda \bar{\bar{G}}\bar{x} \tag{3.1-14}$$

For a three component system, F and G are 3 x 3 matrices. The eigenvalues correspond to n_c-1 characteristic composition velocities. The last eigenvalue is infinite, which implies that changes in overall velocity and density propagate instantaneously throughout the system. Eigenvectors correspond to characteristic directions (paths) in the space $(v_D - z_1, z_2 \ldots z_{n_c-1})$. They indicate directions in composition space along which composition variations satisfy the material balance equations.

Solution Construction

Composition variations that satisfy Eq. (3.1-14) with the initial data, Eq. (3.1-6), are solutions to the Riemann problem posed. Thus, the solution can be found by integrating along eigenvector directions to find a set of paths along which compositions are allowed to vary. The solution route consists of some set of paths that pass through the initial and inlet conditions, and it must then be selected from the infinite set of candidates.

The resulting solution must also be single-valued: fast-moving compositions must lie downstream of slow moving ones, and only one composition can exist at a given spatial location at any time. It is not always possible to satisfy those conditions with solutions that vary continuously. When it is not, shocks (step changes in composition, phase saturation, and flow velocity) form part of the solution. It can be shown that shocks always occur when the solution composition route crosses a phase boundary (Helfferich 1981). A material balance across a shock indicates that its wave velocity, Λ_i, is given by

$$\frac{d\xi}{d\tau} = \Lambda_i = \frac{F_i^{II} - F_i^{I}}{G_i^{II} - G_i^{I}} \tag{3.1-15}$$

where the superscripts I and II refer to opposite sides of the shock. It can be shown (Helfferich 1981; Dumoré et al. 1984) that the eigenvalue associated with a continuous variation along a tie line is

$$\lambda_{tie-line} = v_D \frac{df_j}{dS_j} \tag{3.1-16}$$

In addition, it has been proved that shocks in and out of a two-phase region occur along the extension of a tie line (Helfferich 1981; Dumoré et al. 1984). Such shocks frequently show a continuous variation on one side of the shock. If so, $\Lambda_i = \lambda_{tie-line}$. For additional details of the complexities associated with shocks, see Monroe et al. (1990).

Relative Permeabilities, Fluid Properties and Phase Equilibria

In order to calculate the fractional flow function (flux function), relative permeability relationships are needed. In this study, simple functional forms of relative permeabilities were used.

$$k_{rg} = \left[\frac{S_g}{1. - S_{or}}\right]^{n_g} \tag{3.1-17}$$

$$k_{rl} = \left[\frac{1. - S_g - S_{or}}{1. - S_{or}}\right]^{n_g} \tag{3.1-18}$$

where

k_{rg} = vapor phase relative permeability
k_{rl} = liquid phase relative permeability
n_g = relative permeability exponent for vapor phase
n_l = relative permeability exponent for liquid phase
S_g = vapor phase saturation
S_{or} = residual oil saturation

The relative permeability parameters used in this study are given in Table 3.1-1.

The fractional flow functions for the phases come from Darcy's law with no gravity and capillary pressure effects. The fractional flow equation for phase j is given by

$$f_j = \frac{\dfrac{k_{rj}}{\mu_j}}{\sum_{j=1}^{n_p} \dfrac{k_{rj}}{\mu_j}} \tag{3.1-19}$$

Phase viscosities were calculated from phase compositions with the correlation of Lohrenz et al. (1964), version of the Jossi et al. (1962) correlation.

The permeability equations are only functions of the vapor saturation. However, the saturation is a function of overall composition. For two-phase equilibrium conditions where gas and liquid are present, the vapor saturation is given by

$$S_g = \frac{V}{V + \dfrac{\rho_v}{\rho_l}(1-V)} \tag{3.1-20}$$

V = mole fraction of the vapor (gas) phase
ρ_l = molar density of liquid phase
ρ_v = molar density of vapor phase

The mole fraction of vapor phase can be calculated from the equilibrium phase compositions.

$$V = \frac{z_i - x_{il}}{x_{iv} - x_{il}} \tag{3.1-21}$$

where

x_{il} = mole fraction of component i in liquid phase
x_{iv} = mole fraction of component i in vapor phase

According to Eq. (3.1-20) and Eq. (3.1-21), the phase saturation is a strong function of the density ratio as well as the mole fraction of the both phases. Therefore, estimation of correct phase densities is important for the overall performance of the two-phase flow. Mole fractions and the densities were calculated by Peng-Robinson EOS (Peng and Robinson 1976) with density corrections given by Deo et al. (1989) of the form suggested by Peneloux et al. (1982).

For cases in which the assumption was made of no volume change on mixing, the density of each component was taken to be the pure component density at the displacement conditions. The molar density of the jth phase is then given by

$$\rho_j = \frac{1}{\sum_{i=1}^{n_c} \dfrac{x_{ij}}{\rho_{ci}}} \tag{3.1-22}$$

Table 3.1-1. Parameters for the Example Problems.

Parameter	Value
S_{or}	0.1
n_g	2.0
n_l	2.0

If this definition is substituted into Eq. (3.1-1), the system of equations can be written in terms of volume fractions rather than mole fractions. The volume fraction of component i in phase j is then

$$c_{ij} = \frac{x_{ij}\rho_j}{\rho_{ci}} \tag{3.1-23}$$

where ρ_{ci} = molar density of pure component i.

Since the total volume does not change as components move between phases, the total convective velocity remains constant. Thus, the local velocity is no longer unknown. Instead it is fixed at the value of injection velocity. The new form of the system becomes:

$$\frac{\partial}{\partial t}\sum_{j=1}^{n_p} c_{ij}S_j + \frac{v}{\phi}\frac{\partial}{\partial x}\sum_{j=1}^{n_p} c_{ij}f_j = 0 \quad i=1,n_c-1\,. \tag{3.1-24}$$

The solution of the equation system (3.1-24) is similar to the solution of the case of volume change on mixing. The principal difference is that the order of the eigenvalue problem is reduced by one because flow velocity no longer varies.

3.1.2 Binary Systems

To illustrate the effects of volume change, we consider first the flow of a simple two-component system, CO_2 displacing normal decane (C_{10}) at 1250 psia and 160°F. At these conditions, density of the components are 0.3030 lb-mole/ft^3 and 0.2831 lb-mole/ft^3, respectively. Because constant pressure and temperature are assumed, the compositions of the liquid and vapor phases must be constant, as the Gibbs phase rule indicates. In other words, the displacement takes place on a single tie line. Therefore, a jump from one tie line to another is not possible, and the shocks occur only at the entrance and the exit of the two-phase region along the equilibrium tie line. Figs. 3.1-2 to 3.1-5 illustrate the differences between the two solutions for the CO_2-C_{10} displacement. In the case of volume change on mixing, the slope of the early part of the recovery curve is not unity until breakthrough (Fig. 3.1-2a), an indication that there is a change in the injected volume, behavior that is similar to that shown in Fig. 3.1-1 at a pressure of 5.52 and 6.89 MPa. However, the slope is unity when the volume is conserved (Fig. 3.1-2b).

The details of the composition and saturation profiles are shown in Figs. 3.1-3 and 3.1-4. In both cases, the general form of the solution is the same. There is a leading shock similar to that observed in the Buckley-Leverett solution for displacement of oil by water. In addition, there is a trailing shock, behind which all the C_{10} has evaporated into the vapor phase. Between the two shocks is a zone of continuous variation. Values of compositions and saturations at key points in the profiles are also given in Tables 3.1-2 and 3.1-3.

The most obvious difference between the volume change (VC) and no volume change (NVC) cases is in the velocity of the leading shock. It moves substantially faster in the NVC case. The primary reason for that difference is shown in Fig. 3.1-5. Ahead of the leading shock, the flow velocity is only about 65% of the injection flow velocity in the NVC case. That occurs because CO_2 dissolved in the liquid phase left behind the leading shock in this immiscible displacement occupies less volume that it would in the vapor phase. Note, however, that total flow velocity does not change as the overall composition varies along a tie line, because phase compositions, and, hence, phase densities remain fixed. In the NVC case the flow velocity is everywhere the same.

The strengths of the shocks in the composition (Fig. 3.1-3) and saturation (Fig. 3.1-4) profiles also differ, as the values shown in Tables 3.1-2 and 3.1-3 show. The leading shock in

Table 3.1-2. MOC Solution of Binary Case with Volume Change on Mixing at 160°F and 1250 PSIA.

Comment	Composition (moles)		Total Velocity	Gas Saturation	Amount of Gas (moles)	Wave Velocity $1/PV$
	CO_2	C_{10}				
Injection Gas	1.0000	0.0000	1.0000	1.0000	1.0000	0.0000
Trailing Shock	0.8694	0.1306	0.9835	0.7883	0.6650	0.0441
Continuous Variation	0.8694 0.7273	0.1306 0.2727	0.9835 0.9835	0.7883 0.4275	0.6650 0.2847	0.0441 0.9139
Leading Shock	0.7273	0.2727	0.9835	0.4275	0.2847	0.9139
Initial Oil	0.0000	1.0000	0.6393	0.0000	0.0000	0.9139

Table 3.1-3. MOC Solution of Binary Case with No Volume Change on Mixing at 160°F and 1250 PSIA.

Comment	Composition (moles)		Total Velocity	Gas Saturation	Amount of Gas (moles)	Wave Velocity $1/PV$
	CO_2	C_{10}				
Injection Gas	1.0000	0.0000	1.0000	1.0000	1.0000	0.0000
Trailing Shock	0.8993	0.1007	1.0000	0.7497	0.7450	0.0699
Continuous Variation	0.8993 0.7642	0.1007 0.2358	1.0000 1.0000	0.7497 0.3895	0.7450 0.3836	0.0699 1.2086
Leading Shock	0.7642	0.2358	1.0000	0.3895	0.3836	1.2086
Initial Oil	0.0000	1.0000	1.0000	0.0000	0.0000	1.2086

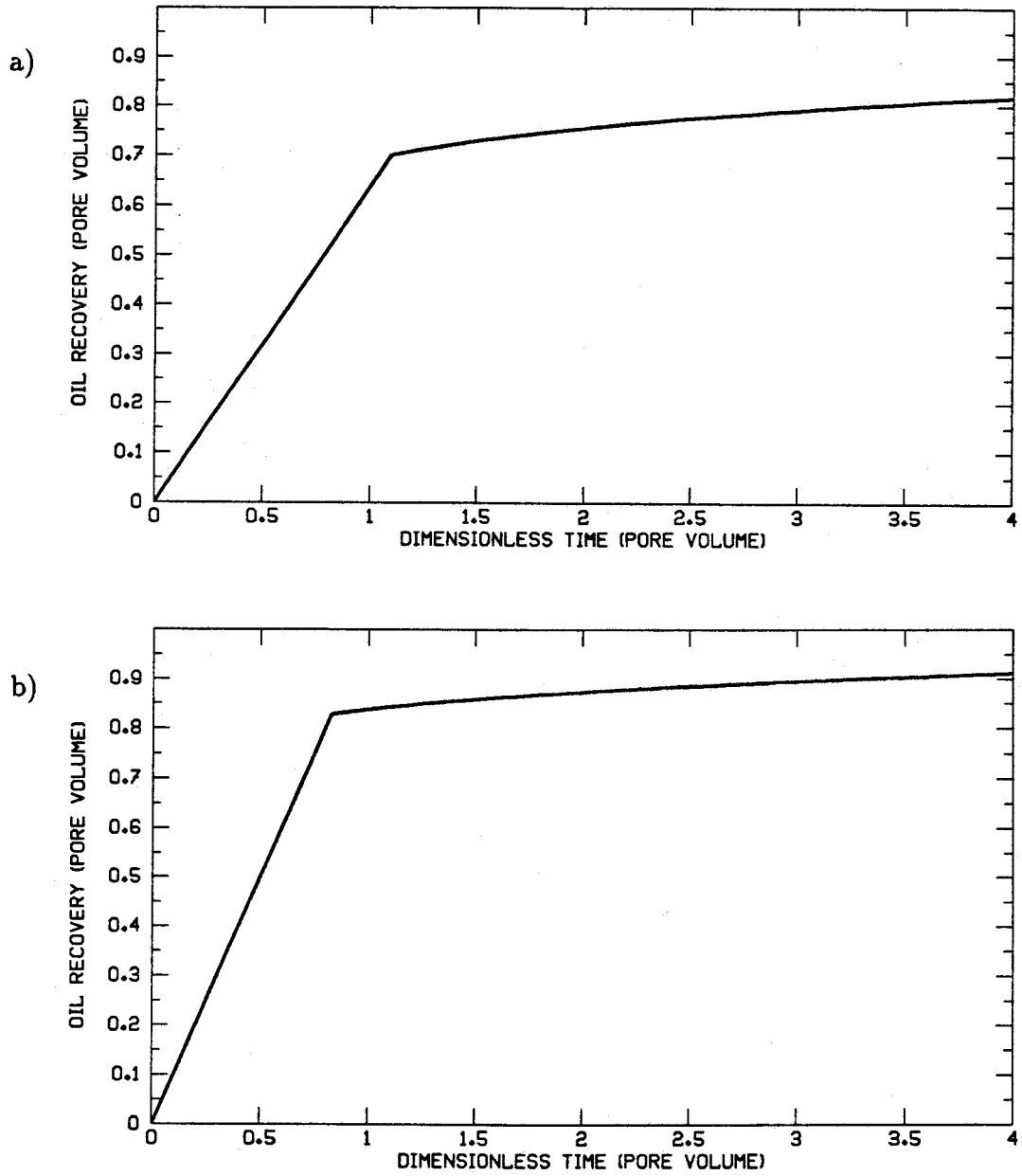

Figure 3.1-2. Oil recovery curves for displacement of C_{10} by CO_2 at 1250 psia and 160°F: a) Volume change on mixing b) No volume change on mixing.

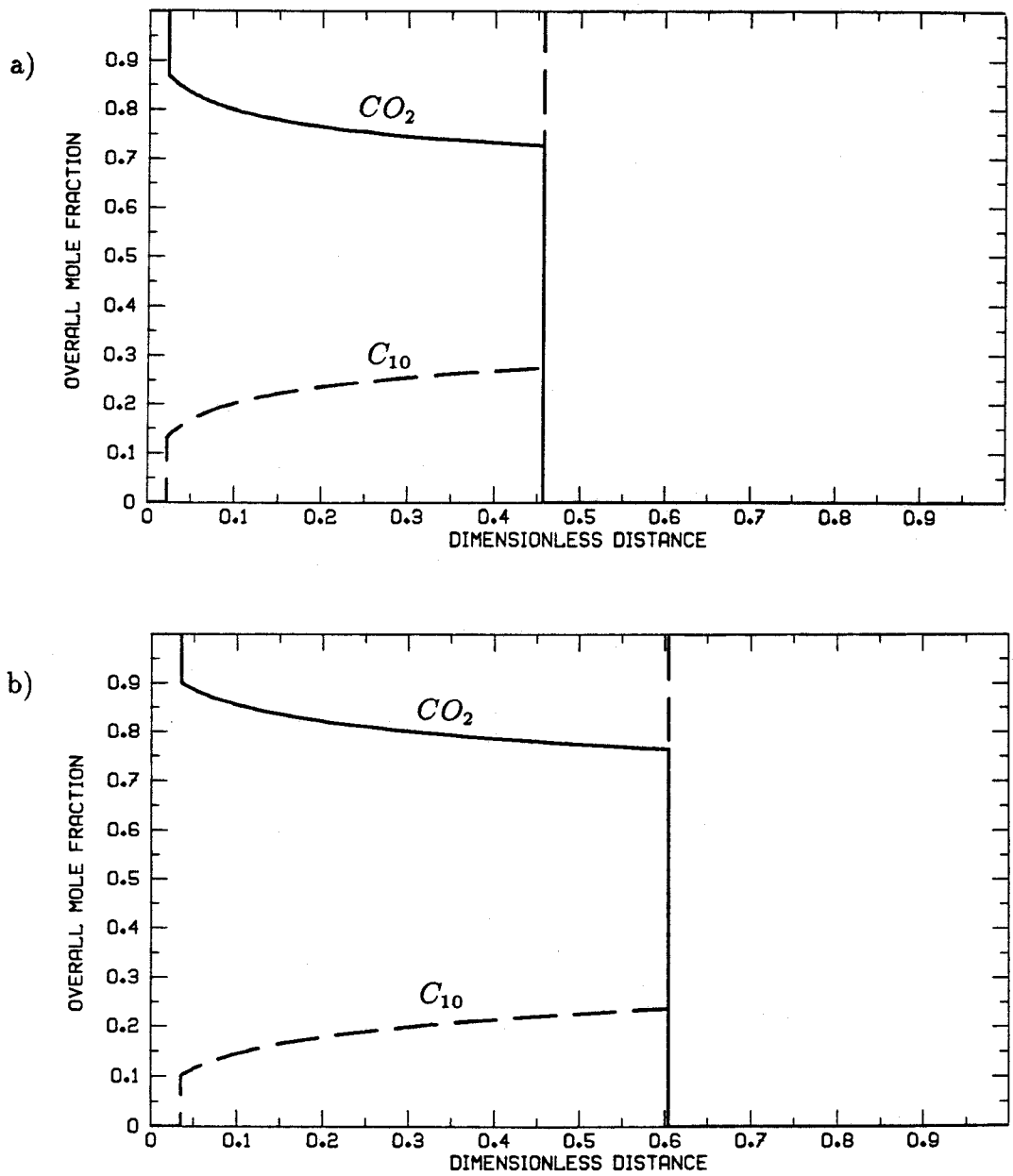

Figure 3.1-3. Composition profiles for displacement of C_{10} by CO_2 at 1250 psia and 160°F: a) Volume change on mixing b) No volume change on mixing.

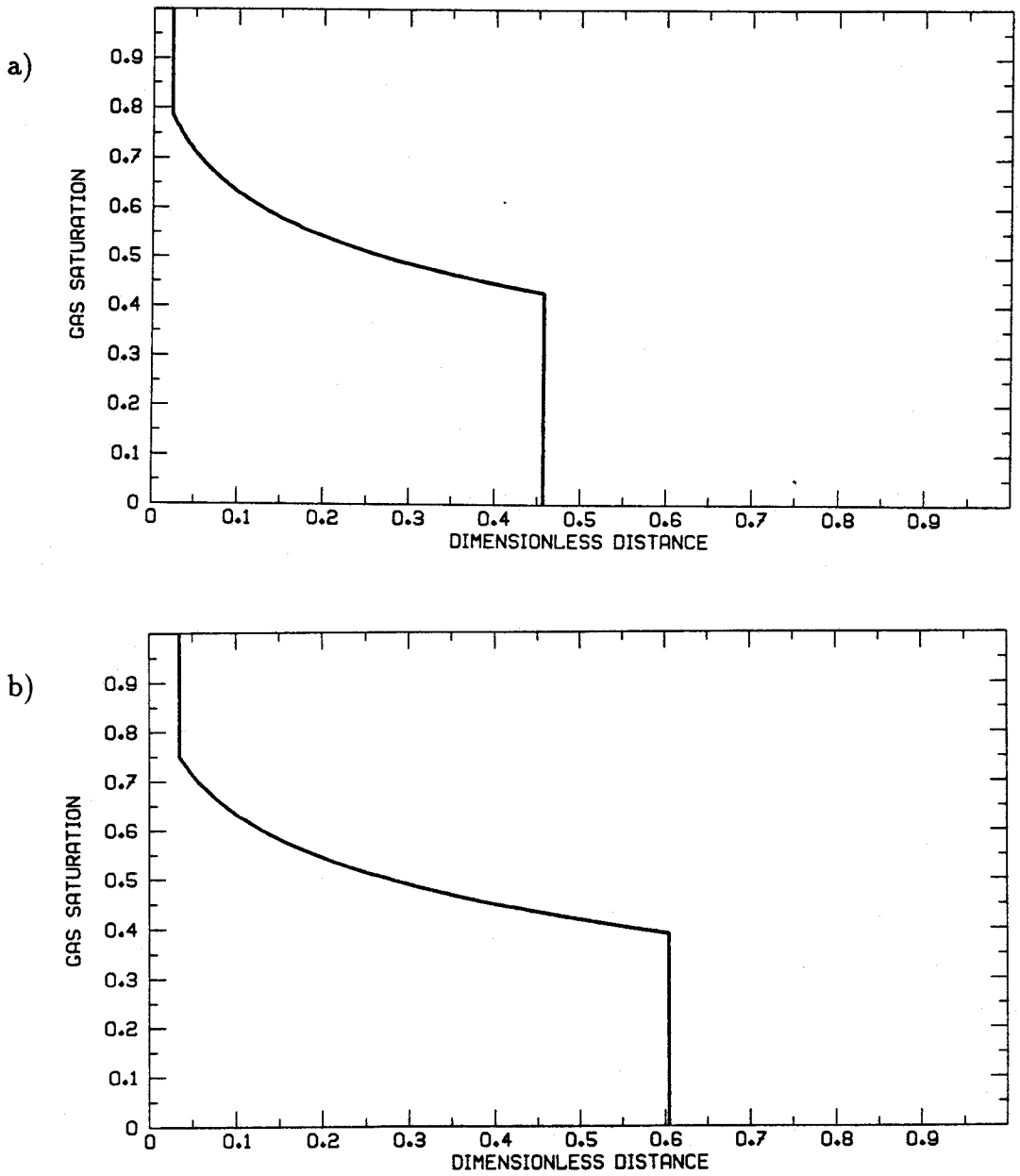

Figure 3.1-4. Saturation profiles for displacement of CO_2 by CO_2 at 1250 psia and 160°F: a) Volume change on mixing b) No volume change on mixing.

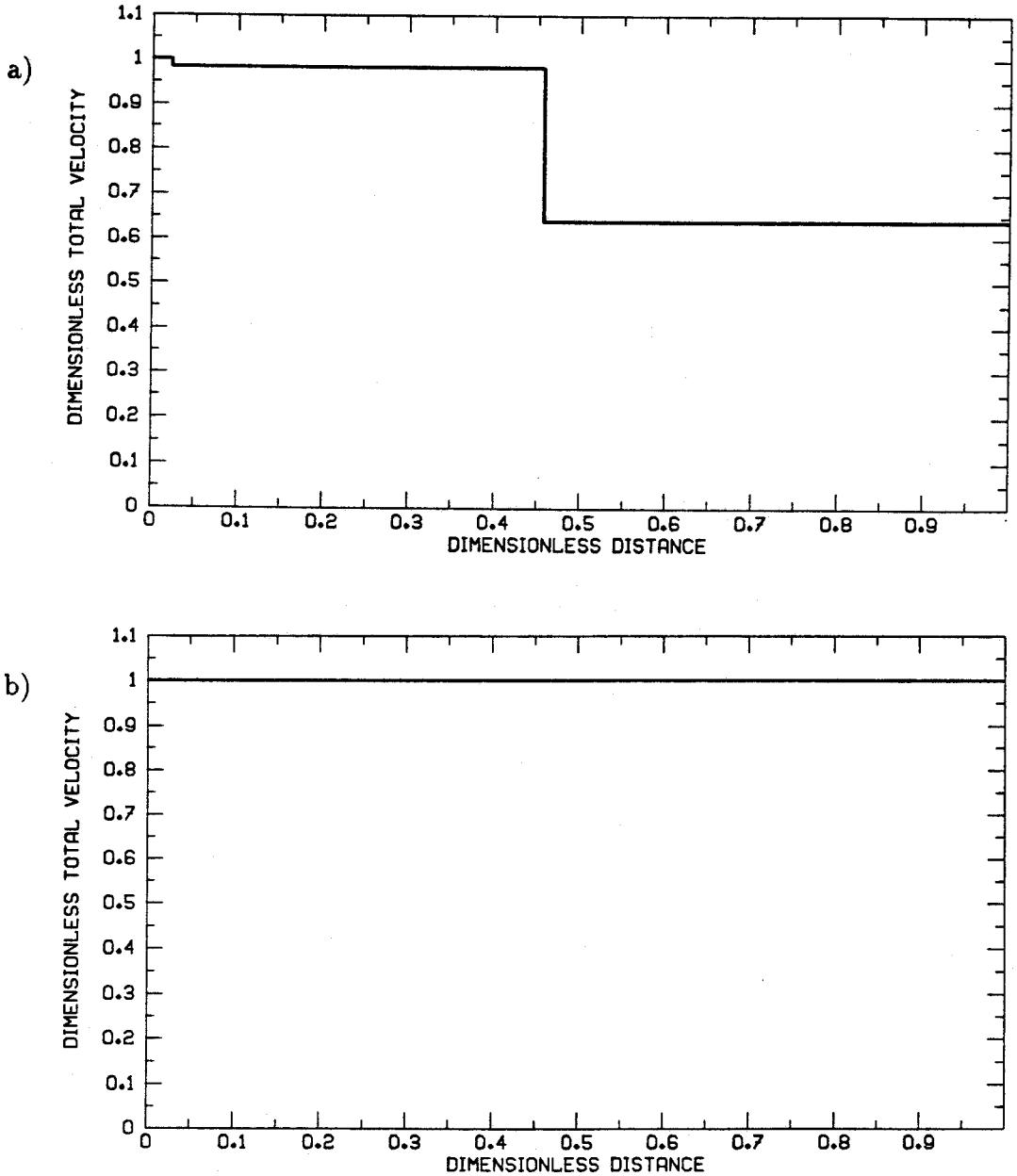

Figure 3.1-5. Total velocity profile for displacement of C_{10} by CO_2 at 1250 psia and 160°F: a) Volume change on mixing b) No volume change on mixing.

the CO_2 concentration profile is weaker in the VC case, but the reverse is true for the saturation profiles. Comparison of the values for V, the vapor mole fraction in Tables 3.1-2 and 3.1-3 indicate that V is larger in the NVC case, as it must be, when the CO_2 concentration is larger. The saturation values are modified by the phase densities, however, as Eq. (3.1-20) indicates. Hence, differences in phase densities in the two cases account for the reversal of the strength of the saturation shocks. Similar reasoning applies to the trailing shock.

Figs. 3.1-2 to 3.1-5 indicate that for this binary displacement, the largest difference observed is in breakthrough time. Differences in shock strengths were relatively small, and, of course, the composition path followed is essentially independent of volume change because only one tie line is available.

3.1.3 Ternary Systems

In this section, we examine the behavior of four cases described in Table 3.1-4. The differences in displacement behavior that are observed for two injection gases, CO_2 and methane (C_1) are considered in the first two cases, both vaporizing gas drives. The third case shows the effect of a lower displacement pressure in a vaporizing gas drive. The last case is a condensing gas drive.

Case 1: CO_2 Injection at 1250 psia

Composition routes for the VC and NVC cases are compared in Fig. 3.1-6 for injection of pure CO_2 at 1250 psia and 160°F into a mixture containing 20 mole percent butane (C_4) and 80 mole percent C_{10}. Composition profiles are shown in Fig. 3.1-7 and saturations and flow velocities in Fig. 3.1-8. Effluent composition and recovery curves are reported in Figs. 3.1-9 and 3.1-10. Additional details of the solutions are given in Tables 3.1-5 and 3.1-6.

In both the VC and NVC examples, the solution begins with a leading shock from the initial composition to a point on the tie line that passes through the initial composition when extended. Behind the leading shock is a zone of continuous variation along the same tie line. That zone is terminated by a shock, with intermediate velocity, from the initial tie line to the tie line that passes through the injection composition. The intermediate shock is required because all paths that connect the initial and injection tie lines violate the rule that wave velocity must increase monotonically from inlet to outlet. Trailing the intermediate shock is a zone of constant state. It forms because the intermediate shock velocity differs from the tie-line eigenvalue at the composition on the injection tie line. A second zone of continuous variation then separates the zone of constant state from the trailing shock.

In these ternary displacements, therefore, two key tie lines are involved in the solution, the initial and injection tie lines, so named because their extensions pass through the initial and injection compositions. As in the binary displacement example, volume change does not affect the qualitative appearance of the solutions. Breakthrough occurs when the leading shock reaches the outlet, as Fig. 3.1-9 indicates. Recovery of C_4 is complete when the intermediate shock arrives at the outlet, and all the C_{10} is recovered when the trailing shock does so. The trailing shock moves so slowly, however, that such recovery by evaporation is impractical.

In this ternary example, the effects of volume change are similar to those observed in the binary example. As Figs. 3.1-7 and 3.1-8 and Tables 3.1-5 and 3.1-6 show, VC slows all the shocks, because the local flow velocity is reduced ahead of the leading shock. The velocity change across the leading shock is much larger than for any of the other shocks. As in the binary case, the flow velocity does not change during composition variations along a given tie line, because phase compositions and molar densities are fixed on a given tie line. The recovery curves shown in Fig. 3.1-10 also indicate that the predictions of displacement behavior are more optimistic for the NVC case. Thus, for displacements in which some oil is left behind in the transition zone, the NVC assumption yields composition routes that are

Table 3.1-4. Initial and Injection Data for the Ternary Example Cases.

Comment	Initial Composition (moles)			Pressure *psia*	Injection Density $lb-mole/ft^3$
CASE 1	CO_2	C_4	C_{10}		
	0.0000	0.2000	0.8000	1250	0.2831
CASE 2	C_1	C_4	C_{10}		
	0.0000	0.2000	0.8000	1675	0.2755
CASE 3	CO_2	C_4	C_{10}		
	0.0000	0.2000	0.8000	800	0.1521
CASE 4	CO_2	C_4	C_{10}		
	0.0000	0.2000	0.8000	1250	0.3215

Table 3.1-5. MOC Solution of Ternary Case with Volume Change on Mixing at 160°F and 1250 PSIA, (CASE 1).

Comment	Composition (moles)			Total Velocity	Gas Saturation	Amount of Gas (moles)	Wave Velocity $1/PV$
	CO_2	C_4	C_{10}				
Injection Gas	1.0000	0.0000	0.0000	1.0000	1.0000	1.0000	0.0000
Trailing Shock	0.8694	0.0000	0.1306	0.9835	0.7883	0.6650	0.0441
Continuous Variation	0.8694	0.0000	0.1306	0.9835	0.7883	0.6650	0.0441
	0.8397	0.0000	0.1603	0.9835	0.7260	0.5855	0.0873
Zone of Constant State	0.8397	0.0000	0.1603	0.9835	0.7260	0.5855	0.0873
	0.8397	0.0000	0.1603	0.9835	0.7260	0.5855	0.4104
Intermediate Shock	0.7588	0.0680	0.1732	0.9947	0.5716	0.4086	0.4104
Continuous Variation	0.7588	0.0680	0.1732	0.9947	0.5716	0.4086	0.4104
	0.7236	0.0741	0.2022	0.9947	0.4600	0.3061	0.9044
Leading Shock	0.7236	0.0741	0.2022	0.9947	0.4600	0.3061	0.9044
Initial Oil	0.0000	0.2000	0.8000	0.6735	0.0000	0.0000	0.9044

Table 3.1-6. MOC Solution of Ternary Case with No Volume Change on Mixing at 160°F and 1250 PSIA, (CASE 1).

Comment	Composition (moles)			Total Velocity	Gas Saturation	Amount of Gas (moles)	Wave Velocity $1/PV$
	CO_2	C_4	C_{10}				
Injection Gas	1.0000	0.0000	0.0000	1.0000	1.0000	1.0000	0.0000
Trailing Shock	0.8993	0.0000	0.1007	1.0000	0.7497	0.7450	0.0699
Continuous Variation	0.8993	0.0000	0.1007	1.0000	0.7497	0.7450	0.0699
	0.8807	0.0000	0.1193	1.0000	0.7005	0.6953	0.1127
Zone of Constant State	0.8807	0.0000	0.1193	1.0000	0.7005	0.6953	0.1127
	0.8807	0.0000	0.1193	1.0000	0.7005	0.6953	0.5852
Intermediate Shock	0.7939	0.0619	0.1442	1.0000	0.5235	0.5108	0.5852
Continuous Variation	0.7939	0.0619	0.1442	1.0000	0.5235	0.5108	0.5852
	0.7592	0.0679	0.1729	1.0000	0.4220	0.4096	1.1682
Leading Shock	0.7592	0.0679	0.1729	1.0000	0.4220	0.4096	1.1682
Initial Oil	0.0000	0.2000	0.8000	1.0000	0.0000	0.0000	1.1682

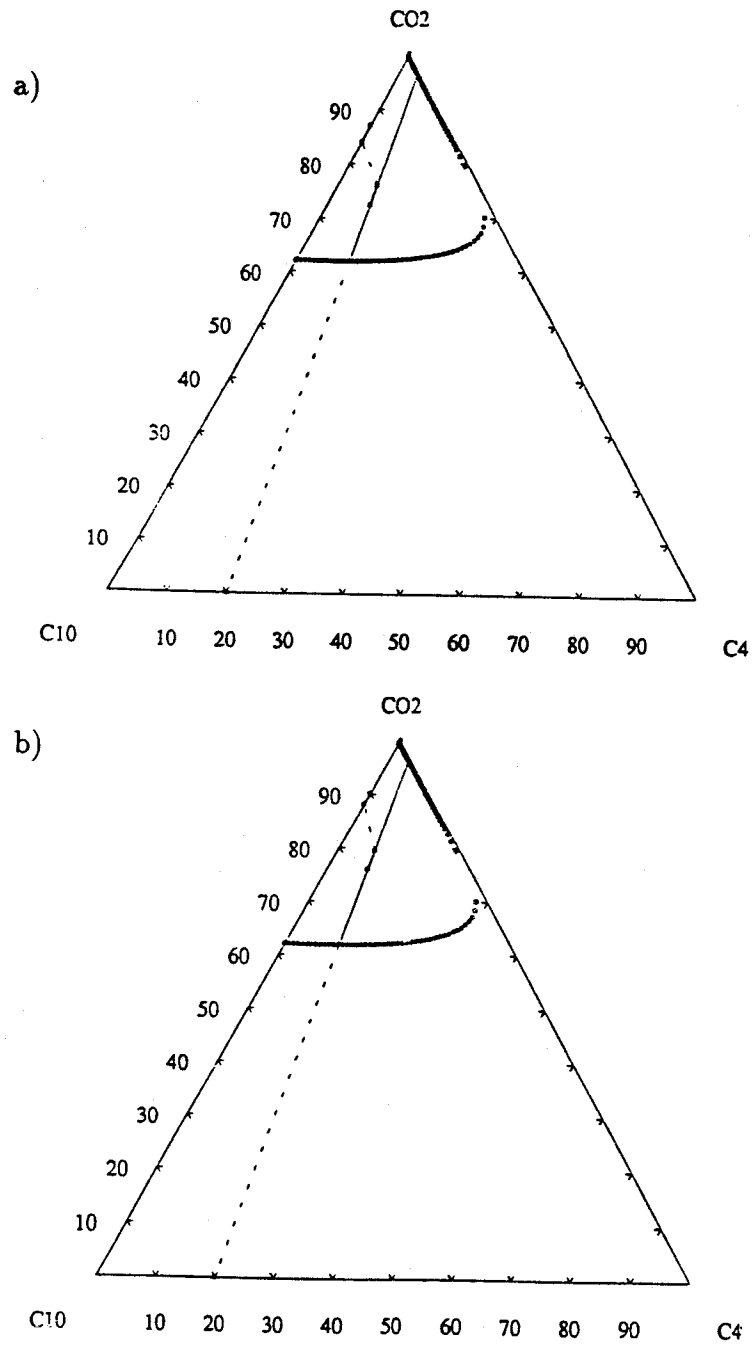

Figure 3.1-6. Composition routes for displacement of a C_4-C_{10} mixture by pure CO_2 at 1250 psia and 160°F: a) Volume change on mixing b) No volume change on mixing.

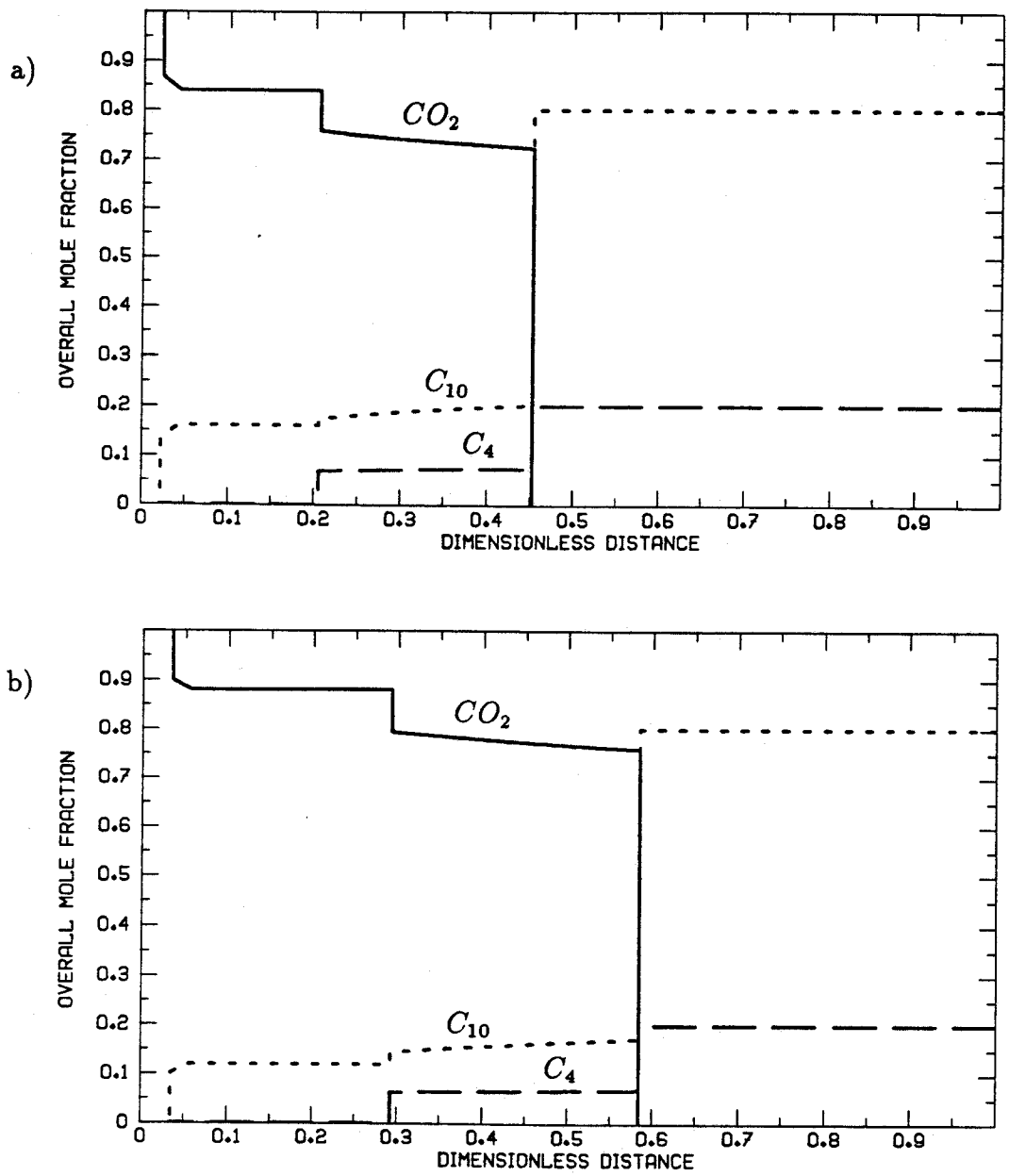

Figure 3.1-7. Composition profiles for displacement of a C_4-C_{10} mixture by pure CO_2 at 1250 psia and 160°F: a) Volume change on mixing b) No volume change on mixing.

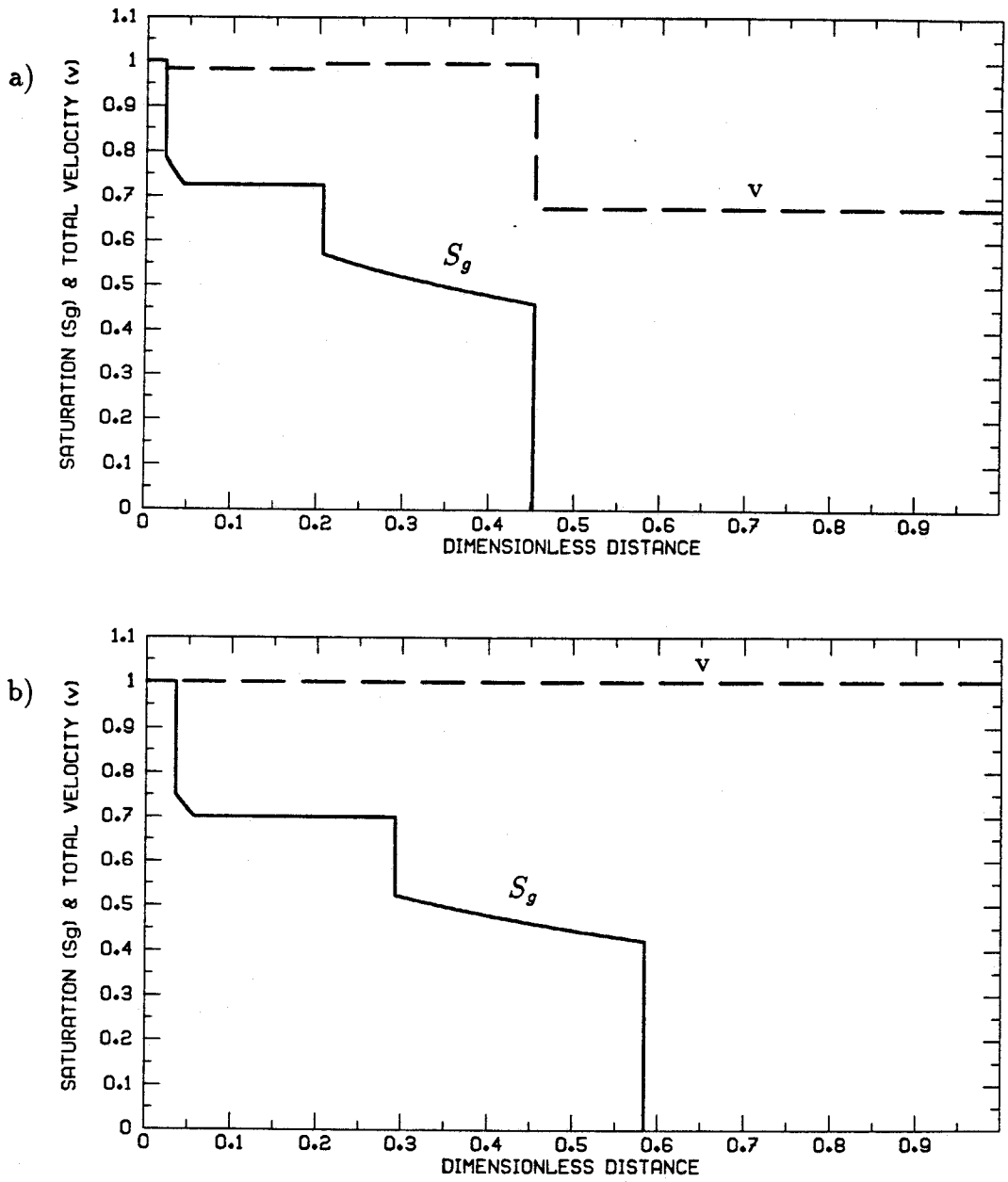

Figure 3.1-8. Saturation and total velocity profiles for displacement of a C_4-C_{10} mixture by pure CO_2 at 1250 psia and 160°F: a) Volume change on mixing b) No volume change on mixing.

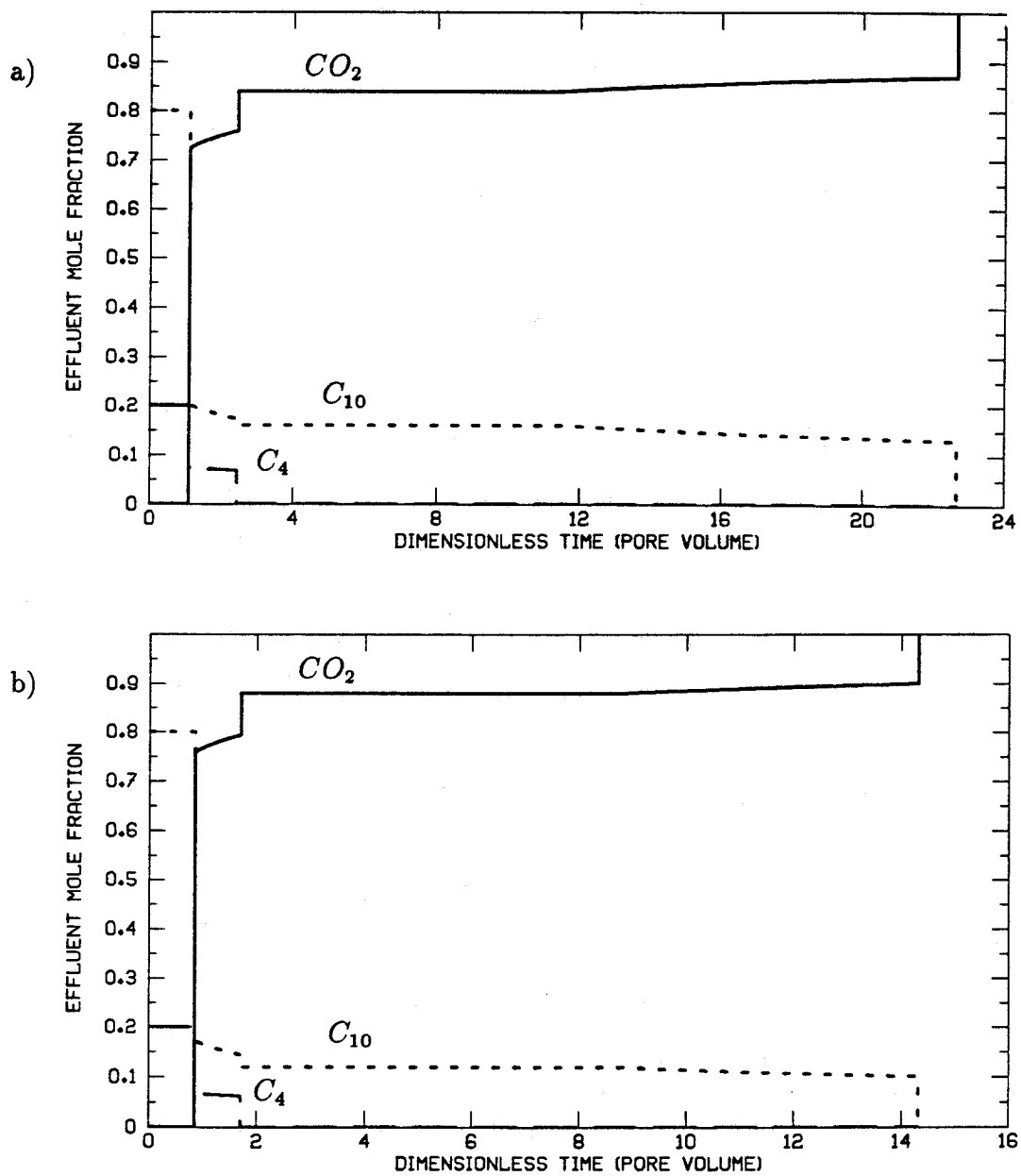

Figure 3.1-9. Effluent mole fractions for displacement of a C_4-C_{10} mixture by pure CO_2 at 1250 psia and 160°F: a) Volume change on mixing b) No volume change on mixing.

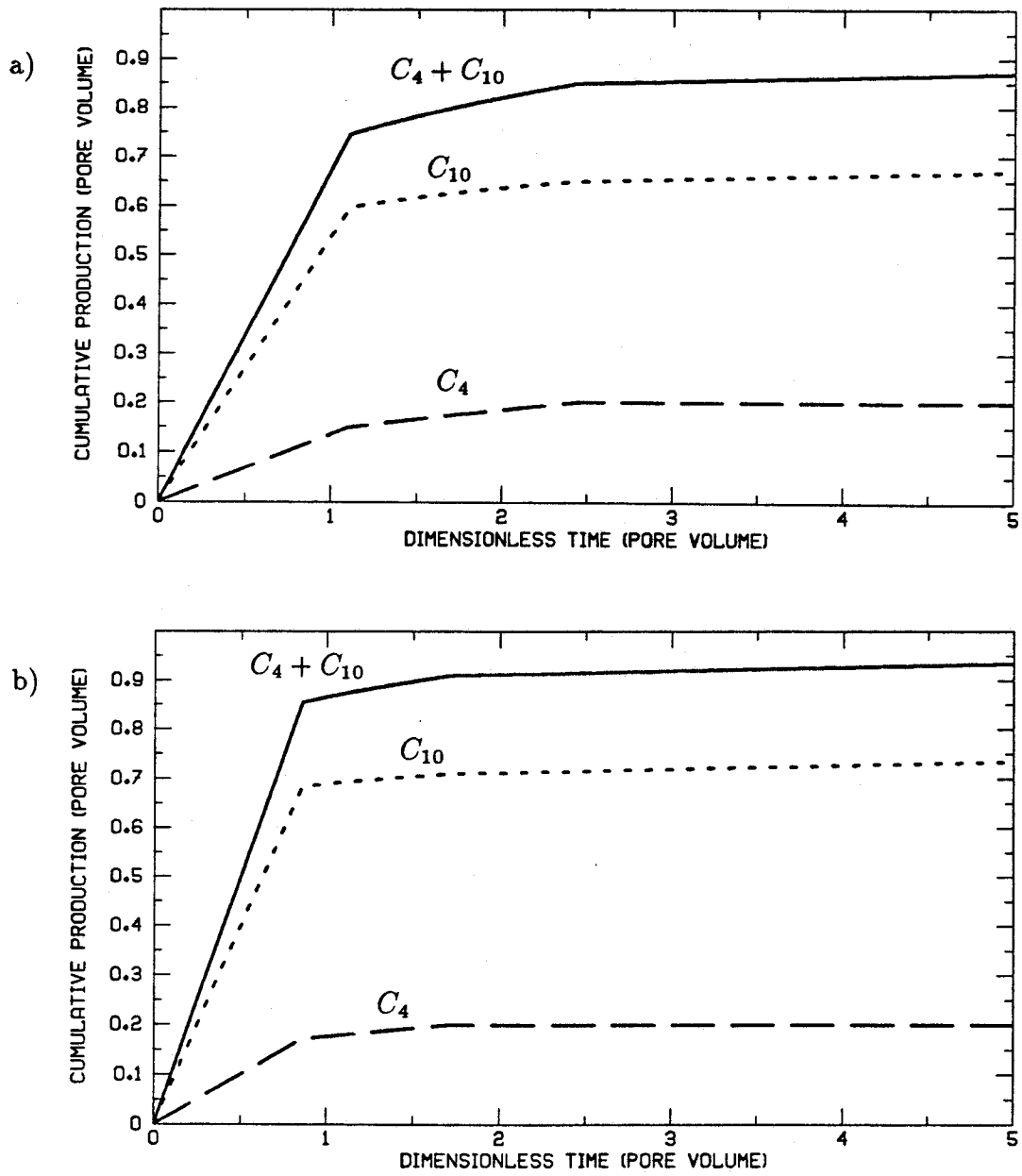

Figure 3.1-10. Recovery curves for displacement of a C_4-C_{10} mixture by pure CO_2 at 1250 psia and 160°F: a) Volume change on mixing b) No volume change on mixing.

qualitatively similar to those observed with volume change, but the timing of recovery changes substantially. For this case, at least recovery is always lower at a given injection time when volume change is present.

Case 2: C_1 Injection at 1675 psia

Fig. 3.1-11 shows composition routes for displacement of the same initial oil composition used in Case 1 by pure C_1 at 1675 psia and 160°F. At those conditions, the molar density of C_1 is approximately the same as that of CO_2 at the conditions of Case 1. Qualitatively, the solutions are very similar to those obtained for Case 1, but there are significant quantitative differences. Figs. 3.1-12 to 3.1-15 show composition and saturation profiles, effluent compositions and recovery curves for Case 2, and additional details are given in Tables 3.1-7 and 3.1-8. The solutions still include three shocks, and all three shocks move more rapidly when volume is conserved.

It is clear, however, that displacement by C_1 is less efficient than displacement by CO_2, even though both displacements were immiscible. In Case 2, the leading shocks move more rapidly than in Case 1 (compare Fig. 3.1-7 with 3.1-12, for example), and recovery by C_1 is lower, as comparison of Figs. 3.1-10 and 3.1-15 indicates. In this case, the difference in behavior is primarily due to the difference in solubility. CO_2 is substantially more soluble as comparison of the phase diagrams in Figs. 3.1-6 and 3.1-11 shows. when CO_2 is the injected fluid, the oil phase left behind the leading shock contains less oil (and more CO_2) than does the oil phase left behind when C_1 is injected. In addition, flow velocity is also affected less for C_1, as Fig. 3.1-13 shows. In Case 2 the flow velocity ahead of the leading shock is about 73% of the injection velocity (Table 3.1-7), while the corresponding value for CO_2 is 67%. Thus, the performance of the displacement by C_1 was less sensitive to the effects of volume change. Calculations performed for nitrogen injection at 1890 psia and 160°F, at which conditions the molar density of nitrogen was again approximately the same, confirm the trend: the solubility of nitrogen is still lower and the difference between VC and NVC cases is still smaller.

Case 3: CO_2 Injection at 800 psia

To confirm that it was a combination of changes in solubility and density that explained the differences in displacement behavior between Cases 1 and 2, additional solutions were calculated for pure CO_2 displacement of the same original oil composition at a lower pressure, 800 psia, and 160°F. At those conditions, the solubility of CO_2 in the oil was lower, as comparison of Figs. 3.1-6 and 3.1-16 shows, and the density of the injected CO_2 was also lower (see Table 3.1-4).

The combined effects of the changes in phase behavior and fluid properties are illustrated in the Figs. 3.1-16 to 3.1-20 and Tables 3.1-9 and 3.1-10. The qualitative features of the solutions are similar to those of Cases 1 and 2: three shocks separated by two zones continuous variation (spreading waves) and one zone of constant state. In this case, the trailing shocks in both the VC and NVC cases move more slowly than they did in either of the two previous cases, because the solubility of C_{10} in the CO_2 is lower at 800 psia, and, hence, evaporation of residual C_{10} takes longer.

The velocity behavior of the leading shock is more complex. In the NVC case, the leading shock velocity is between those observed for Cases 1 and 2. At 800 psia, the Case 3 displacement is less efficient than Case 1, and more oil is left behind the leading shock. In addition, less CO_2 is dissolved in that oil, so more CO_2 is available to create a fast-moving vapor phase. The NVC leading shock in Case 3 moves more slowly than in Case 2, because the solubility of CO_2 at 800 psia is still higher than that of C_1 at 1675 psia (compare Figs. 3.1-11 and 3.1-16) and because the viscosity of CO_2 is slightly higher.

Table 3.1-7. MOC Solution of Ternary Case with Volume Change on Mixing at 160°F and 1675 PSIA, (CASE 2).

Comment	Composition (moles)			Total Velocity	Gas Saturation	Amount of Gas (moles)	Wave Velocity $1/PV$
	C_1	C_4	C_{10}				
Injection Gas	1.0000	0.0000	0.0000	1.0000	1.0000	1.0000	0.0000
Trailing Shock	0.8231	0.0000	0.1769	0.9952	0.7930	0.7237	0.0239
Continuous Variation	0.8231 0.7322	0.0000 0.0000	0.1769 0.2678	0.9952 0.9952	0.7930 0.6677	0.7237 0.5787	0.0239 0.0859
Zone of Constant State	0.7322 0.7322	0.0000 0.0000	0.2678 0.2678	0.9952 0.9952	0.6677 0.6677	0.5787 0.5787	0.0859 0.3497
Intermediate Shock	0.6136	0.0946	0.2918	1.0003	0.5213	0.4115	0.3497
Continuous Variation	0.6136 0.5228	0.0946 0.1102	0.2918 0.3670	1.0003 1.0003	0.5213 0.3512	0.4115 0.2580	0.3497 1.2641
Leading Shock	0.5228	0.1102	0.3670	1.0003	0.3512	0.2580	1.2641
Initial Oil	0.0000	0.2000	0.8000	0.7320	0.0000	0.0000	1.2641

Table 3.1-8. MOC Solution of Ternary Case with No Volume Change on Mixing at 160°F and 1675 PSIA, (CASE 2).

Comment	Composition (moles)			Total Velocity	Gas Saturation	Amount of Gas (moles)	Wave Velocity $1/PV$
	C_1	C_4	C_{10}				
Injection Gas	1.0000	0.0000	0.0000	1.0000	1.0000	1.0000	0.0000
Trailing Shock	0.8476	0.0000	0.1524	1.0000	0.7737	0.7628	0.0305
Continuous Variation	0.8476 0.7718	0.0000 0.0000	0.1524 0.2282	1.0000 1.0000	0.7737 0.6558	0.7628 0.6418	0.0305 0.0956
Zone of Constant State	0.7718 0.7718	0.0000 0.0000	0.2282 0.2282	1.0000 1.0000	0.6558 0.6558	0.6418 0.6418	0.0956 0.4328
Intermediate Shock	0.6461	0.0890	0.2649	1.0000	0.4934	0.4664	0.4328
Continuous Variation	0.6461 0.5533	0.0890 0.1049	0.2649 0.3418	1.0000 1.0000	0.4934 0.3330	0.4664 0.3095	0.4328 1.4436
Leading Shock	0.5533	0.1049	0.3418	1.0000	0.3330	0.3095	1.4436
Initial Oil	0.0000	0.2000	0.8000	1.0000	0.0000	0.0000	1.4436

Table 3.1-9. MOC Solution of Ternary Case with Volume Change on Mixing at 160°F and 800 PSIA, (CASE 3).

Comment	Composition (moles)			Total Velocity	Gas Saturation	Amount of Gas (moles)	Wave Velocity $1/PV$
	CO_2	C_4	C_{10}				
Injection Gas	1.0000	0.0000	0.0000	1.0000	1.0000	1.0000	0.0000
Trailing Shock	0.7962	0.0000	0.2038	0.9973	0.8385	0.6452	0.0124
Continuous Variation	0.7962 0.6854	0.0000 0.0000	0.2038 0.3146	0.9973 0.9973	0.8385 0.7000	0.6452 0.4497	0.0124 0.0687
Zone of Constant State	0.6854 0.6854	0.0000 0.0000	0.3146 0.3146	0.9973 0.9973	0.7000 0.7000	0.4497 0.4497	0.0687 0.2673
Intermediate Shock	0.5808	0.1034	0.3158	1.0023	0.5639	0.2999	0.2673
Continuous Variation	0.5808 0.5188	0.1034 0.1137	0.3158 0.3675	1.0023 1.0023	0.5639 0.4059	0.2999 0.1845	0.2673 0.8874
Leading Shock	0.5188	0.1137	0.3675	1.0023	0.4059	0.1845	0.8874
Initial Oil	0.0000	0.2000	0.8000	0.5460	0.0000	0.0000	0.8874

Table 3.1-10. MOC Solution of Ternary Case with No Volume Change on Mixing at 160°F and 800 PSIA, (CASE 3).

Comment	Composition (moles)			Total Velocity	Gas Saturation	Amount of Gas (moles)	Wave Velocity $1/PV$
	CO_2	C_4	C_{10}				
Injection Gas	1.0000	0.0000	0.0000	1.0000	1.0000	1.0000	0.0000
Trailing Shock	0.8538	0.0000	0.1462	1.0000	0.8041	0.7468	0.0220
Continuous Variation	0.8538 0.7615	0.0000 0.0000	0.1462 0.2385	1.0000 1.0000	0.8041 0.6613	0.7468 0.5840	0.0220 0.0968
Zone of Constant State	0.7615 0.7615	0.0000 0.0000	0.2385 0.2385	1.0000 1.0000	0.6613 0.6613	0.5840 0.5840	0.0968 0.4253
Intermediate Shock	0.6417	0.0932	0.2651	1.0000	0.5004	0.4134	0.4253
Continuous Variation	0.6417 0.5709	0.0932 0.1050	0.2651 0.3241	1.0000 1.0000	0.5004 0.3576	0.4134 0.2814	0.4253 1.2401
Leading Shock	0.5709	0.1050	0.3241	1.0000	0.3576	0.2814	1.2401
Initial Oil	0.0000	0.2000	0.8000	1.0000	0.0000	0.0000	1.2401

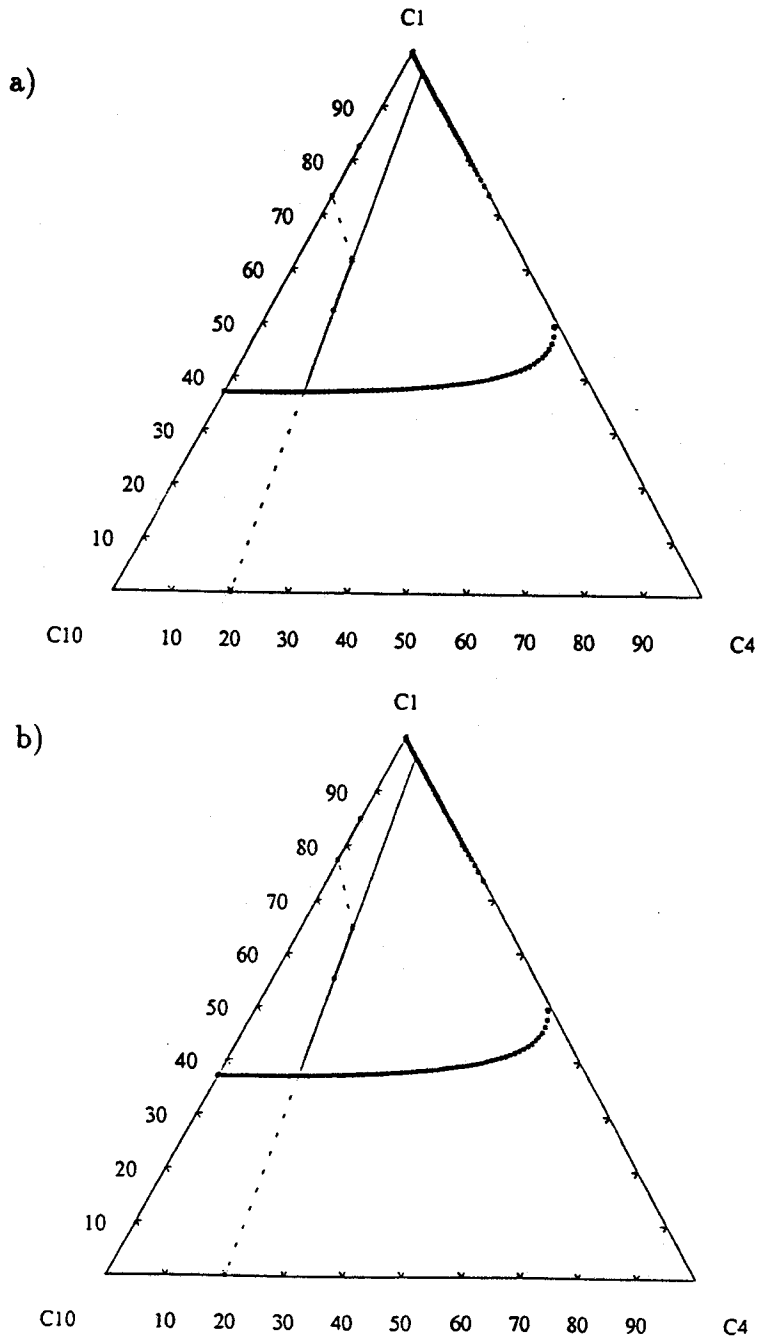

Figure 3.1-11. Composition routes for ternary C_1-C_4-C_{10} system at 1675 psia and 160°F:
a) Volume change on mixing
b) No volume change on mixing.

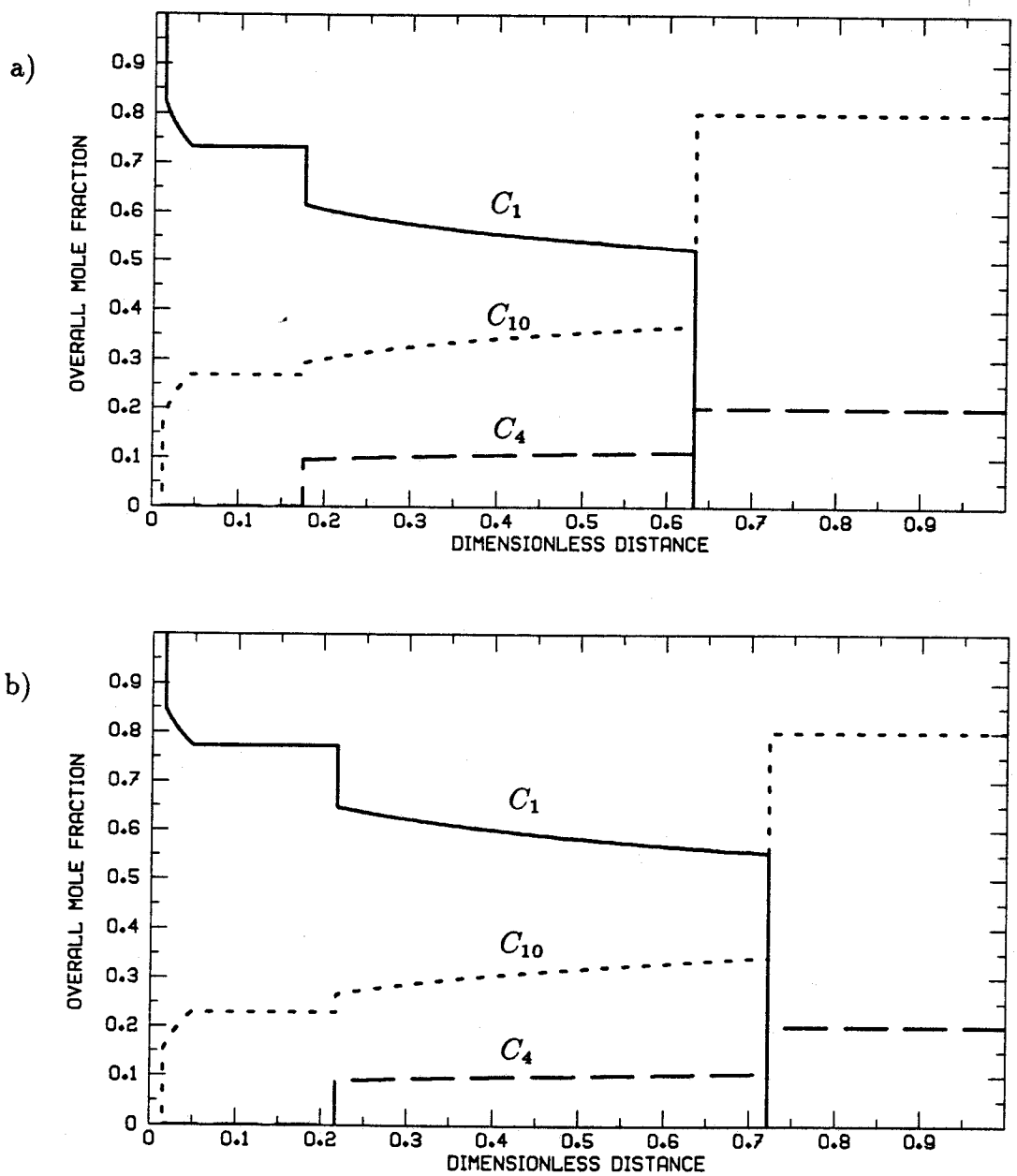

Figure 3.1-12. Composition profiles for displacement of C_4-C_{10} mixture by pure C_1 at 1675 psia and 160°F: a) Volume change on mixing b) No volume change on mixing.

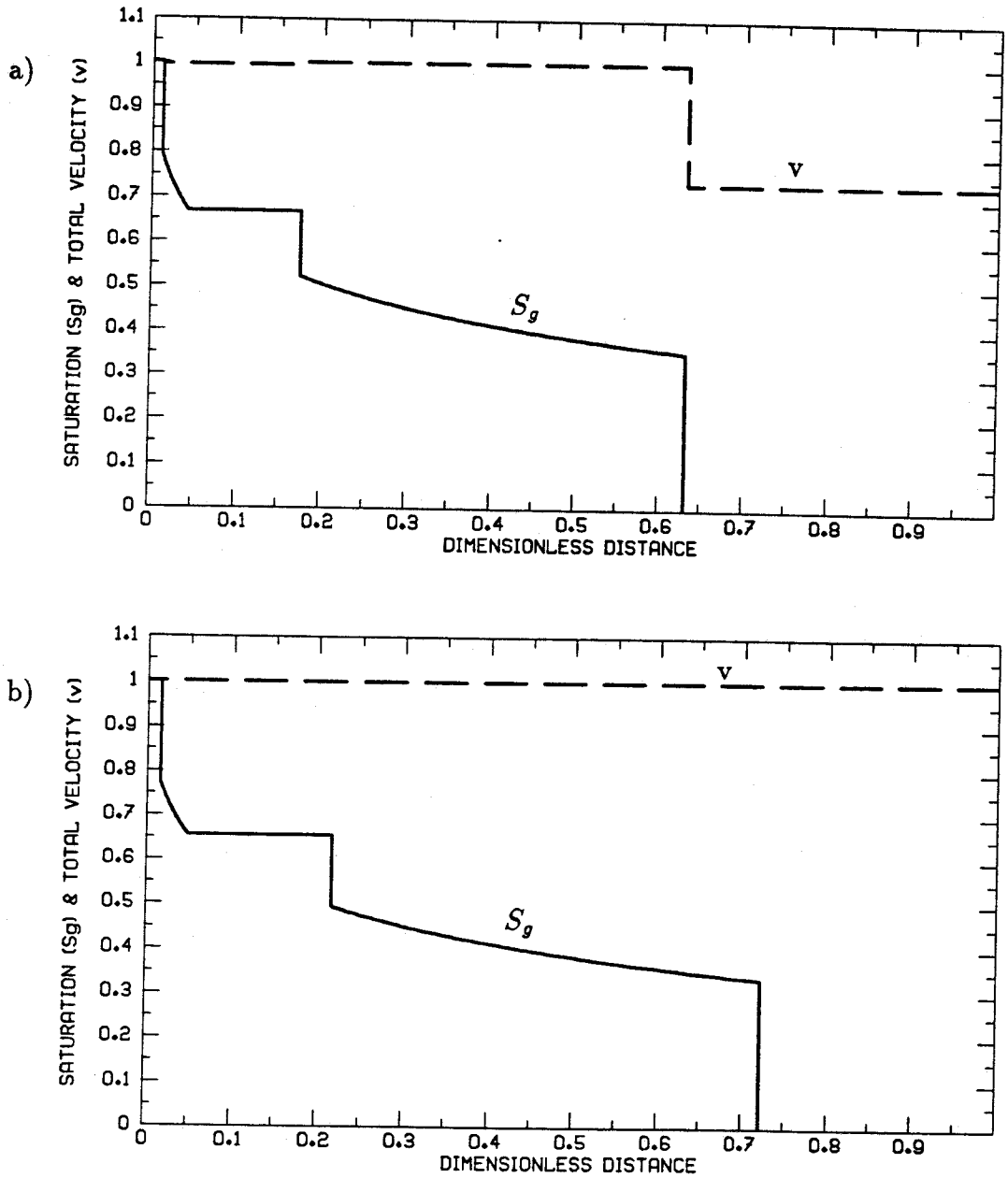

Figure 3.1-13. Saturation and total velocity profiles for displacement of a C_4-C_{10} mixture by C_1 at 1675 psia and 160°F: a) Volume change on mixing b) No volume change on mixing.

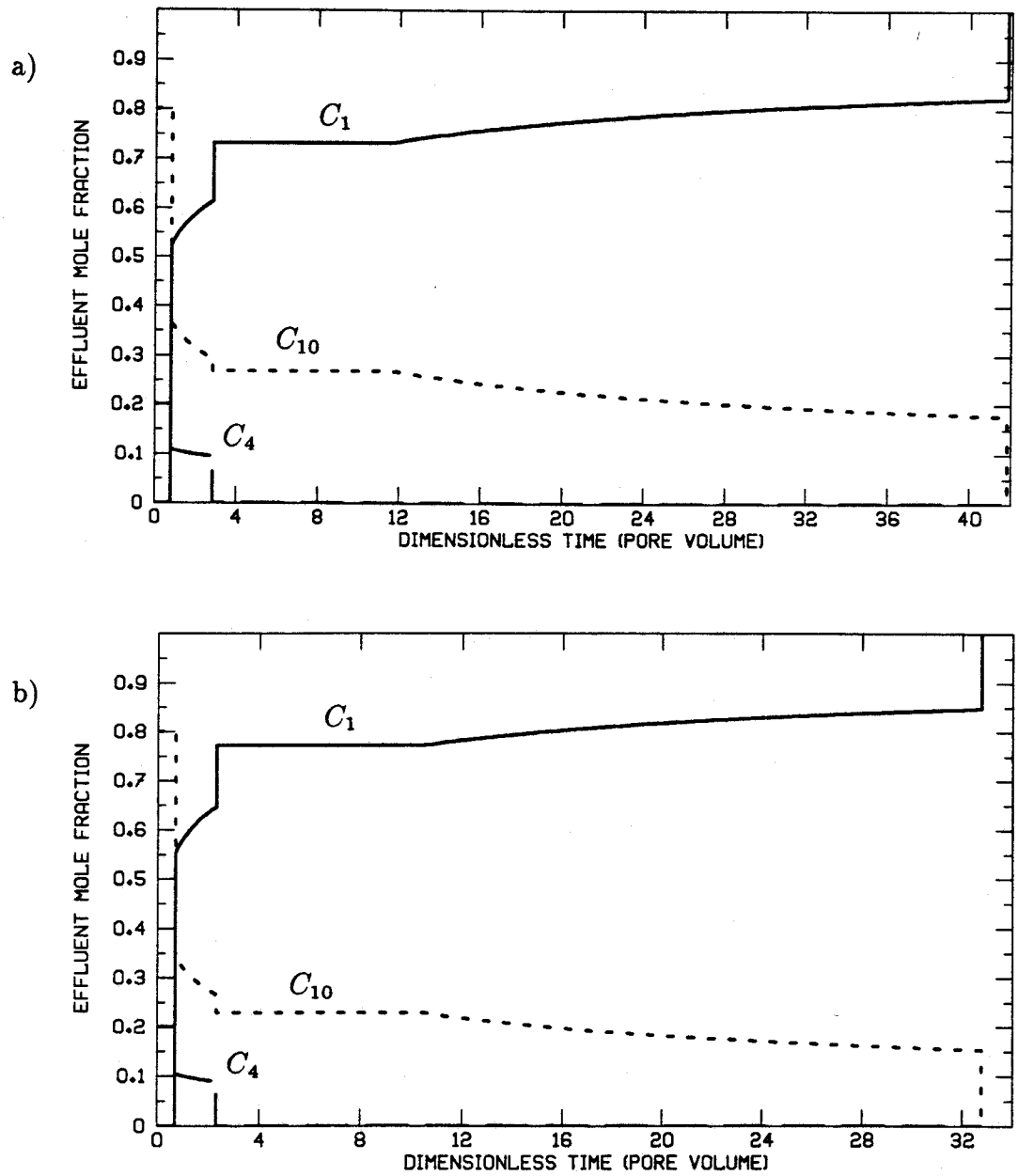

Figure 3.1-14. Effluent mole fractions for displacement of a C_4-C_{10} mixture by pure C_1 at 1675 psia and 160°F: a) Volume change on mixing b) No volume change on mixing.

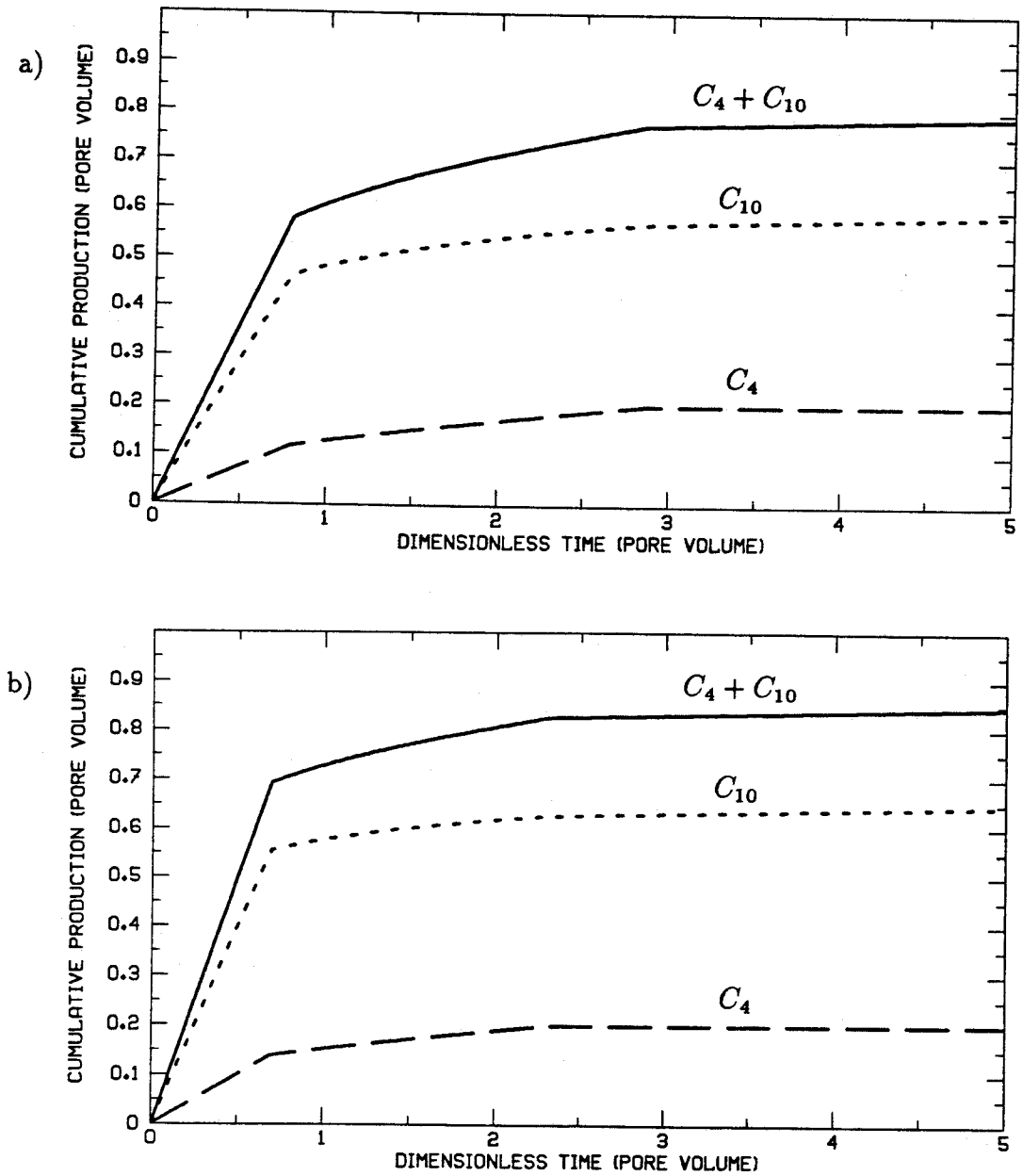

Figure 3.1-15. Recovery curves for displacement of a C_1-C_{10} mixture by pure C_1 at 1675 psia and 160°F: a) Volume change on mixing b) No volume change on mixing.

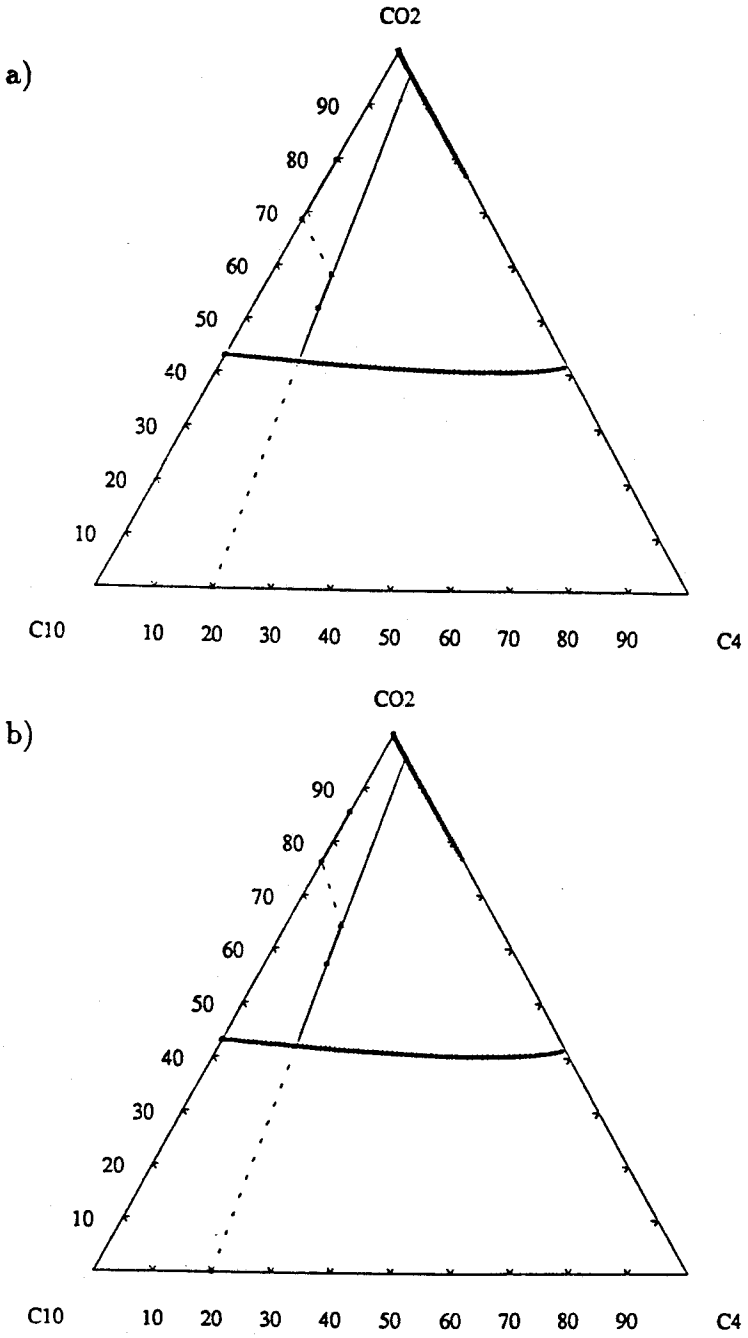

Figure 3.1-16. Composition routes for displacement of a C_4-C_{10} mixture by pure CO_2 at 800 psia and 160°F: a) Volume change on mixing b) No volume change on mixing.

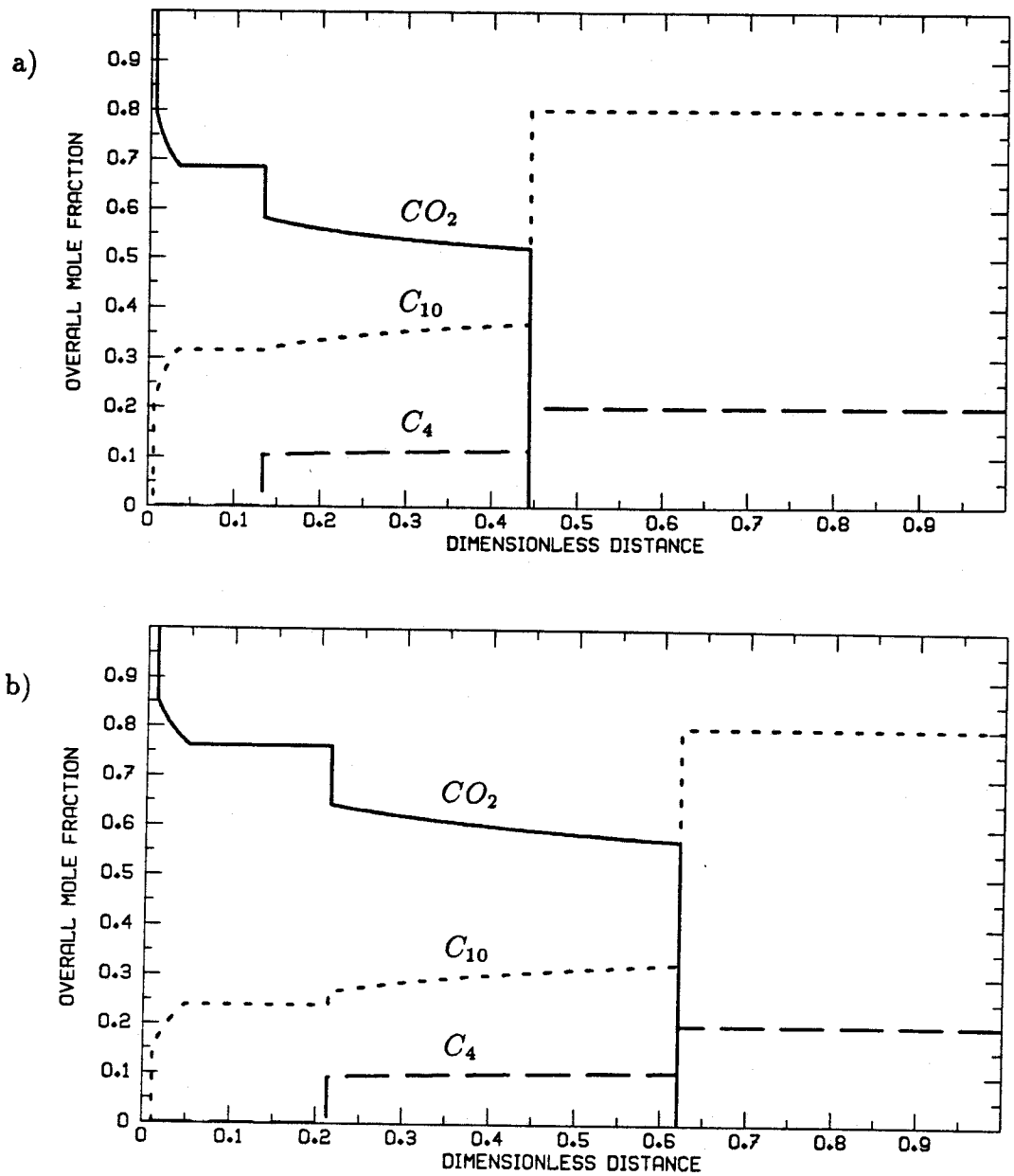

Figure 3.1-17. Composition profiles for displacement of a C_4-C_{10} mixture by pure CO_2 at 800 psia and 160°F: a) Volume change on mixing b) No volume change on mixing.

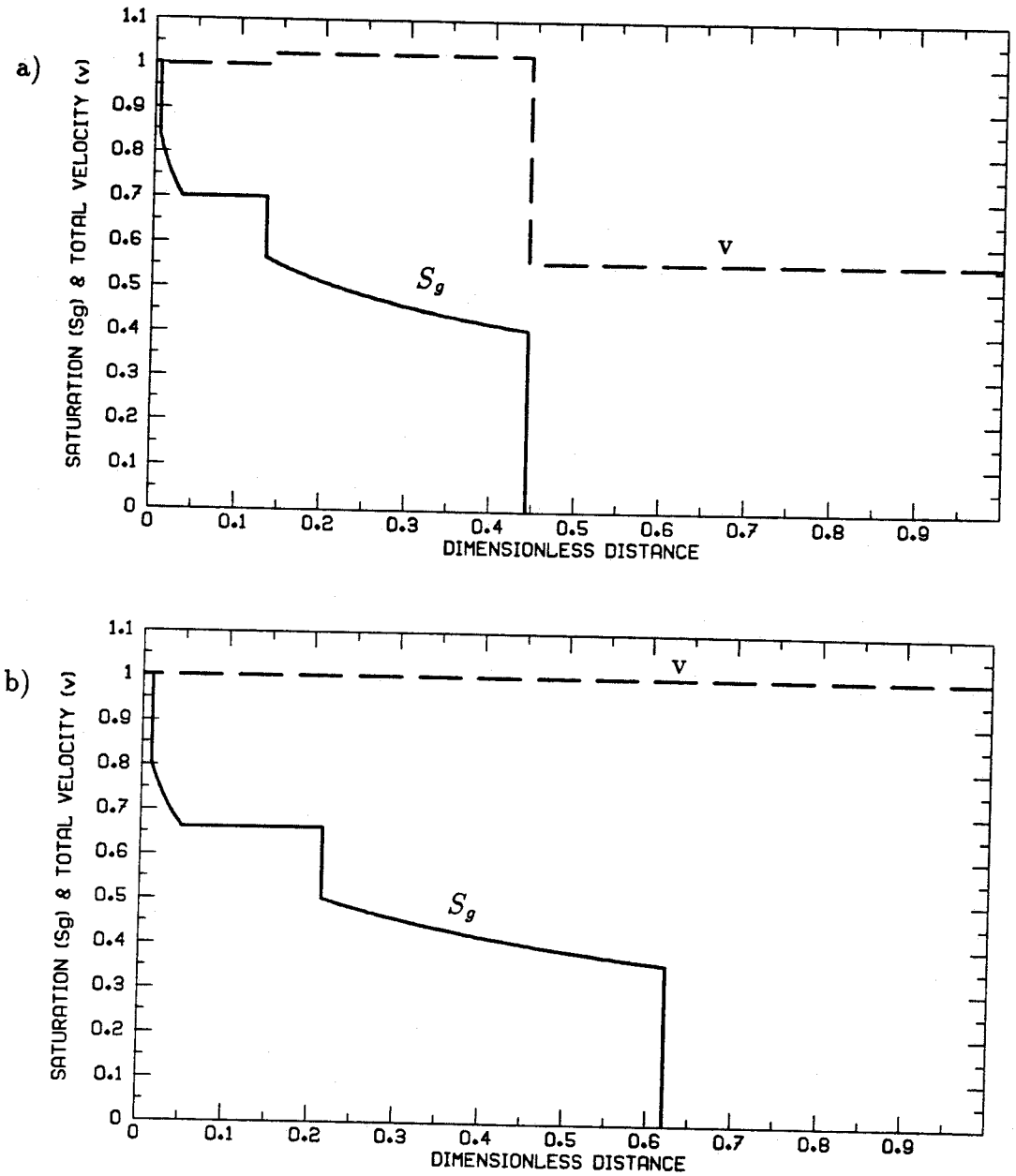

Figure 3.1-18. Saturation and total velocity profiles for displacement of a C_4-C_{10} mixture by pure CO_2 at 800 psia and 160°F: a) Volume change on mixing b) No volume change on mixing.

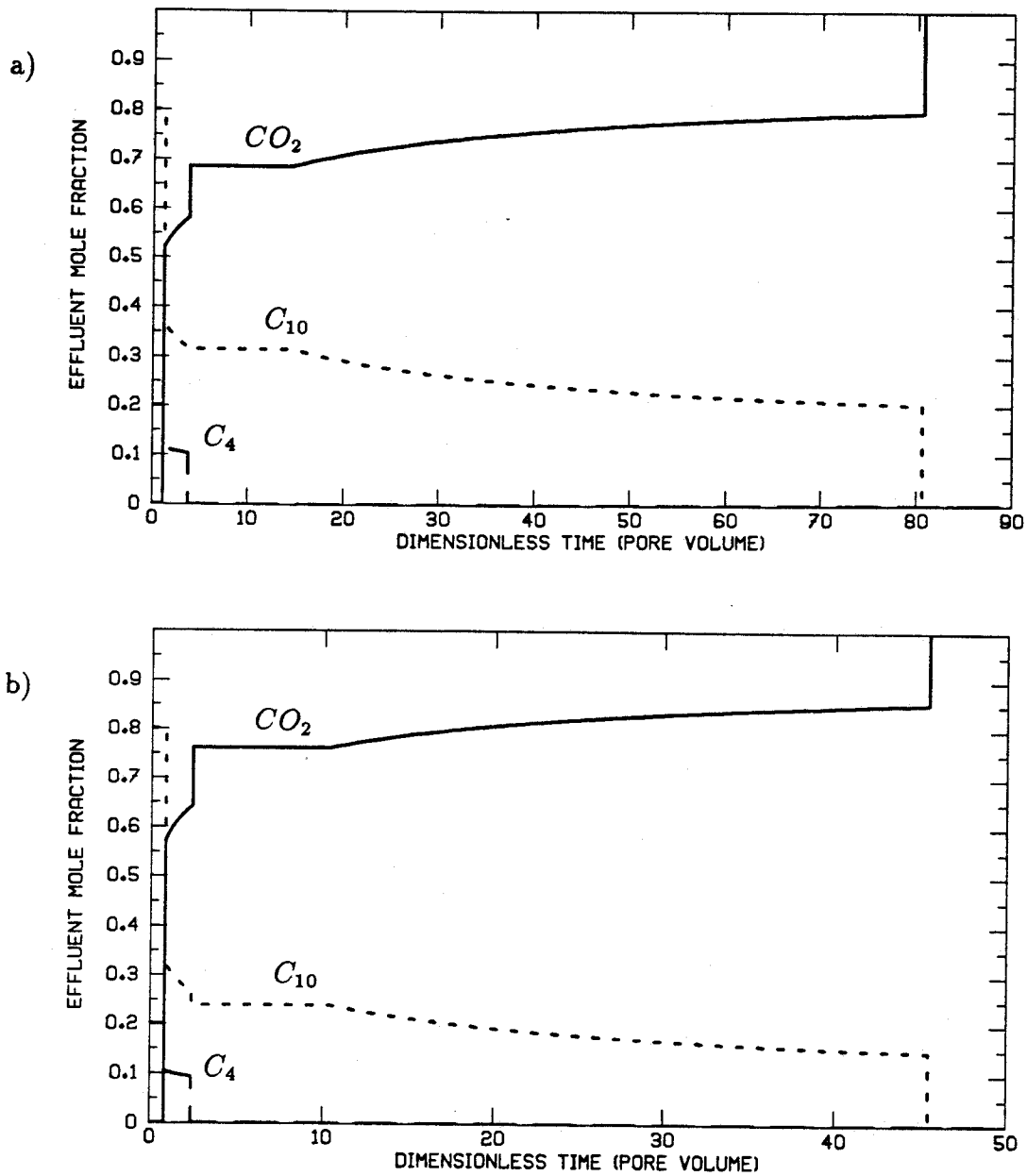

Figure 3.1-19. Effluent mole fractions for displacement of a C_4-C_{10} mixture by pure CO_2 at 800 psia and 160°F: a) Volume change on mixing b) No volume change on mixing.

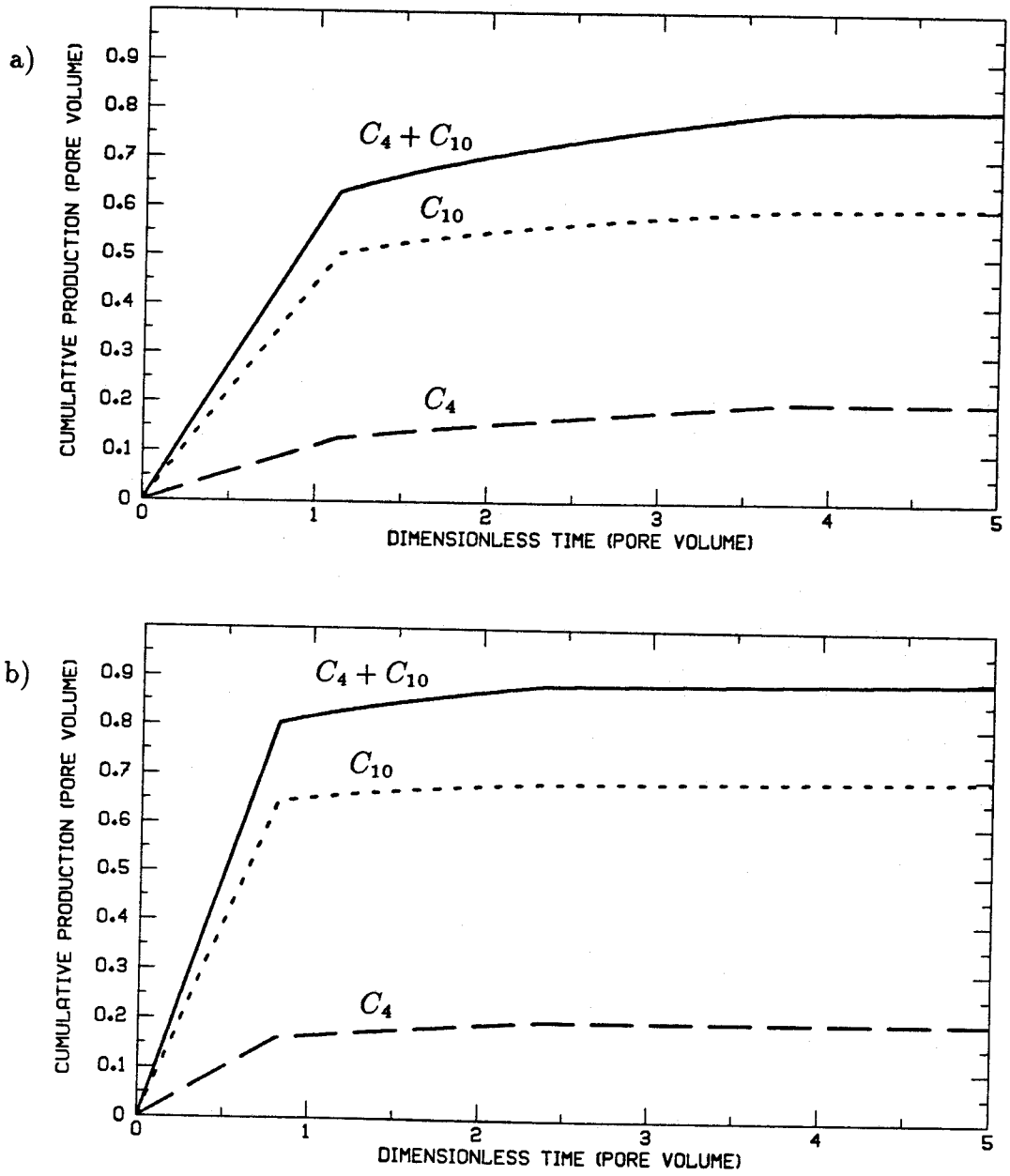

Figure 3.1-20. Recovery curves for displacement of a C_4-C_{10} mixture by pure CO_2 at 800 psia and 160°F: a) Volume change on mixing b) No volume change on mixing.

When there is volume change, however, the ordering of leading shock velocities changes. The leading shock velocity in Case 3 is the slowest of the three. In that case, the solubility of CO_2 in the undisplaced oil is still relatively high, and the density change as the CO_2 dissolves is much larger. The increased change in volume as the CO_2 dissolves is enough to compensate for the decreased solubility. Thus, at the lower pressure, volume change has a significant impact on the timing of oil recovery. As in the previous cases, the NVC assumption leads to optimistic recovery estimates.

Case 4: CO_2-C_4 Injection at 1250 psia

Composition routes for injection of a gas mixture containing 90 mole percent CO_2 with 10 mole percent C_4 are compared for the VC and NVC cases in Fig. 3.1-21. The initial oil composition was the same as in the previous cases. This case is a condensing gas drive, in contrast to the vaporizing gas drives of the previous cases. Composition, saturation and flow velocity profiles are given in Figs. 3.1-22 and 3.1-23. Effluent compositions and component recovery curves are given in Figs. 3.1-24 and 3.1-25. Details of compositions and velocities at key points are reported in Tables 3.1-11 and 3.1-12.

Comparison of corresponding plots for Case 1 and Case 4 reveals several key differences. First, the leading shock is not the limit of a zone of continuous variation. Hence, there is a zone of constant state that trails the leading shock. Second, there is a continuous variation along a nontie-line path from the injection tie line to the initial tie line, in place of the intermediate shock obtained in the vaporizing gas drives. The nontie-line path departs from the injection tie line at a point at which the two finite eigenvalues are equal. That point, labeled a, is clearly visible in Figs. 3.1-22 and 3.1-23, because there is a change in slope of the continuous profiles.

The effect of volume change is similar to that observed in the vaporizing gas drives. The qualitative form of the solutions is the same, but all the wave speeds are larger in the NVC case, and there are some minor differences in shock strengths (see Tables 3.1-11 and 3.1-12).

3.1-4 Discussion

The solutions presented here confirm that volume change on mixing has the largest impact on the timing of recovery, but the amount of recovery is also affected. Qualitative features of the solutions such as the number of shocks, the positions of spreading waves, self-sharpening waves and zones of constant state are not affected, however.

The examples presented were for cases near the immiscible limit shown in the binary CO_2-C_{10} displacement. For pure CO_2 or C_1 injection, volume change becomes less important as miscibility is approached. As the amount of C_4 in the original oil is increased, or as the pressure is increased, the velocities of the leading and trailing shocks approach each other. They are equal when the initial composition lies on the extension of the tie line through the plait points. As miscibility is approached, the amount of oil left behind the leading shock is reduced, and, hence, the total amount of volume change is also reduced. Furthermore, as pressure is increased the contrast in density between injected component in the vapor phase and in the liquid phase decreases. Thus, volume change will have greatest effect at intermediate pressures where solubility of injected fluid in the oil is reasonably high and where there is a significant contrast between the density of vapor and liquid phases.

Table 3.1-11. MOC Solution of Ternary Case with Volume Change on Mixing at 160°F and 1250 PSIA, (CASE 4).

Comment	Composition (moles)			Total Velocity	Gas Saturation	Amount of Gas (moles)	Wave Velocity $1/PV$
	CO_2	C_4	C_{10}				
Injection Gas	0.9000	0.1000	0.0000	1.0000	1.0000	1.0000	0.0000
Trailing Shock	0.7991	0.1539	0.0470	0.9757	0.7814	0.6510	0.1154
Continuous Variation	0.7991	0.1539	0.0470	0.9757	0.7814	0.6510	0.1154
	0.7580	0.1758	0.0662	0.9757	0.6494	0.4915	0.3994
Nontie-line path	0.7580	0.1758	0.0662	0.9757	0.6494	0.4915	0.3994
	0.6952	0.0792	0.2256	0.9593	0.3572	0.2235	0.5079
Zone of Constant State	0.6952	0.0792	0.2256	0.9593	0.3572	0.2235	0.5079
	0.6952	0.0792	0.2256	0.9593	0.3572	0.2235	0.8801
Leading Shock	0.6952	0.0792	0.2256	0.9593	0.3572	0.2235	0.8801
Initial Oil	0.0000	0.2000	0.8000	0.6774	0.0000	0.0000	0.8801

Table 3.1-12. MOC Solution of Ternary Case with No Volume Change on Mixing at 160°F and 1250 PSIA, (CASE 4).

Comment	Composition (moles)			Total Velocity	Gas Saturation	Amount of Gas (moles)	Wave Velocity $1/PV$
	CO_2	C_4	C_{10}				
Injection Gas	0.9000	0.1000	0.0000	1.0000	1.0000	1.0000	0.0000
Trailing Shock	0.8192	0.1431	0.0377	1.0000	0.7461	0.7295	0.1744
Continuous Variation	0.8192	0.1431	0.0377	1.0000	0.7461	0.7295	0.1744
	0.7826	0.1627	0.0547	1.0000	0.6078	0.5871	0.5511
Nontie-line path	0.7826	0.1627	0.0547	1.0000	0.6078	0.5871	0.5511
	0.7188	0.0750	0.2062	1.0000	0.3027	0.2920	0.6985
Zone of Constant State	0.7188	0.0750	0.2062	1.0000	0.3027	0.2920	0.6985
	0.7188	0.0750	0.2062	1.0000	0.3027	0.2920	1.1412
Leading Shock	0.7188	0.0750	0.2062	1.0000	0.3027	0.2920	1.1412
Initial Oil	0.0000	0.2000	0.8000	1.0000	0.0000	0.0000	1.0000

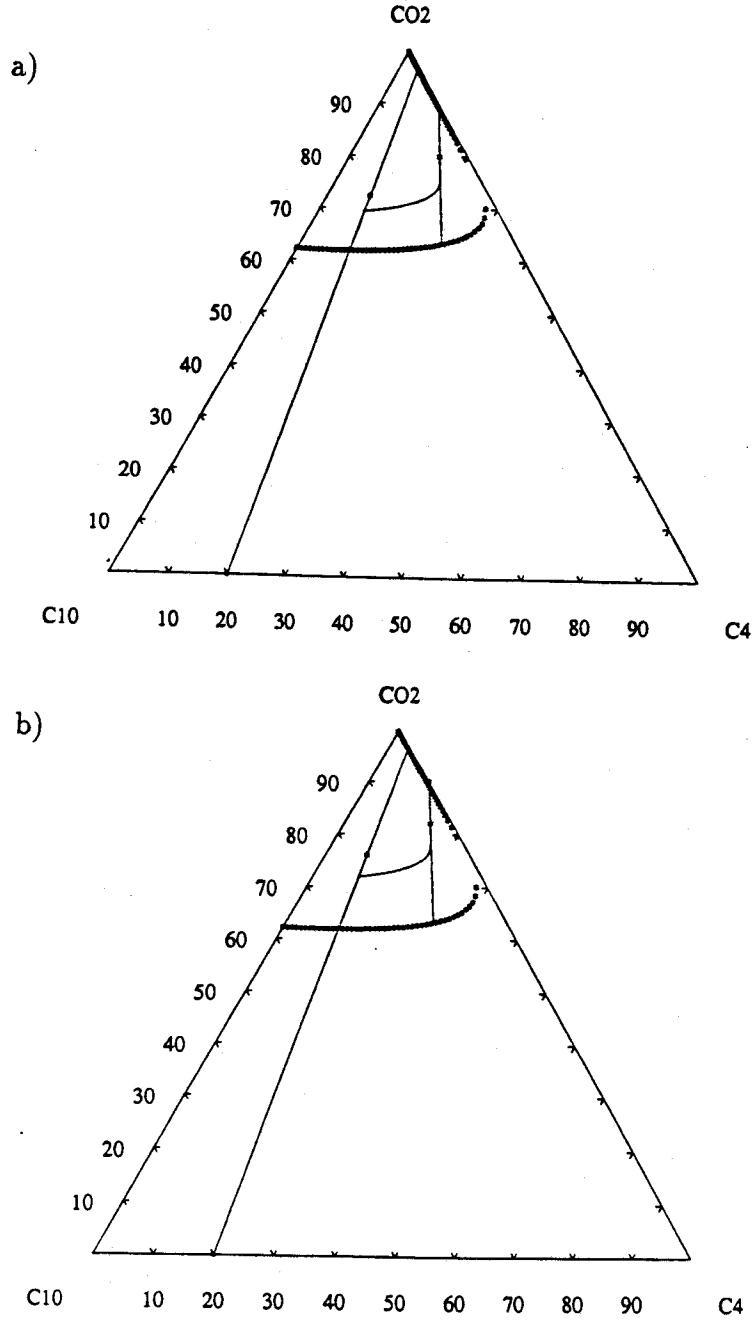

Figure 3.1-21. Composition routes for displacement of a C_4-C_{10} mixture by a CO_2-C_4 mixture (condensing gas drive) at 1250 psia and 160°F: a) Volume change on mixing b) No volume change on mixing.

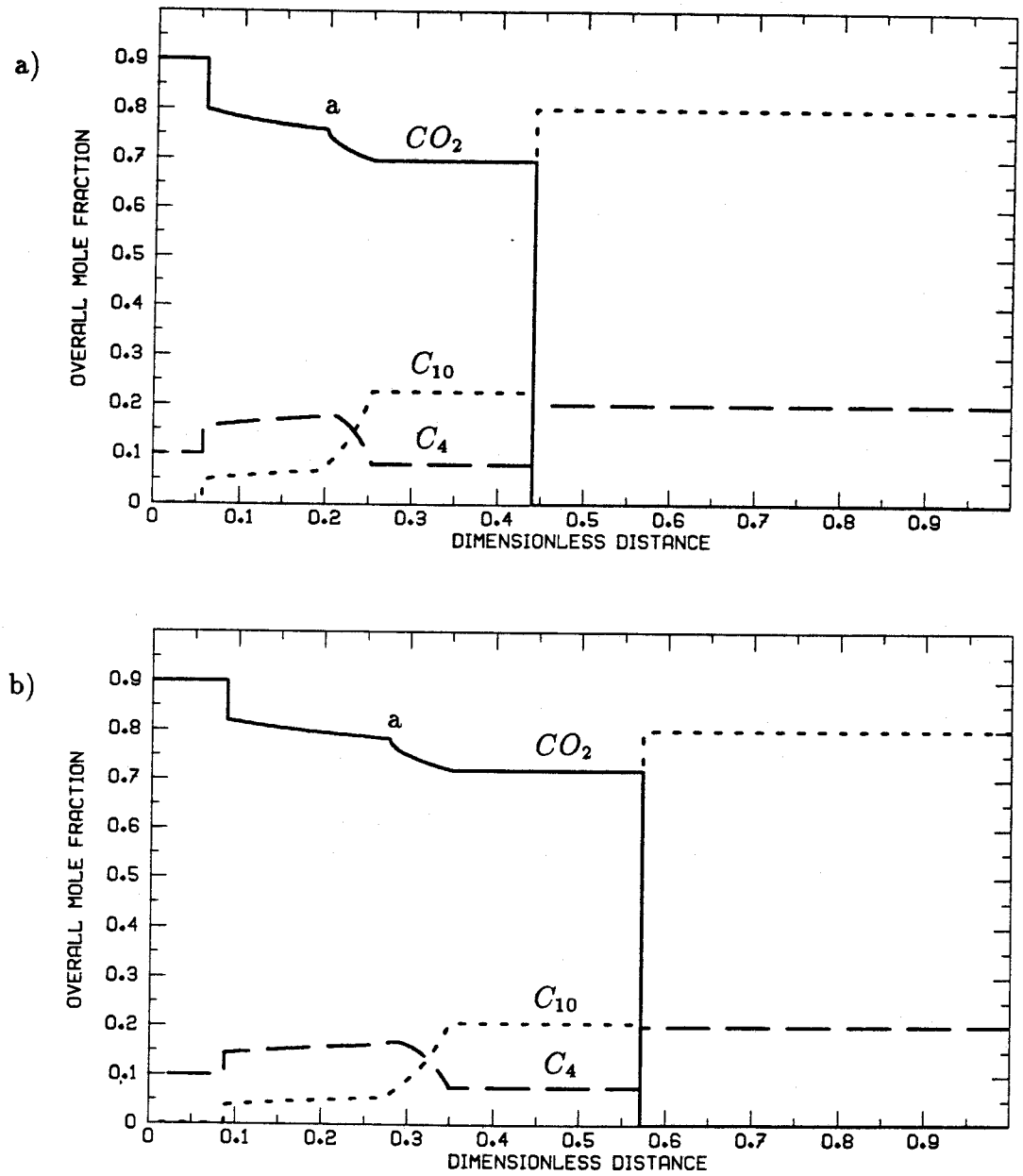

Figure 3.1-22. Composition profiles for displacement of a C_4-C_{10} mixture by a CO_2-C_4 mixture (condensing gas drive) at 1250 psia and 160°F: a) Volume change on mixing b) No volume change on mixing.

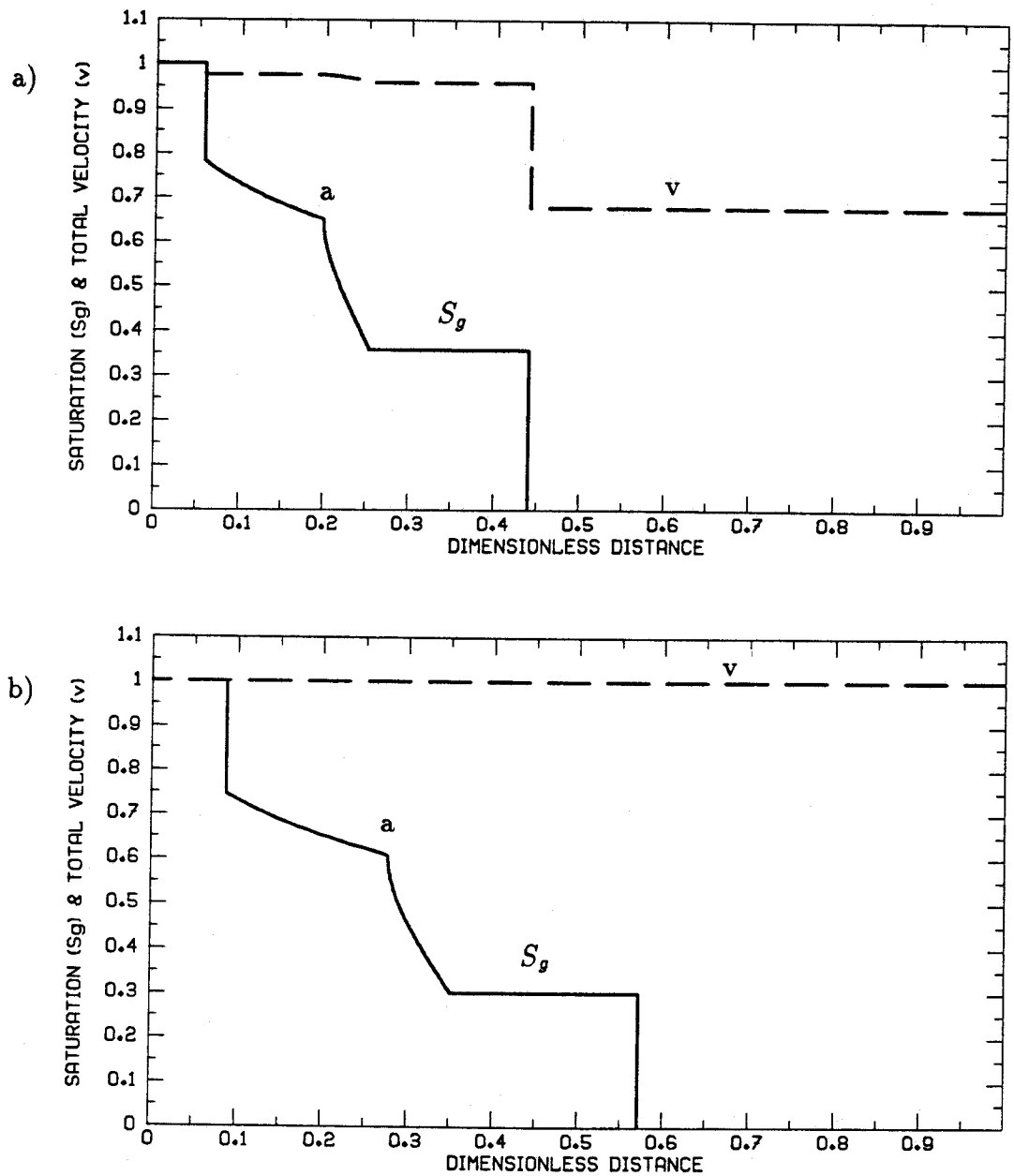

Figure 3.1-23. Saturation and total velocity profiles for displacement of a C_4-C_{10} mixture by a CO_2-C_4 mixture (condensing gas drive) at 1250 psia and 160°F: a) Volume change on mixing
b) No volume change on mixing.

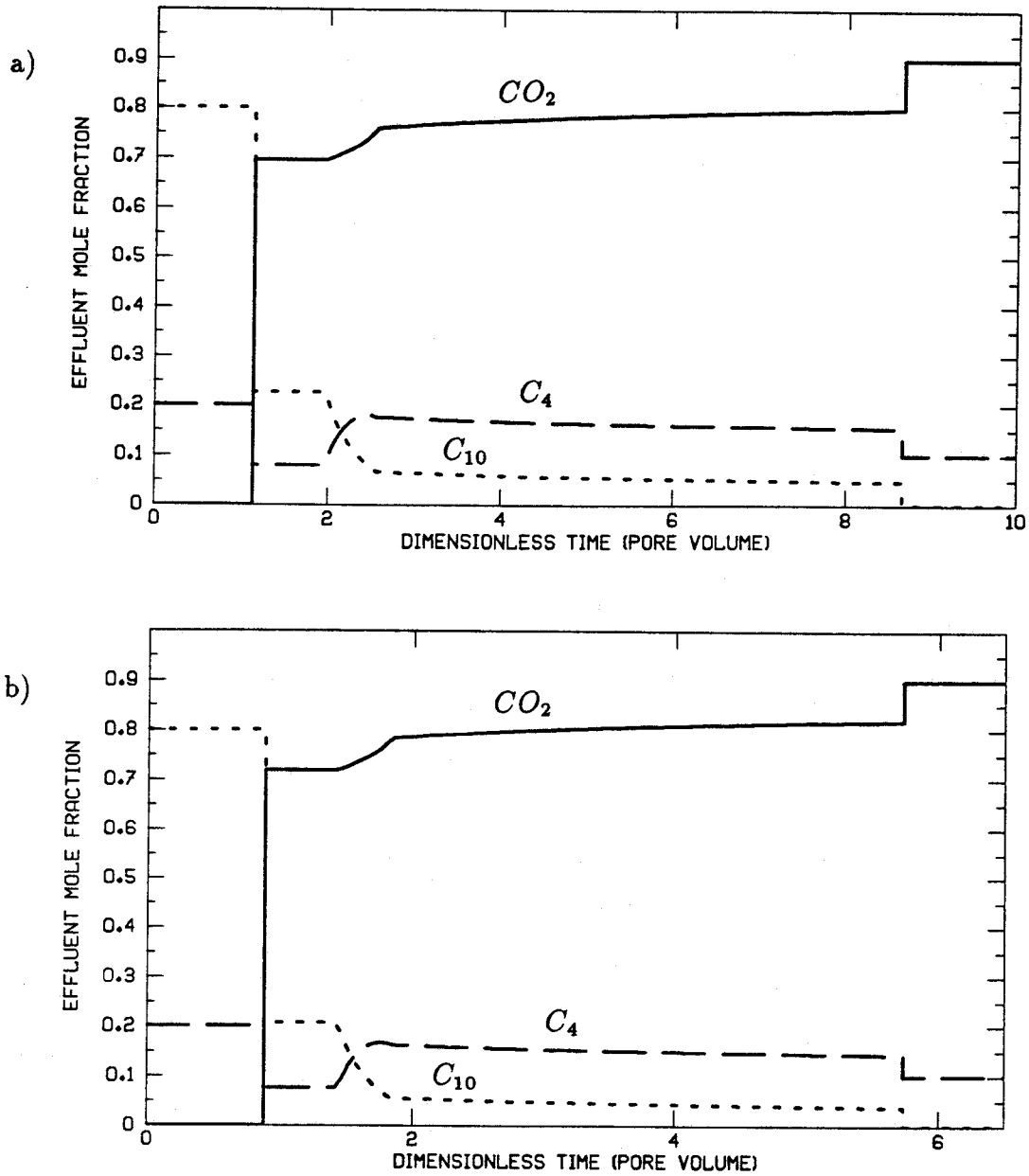

Figure 3.1-24. Effluent mole fractions for displacement of a C_4-C_{10} mixture by a CO_2-C_4 mixture (condensing gas drive) at 1250 psia and 160°F: a) Volume change on mixing b) No volume change on mixing.

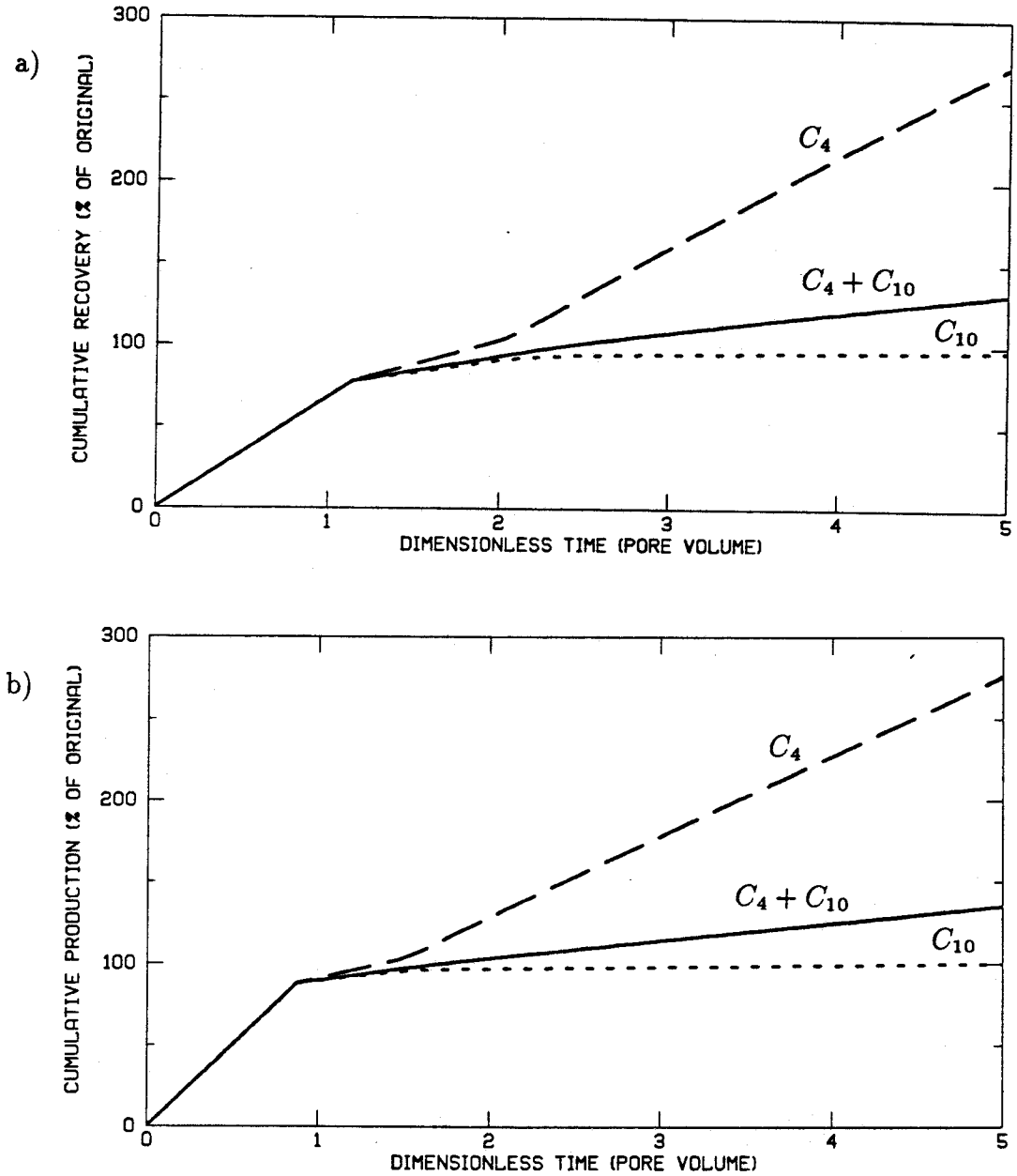

Figure 3.1-25. Recovery curves for displacement of a C_4-C_{10} mixture by a CO_2-C_4 mixture (condensing gas drive) at 1250 psia and 160°F: a) Volume change on mixing b) No volume change on mixing.

3.1-5 Conclusions

One-dimensional conservation laws arising in enhanced oil recovery have been solved for binary and ternary systems analytically. The solutions include the phase behavior through the Peng-Robinson equation of state. The following conclusions have been drawn from the solutions presented.

(1) Volume change on mixing changes composition paths only slightly, but can change flow velocity drastically.

(2) Volume change has greater effect when the density of the injected gas is much lower than that of the oil.

(3) Volume change has smaller effect when the solubility of injectant in the oil is low.

(4) No volume change on mixing is a good assumption if the injectant has weak partitioning with the initial oil.

(5) Breakthrough recoveries are higher when volume is conserved.

3.2 Theory of Three-Component, Two-Phase Flow in Radial Systems

Russell Johns and Birol Dindoruk

The solutions presented in Section 3.1 were for linear flow. In some situations, however, it is desirable to have available solutions for radial flow. For example, analytical solutions would be useful for testing of compositional simulators applied to radial flow systems. In this section, we show how solutions for linear flow can be transformed to represent radial flow.

Welge et al. (1962) showed that the Buckley-Leverett analytical solutions can be transferred to radial one-dimensional systems using a simple transformation. We review that transformation here to set the stage for the extension to multicomponent, multiphase flow. We then illustrate the use of the transformation with several comparisons of linear and radial flow.

3.2.1 Buckley-Leverett Flow

Eq. (3.2-1) is the appropriate material balance equation under the assumptions stated in Section 3.1. If that equation is applied to water and oil, which have no mutual solubility, the result is the familiar Buckley-Leverett equation,

$$\phi \frac{\partial S_w}{\partial t} + \frac{\partial v_w}{\partial x} = 0. \tag{3.2-1}$$

In this dimensional equation, S_w is the water saturation, v_w is the water macroscopic velocity, x is the linear distance, and t is the time.

Consider the transformation of Eq. (3.2-1) into a more useful radial form. We start by writing the radial form of the Buckley-Leverett equation,

$$\phi \frac{\partial S_w}{\partial t} + \frac{1}{r} \frac{\partial (r v_w)}{\partial r} = 0. \tag{3.2-2}$$

Eq. (3.2-2) is complicated by the fact that the second term is dependent on the radial distance, r. However, the macroscopic water velocity is related to the radial distance as $v_w = \frac{f_w Q_{inj}}{2\pi rh}$. Hence, the equation can be simplified. Once substituted, the dependence on the radial distance is partially removed, and the resulting equation is

$$\phi \frac{\partial S_w}{\partial t} + \frac{Q_{inj}}{2\pi rh} \frac{\partial f_w}{\partial r} = 0, \tag{3.2-3}$$

where Q_{inj} is the injection volumetric flow rate, h is the reservoir thickness, and f_w is the fractional flow of water at a given water saturation.

As with many analytical solutions, it is desirable to present the results in dimensionless form. For the one-dimensional linear equation, we use the dimensionless definitions, $x_d = \frac{x}{L}$ and $t_d = \frac{Q_{inj} t}{A\phi L}$, while for the radial form, we use $r_d = \frac{r}{L}$ and $t_d = \frac{Q_{inj} t}{\pi L^2 \phi h}$. The parameters A and L are the cross-sectional area and distance from the injector to producer, respectively.

It is also convenient to express the partial derivatives in terms of water saturation alone. This can be done using the chain rule, and defining $f' = \frac{\partial f_w}{\partial S_w}$. In dimensionless form, we now have the linear one-dimensional equation,

$$\frac{\partial S_w}{\partial t_d} + f' \frac{\partial S_w}{\partial x_d} = 0, \tag{3.2-4}$$

and the radial equation,

$$\frac{\partial S_w}{\partial t_d} + \frac{f'}{2r_d} \frac{\partial S_w}{\partial r_d} = 0. \tag{3.2-5}$$

Eq. (3.2-4) is easily solved by the method of characteristics (Buckley and Leverett 1942). The radial equation, however, is still complicated by the radial distance term in front of the partial derivative. To remove this last complication, a variable substitution is made. Substituting $\varepsilon_d = r_d^2$ into Eq. (3.2-5), a form similar to the linear version is obtained. The new radial equation,

$$\frac{\partial S_w}{\partial t_d} + f' \frac{\partial S_w}{\partial \varepsilon_d} = 0, \tag{3.2-6}$$

is therefore easily solved by the method of characteristics. One simply recognizes that the radial equation is now linear in form, and, thus, the one-dimensional linear solution can be used. Once the linear equation is solved, the radial solution is quickly obtained by taking the square root of the linear distance coordinate. For example, if 80 percent water saturation is obtained at a linear dimensionless distance of 0.50, the radial transformation would give the same value of water saturation but at a dimensionless radial distance of 0.71.

For the same pore volumes injected, therefore, the water front has appeared to move dimensionally further in the radial system. The definitions for dimensionless time (or pore volumes injected), however, are changed after the transformation. Thus, if the radial system has a greater pore volume, the water front will actually move slower. The front moves more slowly since greater volume is contacted as the front advances (the speed of the front is inversely proportional to the radial distance). Table 3.2-1 gives a summary and comparison of the linear and radial waterflood equations.

Table 3.2-1. Buckley-Leverett Immiscible Displacement.

LINEAR	RADIAL
$\phi \frac{\partial S_w}{\partial t} + \frac{\partial v_w}{\partial x} = 0$	$\phi \frac{\partial S_w}{\partial t} + \frac{1}{r} \frac{\partial (r v_w)}{\partial r} = 0$
$v_w = \frac{f_w Q_{inj}}{A}$	$v_w = \frac{f_w Q_{inj}}{2 \pi r h}$
$x_d = \frac{x}{L}\,,\ t_d = \frac{Q_{inj} t}{A \phi L}$	$r_d = \frac{r}{L}\,,\ t_d = \frac{Q_{inj} t}{\pi L^2 \phi h}$
$\frac{\partial S_w}{\partial t_d} + f' \frac{\partial S_w}{\partial x_d} = 0$	$\frac{\partial S_w}{\partial t_d} + \frac{f'}{2 r_d} \frac{\partial S_w}{\partial r_d} = 0$
	$\epsilon_d = r_d^2$
	$\frac{\partial S_w}{\partial t_d} + f' \frac{\partial S_w}{\partial \epsilon_d} = 0$

3.2.2 Multicomponent Multiphase Flow

The detailed derivation of the transformation used in the Buckley-Leverett equations can be easily extended to multicomponent multiphase flow. This section considers partially miscible systems with two or more phases and components. Two cases are considered: volume change on mixing and no volume change on mixing.

No Volume Change on Mixing

When injected fluids mix with in situ oil, components of the oil and injectant will be displaced. How the components partition themselves depends on the representation of the phase behavior. As components readjust to new equilibrium conditions, the resultant volume (hence, densities) may change. Physically, however, many components do not significantly change their volume upon mixing. This is especially true for high pressure miscible floods and for the liquid-liquid systems important in surfactant floods.

If volume is conserved, then the density of a given component, ρ_{ci}, is the same in all j phases. Consider the material balance given by Eq. (3.2-1). The linear one-dimensional system is,

$$\frac{\partial}{\partial t}\left[\sum_{j=1}^{n_p} \phi\, x_{ij}\, \rho_j\, S_j\right] + \frac{\partial}{\partial x}\left[\sum_{j=1}^{n_p} x_{ij}\, \rho_j\, v_j\right] = 0, \tag{3.2-7}$$

and for the radial one-dimensional system,

$$\frac{\partial}{\partial t}\left[\sum_{j=1}^{n_p} \phi\, x_{ij}\, \rho_j\, S_j\right] + \frac{1}{r}\frac{\partial}{\partial r}\left[\sum_{j=1}^{n_p} x_{ij}\, \rho_j\, r v_j\right] = 0. \tag{3.2-8}$$

Using the same procedure as for the Buckley-Leverett case, the dependence on the radial distance can be removed from inside the partial derivative. Upon division by the component density, followed by substitution of the appropriate definitions for the phase velocity (v_j), overall component concentration (C_i), overall component fractional flow (F_i), and dimensionless parameters, the radial equation becomes (see Table 3.2-2),

$$\frac{\partial C_i}{\partial t_d} + \frac{1}{2r_d}\frac{\partial F_i}{\partial r_d} = 0, \tag{3.2-9}$$

and the linear equation,

$$\frac{\partial C_i}{\partial t_d} + \frac{\partial F_i}{\partial x_d} = 0. \tag{3.2-10}$$

The definitions of the overall concentration and flux of a given component, C_i and F_i, are the same for both the radial and linear equations (Lake 1989).

$$C_i = \sum_{j=1}^{n_p} c_{ij}\, S_j \tag{3.2-11}$$

$$F_i = \sum_{j=1}^{n_p} c_{ij}\, f_j$$

Table 3.2-2. Miscible Displacement, No Volume Change on Mixing.

LINEAR	RADIAL
$\frac{\partial}{\partial t}(\sum_{j=1}^{Np}\phi x_{ij}\rho_j S_j)+ \frac{\partial}{\partial x}(\sum_{j=1}^{Np}x_{ij}\rho_j v_j)=0$	$\frac{\partial}{\partial t}(\sum_{j=1}^{Np}\phi x_{ij}\rho_j S_j)+ \frac{1}{r}\frac{\partial}{\partial r}(\sum_{j=1}^{Np}x_{ij}\rho_j r v_j)=0$
$v_j=\frac{f_j Q_{inj}}{A}$	$v_j=\frac{f_j Q_{inj}}{2\pi r h}$
$c_{ij}=\frac{x_{ij}\rho_j}{\rho_{cj}},\ C_i=\sum_{j=1}^{Np}c_{ij}S_j,$ $F_i=\sum_{j=1}^{Np}c_{ij}f_j$	$c_{ij}=\frac{x_{ij}\rho_j}{\rho_{cj}},\ C_i=\sum_{j=1}^{Np}c_{ij}S_j,$ $F_i=\sum_{j=1}^{Np}c_{ij}f_j$
$\frac{\partial C_i}{\partial t}+\frac{Q_{inj}}{A\phi}\frac{\partial F_i}{\partial x}=0$	$\frac{\partial C_i}{\partial t}+\frac{Q_{inj}}{2\pi r\phi h}\frac{\partial F_i}{\partial r}=0$
$x_d=\frac{x}{L},\ t_d=\frac{Q_{inj}t}{A\phi L}$	$r_d=\frac{r}{L},\ t_d=\frac{Q_{inj}t}{\pi L^2\phi h}$
$\frac{\partial C_i}{\partial t_d}+\frac{\partial F_i}{\partial x_d}=0$	$\frac{\partial C_i}{\partial t_d}+\frac{1}{2r_d}\frac{\partial F_i}{\partial r_d}=0$
	$\epsilon_d=r_d^2$
	$\frac{\partial C_i}{\partial t_d}+\frac{\partial F_i}{\partial \epsilon_d}=0$

Just as in the Buckley-Leverett case, we can define a new parameter, ε_d, to reduce the radial one-dimensional equation to the same form as the linear one-dimensional equation. The new radial equation,

$$\frac{\partial C_i}{\partial t_d} + \frac{\partial F_i}{\partial \varepsilon_d} = 0, \tag{3.2-12}$$

is then linear in form and the square root transformation can be used to obtain the radial solution. Table 3.2-2 shows the details of the derivation and definitions.

Volume Change on Mixing

When two fluids (i.e., solvent and oil) are combined, the volume of a mixture is not necessarily conserved. In reservoirs where the solvent density is low (i.e., low pressure floods), the volume of the mixture may shrink. Physically, the reduced volume results in a decreased velocity of the solvent and oil fronts. Even with this added complication, the simple radial transformation can still be applied.

Because the volume is not conserved, the density of a given component is not the same in all phases. Hence, we cannot divide Eq. (3.2-1) by the component density as we did before. As a result, new overall concentrations and fluxes, G_i and F_i, are defined as in Section 3.1. We begin with the linear one-dimensional equation,

$$\frac{\partial}{\partial t}\left[\sum_{j=1}^{n_p} \phi\, x_{ij}\, \rho_j\, S_j\right] + \frac{\partial}{\partial x}\left[\sum_{j=1}^{n_p} x_{ij}\, \rho_j\, v_j\right] = 0, \tag{3.2-13}$$

and the radial equation,

$$\frac{\partial}{\partial t}\left[\sum_{j=1}^{n_p} \phi\, x_{ij}\, \rho_j\, S_j\right] + \frac{1}{r}\frac{\partial}{\partial r}\left[\sum_{j=1}^{n_p} x_{ij}\, \rho_j\, r v_j\right] = 0. \tag{3.2-14}$$

The phase flow velocity in the linear case is related to the total velocity (v) and phase fractional flow (f_j). Due to volume change on mixing, the total velocity at a given cross-section of the reservoir can increase or decrease. The change in velocity for the linear case can be solved by using the MOC (Dumoré et al. 1984; Monroe 1986). For the radial case, however, we again have the dependence on radial distance inside and front of the second partial derivative. Because the total velocity changes, the total volumetric flow rate, Q, will also change. Even with this complication, however, a similar substitution ($v_j = \frac{f_j Q}{2\pi r h}$) can be made to cancel the radial distance parameter inside the partial derivative. Substituting the appropriate parameters into the one-dimensional linear equation results in the dimensionless equation,

$$\frac{\partial}{\partial t_d}\left[\sum_{j=1}^{n_p} x_{ij}\, \rho_{dj}\, S_j\right] + \frac{\partial}{\partial x_d}\left[Q_d \sum_{j=1}^{n_p} x_{ij}\, \rho_{dj}\, f_j\right] = 0, \tag{3.2-15}$$

and the radial equation,

$$\frac{\partial}{\partial t_d}\left[\sum_{j=1}^{n_p} x_{ij}\, \rho_{dj}\, S_j\right] + \frac{1}{2r_d}\frac{\partial}{\partial r_d}\left[Q_d \sum_{j=1}^{n_p} x_{ij}\, \rho_{dj}\, f_j\right] = 0. \tag{3.2-16}$$

Two new dimensionless parameters scaled to the constant injection conditions are defined: Q_d is the dimensionless volumetric flux rate, and ρ_{dj} is the dimensionless density (see Table 3.2-3). To reduce the equations to a simpler form, the parameters, G_i and F_i, can be defined as

$$G_i = \sum_{j=1}^{n_p} x_{ij} \rho_{dj} S_j \tag{3.2-17}$$

$$F_i = Q_d \sum_{j=1}^{n_p} x_{ij} \rho_{dj} f_j$$

These parameters take the place of the overall component concentration and overall component fractional flow. The linear one-dimensional equation simplifies to,

$$\frac{\partial G_i}{\partial t_d} + \frac{\partial F_i}{\partial x_d} = 0, \tag{3.2-18}$$

and the radial equation,

$$\frac{\partial G_i}{\partial t_d} + \frac{1}{2r_d} \frac{\partial F_i}{\partial r_d} = 0. \tag{3.2-19}$$

As before, if the substitution $\varepsilon_d = r_d^2$ is made, the radial equation becomes,

$$\frac{\partial G_i}{\partial t_d} + \frac{\partial F_i}{\partial \varepsilon_d} = 0, \tag{3.2-20}$$

and the same transformation can be used. The only complexity is that solving the equations by the MOC is more difficult. Densities must be calculated at each step and the dimensionless volumetric flux rate (or total velocity) must be included as an unknown (Dumoré et al. 1984; Monroe 1986), as is outlined in Section 3.1.

3.2.3 Example Solutions

Consider the injection of carbon dioxide (CO_2) into a linear core saturated with 80 percent decane (C_{10}) and 20 percent butane (C_4) at a temperature and pressure of 160°F and 800 psia, respectively. Allowing for volume change on mixing, Fig. 3.2-1 gives the linear and radial MOC solutions at a dimensionless time of 0.5 pore volumes injected. Three shocks (discontinuities), two rarefaction waves, and a zone of constant state develop as was shown in Section 3.1.

In the linear solution, the leading shock has moved a dimensionless distance of approximately 0.44, the intermediate shock a distance of 0.13, and the trailing shock a distance of 0.004. By applying the square root transformation to the linear solution, the radial solution is easily calculated. The shocks in the radial solution, for example, have moved to dimensionless distances of 0.66, 0.36, and 0.06. Assuming that L and h are the same, it appears, therefore, that the leading shock in the radial solution has moved further. In actuality, this is not the case. Even though the pore volumes injected are equal ($t_d = 0.5PV$), the definitions of the radial and linear dimensionless times have changed in the transformation. Considering the length scales in the two systems, the pore volume in the radial system will be substantially

Table 3.2-3. Miscible Displacement with Volume Change on Mixing.

LINEAR	RADIAL
$\frac{\partial}{\partial t}(\sum_{j=1}^{Np}\phi x_{ij}\rho_j S_j)+ \frac{\partial}{\partial x}(\sum_{j=1}^{Np}x_{ij}\rho_j v_j)=0$	$\frac{\partial}{\partial t}(\sum_{j=1}^{Np}\phi x_{ij}\rho_j S_j)+ \frac{1}{r}\frac{\partial}{\partial r}(\sum_{j=1}^{Np}x_{ij}\rho_j r v_j)=0$
$v_j=\frac{f_j Q}{A}=f_j v$	$v_j=\frac{f_j Q}{2\pi r h}$
$x_d=\frac{x}{L}\,,\ t_d=\frac{Q_{inj}t}{A\phi L}$ $Q_d=\frac{Q}{Q_{inj}}\,,\ \rho_{dj}=\frac{\rho_j}{\rho_{inj}}$	$r_d=\frac{r}{L}\,,\ t_d=\frac{Q_{inj}t}{\pi L^2\phi h}$ $Q_d=\frac{Q}{Q_{inj}}\,,\ \rho_{dj}=\frac{\rho_j}{\rho_{inj}}$
$\frac{\partial}{\partial t_d}(\sum_{j=1}^{Np}x_{ij}\rho_{dj}S_j)+ \frac{\partial}{\partial x_d}(Q_d\sum_{j=1}^{Np}x_{ij}\rho_{dj}f_j)=0$	$\frac{\partial}{\partial t_d}(\sum_{j=1}^{Np}x_{ij}\rho_{dj}S_j)+ \frac{1}{2r_d}\frac{\partial}{\partial r_d}(Q_d\sum_{j=1}^{Np}x_{ij}\rho_{dj}f_j)=0$
$G_i=\sum_{j=1}^{Np}x_{ij}\rho_{dj}S_j$ $F_i=Q_d\sum_{j=1}^{Np}x_{ij}\rho_{dj}f_j$	$G_i=\sum_{j=1}^{Np}x_{ij}\rho_{dj}S_j$ $F_i=Q_d\sum_{j=1}^{Np}x_{ij}\rho_{dj}f_j$
$\frac{\partial G_i}{\partial t_d}+\frac{\partial F_i}{\partial x_d}=0$	$\frac{\partial G_i}{\partial t_d}+\frac{1}{2r_d}\frac{\partial F_i}{\partial r_d}=0$
	$\epsilon_d=r_d^2$
	$\frac{\partial G_i}{\partial t_d}+\frac{\partial F_i}{\partial \epsilon_d}=0$

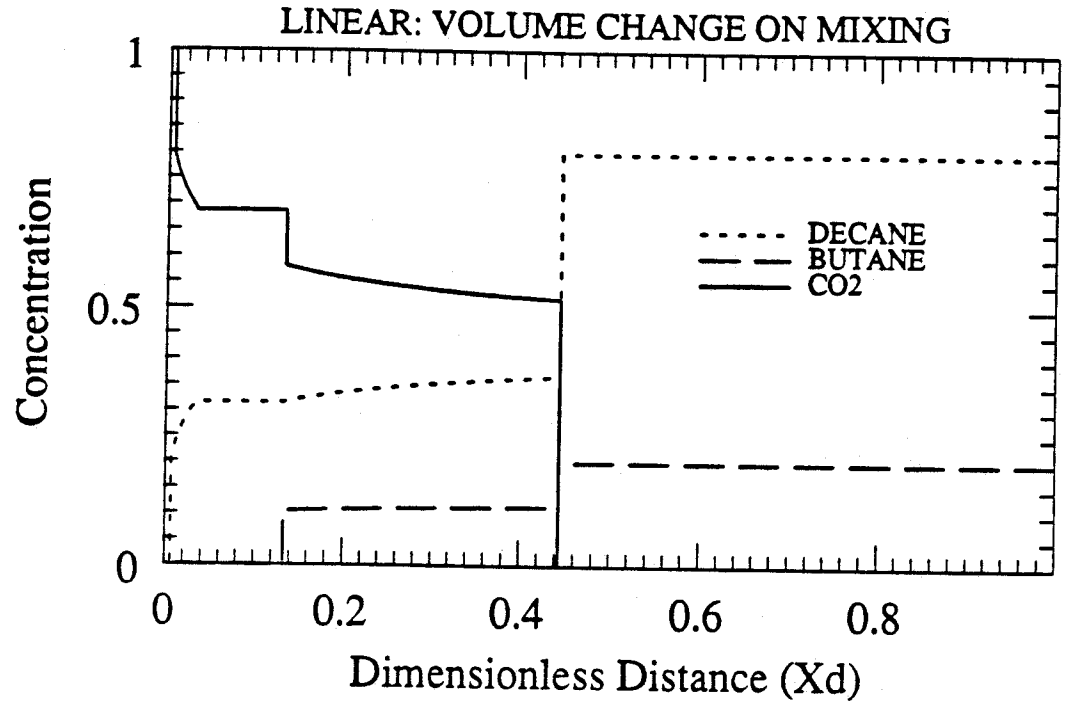

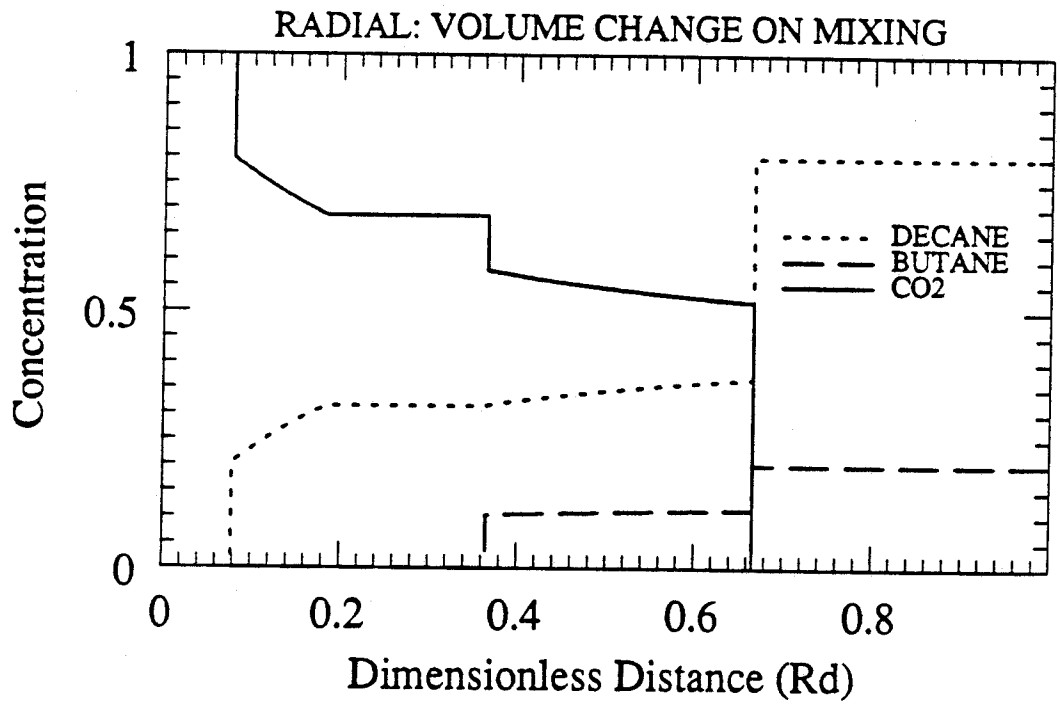

Figure 3.2-1. Comparison of linear and radial solutions at 0.5 PV injected for displacement of a 20 mole % C_4/80 mole % C_{10}.

greater. Hence, at the same pore volumes injected, the actual volume injected will be far greater in the radial system. Furthermore, the velocity of the shocks in the radial system will decrease rapidly with radial distance (inversely proportional to radial distance). The velocity decrease occurs because the fluids injected contact substantially more volume as the distance from the injector increases. One can easily show that the dimensionless velocity (ratio of actual velocity to injection velocity, $\frac{v}{v_{inj}}$) is related to the dimensionless volumetric flow rate as,

$$v_d = \frac{Q_d r_w}{r_d L} , \tag{3.2-21}$$

where r_w is the injector wellbore radius and L is the distance from the injector to the producer.

Fig. 3.2-2 gives the linear and radial analytic solutions for the same ternary system but at a dimensionless time of 1.0 PV. At 1.0 PV, the leading shock in the radial system has slowed down, while the leading shock in the linear system has moved closer. Ultimately, breakthrough of the leading shock will occur at the same dimensionless time for the two systems.

Fig. 3.2-3 shows the radial and linear velocity and saturation profiles. Again, the velocity in the radial system decreases very quickly. The rapid decrease obscures the change in velocity due to mixing effects. Even though volume change on mixing is important to the MOC solution, the resultant velocity decrease (or increase) may be masked by the radial dependence of the velocity.

3.2.4 Conclusions

The analysis and extension of Welge's transformation leads to the following conclusions:

(1) Multicomponent multiphase MOC linear solutions (including volume change on mixing) can be easily transformed to one-dimensional radial systems. A simple square root transformation and dimensionless time adjustment can be made.

(2) The velocity in a radial system significantly decreases with increasing radial distance. This effect overwhelms the velocity changes that occur when volume change on mixing is allowed.

3.3 Interfering Shocks in Slug Injection Processes

Russell Johns

In most miscible injection processes, solvents are not injected continuously, but are alternated or combined with cheaper fluids as slugs. Examples of real life slug injection processes are water-alternating-CO_2 (WAG), methane reinjection with CO_2 or chase gas injection (N_2 following CO_2). The purpose of this research is to derive analytical solutions for slug injection processes by relaxing the assumption of constant injection conditions. If analytical solutions can be developed, then effects of slug injection size and recycling can be quantified.

To illustrate the mathematical issues involved, we consider a simple binary system of water and alcohol and use the method of characteristics (MOC) to construct the analytical solution. Water is initially injected into an alcohol-saturated porous medium followed by continuous alcohol injection. Shocks and rarefaction waves from the two injection periods evolve and ultimately overtake and interfere with each other. This work discusses the resolution of the

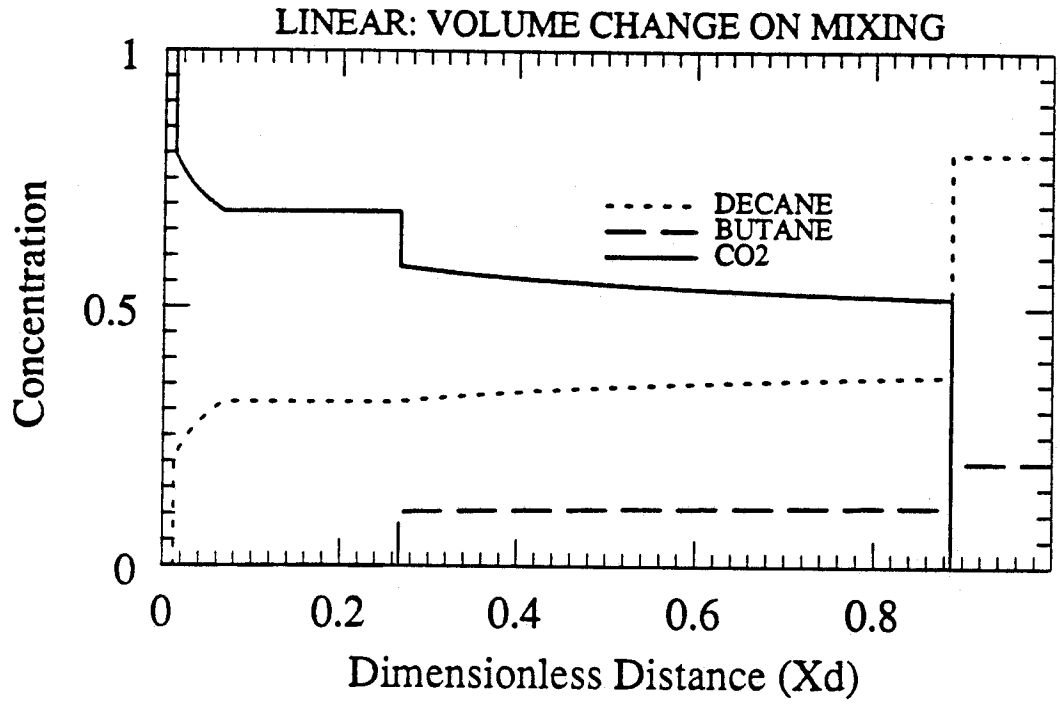

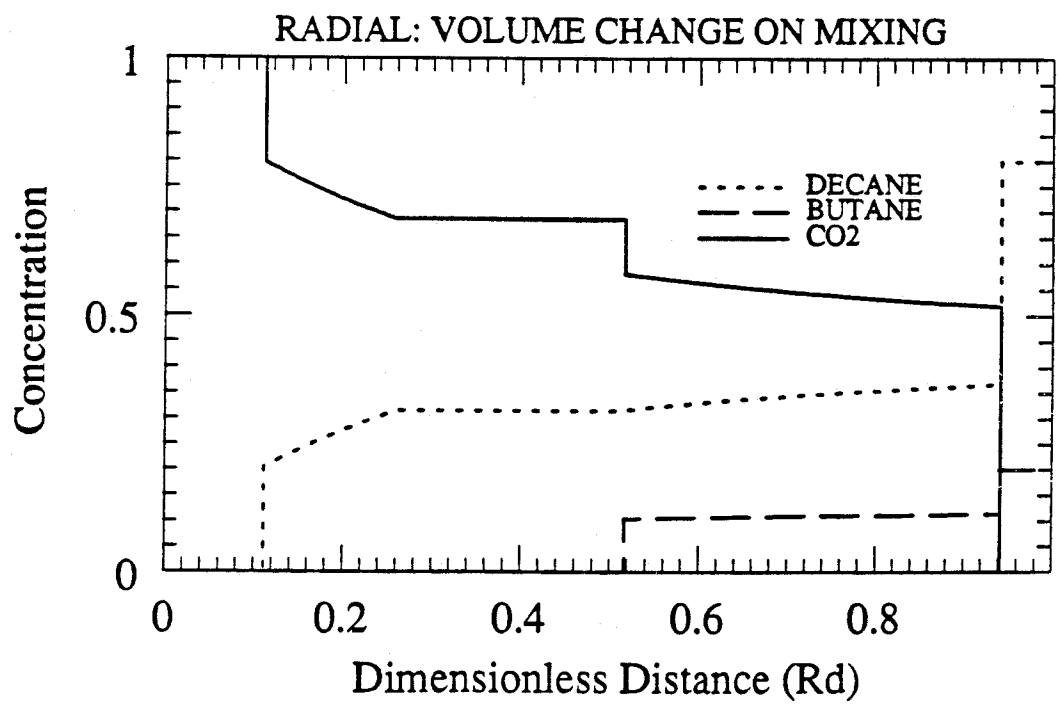

Figure 3.2-2. CO_2-C_4-C_{10} system, linear vs. radial solution at 1.0 pore volumes injected, concentration profile.

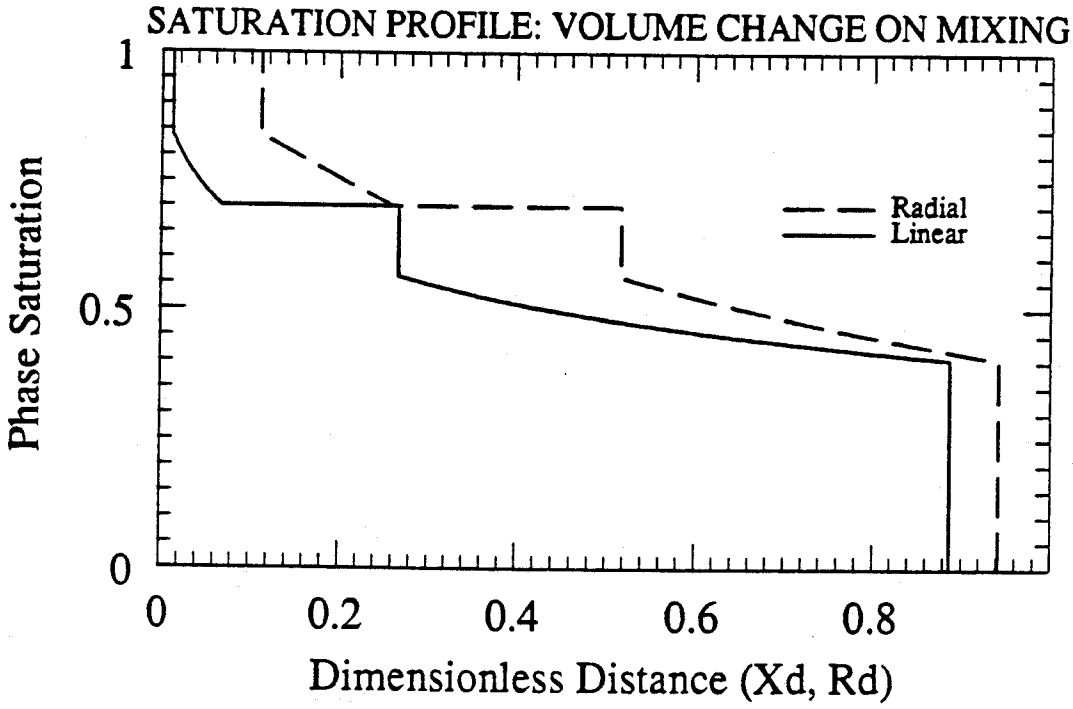

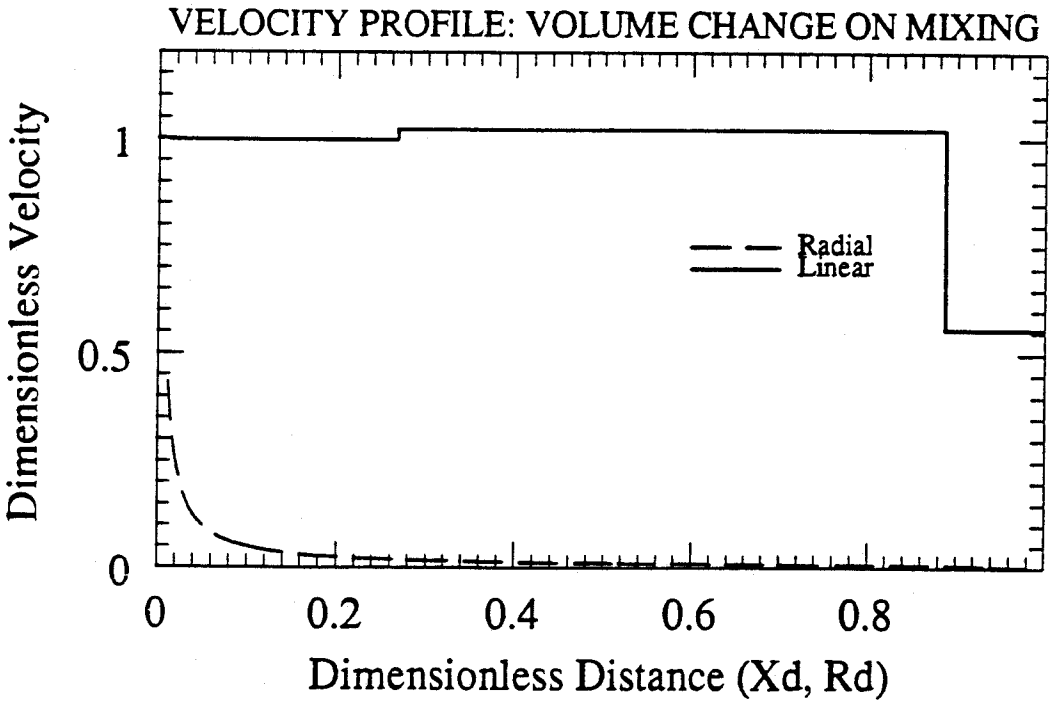

Figure 3.2-3. Comparison of linear and radial flow velocities at 1.0 PV injected.

interference between the primary and secondary injection periods and the implications of the results to oil field slug injection processes.

There is very little previous work on interfering shocks and waves for multiphase systems. Hewett and Behrens (1989) presented a solution for injection of a solvent slug and showed that variations in slug size can be scaled to collapse to one curve. Surfactant flooding was solved analytically by Hirasaki (1981) for a three component system of oil, water, and surfactant. The interference problem was solved for a surfactant slug followed by a water drive. The tertiary system was simplified somewhat by assuming that all tie lines originate from a single point in hodograph space (i.e., ternary phase diagram). Gorell (1989) showed a technique to determine the WAG ratio for tertiary miscible displacements for more realistic phase diagrams. His work, however, assumed that WAG can be treated as if solvent and water were injected simultaneously. Dria (1988) explored the interference of waves for a one-phase system of reactive fluids flowing through a permeable media. Her work did not extend to two-phase flow and only considered interference of waves separated by constant composition states. Pope et al. (1978) considered interaction of chemical waves for two immiscible phases. Rhee et al. (1986) used Riemann invariants to solve one-phase chromatography problems.

The first section discusses the mathematical model and solution techniques (MOC). The general model as well as the water-alcohol system are presented. The idea of a Riemann equivalent is detailed in the next section. It is shown that the complete solution to an interference problem can be obtained by solving a series of unique Riemann problems. Subsequent sections present a procedure for obtaining the analytical solution for the water-alcohol system. Solutions are given for two slug injection sizes using composition profiles and time-distance diagrams. All slug-size solutions are then shown to collapse to one solution on a time-distance diagram. Numerical simulation results are presented along with the analytical solutions. The last section presents the conclusions and important ideas that will be used to solve more complicated three component problems.

3.3.1 Mathematical Model

The appropriate material balance equation is Eq. (3.2-10) derived in section 3.2 with the assumption that volume is conserved.

$$\frac{\partial C_i}{\partial t_d} + \frac{\partial F_i}{\partial x_d} = 0, \quad i=1, \cdots, n_c. \tag{3.3-1}$$

Because $F_i = F_i(C_i)$, the second term may be rewritten as,

$$\frac{\partial F_i}{\partial x_d} = \sum_{k=1}^{n_c-1} \frac{\partial F_i}{\partial C_k} \frac{\partial C_k}{\partial x_d}. \tag{3.3-2}$$

One of the component equations can be removed, because the sums of the overall volume fractions and fractional flows are equal to one $\left[\sum_{i=1}^{n_c} C_i = 1, \sum_{i=1}^{n_c} F_i = 1\right]$. Eq. (3.3-1) can then be written in matrix form as,

$$C_{t_d} + A(C)\, C_{x_d} = 0, \tag{3.3-3}$$

where C is the vector $\left[C_1, C_2, \ldots, C_{n_{c-1}}\right]^T$ and A(C) is the matrix,

$$\begin{bmatrix} \frac{\partial F_1}{\partial C_1} & \frac{\partial F_1}{\partial C_2} & \cdots & \frac{\partial F_1}{\partial C_{n_c-1}} \\ \frac{\partial F_2}{\partial C_1} & \frac{\partial F_2}{\partial C_2} & \cdots & \frac{\partial F_2}{\partial C_{n_c-1}} \\ \vdots & \vdots & \ddots & \vdots \\ \frac{\partial F_{n_{c-1}}}{\partial C_1} & \frac{\partial F_{n_{c-1}}}{\partial C_2} & \cdots & \frac{\partial F_{n_{c-1}}}{\partial C_{n_c-1}} \end{bmatrix} \tag{3.3-4}$$

These first-order partial differential equations are hyperbolic and quasilinear. If the initial and injection conditions are constant, Eq. (3.3-3) is known as a Riemann problem. The solution to Riemann problems may consist of regions of constant state, rarefaction waves, and shocks. For one-dimensional Riemann problems, the solution has been shown to be only a function of the ratio of the independent variables (x/t) (Lax 1957). The eigenvalues of the matrix A(C) describe the characteristic velocities of the solution while the eigenvectors give the characteristic directions. Physically, the solution to Riemann problems must follow the velocity rule that faster compositions are downstream of slower compositions. In essence, the solution must be monotonic in wave velocity.

The velocity rule, however, cannot always be satisfied by continuous solutions. Discontinuous solutions or shocks, therefore, are used to satisfy the velocity rule and Eq. 3.3-3. Shocks are weak solutions that must satisfy the appropriate entropy conditions and Rankine-Hugoniot jump conditions (Courant and Hilbert 1962; Lax 1957). The jump conditions,

$$\Lambda_i = \frac{F_i^u - F_i^d}{C_i^u - C_i^d} \tag{3.3-5}$$

specify the relationship between the speed of the shock and the conditions upstream and downstream for component i.

Binary Model

Consider a two-component model consisting of water (H_2O) and n-butanol (NBA). This simple analogue system was chosen so that an experimental test of the theory can be made at atmospheric pressure. Eq. 3.3-4 for this system reduces to a single equation,

$$\frac{\partial C_{H_2O}}{\partial x_d} + \frac{dF_{H_2O}}{dC_{H_2O}} \frac{\partial C_{H_2O}}{\partial t_d} = 0, \tag{3.3-6}$$

and the auxiliary equations,

$$C_{H_2O} + C_{NBA} = 1 \tag{3.3-7}$$

$$F_{H_2O} + F_{NBA} = 1. \tag{3.3-8}$$

Eq. (3.3-6) clearly shows that the characteristic velocity of the system is given by,

$$\lambda = \frac{dF_{H_2O}}{dC_{H_2O}}. \tag{3.3-9}$$

Hence, continuous solutions are given by compositions that move with a velocity of λ. Discontinuous solutions, however, move with a velocity Λ given by the jump condition,

$$\Lambda = \frac{F^u_{H_2O} - F^d_{H_2O}}{C^u_{H_2O} - C^d_{H_2O}} \tag{3.3-10}$$

where u is for upstream and d is for downstream.

Numerical Solution

A numerical solution was used to verify the analytical results. A simple explicit Euler scheme is used. Specifically, for the H_2O-NBA system. Eq. (3.3-1) can be solved using the numerical scheme,

$$C^{n+1}_{H_2O_k} = C^n_{H_2O_k} + \frac{\Delta t_d}{\Delta x_d}\left[F^n_{H_2O_{k-1}} - F^n_{H_2O_k}\right], \tag{3.3-11}$$

where Δt_d is the time step, Δx_d is the distance step, k is the grid block, and n is the time level. For most of the numerical results presented in this work, 1000 grid blocks were used. To maintain stability and accuracy of the solution, a time step one-tenth of the grid block size was used.

Flow Properties of H_2O-NBA System

In a binary system, the phase behavior at constant temperature and pressure is governed by only one equilibrium tie line. The H_2O-NBA system is partially miscible at atmospheric temperature (25°C) and pressure (14.7 psia) where the tie line is given by,

$$c_{H_2O,1} = 0.9127 \quad c_{NBA,1} = 0.0873, \tag{3.3-12}$$

for phase 1, and,

$$c_{H_2O,2} = 0.1751 \quad c_{NBA,2} = 0.8249, \tag{3.3-13}$$

for phase 2. The densities and viscosities for this tie line are given in Table 3.3-1. Assuming no capillary dispersion, the fractional flow of phase 1 is,

$$f_1 = \frac{k_{r1}/\mu_1}{k_{r1}/\mu_1 + k_{r2}/\mu_2}, \tag{3.3-14}$$

and, hence, for phase 2,

$$f_2 = 1 - f_1, \tag{3.3-15}$$

where μ is the viscosity and k_r is the relative permeability of a given phase. Relative permeability data as a function of the wetting phase saturation (phase 2) were taken from Naar et al. (1962) for flow through unconsolidated glass spheres. Specifically, the data from the drainage gas-oil curves were selected and fitted (Fig. 3.3-1) to a model of the form $k_{rj} = a(s_j - s_{jc})^b$ where a and b are best fit values. It is assumed through out the next sections that the drainage curve is accurate for imbibition as well (i.e., there is no hysteresis).

Table 3.3-1. Densities and Viscosities of H_2O-NBA System.

Volume Fraction		Density (g/cm^3)	Viscosity (cp)
H_2O	NBA		
1.000	0.0000	0.9971	0.8937
0.9127	0.0873	0.9864	1.1800
0.1751	0.8249	0.8440	2.8500
0.0000	1.0000	0.8061	2.5600

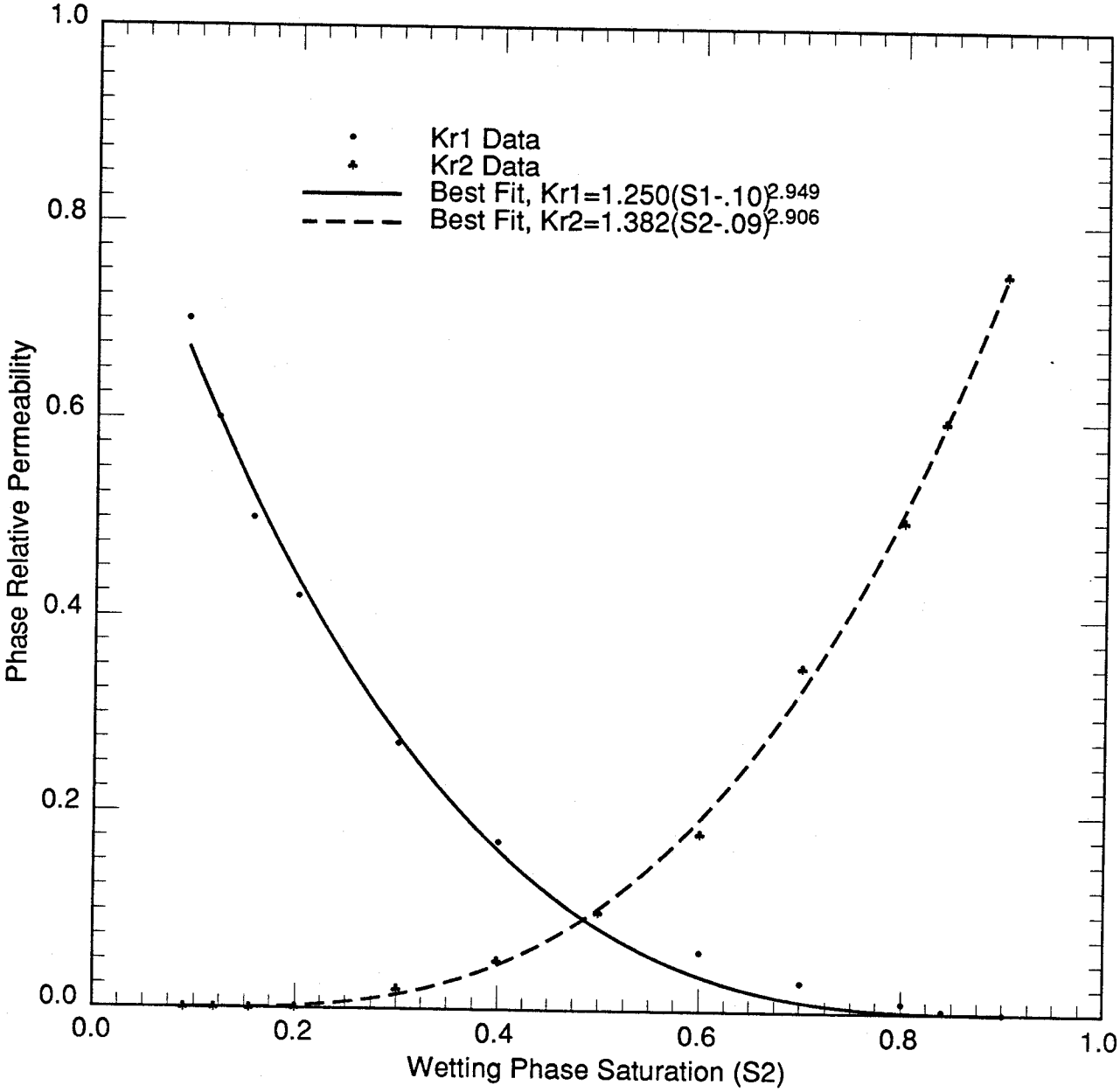

Figure 3.3-1. Measured relative permeabilities for H_2O-NBA system and best fits to data.

The wetting-phase saturation is determined from the tie line by,

$$S_2 = \frac{C_{NBA} - C_{NBA,1}}{C_{NBA,2} - C_{NBA,1}}. \tag{3.3-16}$$

The overall fractional flow can be determined from the expressions given above and Eq. (3.2-11). Fig. 3.3-2 shows the overall fractional flow as a function of overall water composition (solid line) for the H_2O-NBA system. The one-phase region has a slope of unity on the plot, while the two-phase region has a 'S' shape. The dashed lines in Fig. 3.3-2 give the shocks or discontinuities that occur in the analytical solution. The shock solutions will be discussed in detail below.

3.3.2 Riemann Equivalent

If both initial and boundary conditions are constant, the problem represented by Eq. (3.3-6) is called a Riemann problem. In slug injection processes, however, the boundary conditions change. Hence, slug injection solutions are not given by Riemann problems. Nevertheless, for binary systems, the solution to slug injection problems can be found by separating the problem into a series of distinct Riemann problems. Each separate Riemann problem is known as a Riemann equivalent (Dria 1988).

Riemann equivalents can be mapped most easily on time-distance diagrams. Time-distance diagrams display the characteristics of the solution. Characteristics describe the position and time at which a composition is propagated. For the problems of Eq. (3.3-6), the characteristics will be lines on the time-distance plot and will carry a constant value of composition. A shock, for example, is represented by a line on the time-distance diagram where the slope is equal to the inverse velocity of the shock. Therefore, if we know the velocity of a shock and the time and distance in which it originated, we can draw a line that gives its position with time and distance. Composition profiles and histories can then be easily obtained from a time-distance diagram.

Consider the hypothetical time-distance diagram of Fig. 3.3-3 in which there are three shocks separated by three constant states (regions 1, 2 and 3). Suppose a fluid of composition R2 is injected at time zero into a core saturated with a fluid of composition R3. As long as the injection and initial conditions remain constant, this is a Riemann problem. The solution to this Riemann problem is shown to be a shock moving at unit velocity separated by constant states of composition R2 and R3. The shock is represented on the time-distance diagram by a line originating at the origin with a slope of unity. At a later time, however, a second injection period (slug) of composition R1 begins. The overall solution can no longer be represented by a Riemann problem, but must now be composed of distinct Riemann problems or Riemann equivalents. The second injection period is treated as if the core is completely saturated with composition R2. Thus, the solution is given by another Riemann problem with initial composition R2 and injection composition R1. The solution to this Riemann problem is a new shock separated by constant states of composition R1 and R2. Due to the jump conditions, however, this new shock travels at a faster velocity and, if not already produced at the outlet of the core, will ultimately interfere (at t_c and x_c) with the first shock of unit velocity. At interference, the region given by composition R2 no longer exists, and the solution becomes that of a Riemann problem with initial conditions of composition R3 and injection composition R1. A third shock results which has an intermediate velocity given by the jump conditions. Because no more slugs are injected, this shock will continue on indefinitely and is the long-term solution to this hypothetical slug injection problem.

The complete solution, then, is composed of three shocks and three constant states. Three Riemann problems were solved to determine the complete solution. Each of these three

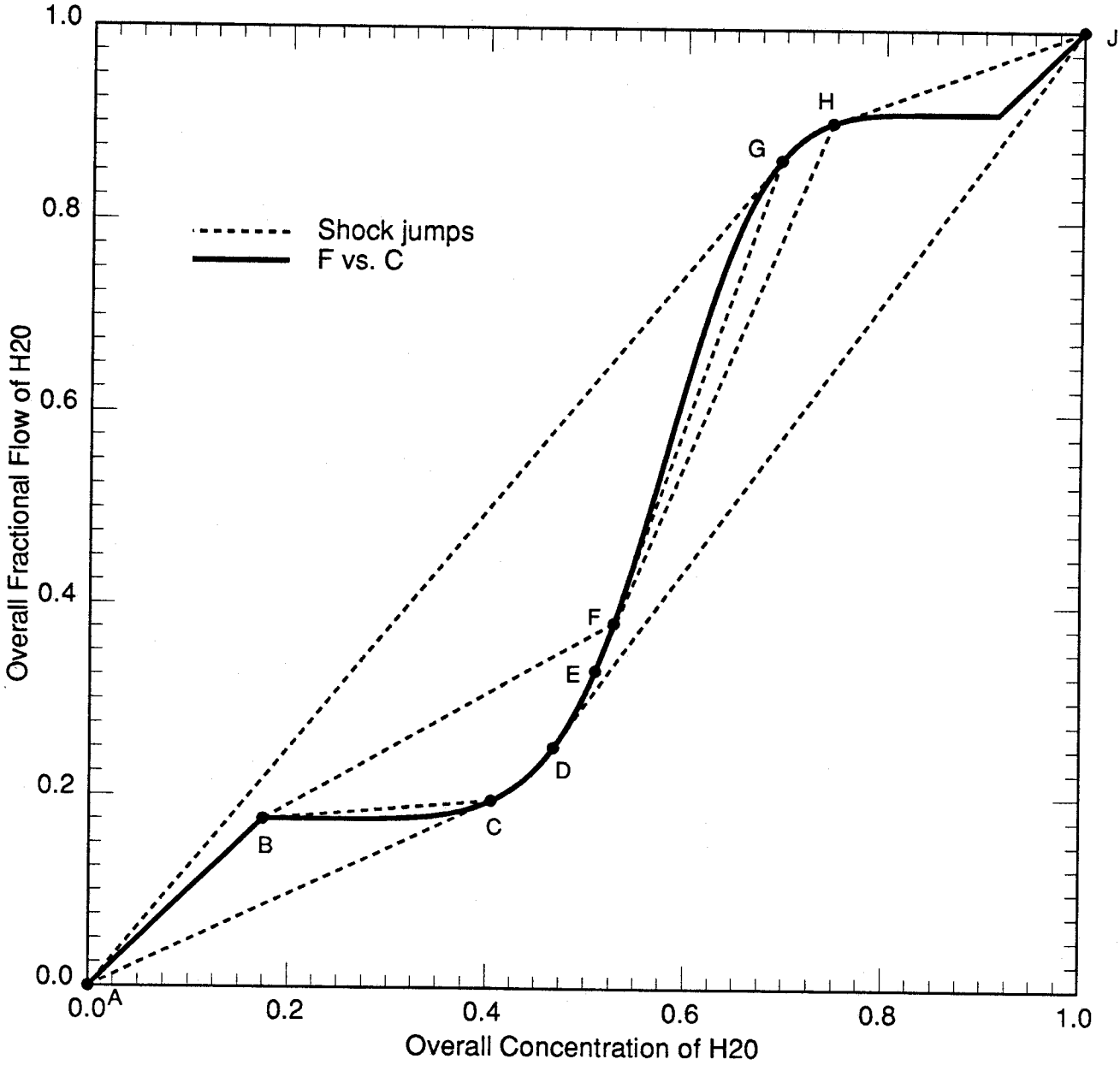

Figure 3.3-2. Overall fractional flow function and shock trajectories.

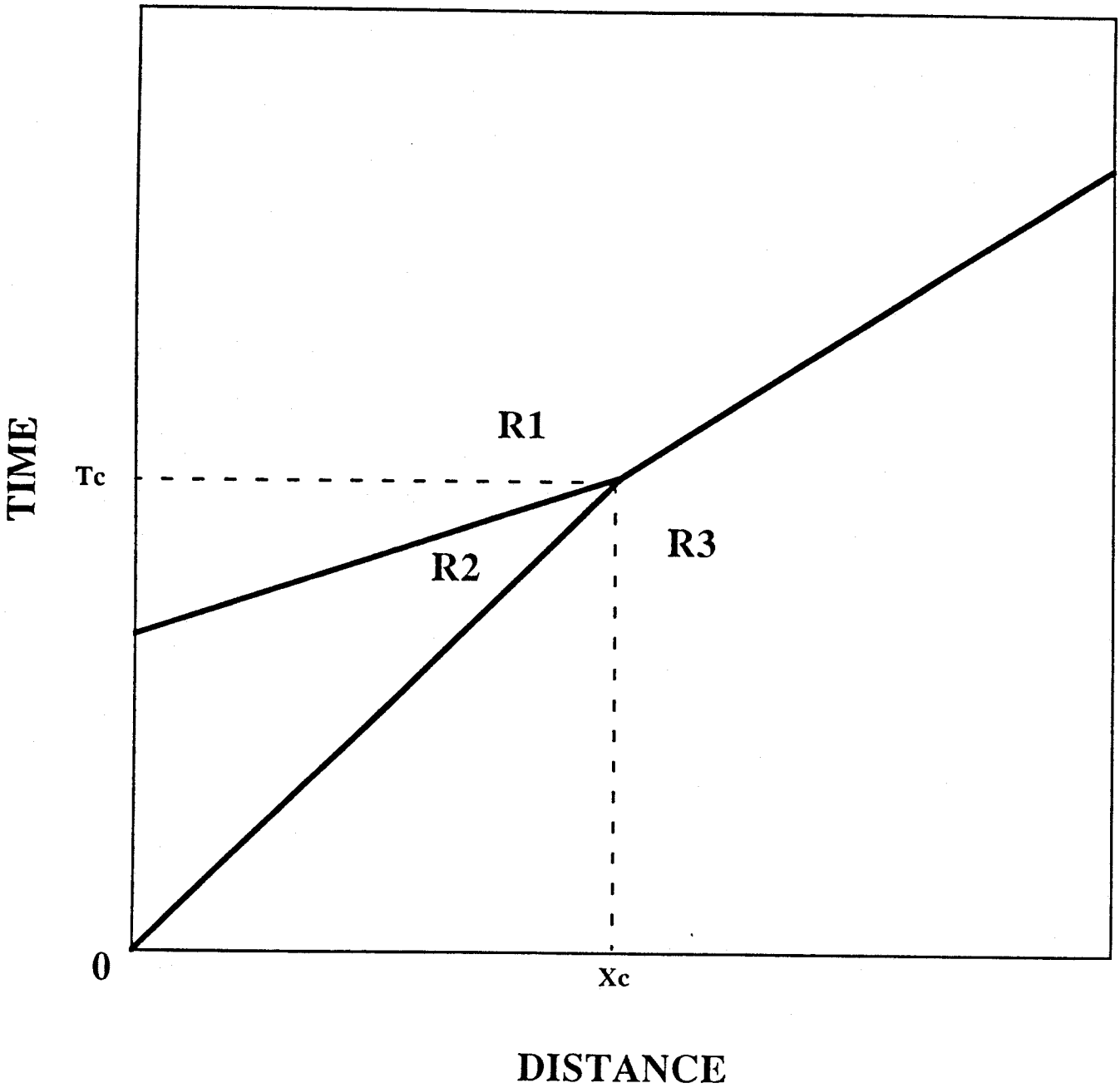

Figure 3.3-3. Hypothetical time-distance diagram showing the idea of a Reimann equivalent.

distinct Riemann problems is known as a Riemann equivalent, because the injection and initial conditions of the overall problem are not constant.

Fig. 3.3-4 demonstrates the same idea, but for a more complex situation in which the Riemann solution consists of multiple shocks separated by constant states. For this more complex case, multiple intersections occur that create many Riemann equivalents. Ultimately, the characteristics may sort themselves out resulting in a late time solution, as Fig. 3.3-5 illustrates.

3.3.3 Analytical Solutions for H_2O-NBA Slug Injection

Consider the Riemann problem for injection of water (H_2O) into a core initially saturated with n-butanol (NBA). The solution is obtained from the F vs. C plot of Fig. 3.3-2. If the velocity rule and conditions are be satisfied, a trailing shock (denoted $\overline{JH}$) must occur from the injection condition (J) to the tangent composition (H), and a leading shock, $\overline{GA}$, from the tangent composition (G) to initial condition (A). These tangent shocks (shown by dotted lines in Fig. 3.3-2) connect the one-phase and two-phase regions. The jump conditions (Eq. 3.3-10) give the velocities of the shocks. The velocities are the slopes of the dotted lines in Fig. 3.3-2. The leading shock ($\overline{GA}$), therefore, has a faster velocity than the trailing shock ($\overline{JH}$). Between compositions G and H, the solution is continuous, and the compositions move at a velocity given by Eq. (3.3-9). These velocities vary continuously from the trailing shock velocity to the leading shock velocity to form a rarefaction (or spreading) wave, $\widetilde{HG}$. The wave is also a centered wave (Fig. 3.3-6), because it emanates from a central point (the origin) and spreads from the leading shock to the trailing shock.

Fig. 3.3-6 shows the solution to the Riemann problem for continuous water injection. Shocks are given by heavier solid lines while characteristics of the rarefaction wave are given by lighter solid lines. The characteristics are plotted such that the distance between them is proportional to the composition they carry. A composition and saturation profile (dashed line in Fig. 3.3-6 is shown in Fig. 3.3-7 at a dimensionless time of 0.5 pore volumes injected (PVI). The numerical solution is also presented and shows excellent agreement with the analytical solution.

Injection of a 0.5 Pore Volume Slug

Next, we consider injection of NBA into the core after injection of a slug of 0.5 pore volumes of water. The solution is given by a Riemann equivalent with initial composition J and injection composition A. This is the reverse of the previous water injection case, and, thus, two tangent shocks and a centered rarefaction wave ($\overline{DJ}$, $\overline{AC}$, and $\widetilde{CD}$ as shown in Fig. 3.3-2) are created. The rarefaction wave originates from the point at $t_d = 0.5$ and $x_d = 0.0$ on the time-distance diagram of Fig. 3.3-8. Eventually, however, interference will occur because the velocities of these new shocks and waves are greater than those of the initial shocks and waves. The leading shock $\overline{DJ}$ is the first to overtake the trailing shocks $\overline{JH}$ at $t_d = 0.688$ and $x_d = 0.265$. At $t_d = 0.6$ PVI, for example, the leading shock is about to overtake the trailing shock (Fig. 3.3-9).

When the shock $\overline{DJ}$ overtakes the shock $\overline{JH}$, the region of constant state J no longer exists. The upstream composition, therefore, is composition D, while the downstream is composition H. The result is a Riemann equivalent with injection composition D and initial composition H (Fig. 3.3-2) given by a centered rarefaction wave $\widetilde{DE}$ and a tangent shock $\overline{EFGH}$. The centered wave originates at the point of intersection and spreads from composition E to composition D. The characteristics of the centered rarefaction wave $\widetilde{DE}$ move more slowly than the new shock, and, hence, will not overtake any more waves. The new shock ($\overline{EFGH}$), however, has a large velocity and will continue downstream overtaking the rarefaction wave, $\widetilde{HG}$. Fig. 3.3-10 shows an enlargement of the shock interaction area.

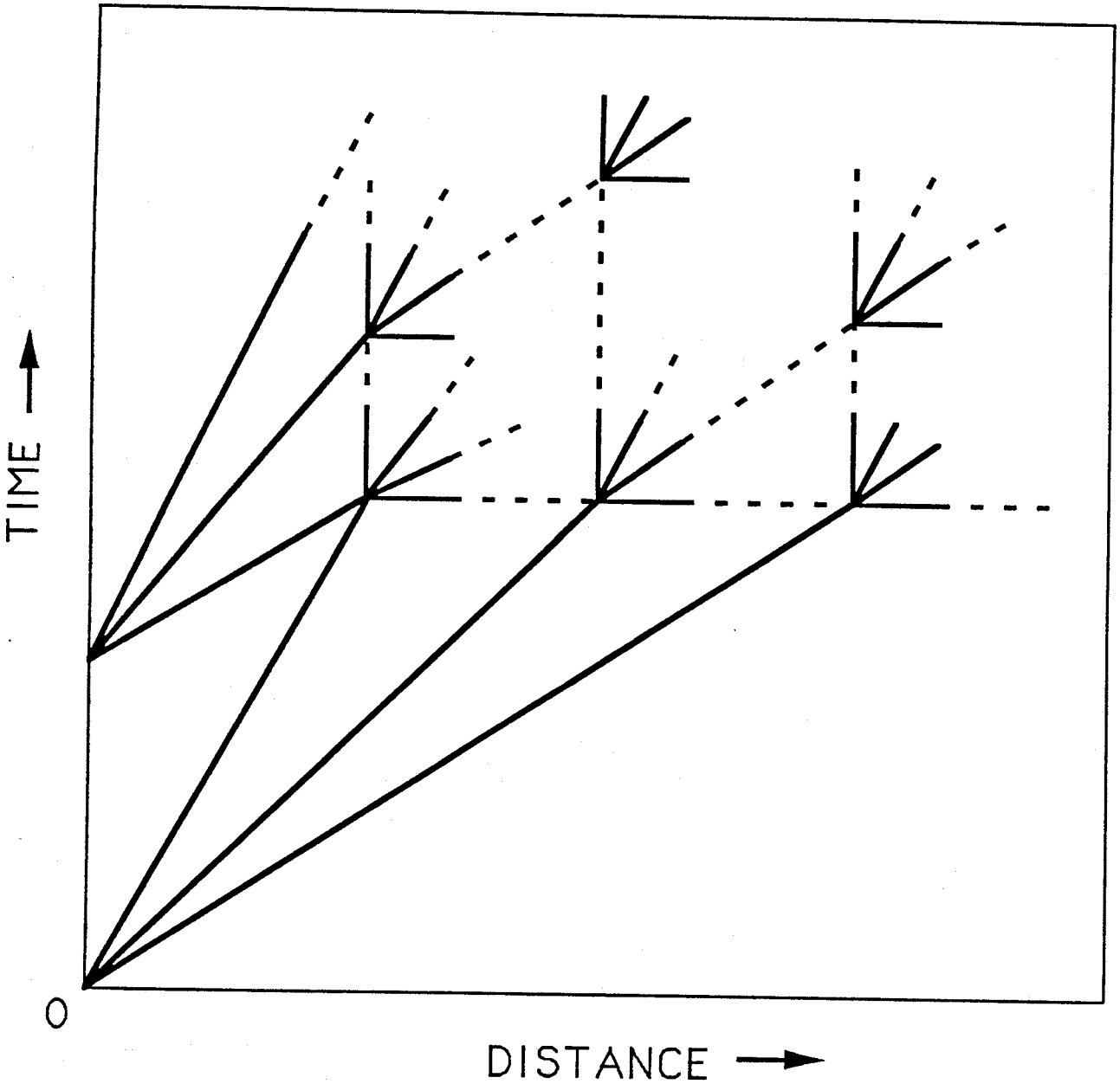

Figure 3.3-4. Complex time-distance diagram with multiple Reimann equivalents.

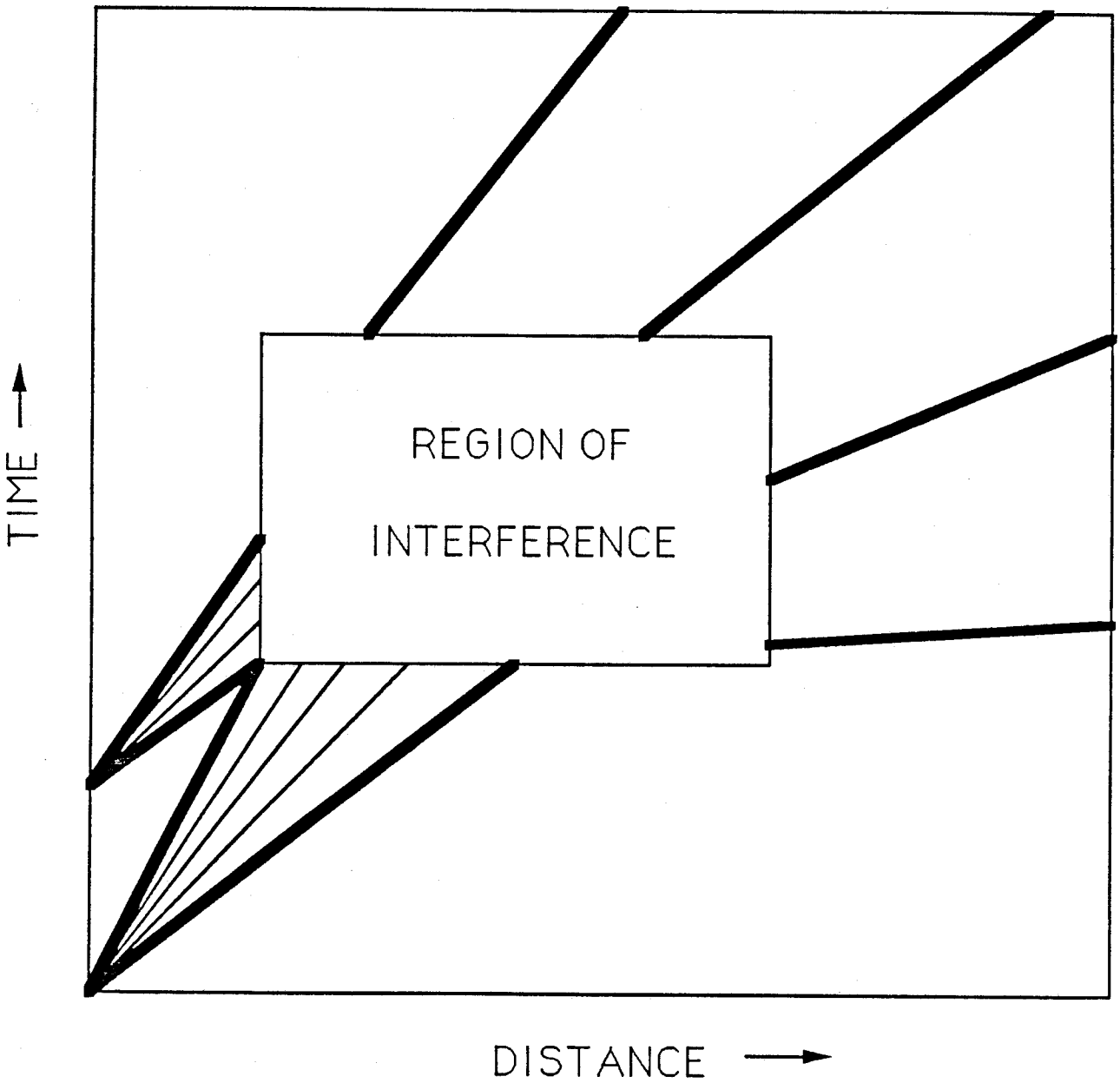

Figure 3.3-5. Time-distance diagram showing the long term solution and the resolution of the interference region.

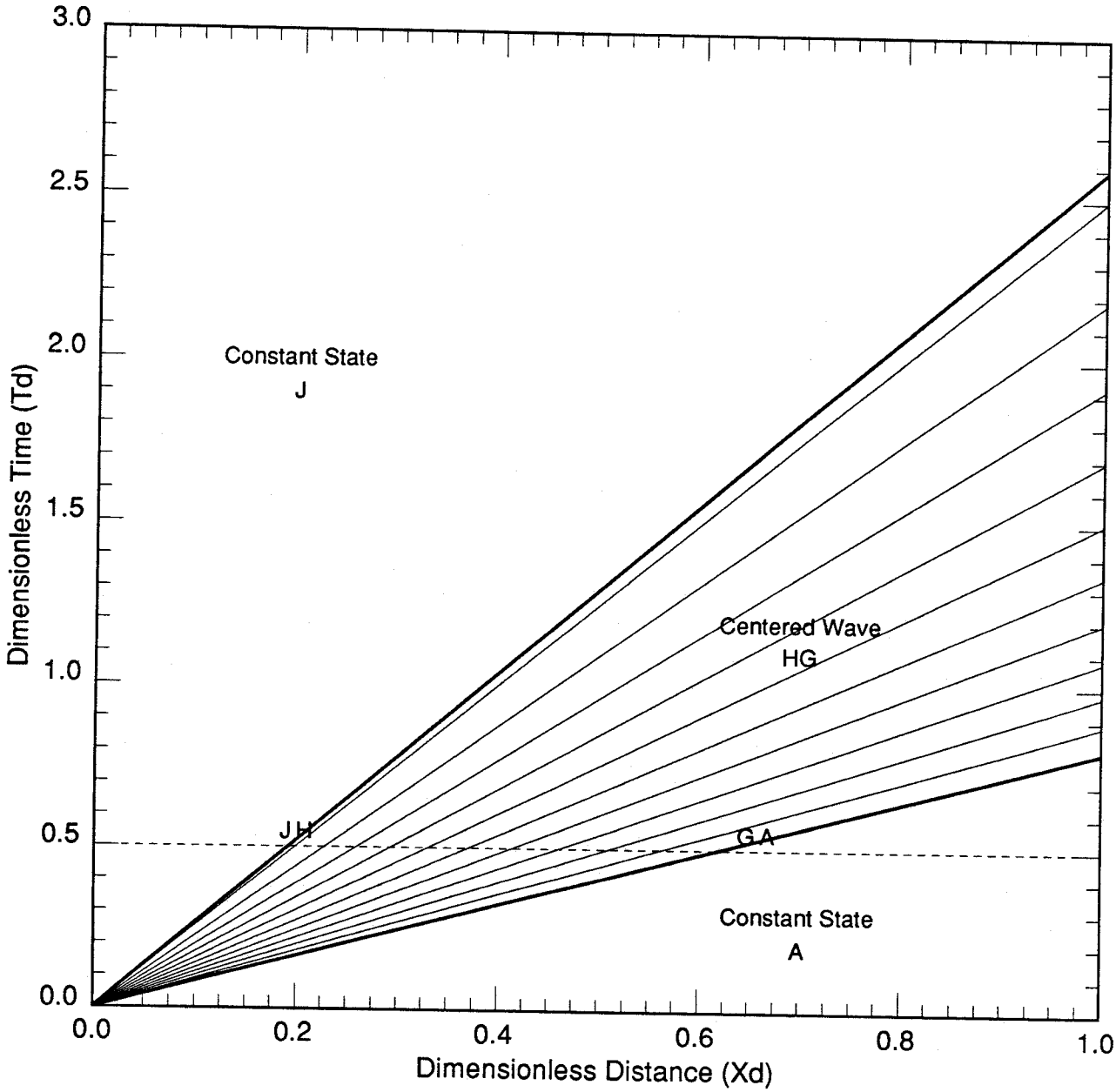

Figure 3.3-6. Analytical solution for constant injection of water.

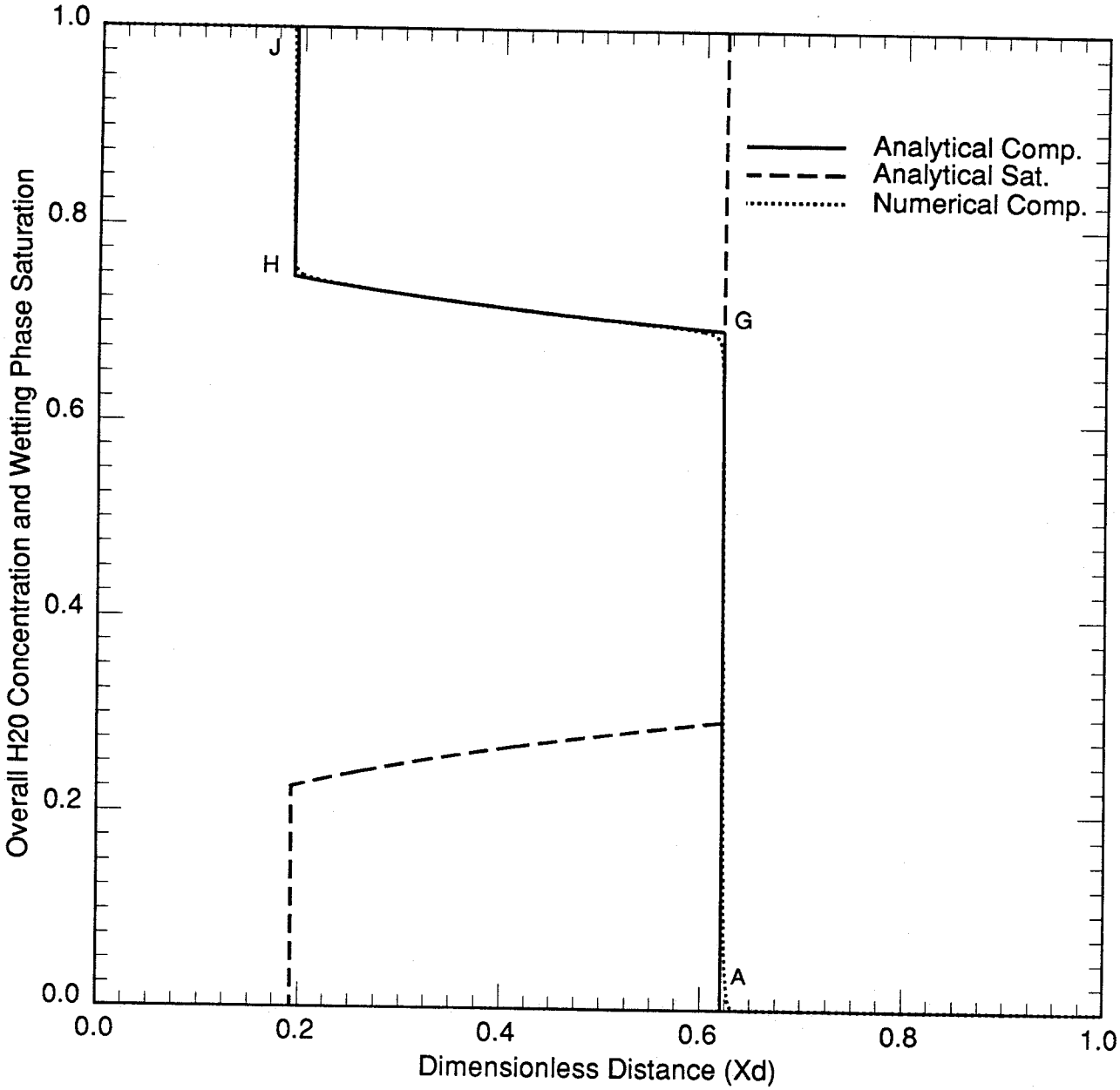

Figure 3.3-7. Analytical and numerical composition and saturation profiles at 0.5 PVI for continuous H_2O injection into pure NBA.

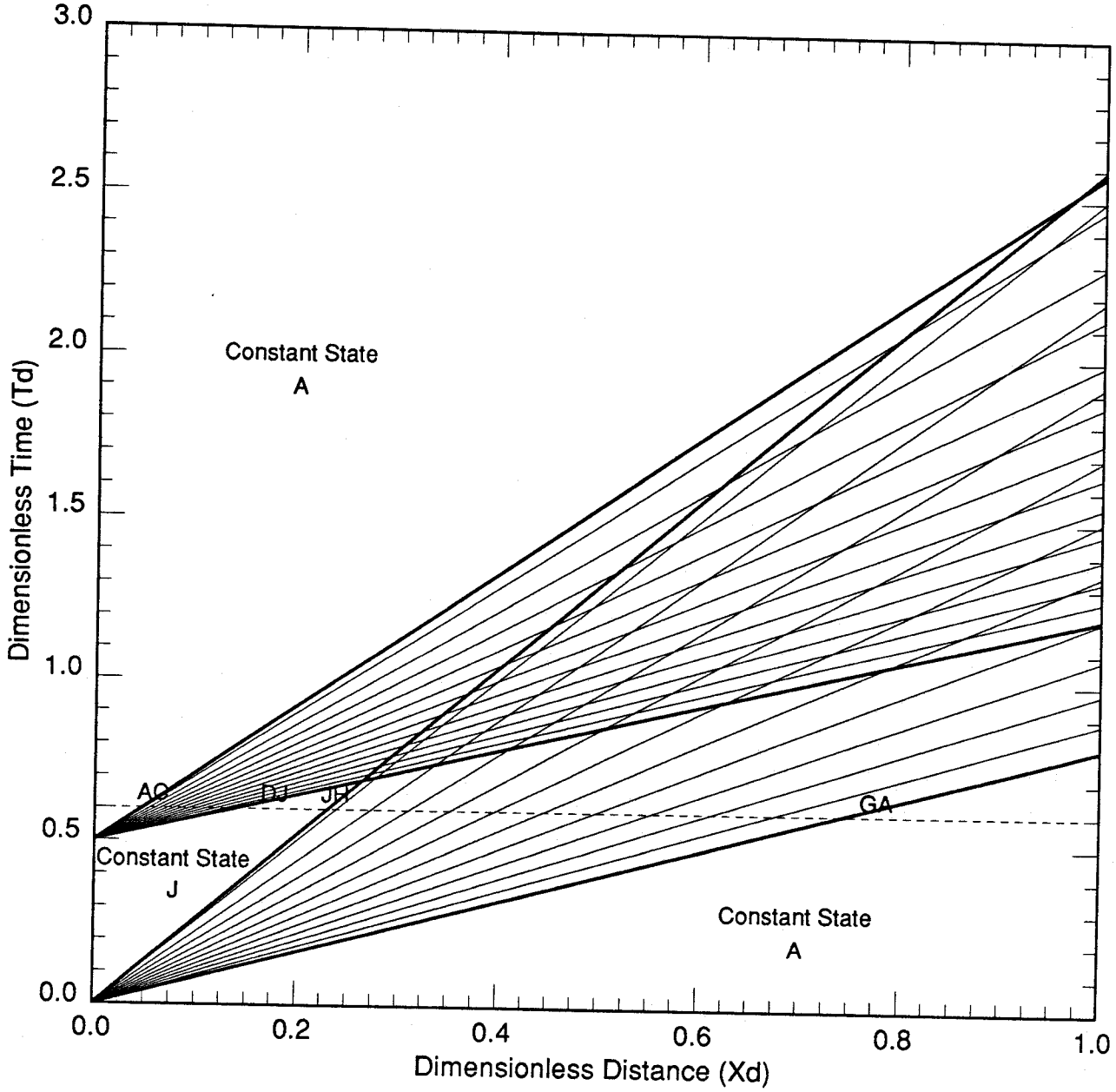

Figure 3.3-8. Interference of shocks and waves for 0.5 PV water slug injection, accurate solution up to first intersection point.

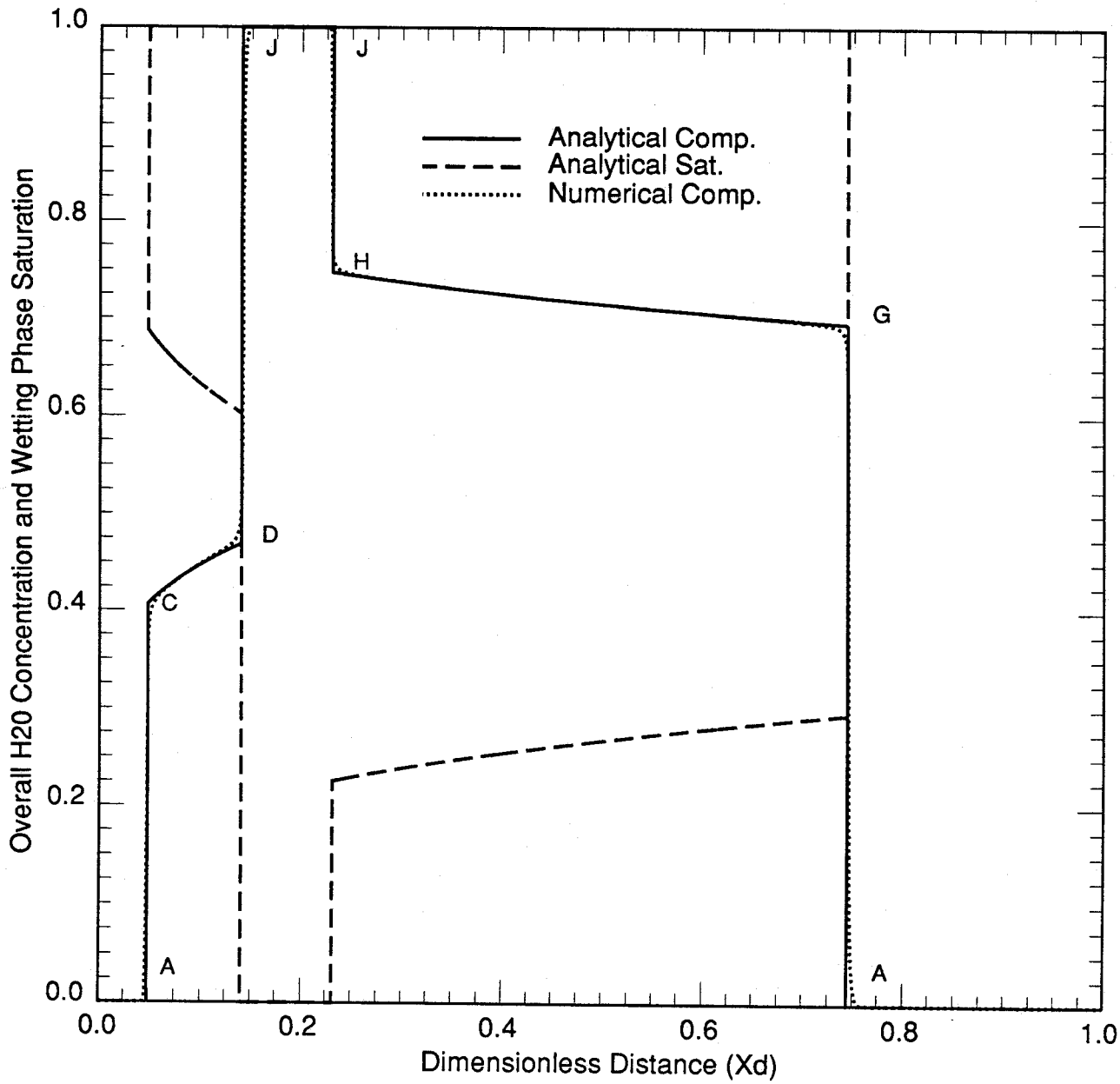

Figure 3.3-9. Analytical and numerical composition and saturation profiles at 0.6 PVI for injection of a 0.5 PV H_2O slug into pure NBA.

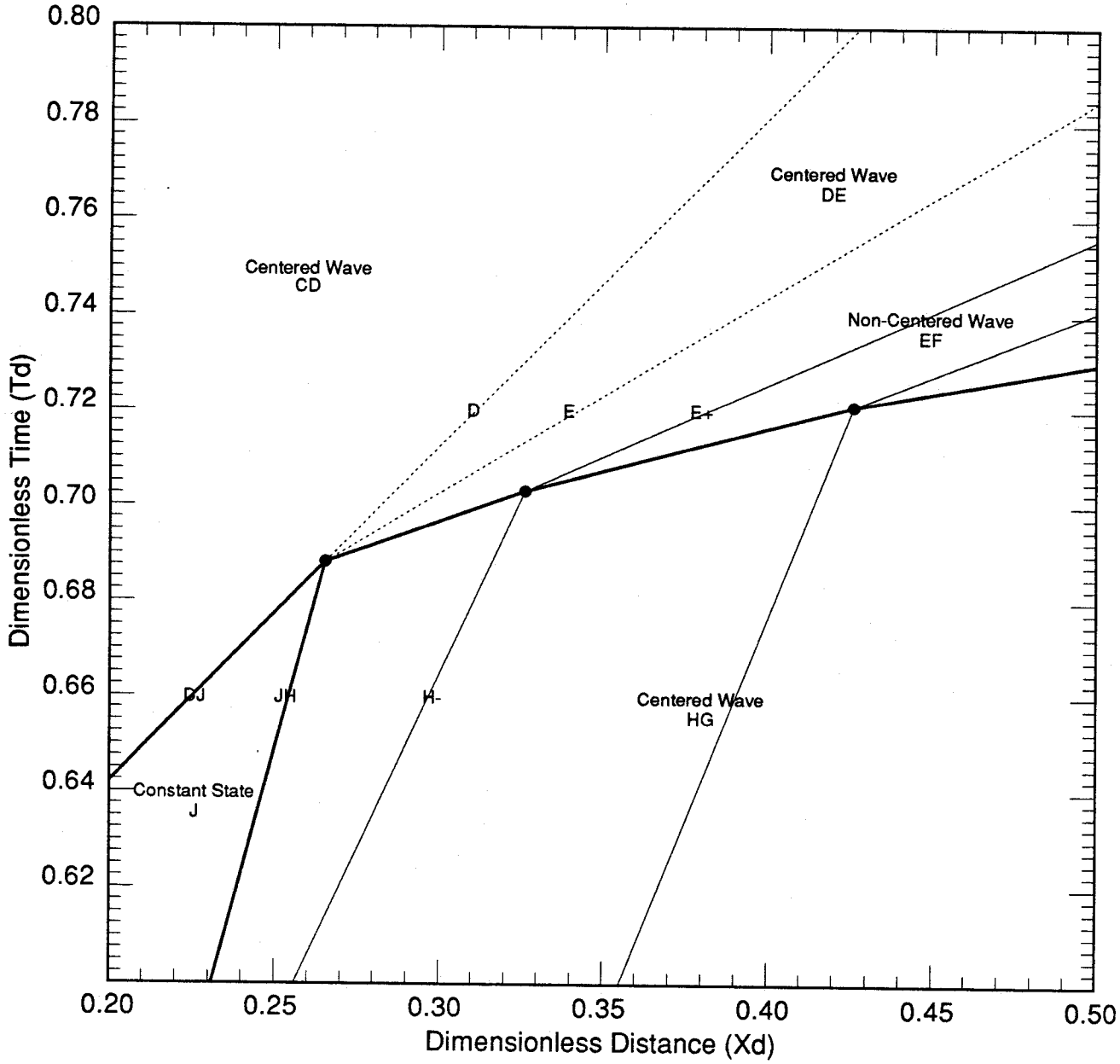

Figure 3.3-10. Enlargement of the interference region on the time-distance diagram.

As the shock overtakes the rarefaction wave, the downstream composition will change. For example, in Fig. 3.3-10, the shock $\overline{EFGH}$ will first overtake the characteristic carrying a composition slightly smaller than H (denoted H–). Hence, a new Riemann equivalent is created instantaneously in time with initial composition H– and injection composition E (Fig. 3.3-2). The result is a tangent shock to composition E+. Hence, a new composition E+ is created which is the injection composition for the next Riemann equivalent. This process of successive Riemann equivalents is repeated until a noncentered rarefaction wave is created. The noncentered rarefaction wave has characteristics that emanate from the upstream side of the shock. Ultimately, the last Riemann equivalent will give a tangent shock with upstream composition F and downstream composition G.

As the shock $\overline{EFGH}$ moves downstream, the shock velocity increases slightly due to the changing downstream condition. As a result, the shock will curve slightly in the time-distance diagram. To determine the shock path, a second-order Runga-Kutta scheme was used. For example, at the first intersection, the jump condition gives the velocity of the shock for upstream composition E and downstream composition H. The slope of the shock in the time-distance diagram is then known, and an equation for the shock line can be determined (Fig. 3.3-10). The shock line is then extended up to the next downstream characteristic H-. Because the Riemann equivalent gives the upstream condition (E+), a new velocity at that location can be determined from the jump conditions. To give a second-order estimate, the shock velocity from the first intersection and the next intersection are averaged to give a corrected velocity. This corrected velocity is then used to determine the slope of the shock line from the first intersection. The shock path is constructed numerically by repeating this process.

Thus, the upstream composition is determined by tangent shocks to the overall fractional flow curve, which are solutions to successive Riemann equivalents. The noncentered wave is created because new upstream compositions arise as the shock progress downstream. Characteristics from the noncentered wave originate on the upstream side of the shock. In terms of Helfferich's coherence theory, the noncentered wave region is the only region that is not coherent (Helfferich 1981).

Fig. 3.3-11 shows the complete solution to a water slug injection of 0.5 PV. The lightly dashed lines on the time-distance diagram separate various rarefaction waves. As is seen, the leading shock $\overline{GA}$ reaches the core outlet at a time of approximately 0.8 PVI. Hence, the leading shock is not overtaken by the quickly approaching upstream shock $\overline{EFGH}$.

Composition and saturation profiles are shown in Figs. 3.3-12 and 3.3-13 for dimensionless times of 0.7 and 0.9 PVI. The agreement between the numerical solution and the analytical solution is excellent. In order to verify the accuracy of the shock locations, ten thousand grid blocks were used to compute the solution shown in Fig. 3.3-13.

Injection of a 0.1 Pore Volume Slug

Now consider the same H_2O-NBA system, but with a slug size of only 0.1 pore volumes. The solution of the problem is similar to the previous case and can be determined by the same methods (Fig. 3.3-14). Now, however, there will be three shock-shock intersections. The result of the first intersection is exactly the same as the previous solution, but occurs earlier at $t_d = 0.138$ and $x_d = 0.053$. Unlike the previous case, however, the resulting shock $\overline{EFGH}$ has more time to move downstream, and, thus, it will overtake the leading shock $\overline{GA}$. The leading shock has not exited the core because the slug size is substantially smaller. Intersection of these two shocks occurs at $t_d = 0.217$ and $x_d = 0.270$. Fig. 3.3-15 shows the composition and saturation profile at $t_d = 0.2$ PVI which is just prior to the second intersection.

When the resulting shock overtakes the leading shock $\overline{GA}$, the centered rarefaction wave $\widetilde{HG}$ no longer exists. The Riemann equivalent, therefore, becomes the solution with initial composition A and injection composition F. The result is an indifferent shock $\overline{BA}$, a genuine

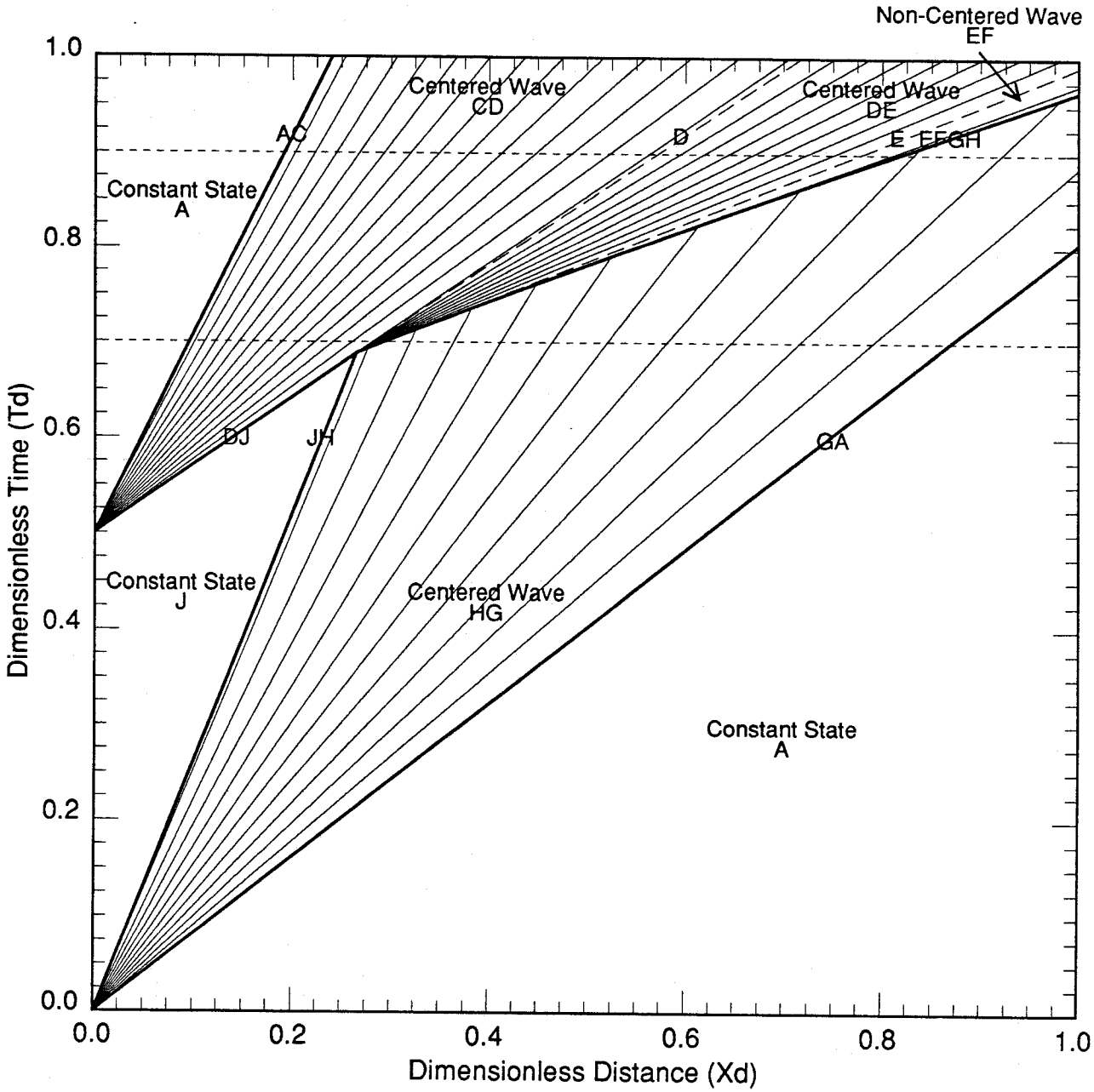

Figure 3.3-11. Complete analytical solution for injection of a 0.5 PV water slug.

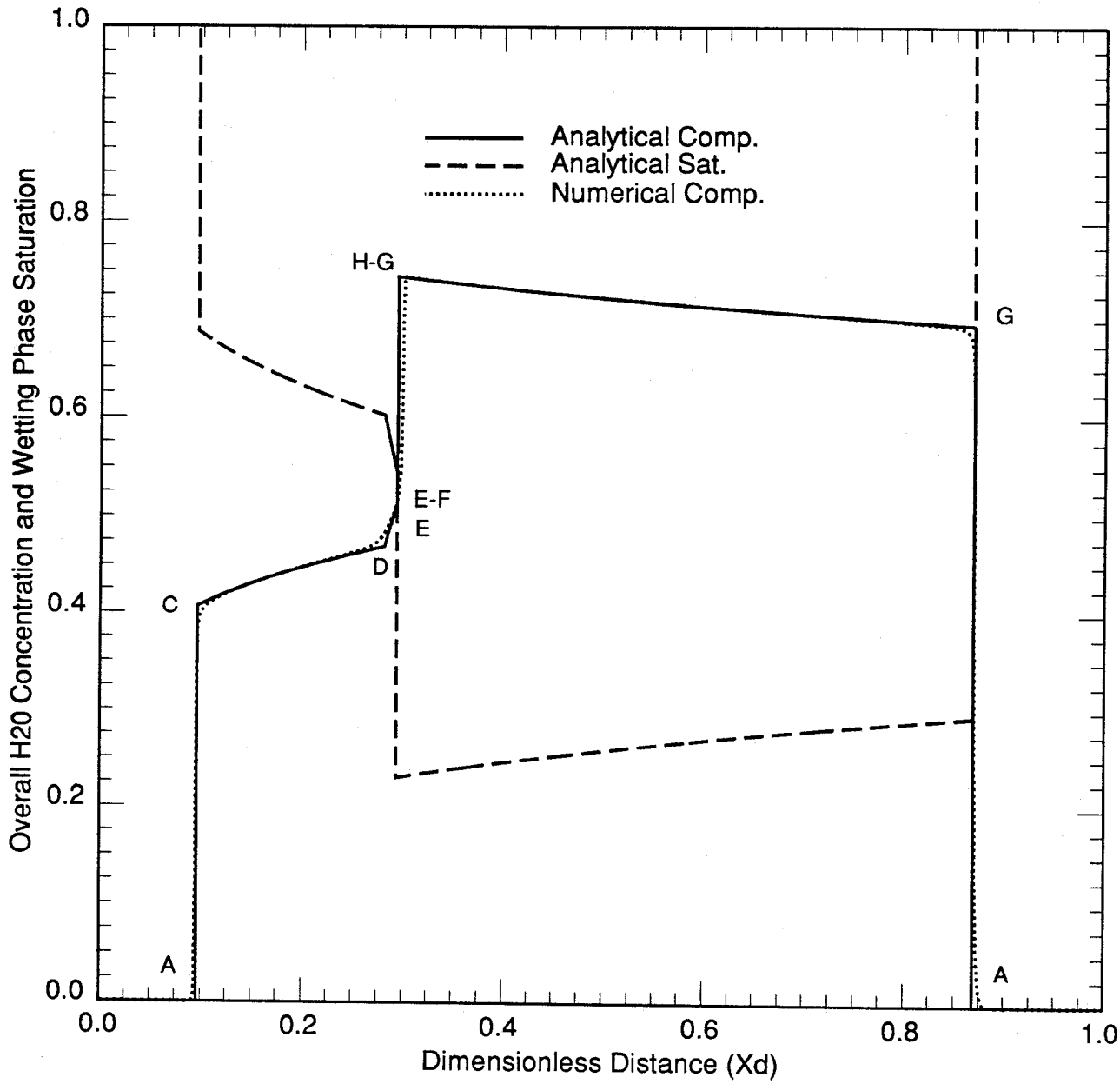

Figure 3.3-12. Analytical and numerical composition and saturation profiles at 0.7 PVI for injection at a 0.5 PV H_2O slug into pure NBA.

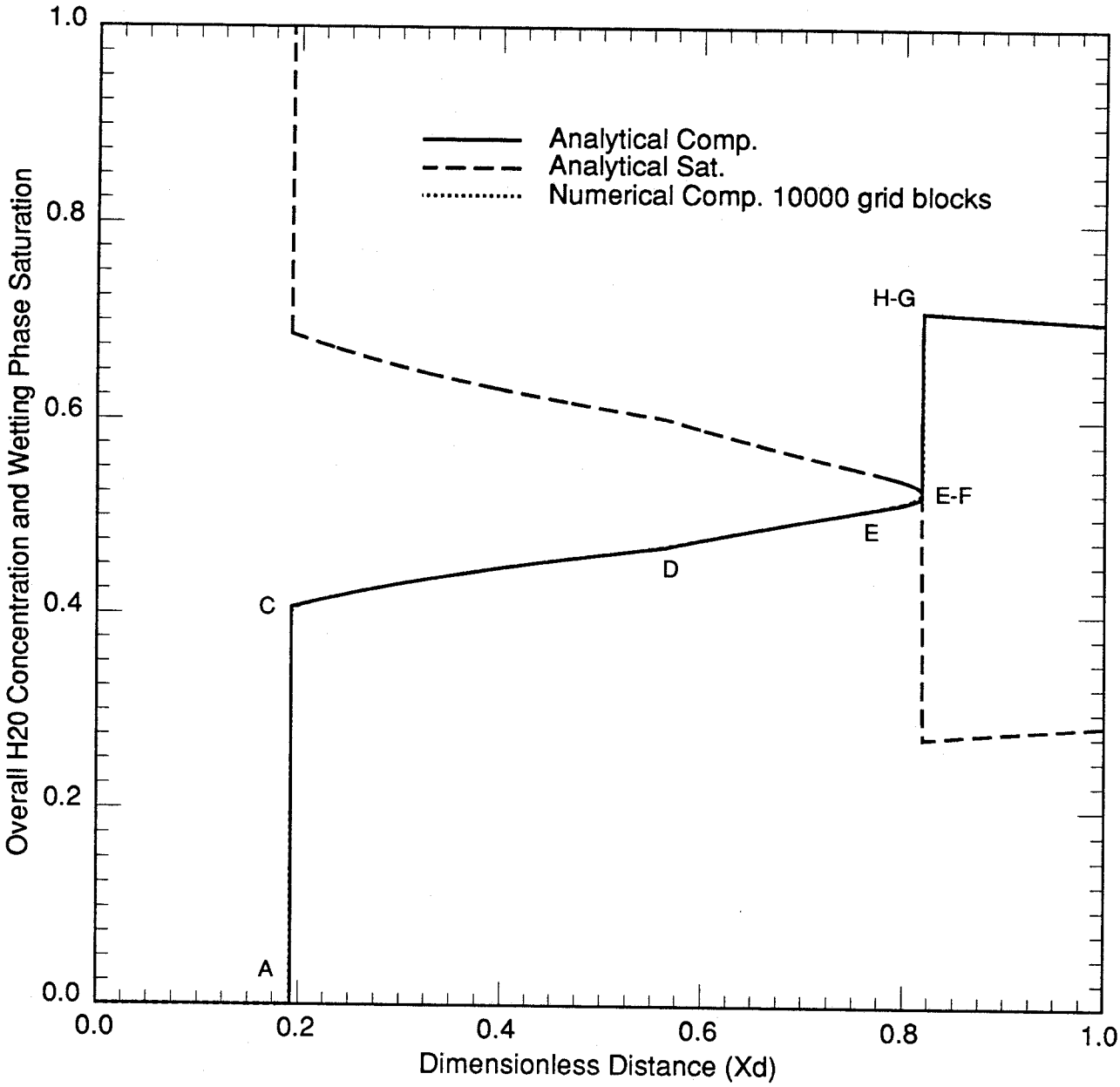

Figure 3.3-13. Analytical and numerical composition and saturation profiles at 0.9 PVI for injection of a 0.5 PV H_2O slug into pure NBA.

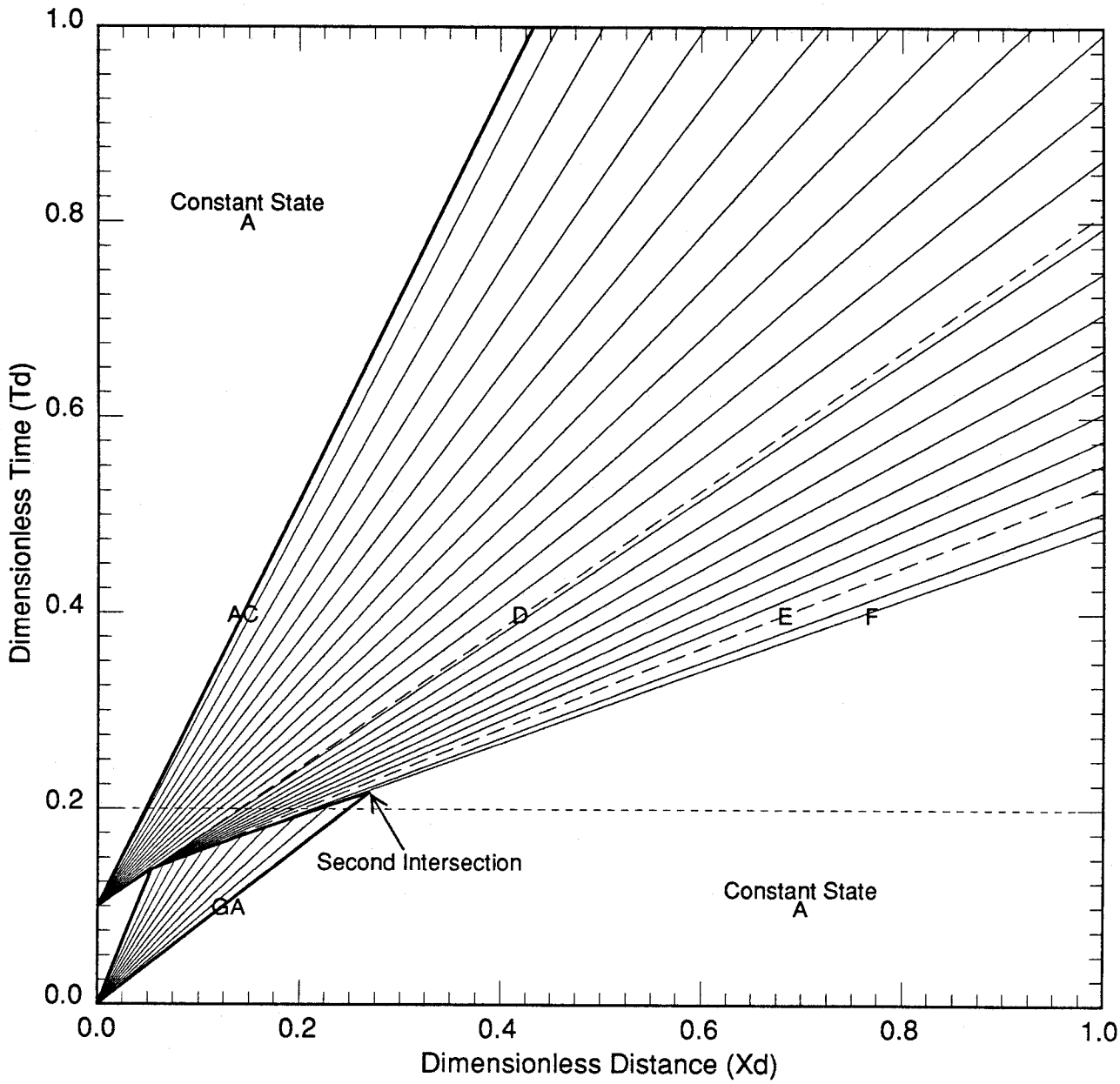

Figure 3.3-14. Interference of shocks at a second intersection point for injection of a 0.1 PV water slug. The solution shown applies only up to the time of the second intersection.

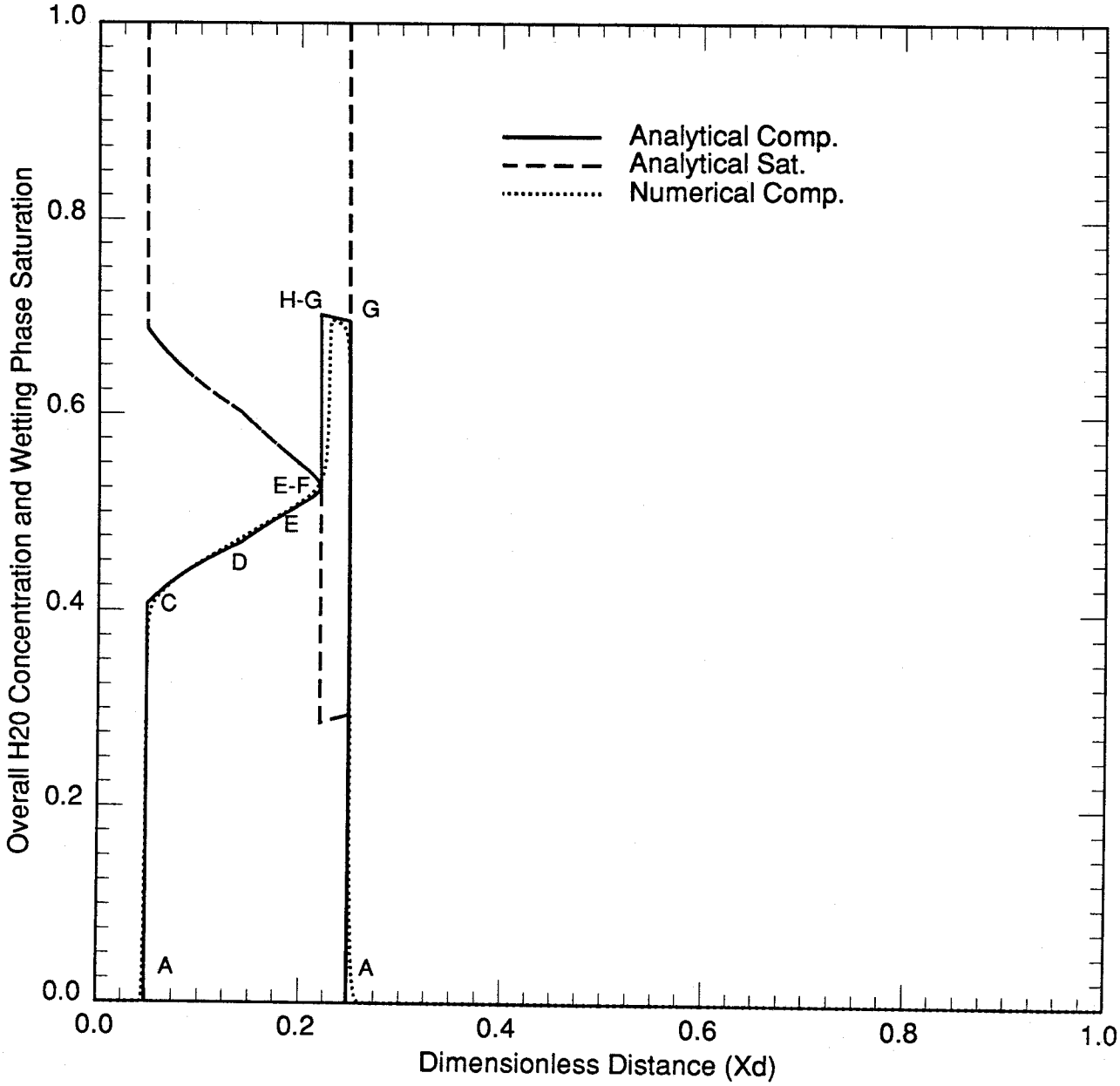

Figure 3.3-15. Analytical and numerical composition and saturation profiles at 0.2 PVI for injection of a 0.1 PV H_2O slug into pure NBA.

shock $\overline{CDEF}$, and a constant state region B (Figs. 3.3-2 and 3.3-16). The shock from composition F to composition B is a genuine shock because it is not tangent to the overall fractional flow curve on the upstream or downstream side. A region of constant state develops because the shock velocity is smaller than the velocity at composition B (unity in this case). The continuous variation from composition B to A is an indifferent shock (or wave) because all the compositions move with equal velocity (again, unity in this case).

Because the shock $\overline{CDEF}$ has slowed significantly (as determined from the jump conditions), the three rarefaction waves ($\widetilde{CD}$, $\widetilde{DE}$, $\widetilde{EF}$) upstream will overtake the new shock $\overline{CDEF}$. Thus, the compositions on the upstream side of the shock are given by the characteristics of these rarefaction waves. In the same manner as for the shock $\overline{EFGH}$, successive Riemann equivalents are formed with injection conditions varying from composition F- to C and initial composition B. The solutions to these Riemann equivalents are genuine shocks to composition B. Because the composition on the upstream side is changing, the velocity of the shock $\overline{CDEF}$ continues to slow down as given by the jump conditions. In fact, the last shock from composition C to B has almost zero velocity (Fig. 3.3-2). The shock path is calculated using the Runga-Kutta scheme.

Ultimately, the trailing shock, $\overline{CD}$, will also overtake the shock $\overline{CDEF}$. This will occur at a dimensionless time of $t_d = 0.907$ and $x_d = 0.388$ for a slug size of 0.1 PVI. After this time, the rarefaction waves no longer exist and a new Riemann equivalent is formed. The solution to the new Riemann equivalent is given by an initial condition of composition B and injection composition A, and, thus, is simply an indifferent shock $\overline{AB}$ traveling at unit velocity. Because there are no new rarefaction waves and both indifferent waves ($\overline{BA}$, $\overline{AB}$) travel at equal velocity, no additional interference can occur. Hence, the long-term solution is simply two indifferent waves separated by a constant state region. The composition in the constant state region is the equilibrium composition B.

The time-distance diagram of Fig. 3-3.16 shows the complete solution for the 0.1 PVI slug size. Composition and saturation profiles are shown in Figs. 3.3-17 and 3.3-18 for 0.5 and 1.0 PVI. As before, the numerical results are nearly identical to the analytical solution except for dispersive effects seen near the indifferent shocks. Indifferent shocks are not self-sharpening since all compositions move with the same velocity. As a result, numerical dispersion effects enhance the dispersion seen for the indifferent waves.

Arbitrary Slug Sizes

The analytical solutions given for the previous two slug sizes can be scaled to give the solution for an arbitrary slug size. This is true because the corresponding waves and shocks in both solutions have the same velocities, and, hence, the same slope on the time-distance diagram. Since only the point of origin has changed, we can scale the time and distance axis to the slug injection size by

$$T_{d_{1pv}} = \frac{T_d}{SS}, \tag{3.3-17}$$

and,

$$X_{d_{1pv}} = \frac{X_d}{SS}, \tag{3.3-18}$$

where, SS is the slug size. With this transformation, Figs. 3.3-11 and 3.3-16 collapse onto one diagram shown in Fig. 3.3-19. Thus, Fig. 3.3-19 is the analytical solution to any slug size injected. To obtain the time-distance diagram for a particular slug size, just multiply the actual slug size by the coordinates in Fig. 3.3-19. Table 3.3-2 gives the details of the general analytical solution.

Table 3.3-2. Detailed Analytic Solution for Arbitrary Slug Size Injection.

Comment	Composition (Vol. Fraction)		Phase 2 Saturation	Wave Velocity	Time-Distance Location	
	H20	NBA		$1/PV$	$t_{d_{1pv}}$	$x_{d_{1pv}}$
Constant State A	0.00	1.00	1.00	-	-	-
Leading Shock $\overline{GA}$	u-.695 d-0.00	u-.305 d-1.00	u-.295 d-1.00	1.24	-	-
Centered Wave $\widetilde{HG}$	G-.695	.305	.295	1.24	0.00	0.00
	H-.747	.253	.225	.386		
Trailing Shock $\overline{JH}$	u-.747 d-1.00	u-.253 d-0.00	u-.225 d-0.00	.386	-	-
Constant State J	1.00	0.00	0.00	-	-	-
Leading Shock $\overline{DJ}$	u-.469 d-1.00	u-.531 d-0.00	u-.602 d-0.00	1.41	-	-
Centered Wave $\widetilde{CD}$	D-.469	.531	.602	1.41	1.00	0.00
	C-.406	.594	.687	.481		
Trailing Shock $\overline{AC}$	u-0.00 d-.406	u-1.00 d-.594	u-1.00 d-.687	.481	-	-
Constant State A	0.00	1.00	1.00	-	-	-
First Intersection	-	-	-	-	1.38	.530
Resulting Shock $\overline{EFGH}$	u-.511 d-.747	u-.489 d-.253	u-.545 d-.225	2.42	1.38	.530
	u-.530 d-.695	u-.470 d-.305	u-.519 d-.295	2.91	2.17	2.70
Non-Centered Wave $\widetilde{EF}$	F-.530	.470	.519	2.91	2.17	2.70
	E-.511	.489	.545	2.42	1.38	.530
Centered Wave $\widetilde{DE}$	E-.511	.489	.545	2.42	1.38	.530
	D-.469	.531	.602	1.41		
Second Intersection	-	-	-	-	2.17	2.70
Indifferent Shock $\overline{BA}$	u-.175 d-0.00	u-.825 d-1.00	u-1.00 d-1.00	1.00	-	-
Constant State B	.175	.825	1.00	1.00	-	-
Resulting Shock $\overline{CDEF}$	u-.530 d-.175	u-.470 d-.825	u-.519 d-1.00	.580	2.17	2.70
	u-.406 d-.175	u-.594 d-.825	u-.687 d-1.00	.088	9.07	3.88
Third Intersection	-	-	-	-	9.07	3.88
Indifferent Shock $\overline{AB}$	u-0.00 d-.175	u-1.00 d-.825	u-1.00 d-1.00	1.00	-	-

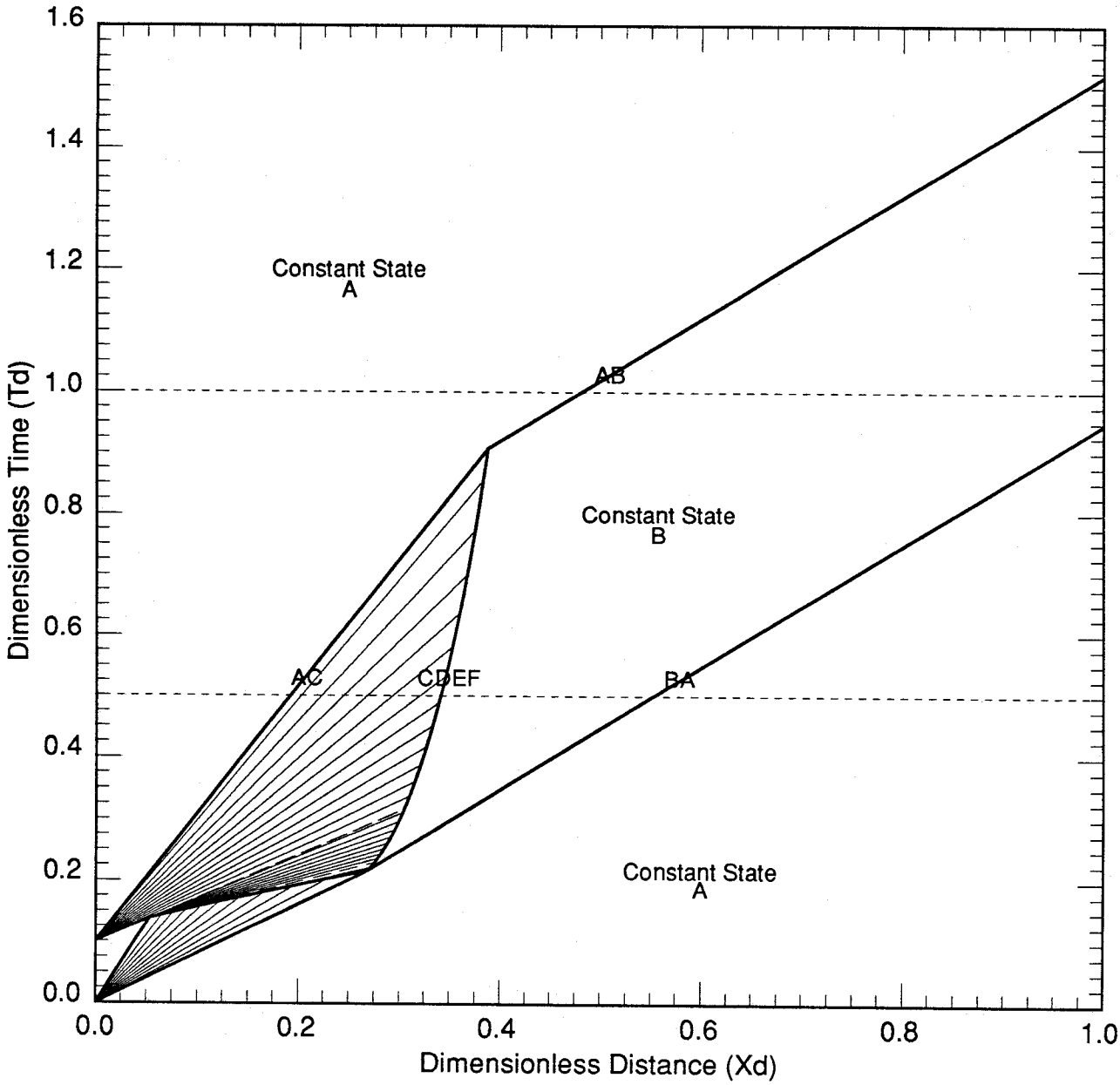

Figure 3.3-16. Complete analytical solution for injection of a 0.1 PV water slug.

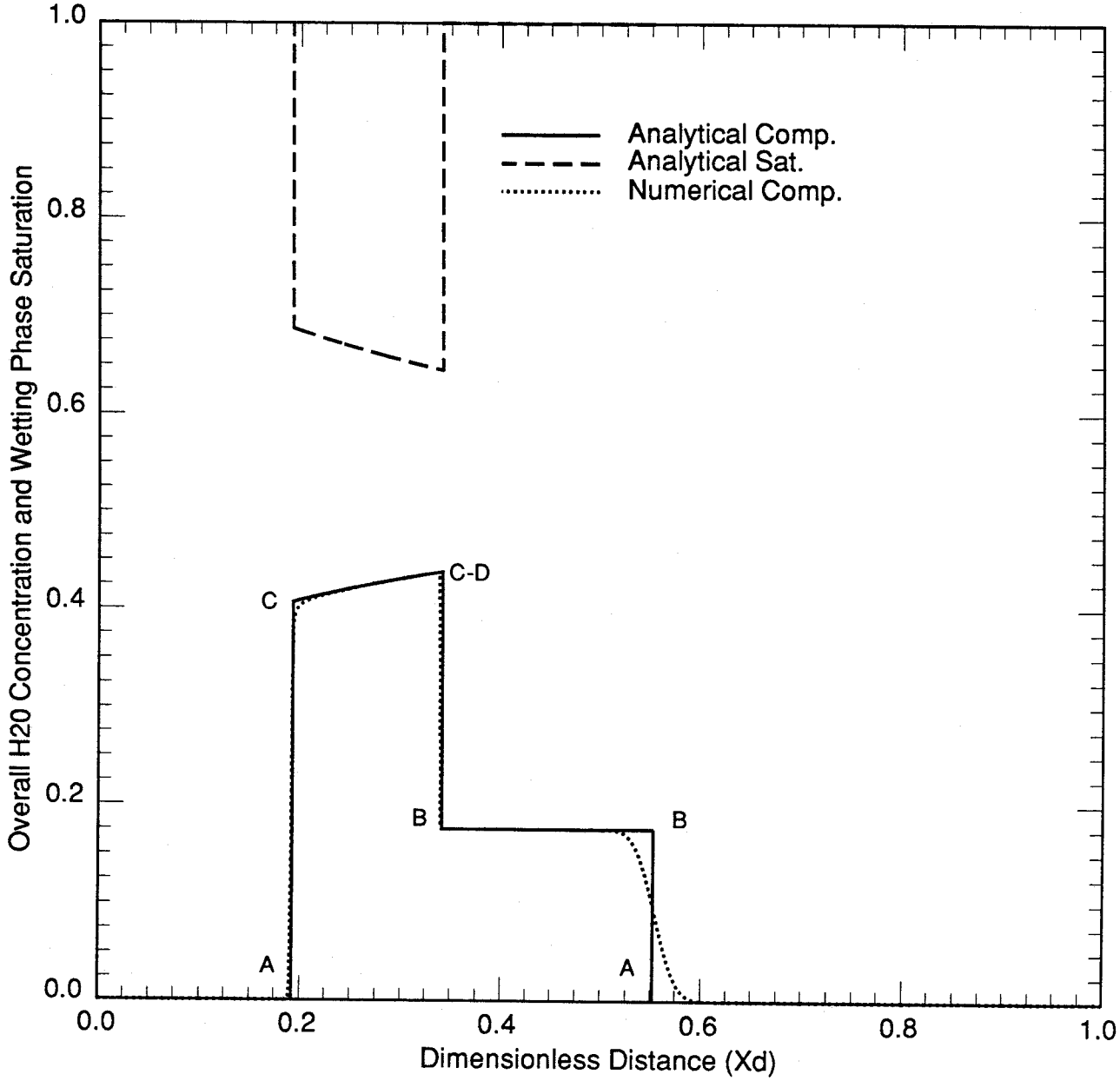

Figure 3.3-17. Analytical and numerical composition and saturation profiles at 0.5 PVI for injection of a 0.1 PV H_2O slug into pure NBA.

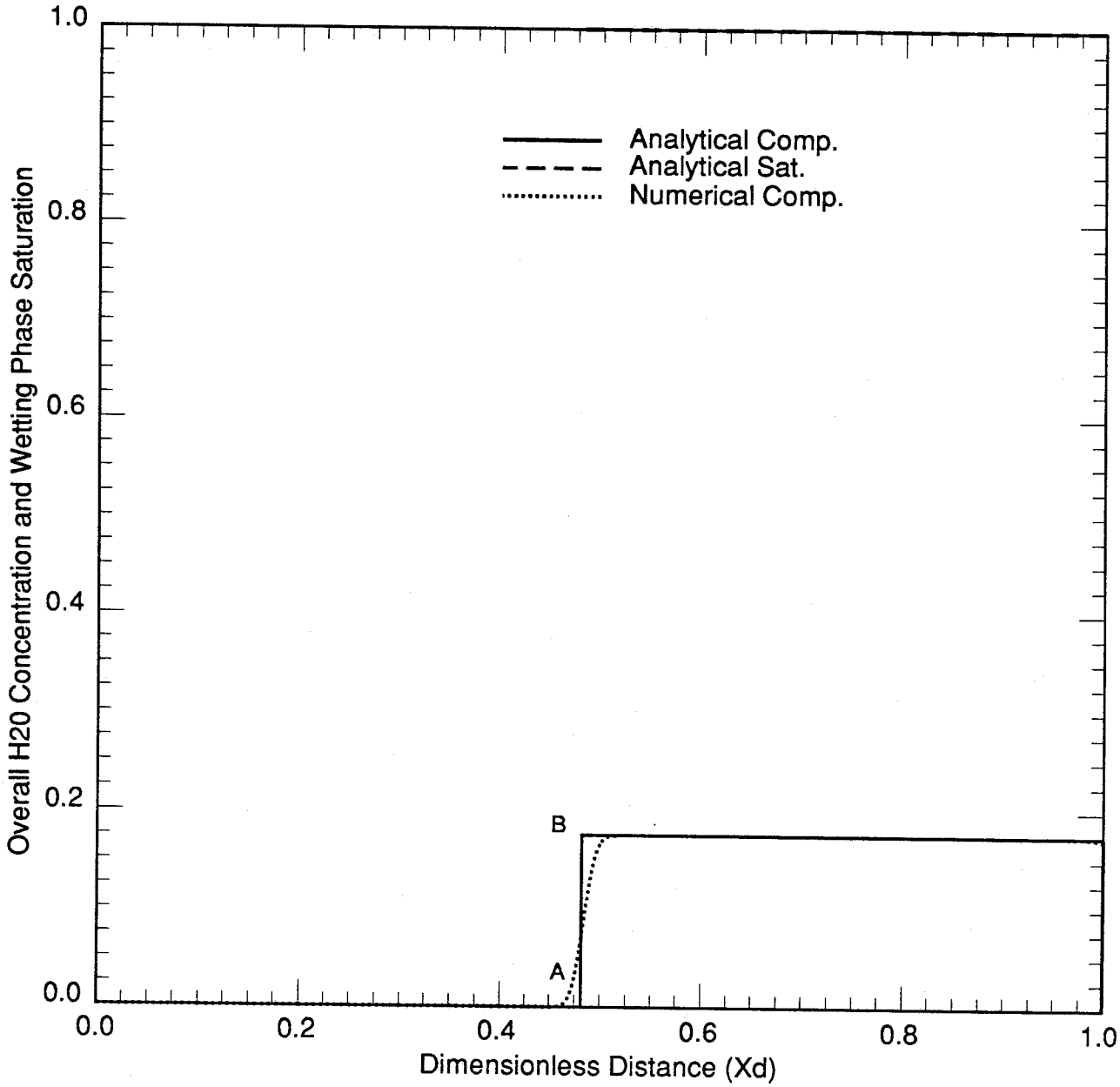

Figure 3.3-18. Analytical and numerical composition and saturation profiles at a 1.0 PVI for injection of a 0.1 PV H_2O slug into pure NBA.

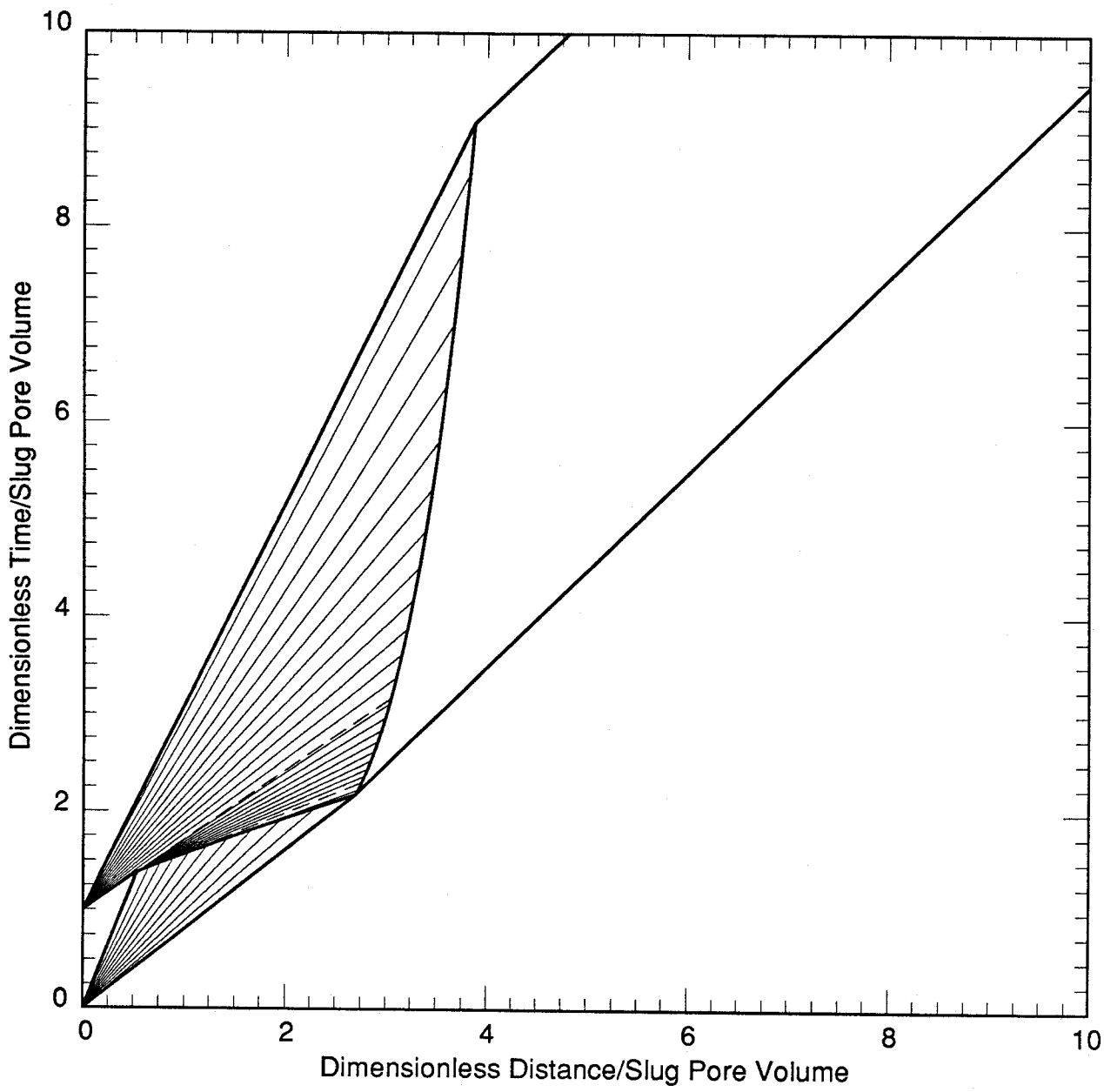

Figure 3.3-19. Complete analytical solution for arbitrary water slug size.

Fig. 3.3-19 is especially useful because it allows us to see the effects of a changing slug size. For example, if the slug size is too small, the expected shock fronts will not be seen at the producer. This is because the shock $\overline{GA}$ will be overtaken by the shock $\overline{EFGH}$. Also, the shock $\overline{CDEF}$ will cut off the two-phase region from the producer. To avoid this, the slug size must be greater than 0.37 PVI (1/2.70) for the H_20-NBA case.

3.3.4 Conclusions

The analysis of slug injection solutions for the binary H_2O-NBA system, leads to the following conclusions:

(1) Two component interference problems can be solved analytically using the idea of Riemann equivalents. The full solution is divided into smaller Riemann problems with different injection and initial conditions.

(2) Use of time-distance diagrams is essential in the construction of the solution, because the full solution is no longer a function of x/t only.

(3) Analytical shock paths can be constructed by using simple numerical schemes such as second-order Runga-Kutta integration. The accuracy of these schemes is excellent.

(4) The analytical solution for all slug sizes can be collapsed to a single time-distance diagram.

(5) Slug size can be critical in determining the effluent composition. Hence, it is expected that slug size will be important in the rate of recovery of hydrocarbons in processes that rely on component transfer between phases to achieve high displacement efficiency.

3.4 Capillary Imbibition and Gravity Segregation: Interactions with Phase Equilibrium in Oil/Brine/Alcohol System

David S. Schechter and Dengen Zhou

The mathematical theory discussed in Sections 3.1 - 3.3 deals with one-dimensional flow. The theory developed is important because it establishes with mathematical rigor the central role of phase equilibrium in the generation of high displacement efficiency in miscible floods. It is clear, of course, that flow in oil reservoirs is not one-dimensional, as permeability heterogeneity and viscous instability (see Chapter 4) cause nonuniform flow. Extensions of the one-dimensional theory to include the combined effects of phase behavior and viscous crossflow between two layers (Pande 1989, Pande and Orr 1989, Pande and Orr 1990a and Pande and Orr 1990b) indicate that crossflow may have significant impact on displacement performance. The extended theory demonstrates that while crossflow induces two-phase flow in floods that would normally be multicontact miscible in one-dimensional flow, the adverse effects of the two-phase flow are more than outweighed by the benefits of mobilizing oil out of the low permeability layer into the faster flow layer and also by a small but favorable reduction in the adverse mobility contrast between the two layers.

The theory developed to date has only dealt with viscous crossflow, but other physical mechanisms also induce crossflow: capillary imbibition, gravity segregation, and the slower processes of transverse diffusion and dispersion. In this section, we examine experimentally the combined effects of capillary imbibition, gravity driven crossflow, and phase behavior.

The experiments were performed in a vertical core holder with an annulus surrounding the core. In a typical experiment, the core was saturated with nonwetting phase and the annular space was then filled with the wetting phase; thus, initiating imbibition. This particular experimental configuration was the limiting case of nonuniform flow: imbibition from a

fracture into adjacent matrix rock. While the goal of of this work is to develop understanding of the role of crossflow between zones of differing permeability, imbibition and gravity driven flow is of interest in its own right, given the number of fractured reservoirs in existence.

The principal parameters that determine the rate of imbibition recovery and the total amount of nonwetting phase produced are: viscosity of the wetting phase, block size and permeability and the capillary pressure of the fluid phases in contact. Experiments such as those by Mattax and Kyte (1962) and Kleppe and Morse (1974) have primarily focused on scaling the dimensions and properties of the matrix block. They found that imbibition oil recovery increases as a function of dimensionless time:

$$t_d \sim \frac{\sqrt{k}}{\phi} \frac{\sigma}{\mu_w L^2} \tag{3.4-1}$$

where t is the time, k the permeability, ϕ the porosity, σ the IFT, μ_w the water phase viscosity and L the length of the block. Very little experimental work concerning the influence of phase behavior on imbibition has been reported. Previously it was assumed that reduction of the capillary forces by decreasing the interfacial tension would lead to reduced recovery since capillary pressure was regarded as the motive force during imbibition. However, Cuiec et al. (1990) observed that the the total recovery of the oil phase increased in the hexane/water/ethanol system when the equilibrium IFT was decreased below 10 mN/m. It was also reported that the imbibition rates decreased as the IFT was lowered, yet there was no mention of scaling such behavior to previously developed rate equations. Thus, there appears to be sparse evidence concerning the effect of phase behavior on scaling imbibition rates.

Scaling of crossflow behavior is an important component of understanding the impact of crossflow on miscible floods. Imagine a layer of high permeability rock that is swept rapidly by the injected fluid (CO_2, for instance). If the pressure is above the minimum miscibility pressure (MMP), the CO_2 will displace nearly all of the oil from the portion of the rock that is swept. In the adjacent zones, however, uncontacted oil will remain stationary. That oil will be the wetting phase relative to the CO_2-rich phase (Campbell and Orr 1985), and some oil will presumably imbibe into the swept layer. In addition, IFT's are likely to vary significantly through the transition zone in CO_2 concentration, because CO_2 displacements at or above the MMP create composition paths that pass through or near the critical region. Thus, the rate dependence of capillary crossflow on phase compositions and fluid properties in the transition zone is of interest in calculations of the effect of that crossflow on composition routes followed by the flowing fluids.

While the eventual goal is a set of measurements of imbibition behavior in CO_2/crude oil systems, high-pressure experiments are sufficiently time consuming and difficult to perform that development of an experimental technique at atmospheric pressure seemed a desirable first step. In the following section, we describe the experimental procedure and the results of experiments performed to date.

3.4.1 Experimental Apparatus and Procedures

The following set of experiments was performed to investigate imbibition near a plait point where the IFT's are very low and the phases are approaching miscibility. Both equilibrium and non-equilibrium experiments are in progress to determine the relative effect upon imbibition. A well described ternary fluid system (Morrow et al. 1988) consisting of isooctane, brine (2% $CaCl_2$) and isopropanol alcohol (IPA) as a tension reducer (see Fig. 3.4-1 and Table 3.4-1) has been utilized for this study. Analyses by gas chromatography (GC) of the equilibrated phases reported here agree well with Morrow's data (Table 3.4-2). Two-foot sections of 2.5" diameter Berea sandstone with permeabilities of 15, 100 and 500 md and a 700 md core of brown sandstone from the Masalan formation are currently under investigation.

Table 3.4-1. Properties of Equilibrated Phases (Morrow et al. 1985).

Tie Line	Density Difference (g / cm^3)	IFT (mN / m)	Viscosity (μ_w / μ_o)
1	0.33	38.1	2.0
2	0.21	1.07	6.25
3	0.11	0.10	3.71

Table 3.4-2. Compositions of Equilibrated Phases.

Tie Line	Brine Phase (Vol %)			Oil Phase (Vol %)		
	IPA	$i-C_8$	Brine	IPA	$i-C_8$	Brine
1	0	0	100	0	100	0
2	55.3	2.6	42.1	11.8	87.6	0.6
3	63.7	16.5	19.8	26.4	71.8	1.8

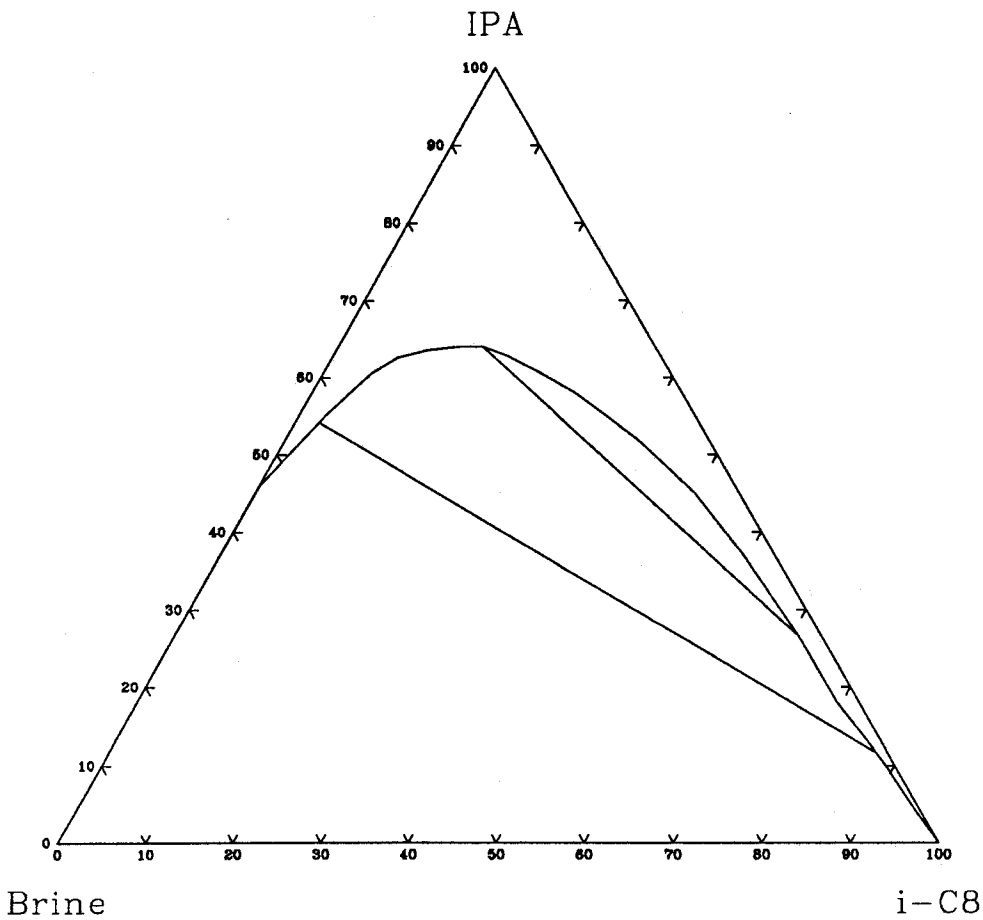

Figure 3.4-1. Phase diagram for IPA, 2% $CaCl_2$ and isooctane (Morrow et al. 1985).

The experimental procedure begins with vacuum saturation of the cores with either nonequilibrated or equilibrated nonwetting phase. This is accomplished in a core holder equipped with an overburden sleeve. The system schematic is shown in Fig. 3.4-2. The core (which is saturated with 100% nonwetting phase) is then transferred to a plexiglass cell with an annular space of 1/32" between the side of the core and the wall (Fig. 3.4-3). The air in the fracture is displaced by the nonwetting phase until the entire core is immersed in the nonwetting fluid. At this point, the wetting phase is introduced into the bottom of the cell, and the nonwetting phase is displaced from the annular space until the core is completely surrounded. Flow is discontinued, and the entrance and exit valves are closed. The core is allowed to remain immersed in the wetting phase until oil production is complete. The volume of nonwetting phase produced is measured at arbitrary intervals, and a material balance on the fluids is performed. Thus, the amount of oil recovered by spontaneous imbibition may be obtained.

3.4.2 Results of Experiments with Equilibrated Fluids

Three different tie-lines have been investigated (i.e., three values of IFT) in experiments with wetting and nonwetting phases equilibrated prior to the start of the experiment. For isooctane and brine mixtures containing no IPA, the IFT is 38 dyne/cm (high). For equilibrated mixtures containing 34% and 44% IPA, the IFT is reduced to 1.0 (moderate) and 0.1 dynes/cm (low), respectively (see Table 3.4-1). The concentration of IPA refers to the volume of IPA per total volume of all three components. The volume of the two equilibrated phases was kept equal by varying the amount of IPA added to the aqueous phase and holding the volume of oil constant.

Figs. 3.4-4 and 3.4-5 demonstrate the effect of changing IFT on ultimate recovery for the 100 and 500 md cores. They show that reducing the IFT increases the ultimate recovery by as much as 20%. Figs. 3.4-4 and 3.4-5 do not provide unambiguous rate information, however, because, originally, the oil was allowed to collect in the annular space. As oil was produced, the interface level moved downward, thereby reducing the area open to imbibition. Figs. 3.4-6 and 3.4-7 are recovery curves for the 500 and 700 md cores obtained when the cores were completely immersed in the wetting phase during the entire experiment. The oil was collected at the top of the cell, and the interface level was not allowed to reach the annular space. Thus the boundary condition remained constant in the second version of the experiment. Continuous immersion allowed imbibition to proceed much faster than it did in the previous moving boundary experiments, as comparison of the recovery curves for 38.1 mN/m in Figs. 3.4-5 and 3.4-6 indicate. (Note the difference in the time scales in the two plots). Fig. 3.4-8 shows that even when the rate of recovery is normalized by the total amount to be recovered, the rate is still higher for the low tension case. The imbibition rate behavior shown in Fig. 3.4-8 is clearly inconsistent with the time scale implied by Eq. (3.4-1).

3.4.3 Results of Experiments with Nonequilibrium Fluids

Experiments were also performed to investigate nonequilibrium effects on imbibition. In this case, the core was saturated with pure isooctane and immersed in an aqueous alcohol solution. Unlike equilibrium studies, in which the volume of oil produced equaled the volume of wetting phase imbibed, the oil produced in the nonequilibrium situation contained some alcohol that partitioned into the oil phase from the brine phase. Therefore, all oil produced was analyzed by gas chromatography, so that appropriate mass balances could be performed. In all the nonequilibrium experiments, oil phase collected in the annulus, and hence recovery rate was probably reduced somewhat, as was observed in similar experiments described in Section 3.4-2.

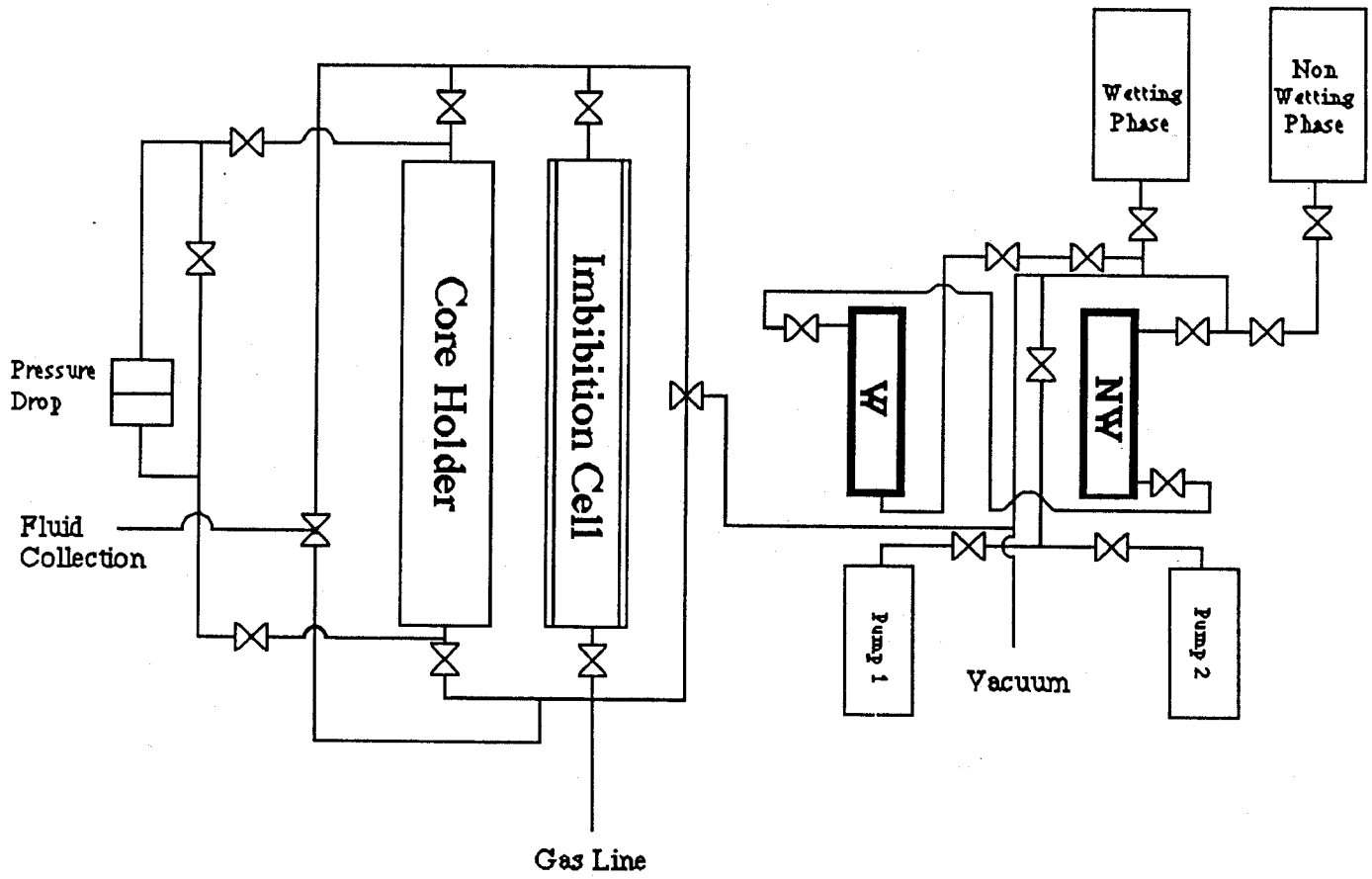

Figure 3.4-2. Schematic of imbibition apparatus.

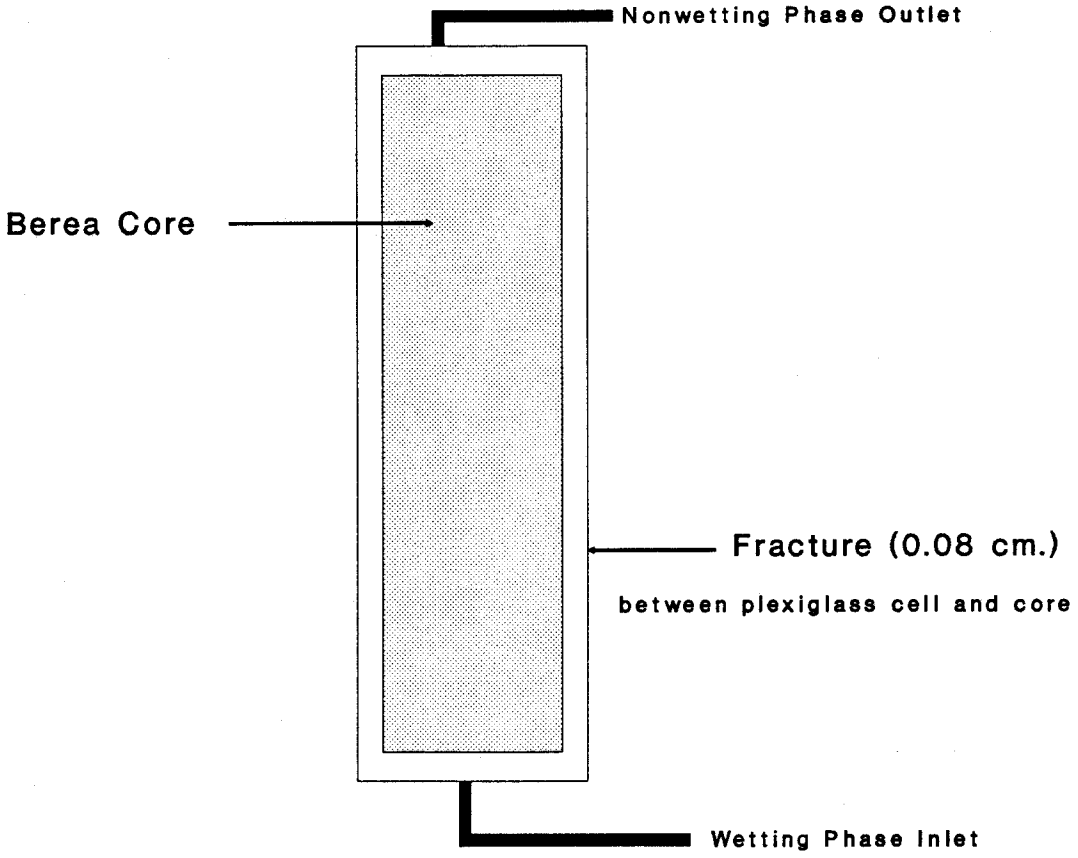

Figure 3.4-3. Schematic of plexiglass core holder.

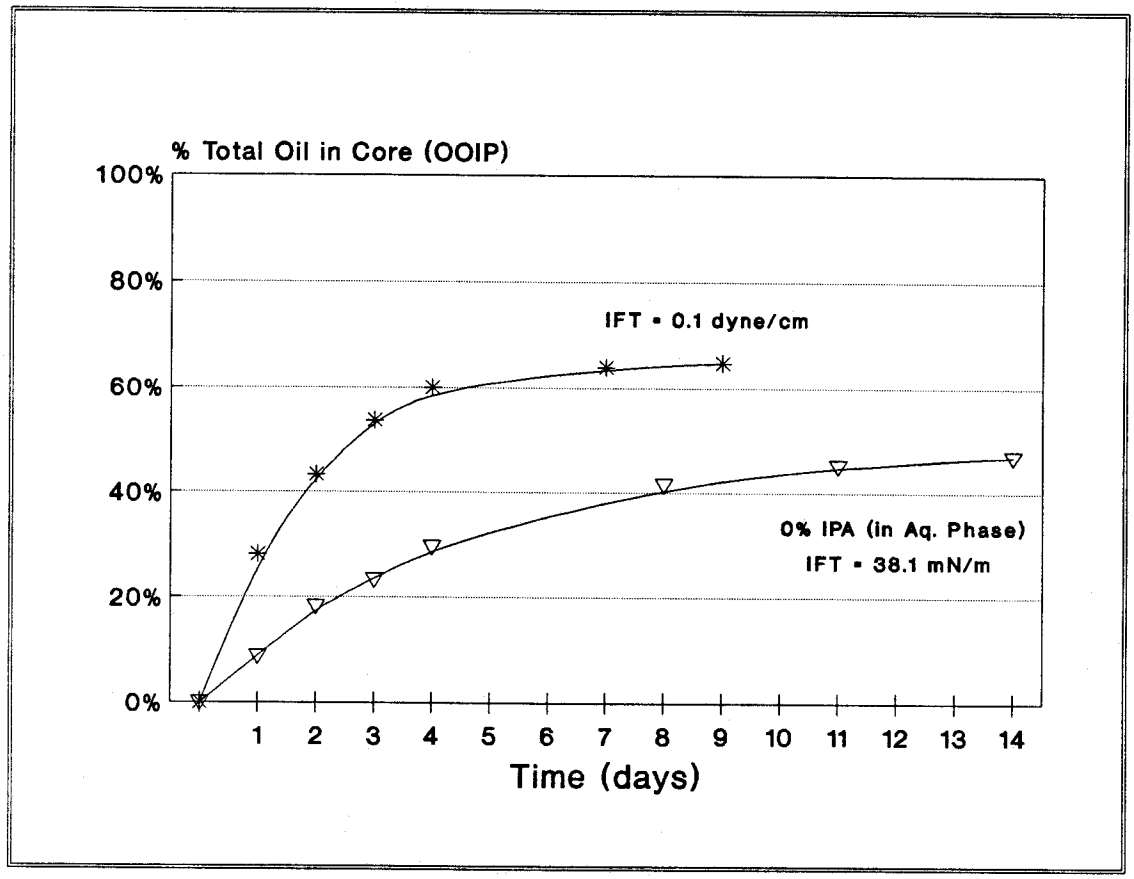

Figure 3.4-4. Oil production during imbibition experiments with equilibrated fluids in a Berea sandstone core with permeability k = 100 md. In these experiments produced oil phase collected in the fracture, reducing the area available for imbibition.

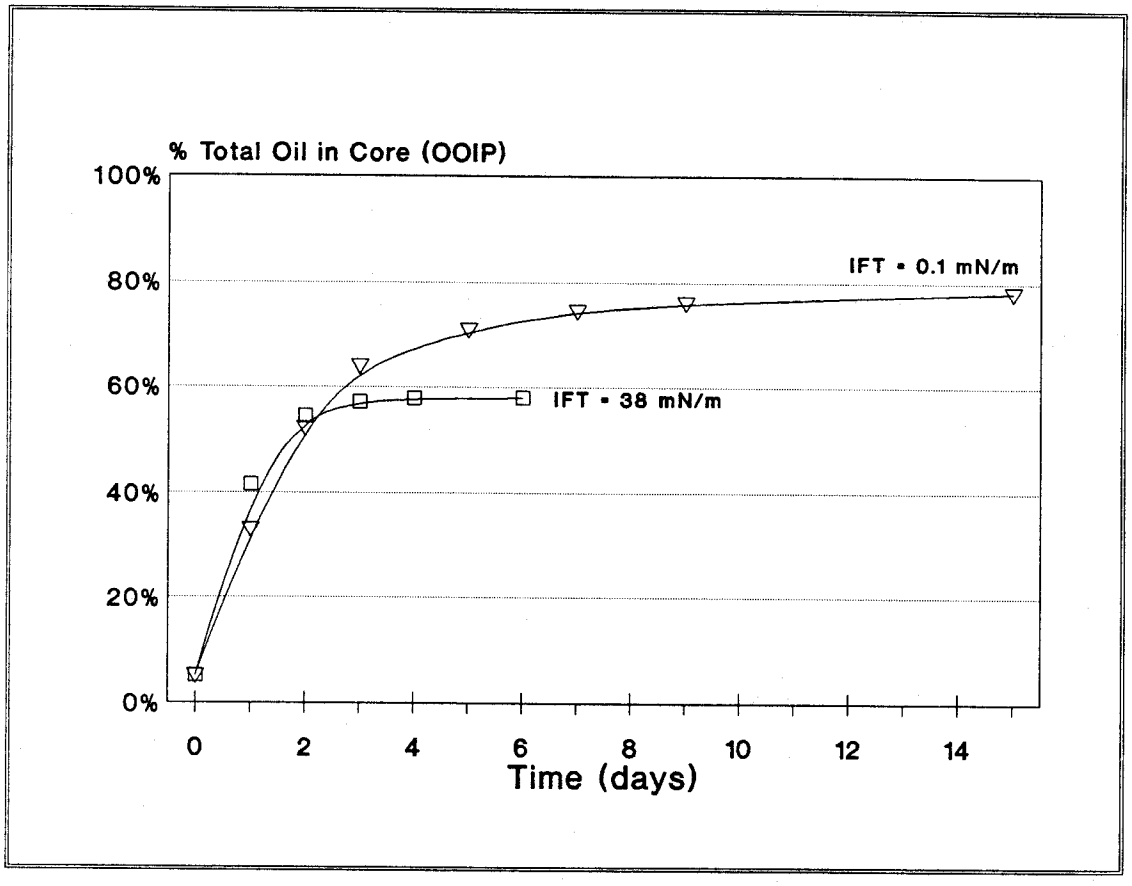

Figure 3.4-5. Oil production during imbibition experiments with equilibrated fluids in a Berea sandstone core with permeability k = 500 md. In these experiments produced oil phase collected in the fracture, reducing the area available for imbibition.

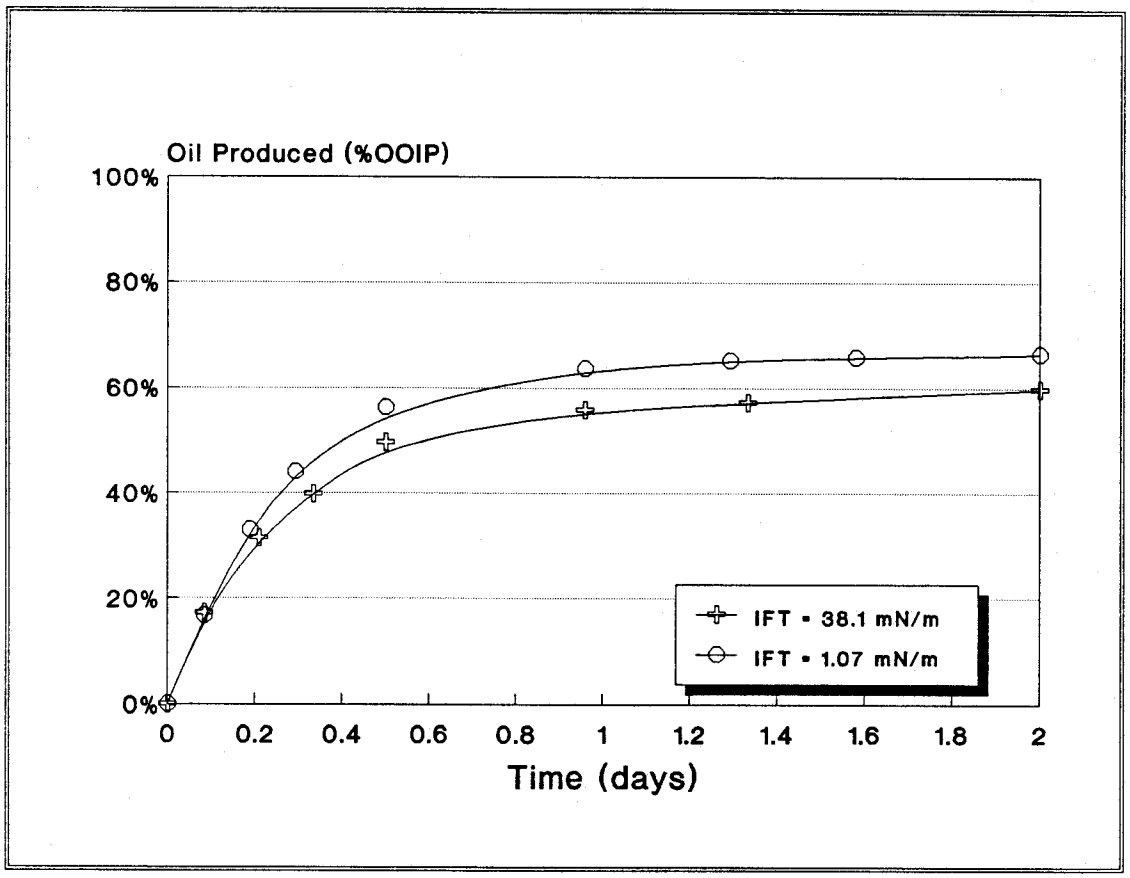

Figure 3.4-6. Oil production during imbibition experiments with equilibrated fluids in the 500 md Berea core. In these experiments produced oil collected above the top face of the core, allowing the core to be immersed continuously in the wetting phase.

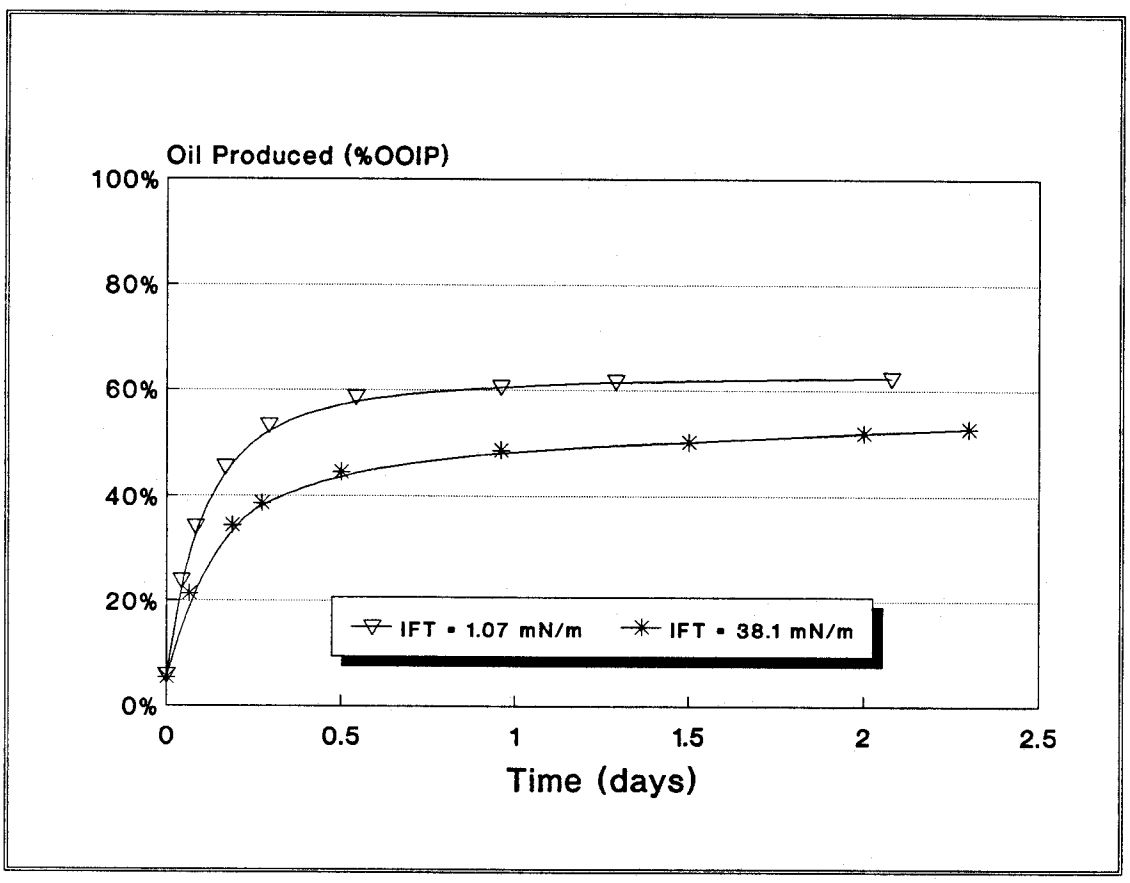

Figure 3.4-7. Oil production in a brown sandstone core from the Masalan formation with a permeability of k = 700 md. In these experiments, produced oil collected above the top face of the core, allowing the core to be immersed continuously in the wetting phase.

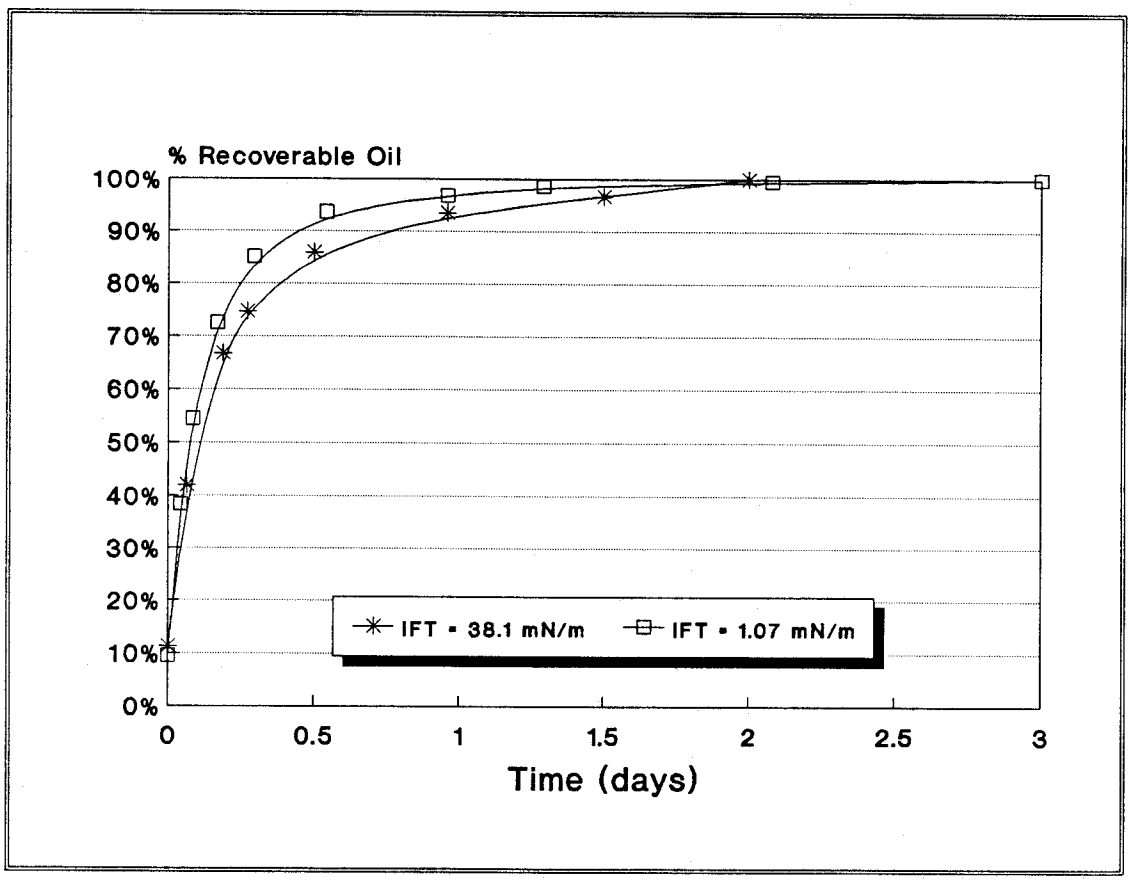

Figure 3.4-8. Scaled imbibition rates for the oil production curves in Fig. 3.4-7.

Fig. 3.4-9 compares results of two experiments with fluids at equilibrium with two experiments not at equilibrium in the 500 md core. Experiment 1 was the no-alcohol reference case in which the IFT is high. Experiment 2 was the equilibrated case at the low value of IFT (0.1 mN/m). In experiment 3, the core was saturated with a single-phase mixture of 45% IPA - 55% i-C8 (note that all concentrations in this section are in volume fractions) and immersed in an imbibing fluid of pure brine. For experiment 4, the core was initially saturated with pure isooctane and immersed in the equilibrated wetting phase with a high alcohol concentration (Table 3.4-2, wetting phase composition at 0.44 volume fraction IPA). The amount of oil produced in experiments 3 and 4 does not include the alcohol transferred to the oil phase.

The differences between curve 1 and curves 2 and 4 in Fig. 3.4-9 show again that increasing the alcohol concentration in the wetting phase (decreasing the IFT) increases the total volume of oil recovered by imbibition. Furthermore, comparison of curves 2 and 4 indicates that if a high concentration alcohol solution is allowed to imbibe into the core saturated initially with pure isooctane, more oil is produced even though the final equilibrium IFT is the same. This suggests that IFT gradients caused by compositional imbalances may aid imbibition mechanisms. In experiment 4, brine phase that imbibed was steadily stripped of its alcohol as it encountered fresh oil not yet saturated with IPA. Thus, the IFT must have increased with depth of penetration into the core. Hence, the IFT gradient must have acted to enhance imbibition. Experiment 3 verifies this idea. Release of oil from the matrix is adversely affected by causing the IFT gradient to act in the opposing direction for recovery (i.e. high alcohol concentration in the oil phase).

Fig. 3.4-10 shows results of a similar experiment carried out on the 100 md core. Experiment 1 was again the reference case with no alcohol. Experiment 2 is the equilibrated case at low IFT (0.1 mN/m). Experiment 3 was not at equilibrium, but the aqueous phase contained only a dilute alcohol concentration (15%), which according to the phase diagram would decrease the eventual equilibrium IFT only threefold to about 10 mN/m. Experiment 4 was performed with the same fluids as with the experiment 4 in the 500 md core, but the lateral face of the core was covered with a teflon sleeve. Thus, imbibition occurred only through the top and bottom faces. In this case, the rate of imbibition was slowed considerably, yet the ultimate recovery eventually exceeded the equilibrium case.

3.4.4 Discussion

Conventional interpretations of imbibition regard capillary pressure as the driving force behind imbibition. For low IFT immiscible phases, one would expect a decrease in capillary forces and therefore slower mobilization of the nonwetting phase during imbibition. According to the experiments outlined here, this is not necessarily the case. Indeed, reducing the equilibrium IFT greatly increases the amount of oil recovered by spontaneous imbibition for the sandstone cores currently under investigation.

Cuiec et al. (1990) observed that reducing the IFT resulted in a decrease of imbibition rates. Their results were obtained in tight chalk with permeabilities between 1 and 3 md; whereas, the results presented here are from sandstone cores with much larger permeabilities. The following analysis suggests that buoyancy will dominate in the high permeability regions investigated in the experiments described and capillarity in the low permeability studies of Cuiec et al. This suggests that a crossover occurs between capillary and gravity driven imbibition which is dependent on the average pore size, the pore size distributions, and the phase behavior of the fluids considered. Therefore, we may classify imbibition for three differing regions: capillary dominated, gravity dominated, and a region where both forces affect imbibition.

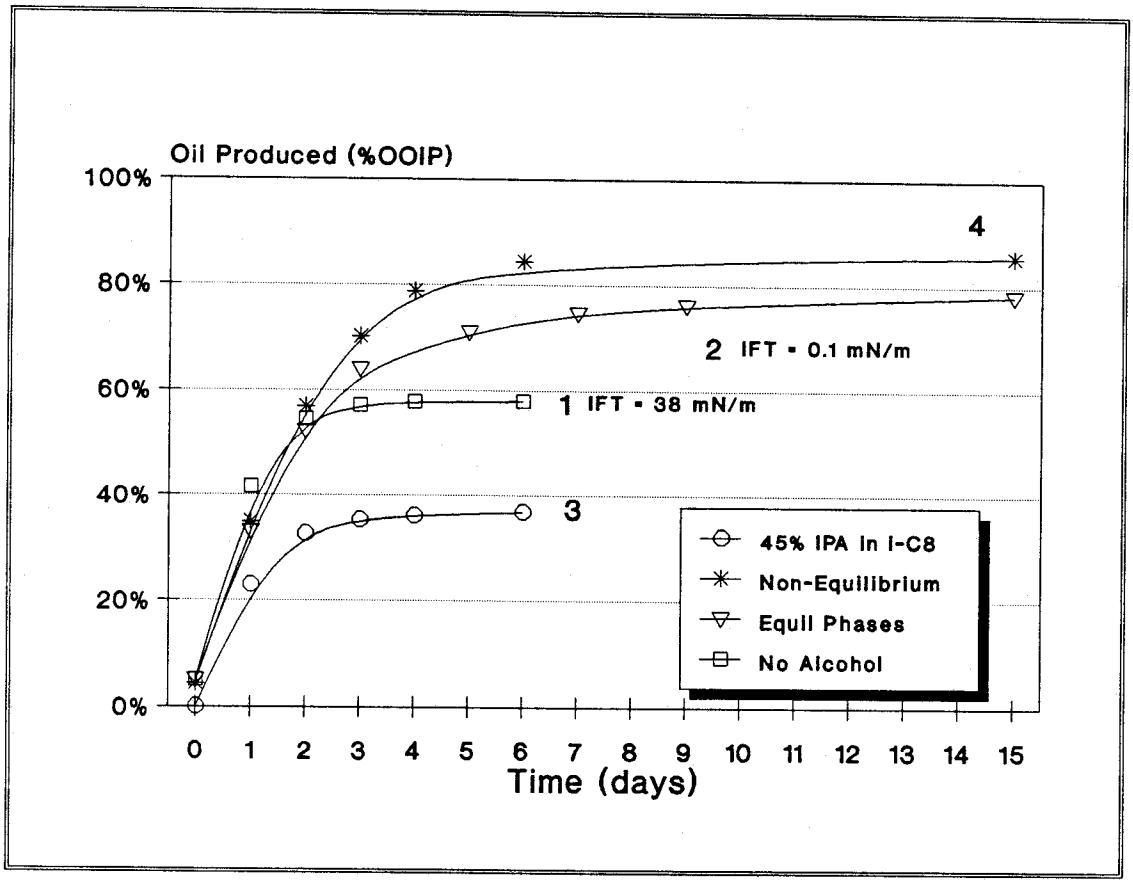

Figure 3.4-9. Comparison of equilibrium and nonequilibrium imbibition for the 500 md core.

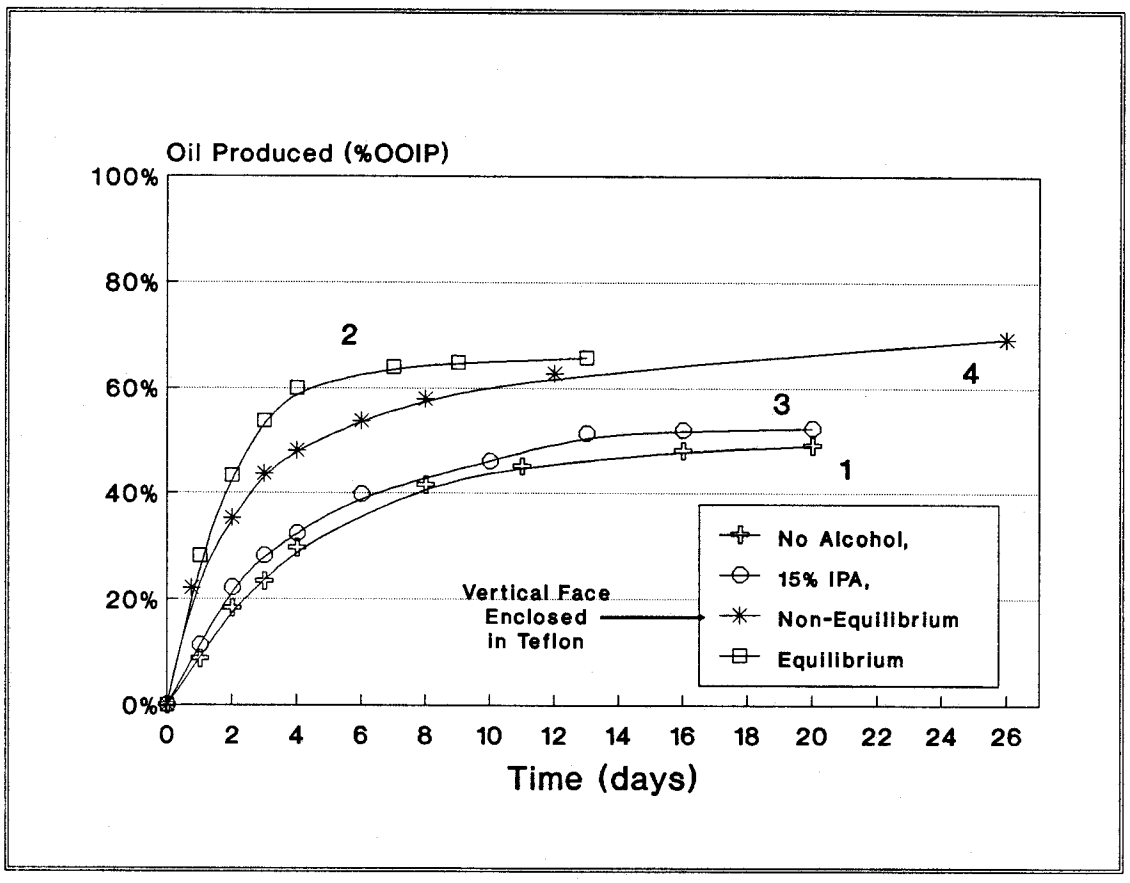

Figure 3.4-10. Comparison of equilibrium and nonequilibrium recovery data for the 100 md core.

Capillary Pressure Dominated Imbibition

Consider a trapped oil droplet free from gravity effects. The criterion for stability within porous medium is that all curvatures of this oil droplet are equal; otherwise, it changes its shape to attain a state of minimum free energy.

$$J_1 = J_2 = J_i \tag{3.4-2}$$

where J is the curvature of an oil interface suspended in an aqueous medium within the pore space. In the sandstone cores studied here, the core is not in capillary equilibrium. Instead, brine phase will imbibe into some pores, while oil is displaced from others. Pore sizes vary considerably, of course, so the aqueous wetting phase imbibes into the small pores and forces the oil out of the larger pores. In the analysis that follows, we assume that the driving force for imbibition is given by

$$P_c^* = 4\sigma(1/D_i - 1/D_o)\cos\theta \tag{3.4-3}$$

where θ is the contact angle at the solid surface, D_i is the diameter of the pore in which the water is imbibing and D_o the pore diameter in which the oil flows out.

Now consider the simple material balance illustrated in Fig. 3.4-11 for imbibition into a core with square cross section. Water imbibes from the ends of the core, and oil is expelled by countercurrent flow. For this simple analysis, we assume that the displacement is piston-like. The flow velocities of the oil and water phases are

$$\frac{q_w}{A} = -\frac{kk_{rw}}{\mu_w}\frac{\partial P_w}{\partial x} = -k\lambda_w\frac{\partial P_w}{\partial x} \tag{3.4-4}$$

$$\frac{q_o}{A} = -\frac{k\,kro}{\mu_o}\frac{\partial P_o}{\partial x} = -k\lambda_o\frac{\partial P_w}{\partial x} \tag{3.4-5}$$

where A is the area open for imbibition, k is the permeability, k_{ro} and k_{rw} are the relative permeabilities of oil and water, μ_o and μ_w are the viscosities of the phases, and λ_o and λ_w are the mobilities, and P_o and P_w are the pressures in the oil and water phases. The total flow velocity is

$$\frac{q_o+q_w}{A} = -k\left\{\lambda_o\frac{\partial P_o}{\partial x} + \lambda_w\frac{\partial P_w}{\partial x}\right\} \tag{3.4-6}$$

Because the flow is assumed to be strictly countercurrent, $q_o = -q_w$, and hence

$$\frac{\partial P_o}{\partial x} = -\frac{\lambda_w}{\lambda_o}\frac{\partial P_w}{\partial x} \tag{3.4-7}$$

From the definition of the capillary pressure, P_c, we write

$$\frac{\partial P_w}{\partial x} = -\frac{\partial P_c}{\partial x} + \frac{\partial P_o}{\partial x} = -\frac{\partial P_c}{\partial x} - \frac{\lambda_w}{\lambda_o}\frac{\partial P_w}{\partial x} \tag{3.4-8}$$

Rearrangement of Eq. (3.4-8) gives

$$\frac{\partial P_w}{\partial x} = -\frac{1}{1+\lambda_w/\lambda_o}\frac{\partial P_c}{\partial x} \tag{3.4-9}$$

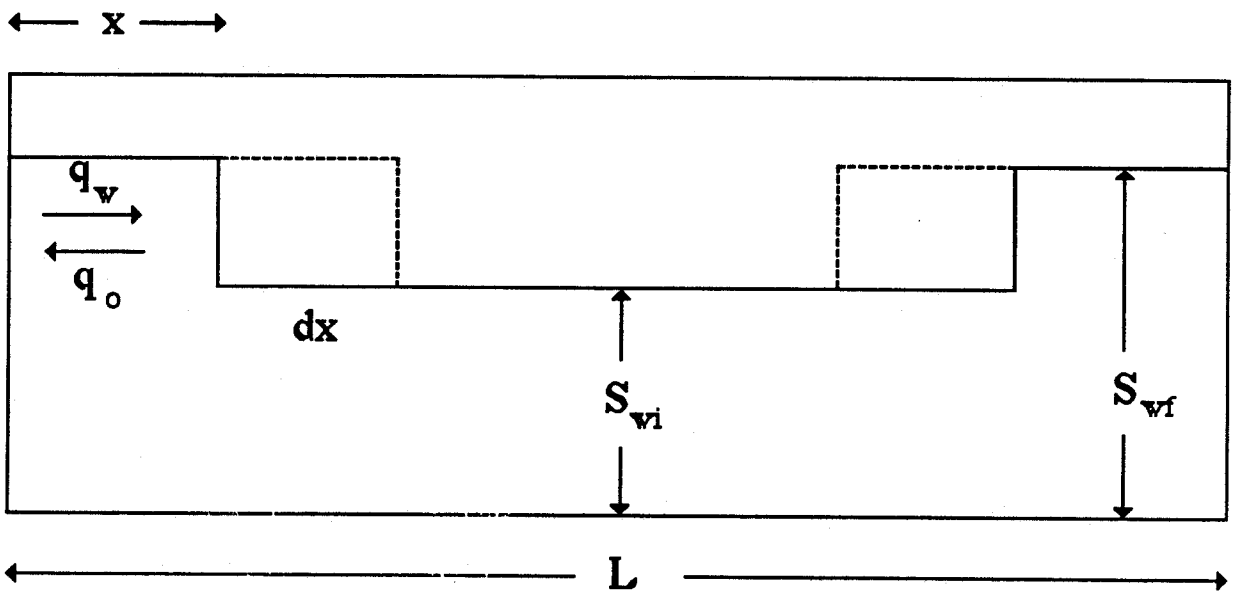

Figure 3.4-11. Limiting case analysis of capillary dominated imbibition.

Hence, Eq. (3.4-4) can be written as

$$q_w = \frac{Ak\lambda_w}{1+\lambda_w/\lambda_o}\frac{\partial P_c}{\partial x} \tag{3.4-10}$$

We now assume that the gradient of capillary pressure can be estimated as

$$\frac{\partial P_c}{\partial x} = \frac{4\sigma\cos\theta}{x}\left[\frac{1}{D_{in}} - \frac{1}{D_o}\right] = \frac{P_c^*}{x} \tag{3.4-11}$$

A material balance on water yields, then

$$\frac{Ak}{\frac{1}{\lambda_w}+\frac{1}{\lambda_o}}\frac{P_c^*}{x}\,dt = \phi A\left[S_{wf}-S_{wi}\right]dx \tag{3.4-12}$$

where Sw_i and Sw_f are the initial and final water saturations. Eq. (3.4-12) can be integrated to yield

$$\frac{kP_c^*}{\frac{1}{\lambda_w}+\frac{1}{\lambda_o}}\,t^{cap} = \frac{1}{2}\phi\left[S_{wf}-S_{wi}\right]x^2 \tag{3.4-13}$$

Because the imbibition process is complete when $x = L/2$, Eq. (3.4-13) can be rewritten in terms of the fractional recovery, $R = 2x/L$, as

$$\frac{8kP_c^*}{L^2}\left(\frac{1}{\lambda_w}+\frac{1}{\lambda_o}\right)t^{cap} = \phi\Delta S R^2 \tag{3.4-14}$$

where $\Delta S = S_{wf} - S_{wi}$. Eq. (3.4-14) can be rearranged to give

$$t_D^{cap} = \frac{kP_c^*\lambda_o}{\phi\Delta S L^2}\,t = \frac{R^2}{8}(M+1) \tag{3.4-15}$$

where $M = \lambda_o/\lambda_w$.

To verify Eq. 3.4-15, we made a comparison with the experimental data presented by Cuiec et al. (1990) for low-permeability chalk samples. The main parameters of the chalk samples are listed in Table 3.4-3. The values of the pore diameters shown in Table 3.4-3 were estimated from reported pore size distribution data. For the calculations that follow, $\cos\theta$ was assumed to be 1.0. For a 20-cm length of core, the gravity force, $P_g = \Delta h\Delta\rho g$ is about 3% of the capillary force, $P_c = 4\sigma(1/D_i - 1/D_o)$. One data point was used to determine the value of $\left[\frac{1}{\lambda_w}+\frac{1}{\lambda_o}\right]$ in Eq. (3.4-15). Then the remainder of the recovery could be calculated. The value obtained for $\left[\frac{1}{\lambda_w}+\frac{1}{\lambda_o}\right]^{-1}$ was 0.07. That value is close to what could be observed for water with and endpoint k_{rw} near 0.1. Thus, the value obtained is consistent with typical sandstone relative permeability data. Fig. 3.4-12 shows the comparison of the predicted and experimental data for different chalk samples.

Table 3.4-3. Chalk Core Data from Cuiec et al. (1990).

Sample No.	Length (cm)	k (md)	P_g/P_c	$\Delta\rho$ (g/cc)
Sample 1	20.0	6.4	0.028	0.3
Sample 2	9.0	3.7	0.013	0.3

Table 3.4-4. Core Properties for Calculated Recovery Curves Shown in Fig. 3.4-14.

N_B^{-1}	D_o (cm)	L (m)	$\Delta\rho$ (g/cm^3)	σ (mN/m)	m
0.1	1.0×10^{-2}	2.67	300.0	20.0	1.0
0.2	1.0×10^{-2}	2.67	300.0	40.0	1.0

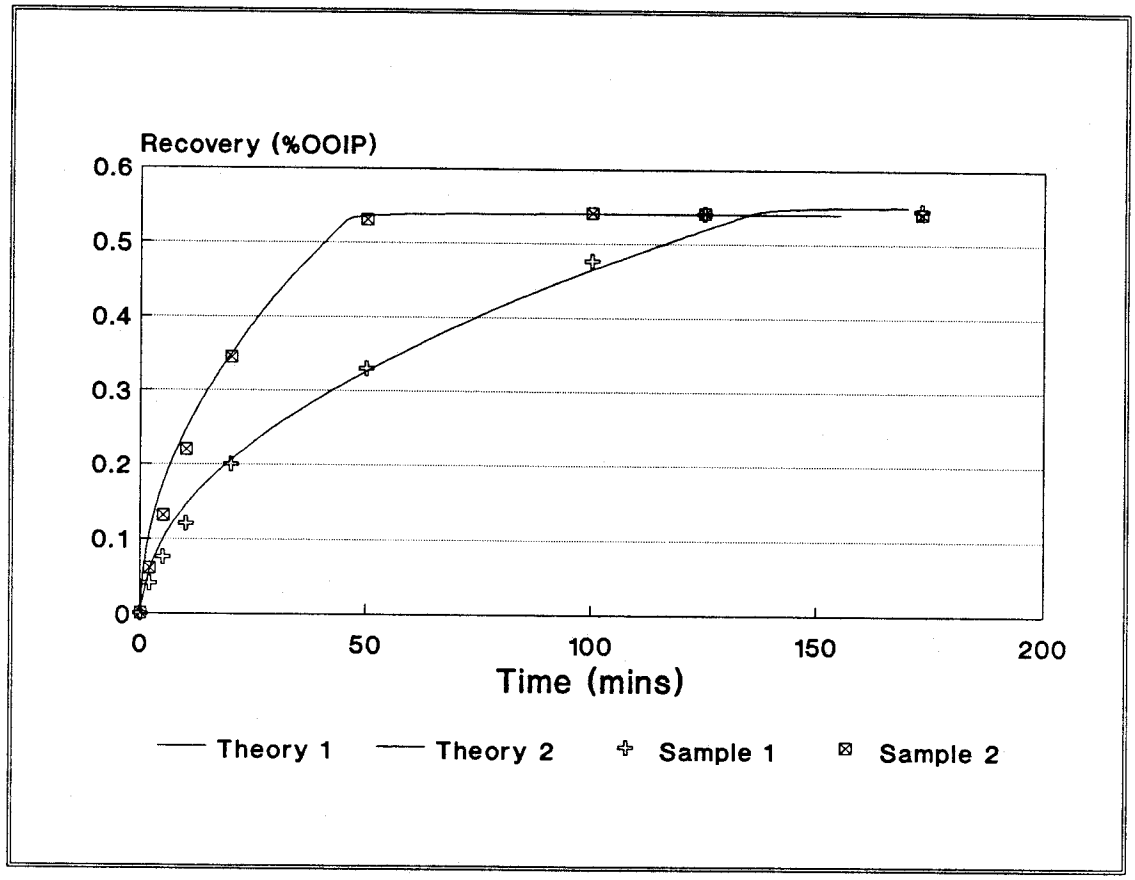

Figure 3.4-12. Comparison of theory with data of Cuiec et al. (1990).

Fig. 3.4-13 details scaling of Cuiec's IFT data for a single core. These results are in reasonable agreement with only a single parameter adjusted to obtain the relative permeability data. The agreement confirms that for very small gravity effects, imbibition may be scaled according to Eq. (3.4-1) or the version of it obtained here, Eq. (3.4-15).

Gravity Dominated Flow

When gravity effects are much larger than capillary pressure effects, another limiting case solution can be constructed. Again, we assume that the displacement is piston-like, but this time the flow is cocurrent, not countercurrent. All the water phase enters the core at the base and all oil exits the core at the top. The flow rate in the water phase is

$$q_w = -Ak\lambda_w\left[\frac{\partial P_w}{\partial x} + P_{wg}\right] \tag{3.4-16}$$

At any given time, t, the flow rate of water, q_w, is everywhere the same, though q_w does change with time, of course. Hence, Eq. (3.4-16) can be integrated to yield

$$P_w = \left[-\rho_w g - \frac{q_w}{Ak\lambda_w}\right]x + C_1 \tag{3.4-17}$$

The constant C_1 can be evaluated as $C_1 = \rho_w gL$ at $x = 0$. Similarly for the oil phase,

$$q_o = -Ak\lambda_o\left[\frac{\partial P_o}{\partial x} + \rho_o g\right] \tag{3.4-18}$$

and integration gives

$$P_o = \left[-\rho_o g - \frac{q_o}{Ak\lambda_o}\right]x + C_2 \tag{3.4-19}$$

The constant C_2 is determined as follows: We assume that the pressure in the water phase is zero at $x = L$, while the pressure in the oil phase is slightly higher, $P_o = \frac{4\sigma}{D_o}$, the capillary pressure required for oil to leave large pores at the top of the core. The result is

$$P_o = \left\{\rho_o g + \frac{q_o}{Ak\lambda_o}\right\}(L-x) + 4\frac{\sigma}{D_o} \tag{3.4-20}$$

Because the flow is cocurrent, $q_o = q_w$, and we take the oil and water phase pressures at the water-oil front to be equal. Hence, Eqs. (3.4-17) and (3.4-20) can be solved for the water flow rate as a function of the front position, x.

$$q_w = \frac{\Delta\rho g(L-x) - 4\frac{\sigma}{D_o}}{L - \frac{x}{Ak\lambda_o} + \frac{x}{Ak\lambda_w}} \tag{3.4-21}$$

where $\Delta\rho = \rho_w - \rho_o$.

The expression for q_w in Eq. (3.4-21) can now be used in a material balance on water, which gives

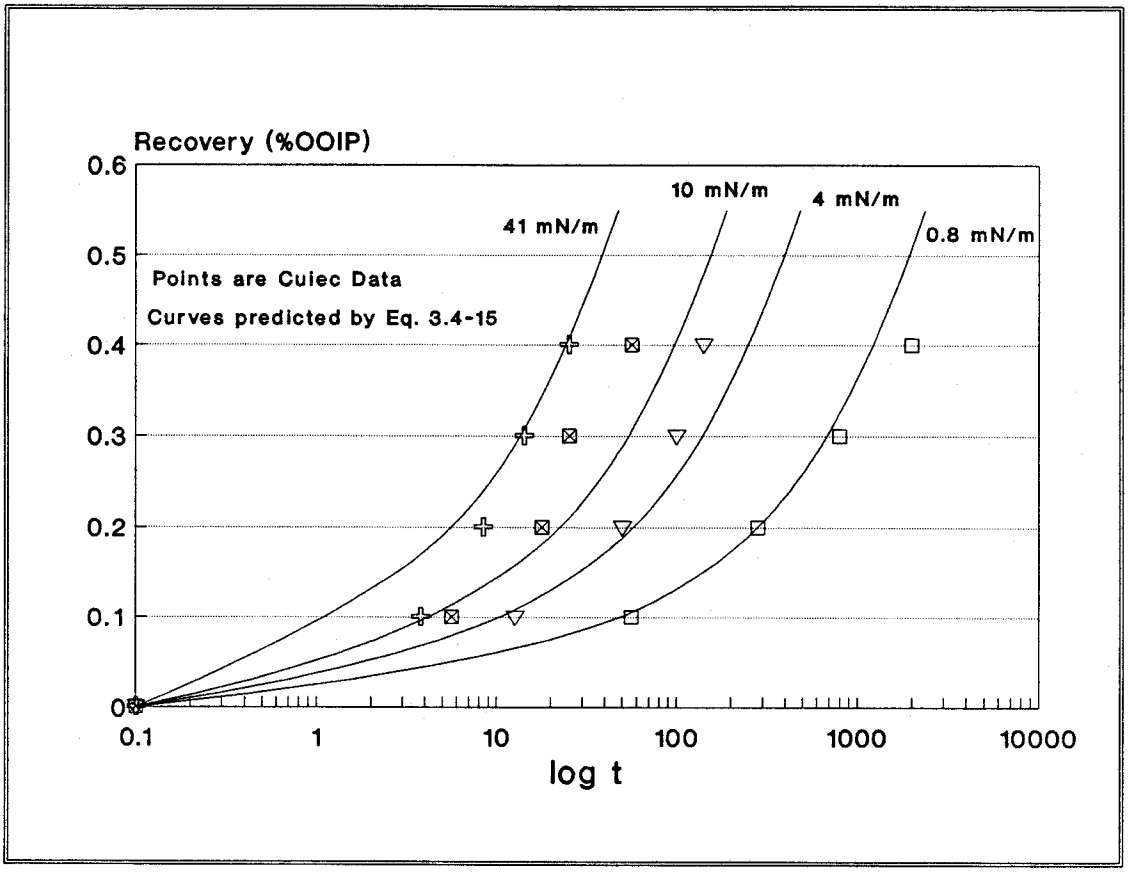

Figure 3.4-13. Comparison of Eq. (3.4-15) with data of Cuiec et al. (1990).

$$\frac{\Delta\rho g(L-x) - 4\frac{\sigma}{D_o}}{\frac{L-x}{k\lambda_o} + \frac{x}{k\lambda_w}}\, dt = \phi\Delta S\, dx \tag{3.4-22}$$

which can integrated to give

$$t_D^{grav} = (1-M)N_B^{-1} + \left[M + (1-M)N_B^{-1}\right] \ln\left[\frac{1-N_B^{-1}}{1-N_B^{-1}R}\right] \tag{3.4-23}$$

where

$$N_B = \frac{D_o L \Delta\rho g}{4\sigma}$$

$$R = x/L$$

$$t_D^{grav} = \frac{k\lambda_o \Delta\rho g}{\phi\Delta SL}\, t$$

Fig. 3.4-14 shows the response calculated according to Eq. (3.4-23) for two values of N_b. The physical data used are shown in Table 3.4-4. As Fig. 3.4-14 shows, Eq. (3.4-23) predicts that recovery rate increases as N_B^{-1} decreases, a result that is consistent with the observations shown in Figs. 3.4-6 and 3.4-7. It must be noted, however, that the derivation of Eq. (3.4-23) required an assumption that capillary forces played a role only at the core exit. Similar forces at the water displacement front were ignored, an apparently inconsistent assumption. Thus, it is clear that additional analysis of flow in the gravity-dominated case will be required.

While there is uncertainty about the cause of the increased rate as IFT is reduced, there is more information available about the combined effects of low IFT and gravity on the residual oil saturation eventually reached in each displacement. Morrow and Songkran (1982) determined that for low IFT systems, buoyancy forces may play a significant role in displacement mechanisms. The reduction of the residual saturation for random packings of equal spheres was correlated with an inverse Bond number defined as $N_B = \frac{R^2\Delta\rho g}{\sigma}$, where R is a characteristic particle radius. They reported that residual saturation was unaffected for inverse Bond numbers above approximately 200. For the displacements described here, values of the Morrow and Songkran version of the Bond number were estimated. Particle radii were estimated with the Kozeny-Carman equation (Morrow and Songkran 1982). Table 3.4-5 shows resulting values of N_B^{-1} for the equilibrated experiments in the three cores described here. Results of those displacements are shown in Figs. 3.4-4 to 3.4-8. The inverse Bond numbers in Table 3.4-5 suggest that IFT's were low enough to cause some reduction in residual oil saturation for all three cores when σ was 0.1 mN/m, and for the 500 and 700 md cores, σ = 1.07 mN/m was low enough to provide some reduction. Thus, the observation of higher ultimate recovery at low IFT is consistent with the results of Morrow and Songkran (1982) for bead packs, though the reason for observation of higher recovery rates remains to be explained satisfactorily.

Table 3.4-5. Inverse Bond Numbers for Core Displacements.

k (md)	N_B^{-1} $\Delta\rho = 0.33$ g/cm^3 $\sigma = 38.1$ mN/m	N_B^{-1} $\Delta\rho = 0.21$ g/cm^3 $\sigma = 1.07$ mN/m	N_B^{-1} $\Delta\rho = 0.11$ g/cm^3 $\sigma = 0.1$ mN/m
100	2.5×10^5	1150	200
500	7900	350	60
700	3500	150	30

Table 3.4-6. Parameters for Nonequilibrium Analysis.

Case #	σ_i (mN/m)	σ_o (mN/m)
1	41	41
2	41	13.7
3	41	1.0

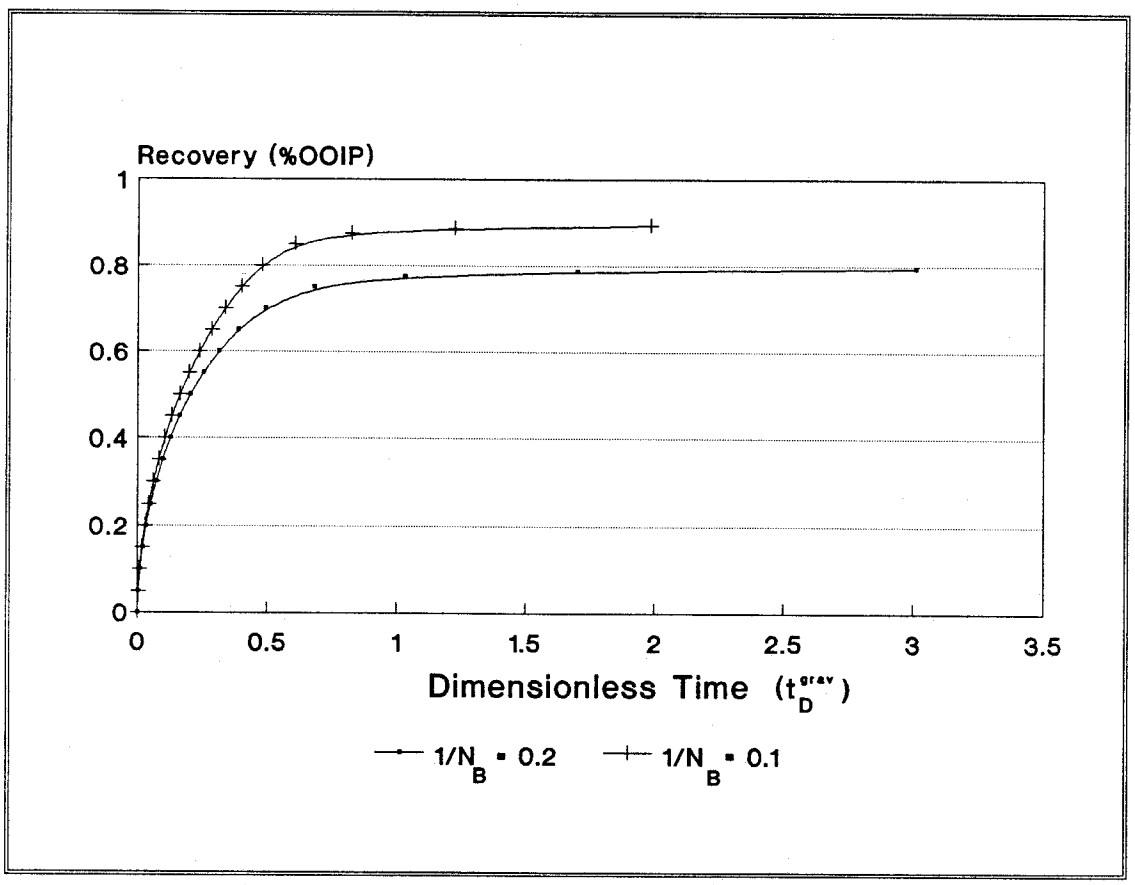

Figure 3.4-14. Effect of reduction in IFT on recovery rate according to Eq. (3.4-23).

Nonequilibrium Imbibition

Finally, we consider a case in which the water phase enters the core from the bottom and top faces, and the oil exits from both of the faces as well. For the nonequilibrium condition, for instance when the core is saturated with pure isooctane and contacted with aqueous phase with a high alcohol concentration, alcohol will be transferred to the oil phase as the oil contacts the aqueous phase. With increasing penetration, the concentration of alcohol in the aqueous phase will decrease. Therefore the IFT, between the oil and water increases as penetration proceeds. We assume again that the oil will flow from the larger pores as the water penetrates the smaller pores. This implies that the IFT of the oil flowing from the core is the lowest while the IFT of the water phase is the largest in the system.

The driving force for imbibition in the nonequilibrium case is

$$P_{cn} = 4\sigma_i\left(\frac{1}{D_i} - \frac{\sigma_o}{\sigma_i D_o}\right) \tag{3.4-24}$$

where σ is the IFT at the waterfront and σ_o is the IFT at the outlet of the medium. From this equation, it is noted that P_{cn} (nonequilibrium capillary pressure) is greater than P_c for the equilibrium case. To make the system comparable, we assume that the medium is large enough that the oil and water phase are in equilibrium on the surface of the core, while at the water front there is no alcohol in both the oil and water phase. Therefore, the IFT's at the outlet and at the waterfront are constants. Equation 3.4-15 may be used by interchanging P_c with P_{cn}. The ratio of recovery in the nonequilibrium to that in the equilibrated experiment is then

$$\frac{R_n}{R} = \left[\frac{\dfrac{1}{D_i} - \dfrac{\sigma_o}{\sigma_i D_o}}{\dfrac{1}{D_i} - \dfrac{1}{D_o}}\right]^{1/2} \tag{3.4-25}$$

Fig. 3.4-15 shows a comparison of oil recovery rates for equilibrium and nonequilibrium systems where $U = \sigma_i/\sigma_o$. The principal parameters are listed in Table 3.4-6. It is observed that with the nonequilibrium system, more oil is produced at a faster rate. Thus, the simple theory is consistent with the observations reported in Figs. 3.4-9 and 3.4-10.

Scaling Behavior of Imbibition Data

The analyses given above were based on the assumptions that the displacement was dominated either by gravity or by capillarity. In many displacements, however, both driving forces will contribute. The limiting case analyses given above can be used, however, to bound the transition from capillary-dominated to gravity-dominated flow. In the discussion below, we make use of still another form of a Bond number,

$$N_B^* = \frac{\sqrt{k}\,L\,\Delta\rho\,g}{\sigma} \tag{3.4-26}$$

We also define a characteristic time as

$$t_t = \frac{L^2\mu_o}{\sigma\sqrt{k}}. \tag{3.4-27}$$

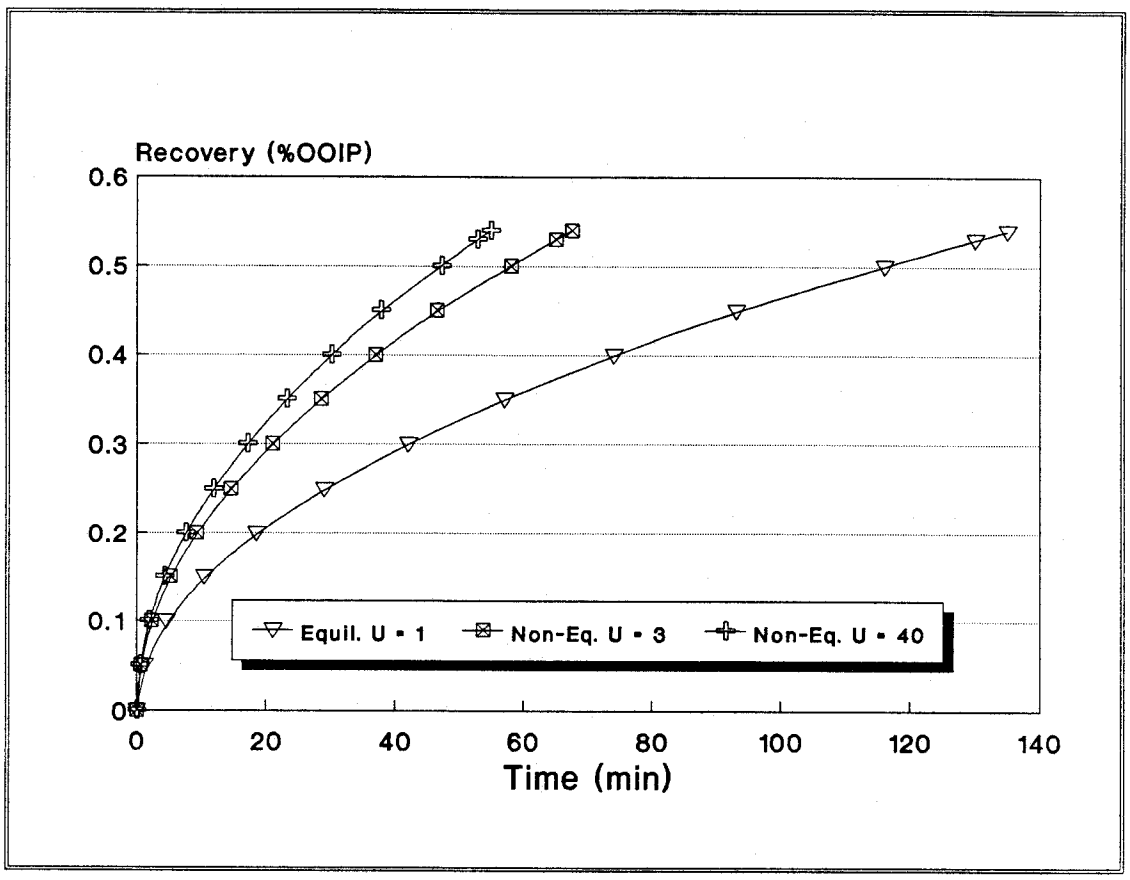

Figure 3.4-15. Imbibition for fluids not in equilibrium.

The time scales of Eqs. (3.4-15) and 3.4-23) for capillary and gravity-dominated flows can be rescaled by the characteristic time of Eq. (3.4-27). The resulting dimensionless time scales are

$$t_d^{cap} = \frac{t^{cap}}{t_t} = \frac{\phi \Delta S}{4 k_{ro}\sqrt{k}\left[\frac{1}{D_i} - \frac{1}{D_o}\right]} \frac{R^2}{8}(M+1) \tag{3.4-28}$$

We assume now that the permeability is related to an average pore diameter by

$$k = \gamma \phi D_e^2 \tag{3.4-29}$$

where γ is a constant. Substitution of Eq. (3.4-29) into (3.4-28) gives

$$t_d^{cap} = \frac{\Delta S}{4 k_{ro} \gamma \frac{D_e}{D_i}\left[1 - \frac{D_i}{D_o}\right]} \frac{R^2}{8}(M+1) \tag{3.4-30}$$

According to Eq. (3.4-30), the dimensionless time scale is independent of N_B^*. Similar manipulations of Eq. (3.4-23) yield another dimensionless time scale for gravity-dominated flow.

$$t_d^{grav} = \frac{1}{N_B^*}\left\{\frac{\phi \Delta S}{k_{ro}}(1-M)R + \frac{\phi \Delta S}{k_{ro}} + \frac{\phi \Delta S}{k_{ro}} \frac{4\sqrt{k}}{D_o} \frac{(1-M)}{N_B^*}\right\} \ln \frac{\left(1 - \frac{4\sqrt{k}}{N_B^* D_o}\right)}{\left[1 - \frac{4\sqrt{k}}{N_B^* D_o} - R\right]} \tag{3.4-31}$$

At a given value of R, the leading terms of Eq. (3.4-31) are linear in $(N_B^*)^{-1}$.

Fig. 3.4-16 is a plot of experimental values of $t_D = t\sigma\sqrt{R}/L^2\mu_o$ required to achieve $R = 0.5$ against $(N_B^*)^{-1}$. According to Eqs. (3.4-30) and 3.4-31), the dimensionless time at $R = 0.5$ should be constant at high values of $(N_B^*)^{-1}$, and should be proportional to $(N_B^*)^{-1}$ at low values. The limited data in Fig. 3.4-16 suggest that most of the experiments here were influenced by gravity effects. The two separate estimated curves shown are for the two different boundary conditions used in the experiments. Though data in the transition region are sparse, the points shown suggest a region of constant t_d with increasing $(N_B^*)^{-1}$ with the crossover occurring in the neighborhood of $(N_B^*)^{-1} = 40$.

The experiments and simple analyses prescribed here indicate that much remains to be learned about the interplay of capillary and gravity-driven crossflow, especially when compositional effects of phase behavior also act. The results obtained thus far, however, indicate that in some circumstances at least, the combination of low IFT and gravity segregation can lead to substantial crossflow of wetting phase. Because crude oil is likely to be the wetting phase in comparison with CO_2, at least, and because low IFT's are likely to occur in some regions of CO_2 floods as near-critical mixtures arise from the multiple contact miscibility mechanism, it is possible that significant amounts of oil that otherwise would be unswept can be contacted by crossflow.

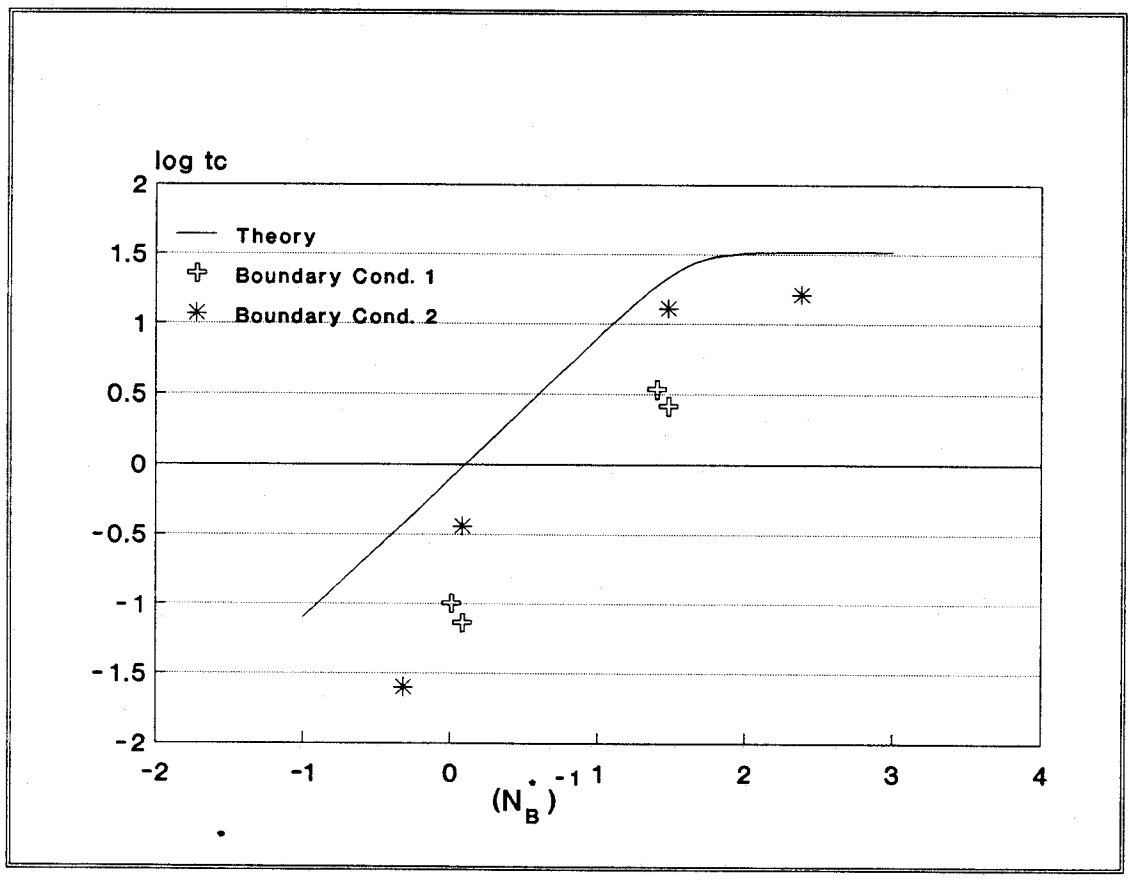

Figure 3.4-16. Dimensionless time required for recovery of half the movable oil. BC 1 refers to cases in which the core was completely immersed in wetting phase. BC 2 refers to cores that were partially immersed.

3.4.5 Conclusions

A series of experiments at atmospheric pressure have been presented in order to assess the effect of phase behavior on imbibition phenomena. The experimental work and analysis described is intended as a precursor to imbibition investigations at high temperatures and pressures which are associated with low IFT phase behavior of CO_2/crude oil systems. The following conclusions can be drawn from the work performed:

(1) Conventional scaling for the imbibition process is valid only for capillary-dominated imbibition. However, for many sandstones, both gravity and capillary forces are responsible for imbibition recovery. Hence, more theoretical and experimental work is required.

(2) For reservoirs with relatively high permeabilities, reduction of the IFT between immiscible phases will enhance both recovery rates and final oil production during imbibition.

(3) Imbibition of nonequilibrium fluids is very different from fluids at equilibrium. Nonequilibrium systems are able to produce more oil at a faster rate than an equilibrium system using the same amount of chemicals if the IFT gradient is in the appropriate direction.

3.5 Summary

The theory and experiments described in this chapter are part of a systematic investigation of the relationships between physical mechanisms that act and interact to determine displacement performance in miscible floods. The theoretical analysis by the method of characteristics (MOC) in Section 3.1 shows, for example, that while qualitative features of solutions are similar, analyses that ignore the effects of volume change on mixing overestimate recovery at pressures below the minimum miscibility pressure (mmp). Timing of recovery is also inconsistent with physical observations when volume change is ignored. Thus, the more complex theory that includes the flow velocity variations induced when volume is not conserved gives a more accurate picture of the physical mechanisms.

The analysis of Section 3.2 indicates that analytical solutions obtained for linear one-dimensional flow can be transformed easily to give solutions for flow in radial systems. The radial solutions are of value because they delineate the relative importance of flow geometry and volume change. Because the solutions are for dispersion-free flow, they also permit direct evaluation of the impact of numerical dispersion in finite difference simulations of similar compositional problems.

An example of the determination effects of numerical dispersion was given in Section 3.3. There, fine-grid finite difference solutions were obtained to check analytical solutions for the theory of interfering shocks in slug injection processes. That theory, when extended to three or more components, will be the basis for rational optimization of slug sizes. In the past, dispersion effects were emphasized in slug sizing. Because it focuses on convective phenomena, which probably dominate in many reservoir flows, the extended theory promises to be a much more realistic tool for slug design.

The interplay of phase equilibrium and crossflow was examined in a series of displacement experiments in sandstone cores. The experiments indicate that surprisingly rapid and high total recovery is obtained through a combination of gravity segregation and capillary imbibition when interfacial tension (IFT) is low in the analog oil/water/alcohol systems used. The results obtained to date suggest that capillary and gravity-driven crossflow may be more important than was thought previously. Furthermore, recovery processes for fractured reservoirs based on low IFT's may be feasible and should be investigated.

4. Viscous Fingering and Reservoir Heterogeneity

The experiments and analyses of Chapters 2 and 3 dealt with the interplay of phase behavior and multiphase flow in a variety of settings. In this chapter we turn to the question of the influence of viscous instability on displacement performance in miscible floods. In this chapter we ignore effects of phase behavior as we examine flows that are not one-dimensional.

In many, if not most, miscible floods, fluid with relatively low viscosity displaces more viscous oil. An inevitable hydrodynamic instability results, as has long been known (Blackwell et al. 1959). The initiation of the instability in homogeneous porous media has been studied extensively via linear stability theory (see Tan and Homsy 1986 for relevant references). In field-scale miscible floods, however, the most important portions of the flow occur long after the initiation period, a time when the assumptions of linear stability theory are no longer valid. For such flows, numerical solutions to the flow equations are required. Examples of the variety of numerical approaches that have been used to examine the problem are given by Christie and Bond (1987), Tan and Homsy (1988), and Araktingi and Orr (1988).

In this chapter we examine two questions:

(1) Do particle-tracking simulations represent accurately the growth of viscous fingers in heterogeneous porous media?

(2) For displacements in real porous media, what dominates the flow pattern: the permeability distribution or the viscous instability?

The simulator used is an extension of that developed by Araktingi (1988). In Section 4.1 we compare simulations with flow visualization experiments performed in glass bead packs in an attempt to answer the first question. In Section 4.2 we use the particle-tracking simulator to examine sensitivity of the growth of fingers to representation of boundary conditions and to examine finger growth in a porous medium for which measured permeability data are available.

4.1 Experimental Investigation of Viscous Fingering in Heterogeneous Porous Media

David C. Brock

Given the complexity of miscible displacements at field scale, some sort of numerical simulation will be required for predictions of process performance. In this section we attempt to verify experimentally the physical representation of viscous instability used in the particle-tracking simulator developed by Araktingi (1988). Details of the formulation of the current version of the simulator are given in Section 4.2. If it can be shown that the simulator represents accurately the relevant physical mechanisms, then the simulator can be used to explore scaling issues. Because numerical simulations are the only technique available for predictions of the performance of large-scale flows, it is especially important that an experimental test of simulator accuracy be performed. This section describes such a test.

4.1.1 Experimental Apparatus and Procedures

To test the simulation representation of the combined effects of viscous instability and permeability heterogeneity, flow visualization experiments were performed in two-dimensional packs of glass beads. Properties of fluids used in displacement experiments are reported in Table 4.1-1. Dimensions of a typical flow model are shown in Fig. 4.1-1. The relatively thin bead pack (thickness 6.4 mm) is contained between glass plates. Inlet and outlet headers distribute fluid in such a way that the flow is nearly linear. In the model shown in Fig. 4.1-1,

Table 4.1-1. Densities and Viscosities of the Fluids Used in the Experiments.

FLUID	density g/cm^3	viscosity cP
Light Mineral Oil	0.836	23.
Medium Mineral Oil	0.854	46.
Fluid F	0.854	0.58
Fluid G	0.836	0.58

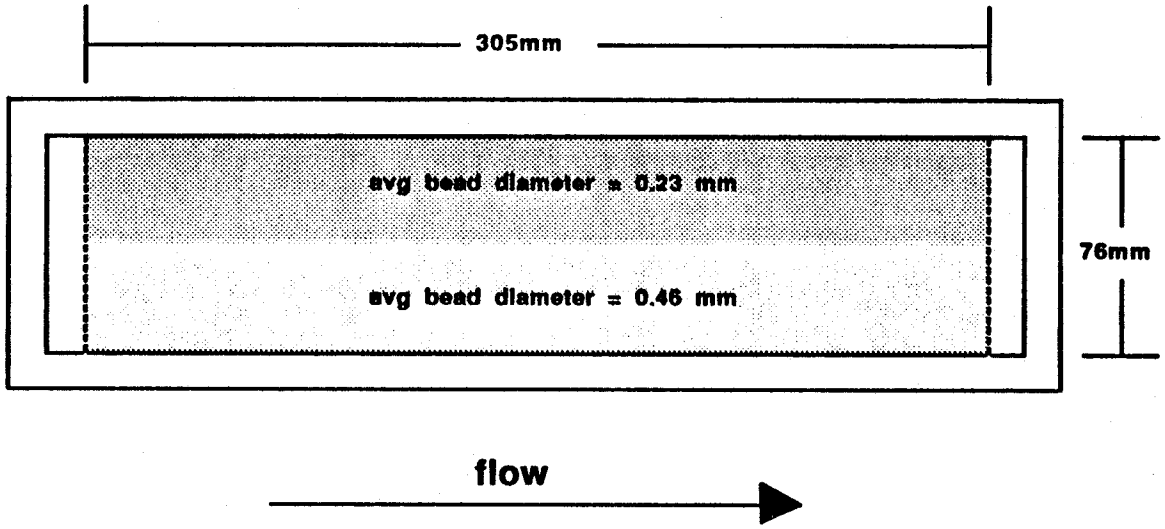

Figure 4.1-1. Dimensions of two-dimensional bead packs.

two layers with different permeabilities were created with beads of two diameters (0.23 and 0.46 mm). Permeability of a sphere pack can be estimated from the Blake-Kozeny equation as

$$k = \frac{d_p^2}{150} \frac{\phi_3}{1-\phi^2} \tag{4.1-1}$$

According to Eq. (4.1-1), the permeabilities of the layers were 46 and 182 Darcies. In the displacements described below, the model was horizontal and fluids used had matched densities. Hence, gravity did not influence displacement performance.

A schematic of the flow system is shown in Fig. 4.1-2. In a typical displacement, oil containing a dye (Automate Red B) was injected into the model containing undyed oil, and the entire displacement was recorded on videotape. Video images were digitized to yield 512 x 480 arrays of integer intensities from 0 to 255. Intensities were calibrated pixel by pixel by performing displacements with mixtures of dyed and undyed fluid of known composition. Hence, video images could be converted to composition maps. From such maps, the location of the contour of 50% concentration of the injected fluid could be located as a function of displacement throughput.

Each flow model was packed (Brock 1990) using a combination of vibration and capillary and physical compaction in an attempt to create layers with uniform permeability. Displacements with fluids with matched viscosity and density indicated, however, that the presence of some local variations in permeability was unavoidable. Fig. 4.1-3 shows results of such a displacement for the model of Fig. 4.1-1, reported as the location of the displacement front at intervals of about 30 seconds. If the layers had been perfectly uniform, then piston-like fronts would have moved through each layer. While on average, fronts in the lower (high permeability) layer, moved about four times faster than those in the low permeability layer, the irregularity of the fronts shown in Fig. 4.1-3 indicates that the local flow velocity varied to some extent within each layer. Because the displaced and injected fluids were identical except for the presence of dye, the flow velocity variations must have been due to local permeability variations.

4.1.2 Estimation of Permeability

If measurements or estimates of the local pressure gradient are available, then successive contour positions of the type shown in Fig. 4.1-3 can be used to estimate local permeability. In the experiments described here, pressures were measured only at the inlet and outlet. Hence, only the average pressure gradient was known, though for the nearly linear flow, that estimate was certainly reasonable. Local flow velocities were determined from the contour data. The spacing between successive contours determines the minimum length scale on which permeability variations can be detected. To reduce the impact of noise in the concentration determination, the contours were smoothed by local averaging of the composition data. For each permeability block, the smoothed concentration was taken to be the average of the measured block concentration with the average of the eight surrounding block concentrations. Evenly spaced points were then selected along each contour, and vectors were drawn from each point along the direction of the pressure gradient. The local frontal velocity was measured from the length of the vector between successive contours and the time difference. The permeability at each vector position is then given by Darcy's law

$$\frac{k}{\phi} = \frac{v_f \mu}{\frac{\partial p}{\partial x}} \tag{4.1-2}$$

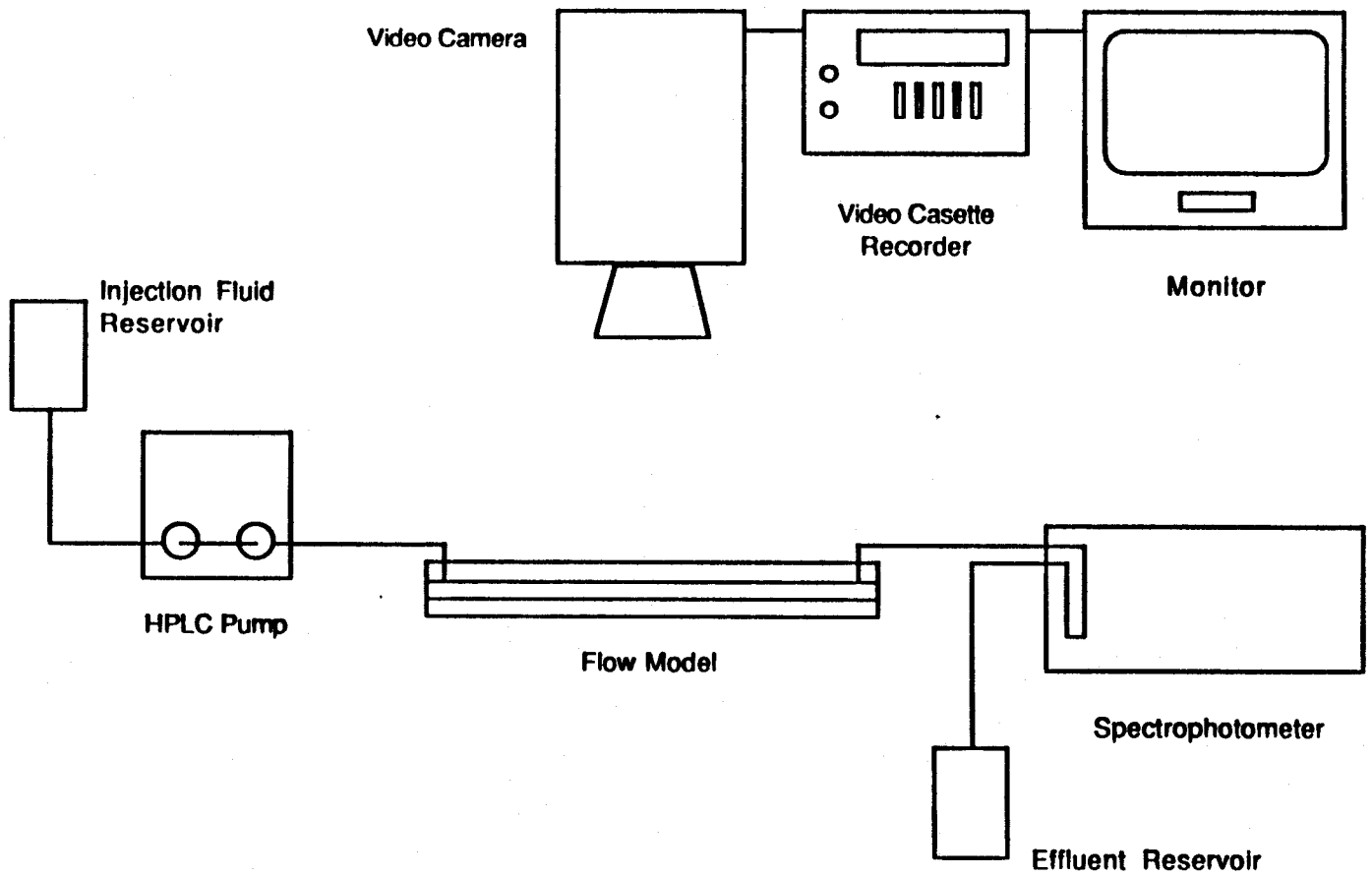

Figure 4.1-2. Schematic of equipment for flow visualization experiments.

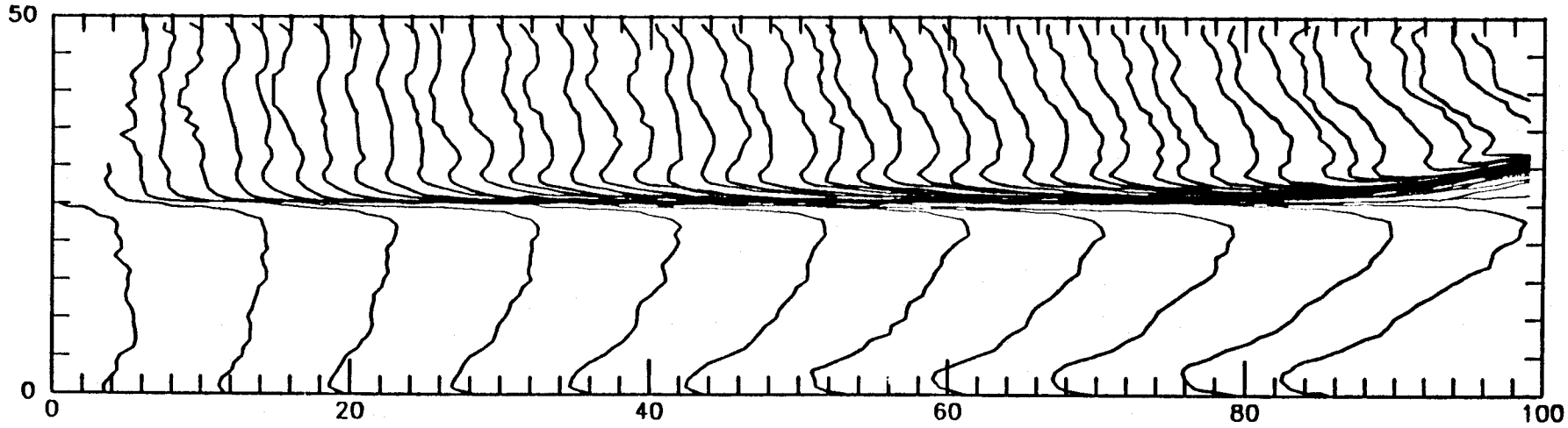

Figure 4.1-3. Measured front positions during displacement of undyed oil by dyed oil with the same viscosity and density.

The porosity was estimated by a material balance on the area between successive contours. For sphere packs, the porosity varies only slightly, so the corrections due to porosity variations were also small. Permeabilities estimated from the contour data in Fig. 4.1-3 are shown in Fig. 4.1-4. As expected from the Blake-Kozeny equation, the measured permeabilities in the fast layer were approximately four times those of the slow layer (note that the positions of the fast and slow layers in Fig. 4.1-3 have been reversed in Fig. 4.1-4). Apparently, there is a ridge of slightly higher permeability close to the boundary between the layers. Otherwise, the permeabilities show relatively small variations that are due, presumably, to local heterogeneities in the packing.

The technique described here allows the use of flow visualization data to improve estimates of local permeability obtained from the Blake-Kozeny equation, but it is not without limitations. For example, the layers used here were parallel to the flow direction, and hence the difference in permeability was immediately obvious in the flow visualizations. If the layers had been arranged transverse to the direction of flow, the flow visualizations would have shown no distortion of the fronts. Either more detailed pressure data or, alternately, flow in the transverse direction would have been required to detect the permeability variations in such a case. If such data were available, then the technique demonstrated here could also be used to interpret flow visualizations obtained by X-ray tomography of core samples, for example.

4.1.3 Viscous Fingering in Heterogeneous Porous Media

Flow visualization experiments were performed in bead packs with four permeability distributions illustrated in Fig. 4.1-5. The first model was homogeneous; the others included heterogeneities created with sections of large and small beads. In each model, displacements were performed at three viscosity ratios (M = 1, M = 40, and M = 80) and at three different flow rates. Properties of fluids used are summarized in Table 4.1-1. Detailed descriptions of all the experimental results are given by Brock (1990). Here we illustrate typical results and compare them with simulations of the experiments.

Homogeneous Model

Results of an unstable displacement at an injection flow rate of $q = 6\,cm^3/min$ and a mobility ratio of M = 40 are shown in Fig. 4.1-6. Early in the displacement, at 0.05 PVI, fingers started to grow (Fig. 4.1-6a). Because injection took place through a slotted baffle, the displacement started with 15 fingers. Already at 0.05 PVI, the 15 fingers were no longer in evidence. Instead, approximately seven fingers had formed. At 0.10 PVI (Fig. 4.1-6b), fingers were still evolving, and one finger at the lower edge had moved ahead of the others, due to the higher permeability there. By 0.20 PVI (Fig. 4.1-6d), only four main fingers remained. Although the total number of fingers was decreasing, fingers were continually being created as well as destroyed. As tips spread, they were seen to split into smaller fingers (Fig. 4.1-6c). Most of the fingers that were formed in this way, however, did not grow, but instead were shielded from growth by larger fingers. At 0.20 PVI (Fig. 4.1-6d), coalescence of fingers left behind isolated unswept zones. By 0.30 PVI, four fingers persisted, with the longest growing in the higher permeability zone along the lower edge of the model.

Results of a simulation of the displacement are shown in Fig. 4.1-7. In that simulation, the dispersion and longitudinal dispersion coefficients were set from the correlations of Pozzi and Blackwell (1963) as $D_t = 0.15 \times 10^3\ cm^2/s$ and $D_l = 3.6 \times 10^3\ cm^2/s$. The finger growth mechanisms identified in the experiment were also seen in the simulations. Of the many fingers that formed initially, only six remained at 0.115 PVI (Fig. 4.1-7c). The fingers in the simulation clearly show spreading at the tips. By 0.25 PVI (Fig. 4.1-7e), there were two main fingers, one in the middle and one along the lower edge, and at 0.30 PVI, most of the other fingers were coalescing into the wakes of the main fingers. In a perfectly homogeneous model,

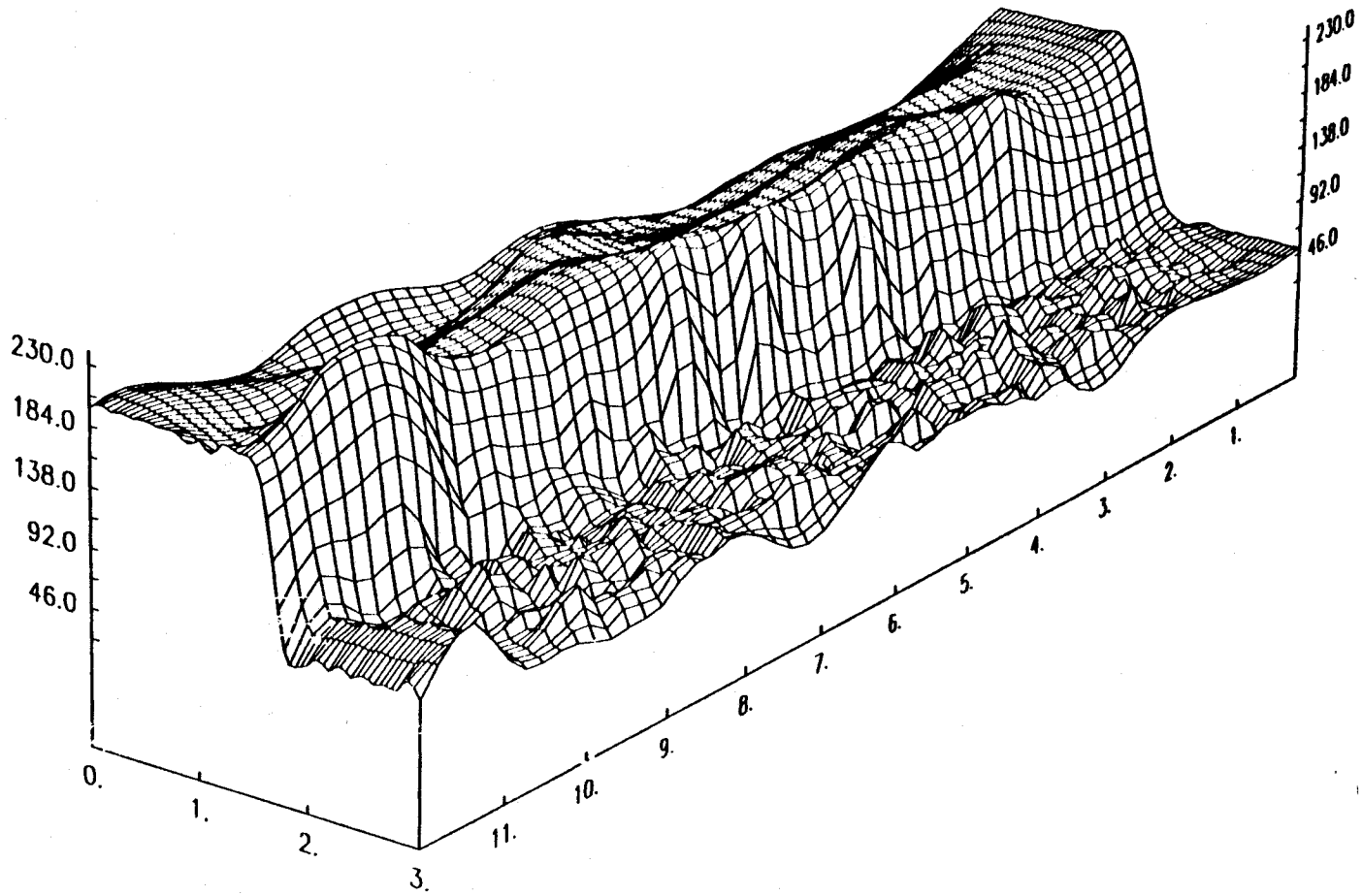

Figure 4.1-4. Permeability distribution estimated from the front position of Fig. 4.1-3 for the two-layer model of Fig. 4.1-1.

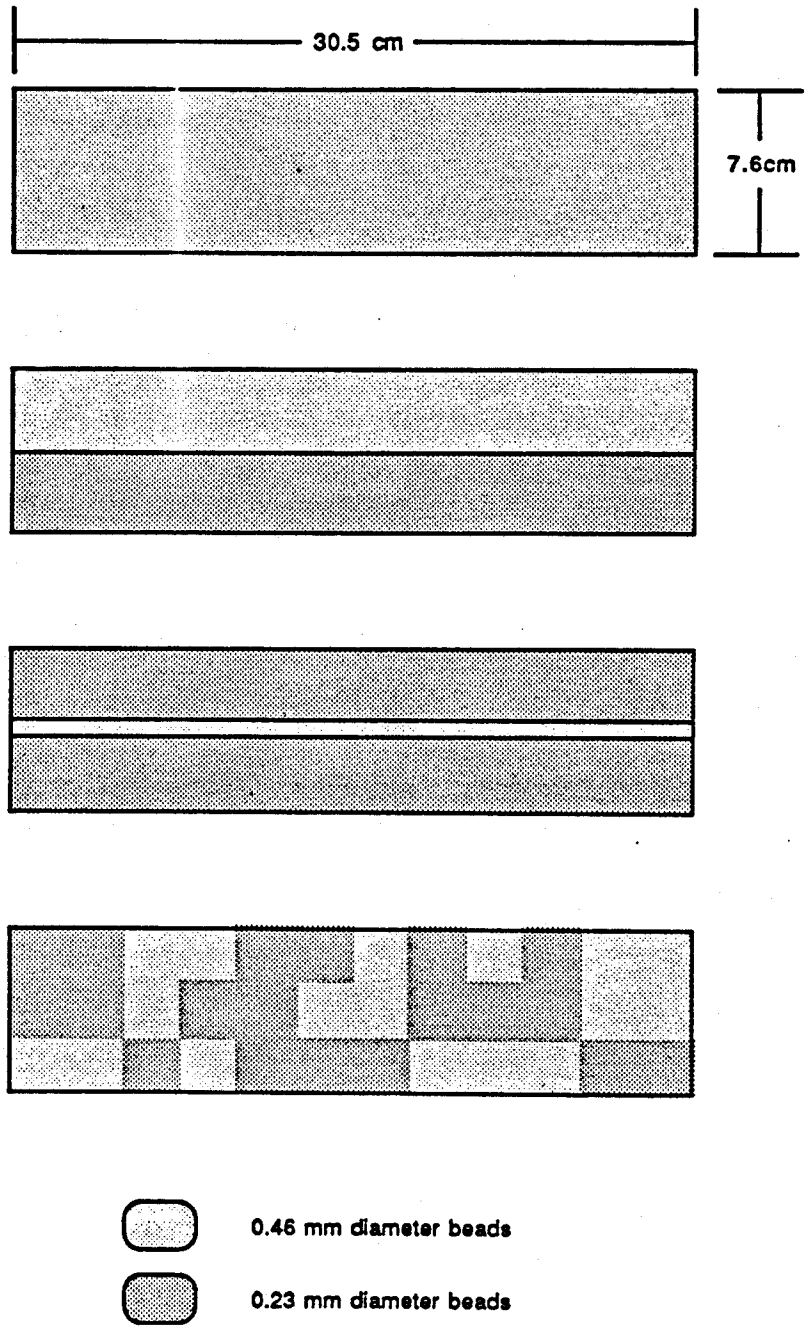

Figure 4.1-5. The four models used in experiments.

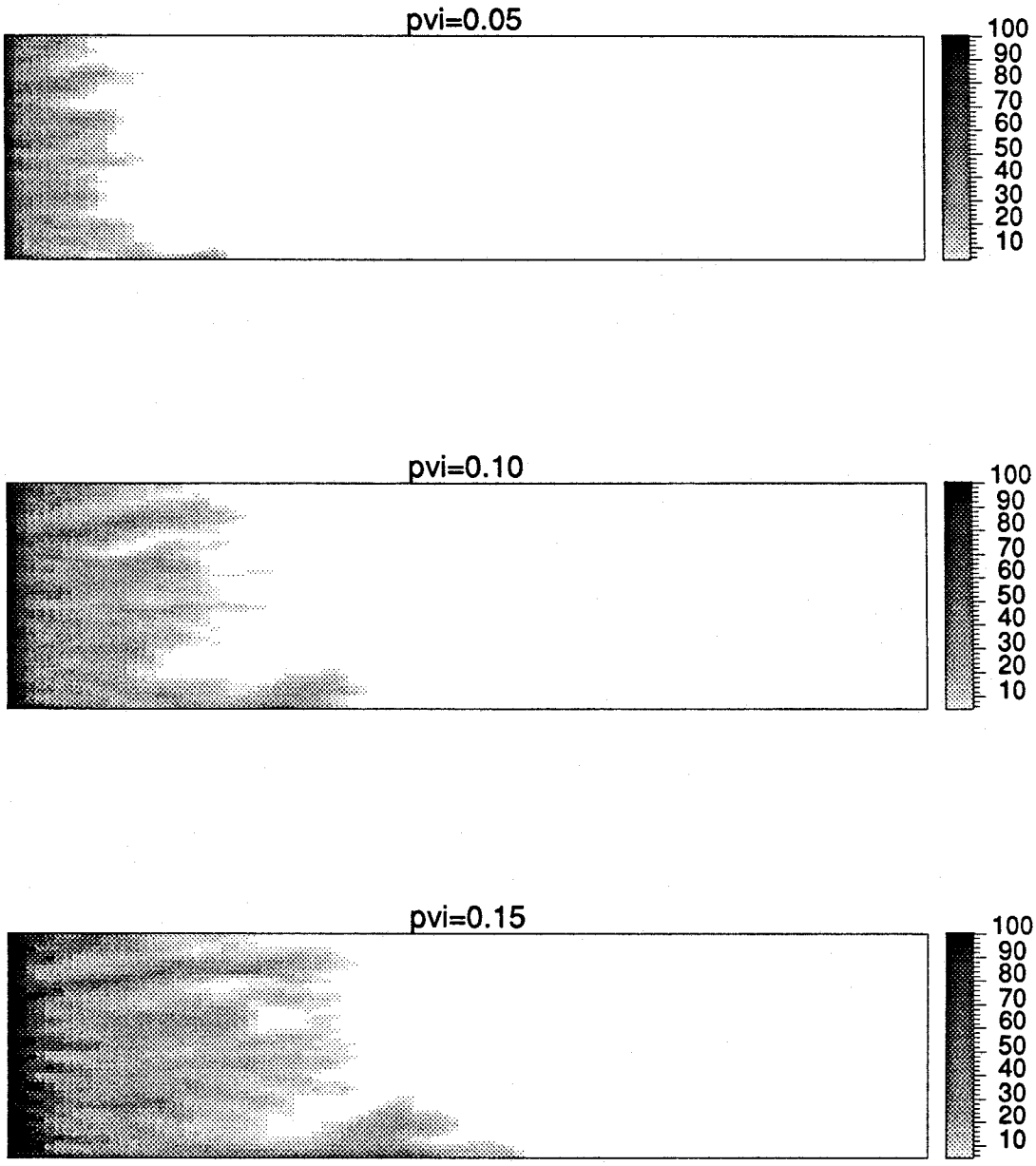

Figure 4.1-6(a-c). Injected fluid concentrations in an experimental displacement at M=40 and q=6 ml/min in the homogeneous model.

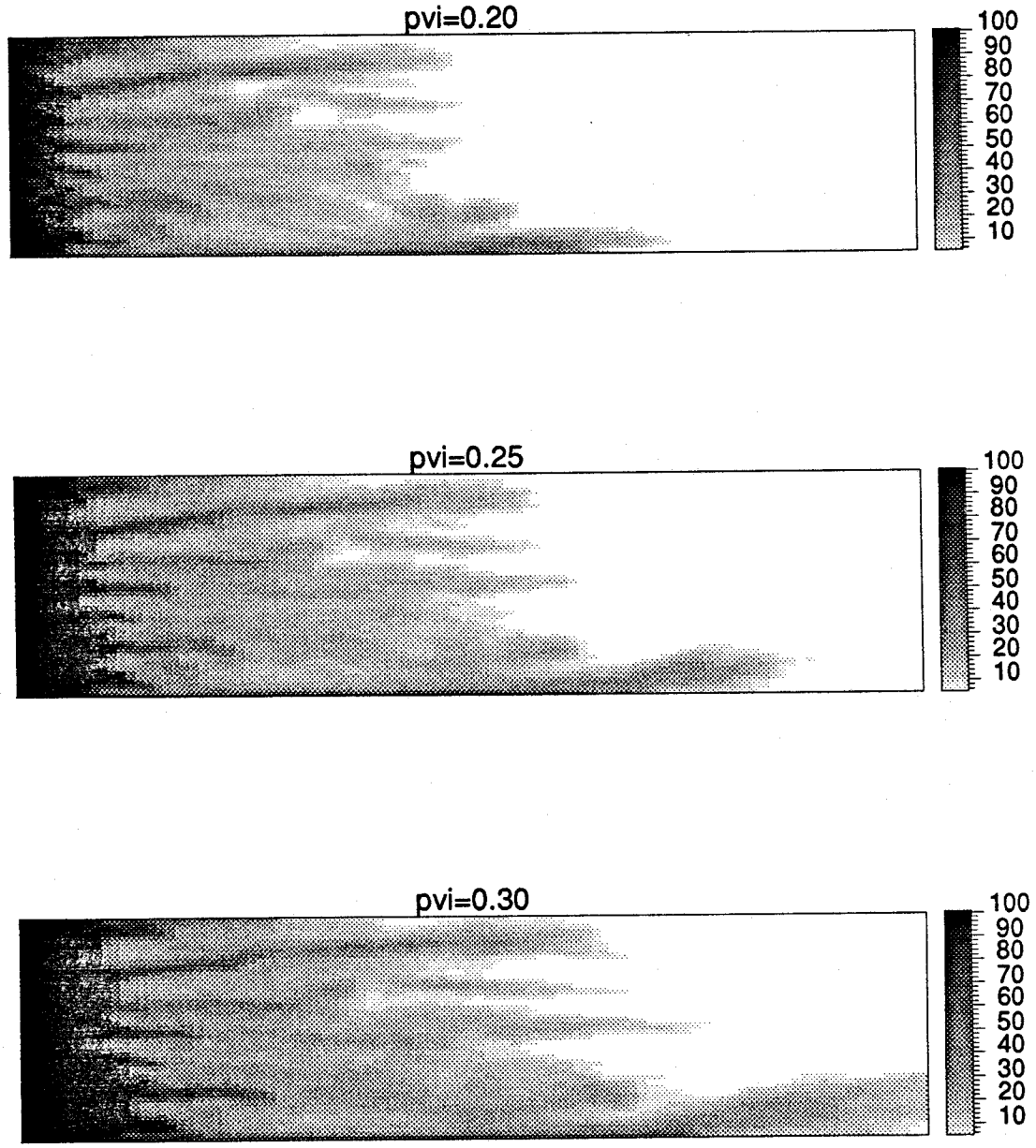

Figure 4.1-6(d-f). Injected fluid concentrations in an experimental displacement at M=40 and q=6 ml/min in the homogeneous model.

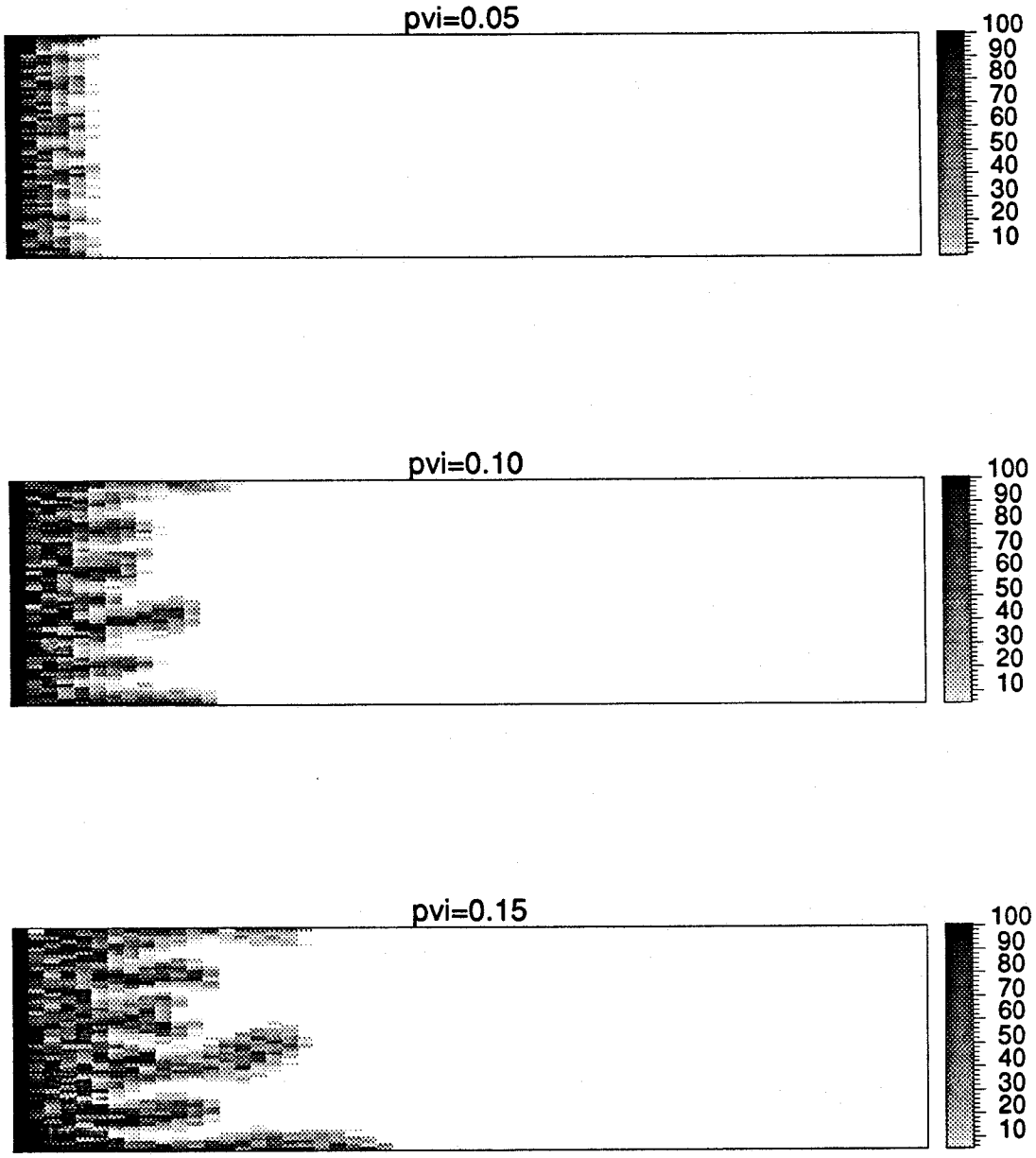

Figure 4.1-7(a-c). Simulated concentration distributions for a displacement at M=40 in the homogeneous model.

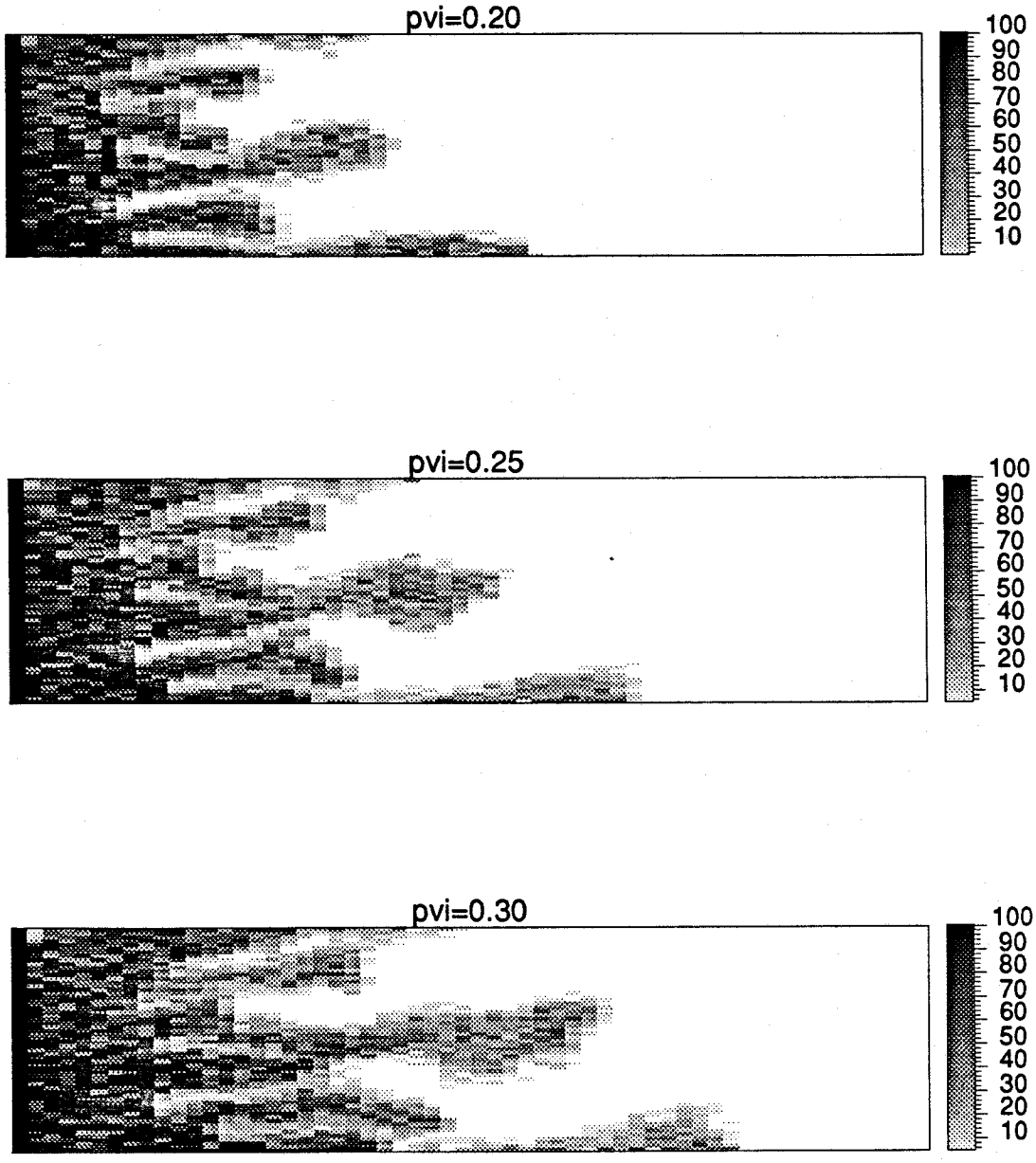

Figure 4.1-7(d-f). Simulated concentration distributions for a displacement at M=40 in the homogeneous model.

one would not expect simulated fingers to match the locations of experimental fingers, because finger locations are determined by random perturbations. Here, there was a slightly higher permeability detected along the lower edge. That higher permeability was responsible for the strong finger growth along the lower edge in experiment and simulation. At 0.20 PVI, the similarity of the appearance of the front in the experiment (Fig. 4.1-6f) and simulation (Fig. 4.1-7f) is striking. Both had a dominant finger along the lower edge, with three or four slower fingers.

Penetration rates—the rates at which the tips of fingers advanced—did not show such good agreement. Fig. 4.1-8 shows a comparison between the experiment and simulation of the base case at 0.30 PVI. In the experimental fingers, a low concentration had penetrated farther than in the simulation. In the experiment, however, much of the finger showed low concentrations of injected fluid. Comparison of the cross-sectional averaged compositions (Fig. 4.1-9) indicates that the largest discrepancy is indeed in the low (<15%) concentrations, while the rest of the concentrations match much better. Comparison of the 20% contours (Fig. 4.1-10), for example, gives satisfactory agreement. Fig. 4.1-11 is a comparison of effluent composition in experiment and simulation. The experiment had breakthrough at 0.28 PVI, and effluent composition rose steadily thereafter. The simulation did not break through until 0.38 PVI. However, its effluent curve rose rapidly until it reached the experimental curve at 0.50 PVI, at an effluent composition of approximately 25%. Thereafter, the curves agreed well. Thus, agreement between the experiments and simulations was poor only at low concentrations. While the difference could imply a shortcoming in the method with which the simulator handles low concentrations, it is more likely that the difference arose from limitations of the experiment. It is probable that in the porous model, a higher permeability existed along the faces where glass beads met flat glass plate. Such a high permeability zone could cause an apparent low concentration to move quickly, while the rest of the solvent in the bulk of the pack moved more slowly at predictable rates determined by the porous media.

Two-Layer Model

Fig. 4.1-12 shows results of the unstable displacement at $M = 40$ and $q = 6\ cm^3/min$ in the two-layer model. As early as 0.05 PVI (Fig. 4.1-12a), two fingers had already formed from the many fingers initially present. By 0.1 PVI (Fig. 4.1-12b), the finger near the interface dominated flow in the fast layer. Spreading and splitting was evident, especially in the slower finger. The slow layer was nearly stagnant, due to the high mobility fluid filling the high permeability layer. Later, at 0.15 PVI (Fig. 4.1-12c), the smaller finger began to coalesce into the wake of the long finger. Much later, at 0.3 PVI, injected fluid contacted most of the fast layer, and growth in the slow layer was virtually stopped. The simulation of that displacement is shown in Fig. 4.1-13. As in the experiment, flow occurred mainly in the fast layer with a single main finger established at 0.05 PVI (Fig. 4.1-13a), with two small fingers also growing. By 0.15 PVI (Fig. 4.1-13c), the main finger grew along the layer interface, with a single smaller finger growing below. The smaller finger coalesced into the main finger at 0.20 PVI (Fig. 4.1-13d). Also as in the experiments, hardly any flow occurred in the slow layer. The correspondence of finger positions in the experiment and simulation is striking, with the main finger near the layer interface and the secondary finger coalescing below, and almost no penetration into the slow layer.

High Permeability Streak Model

Displacements were performed in a model with uniform permeability except for a thin higher permeability streak from inlet to outlet (streak model). The same bead sizes were used as in the two-layer model. Thus, the streak had approximately four times higher permeability than the rest of the model. While the permeability contrast and direction of layering are the

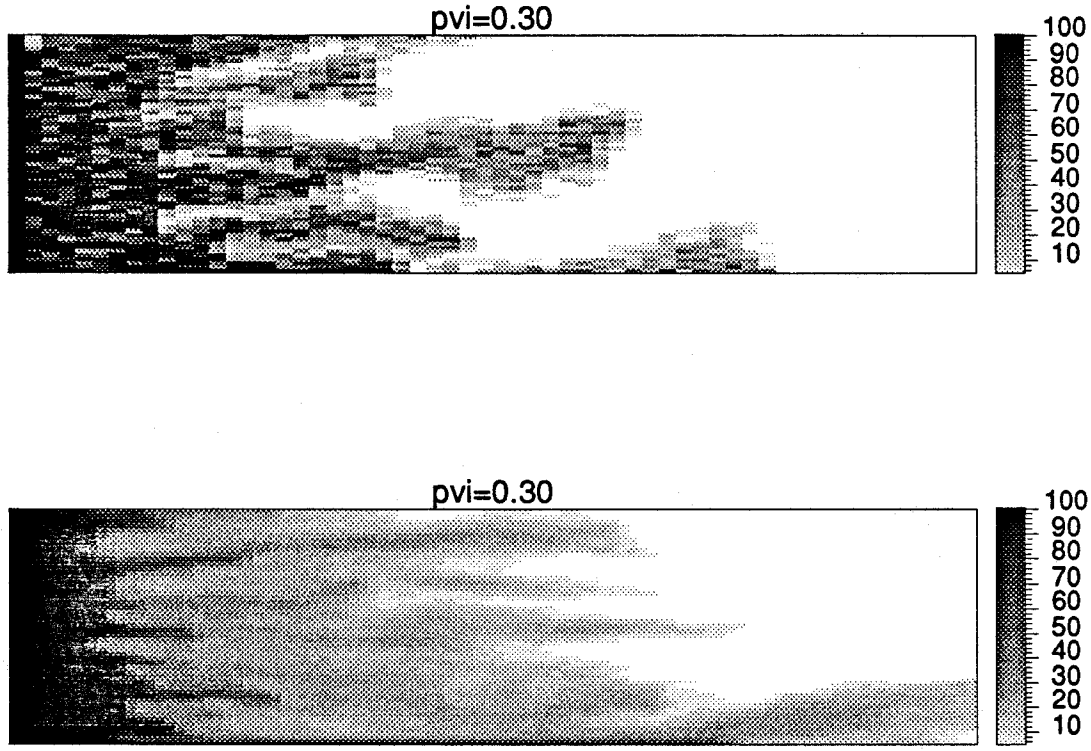

Figure 4.1-8. Comparison of the appearance of fingers in the simulation (a) and experiment (b) for a displacement at M=40 and q=6 ml/min in the homogeneous model.

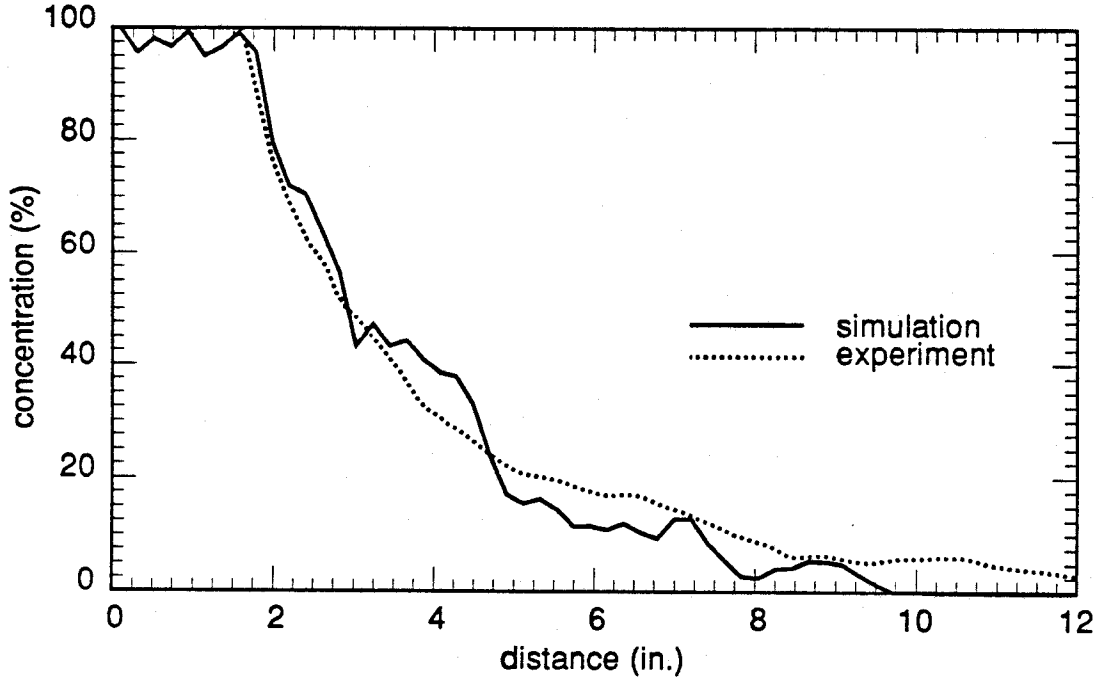

Figure 4.1-9. Comparison of cross-sectional averaged compositions in experiment and simulation of a displacement at M=40 and q=6 ml/min in the homogeneous model.

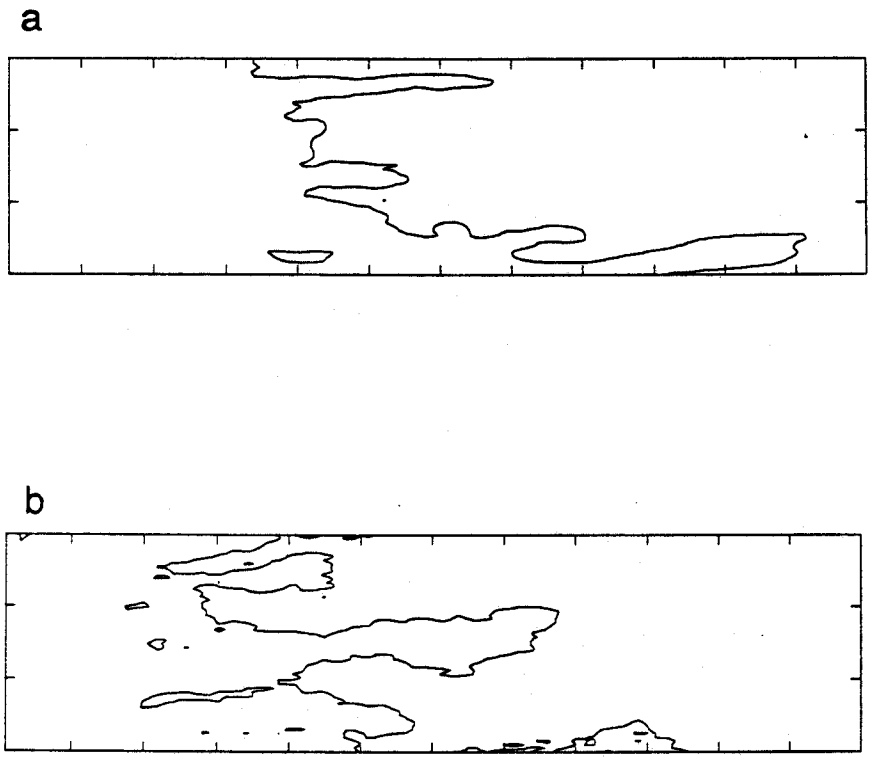

Figure 4.1-10. Comparison of the 0.2 concentration contour in experiment (a) and simulation (b) at M=40 and q=6 ml/min in the homogeneous model.

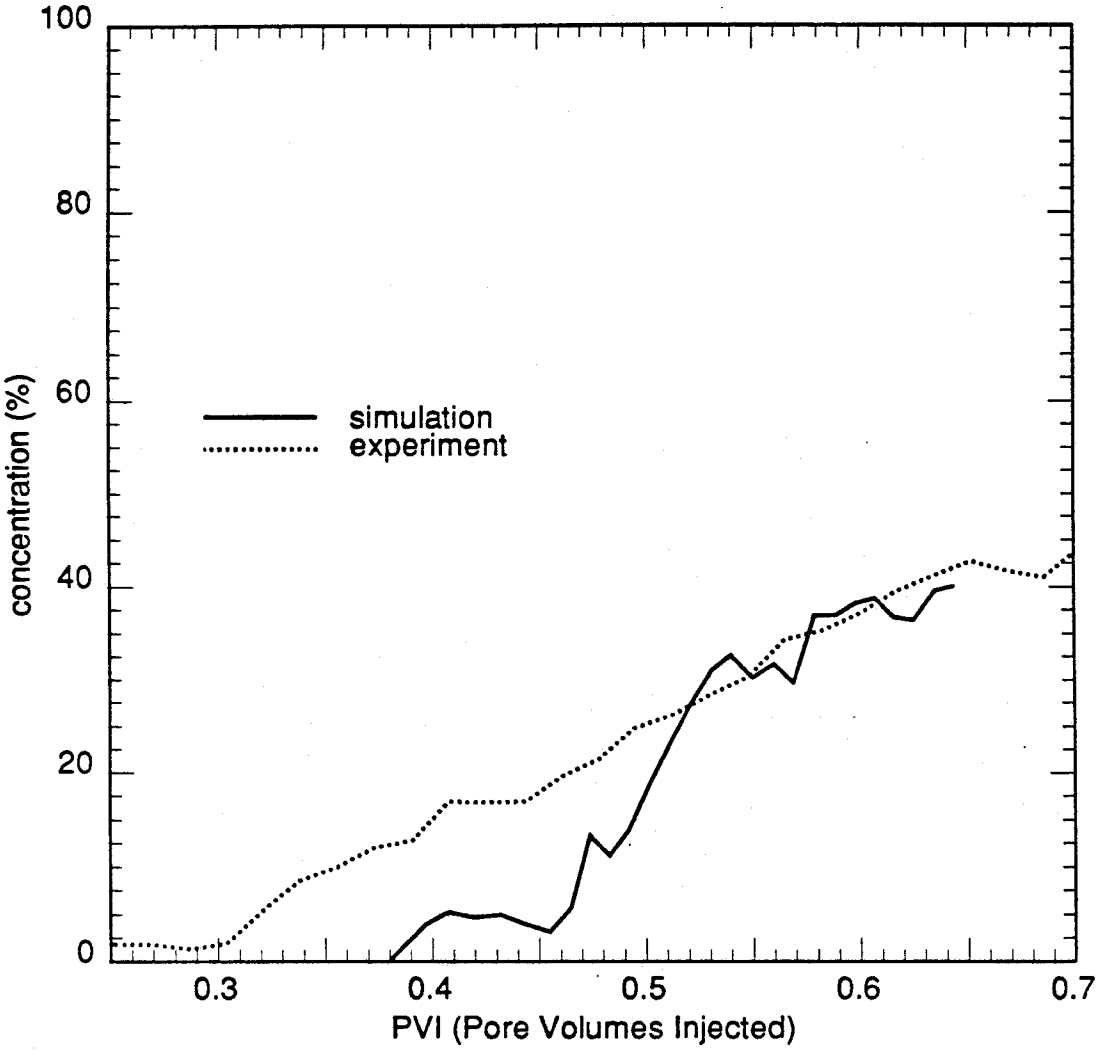

Figure 4.1-11. Comparison of the effluent composition curves in experiment and simulation at M=40 and q=6 ml/min in the homogeneous model.

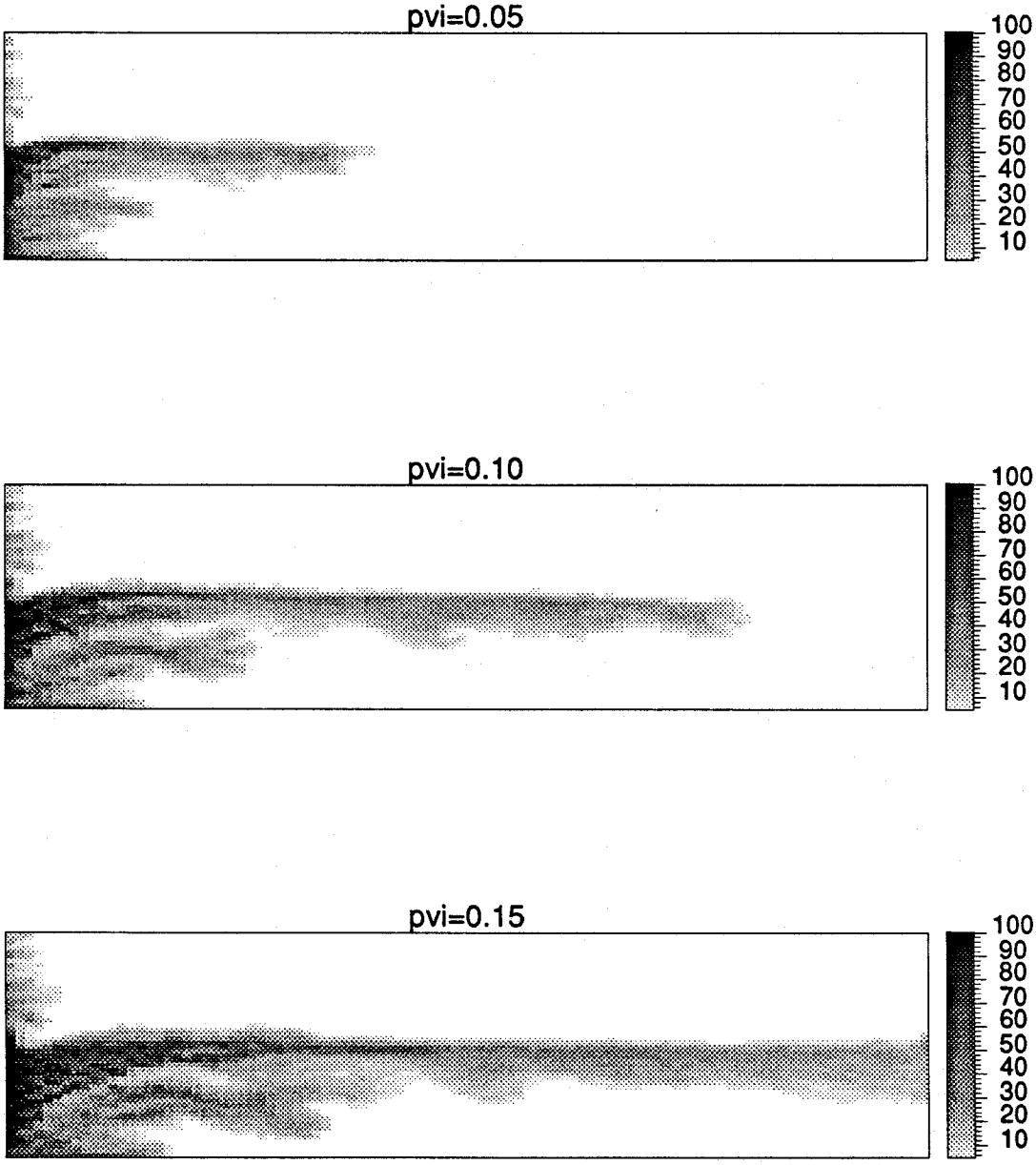

Figure 4.1-12(a-c). Injected fluid concentration in an experimental displacement at M=40 and q=6 ml/min in the two-layer model.

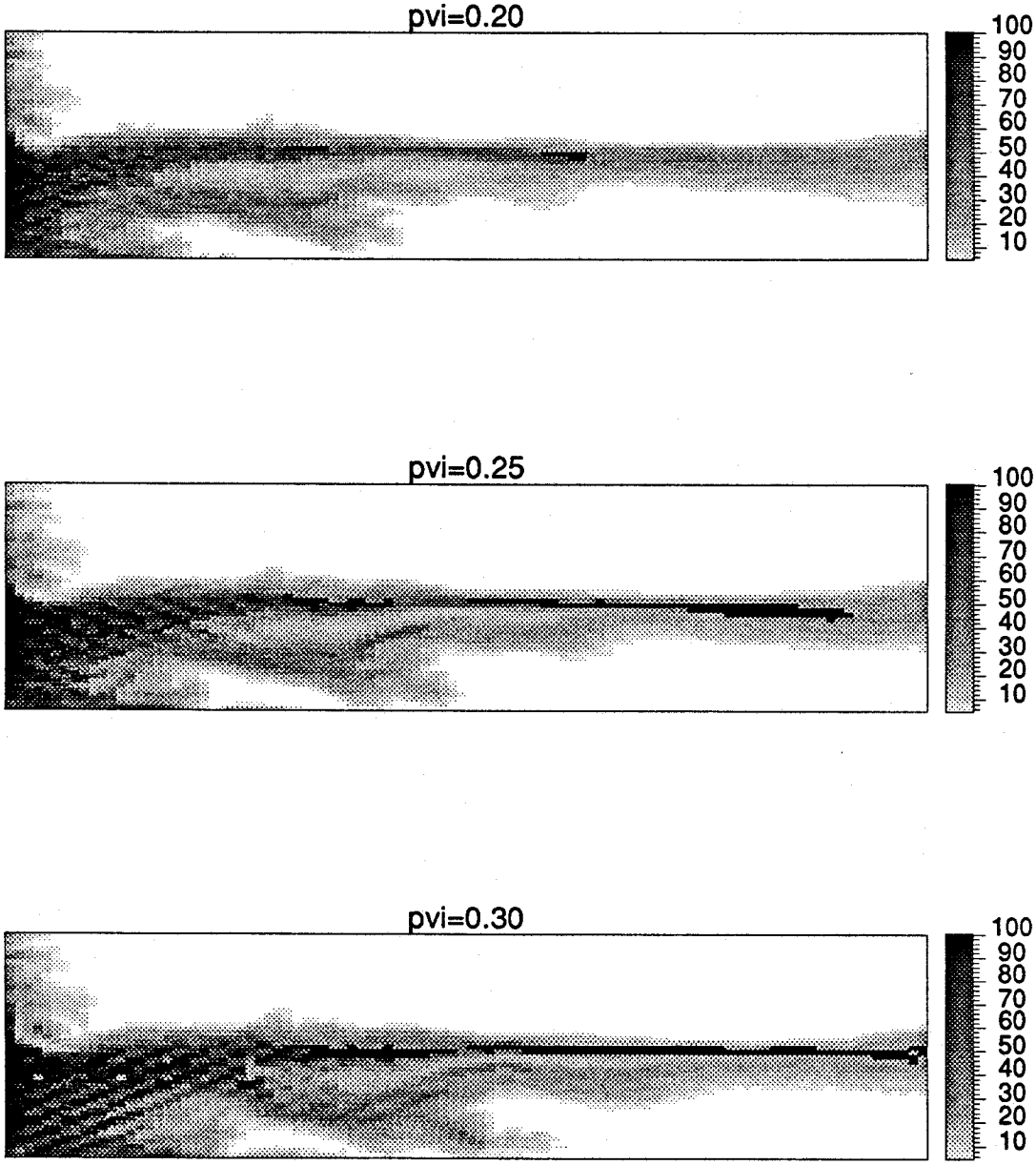

Figure 4.1-12(d-f). Injected fluid concentration in an experimental displacement at M=40 and q=6 ml/min in the two-layer model.

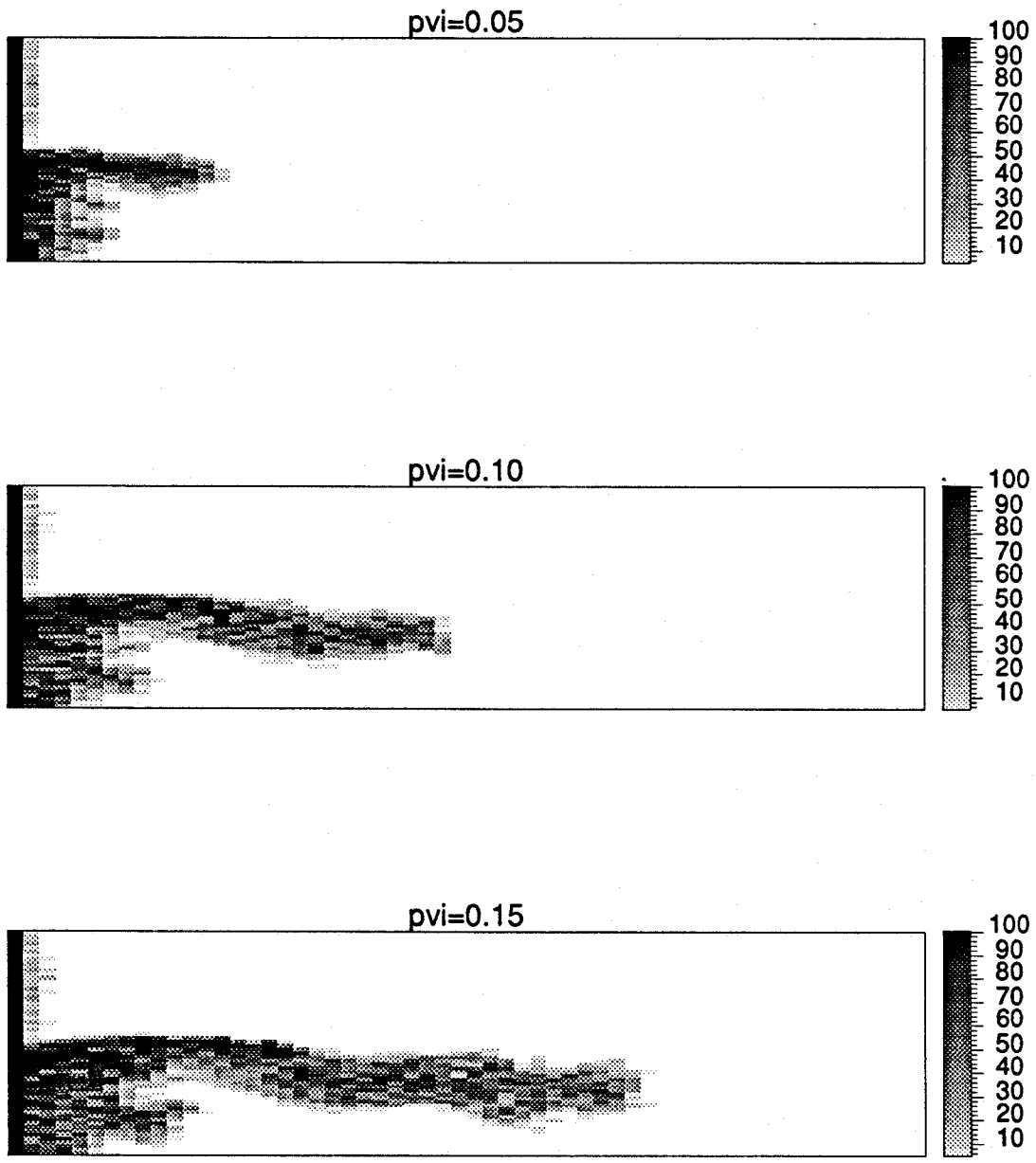

Figure 4.1-13(a-c). Simulated concentration distributions for displacement at M=40 in the two-layer model.

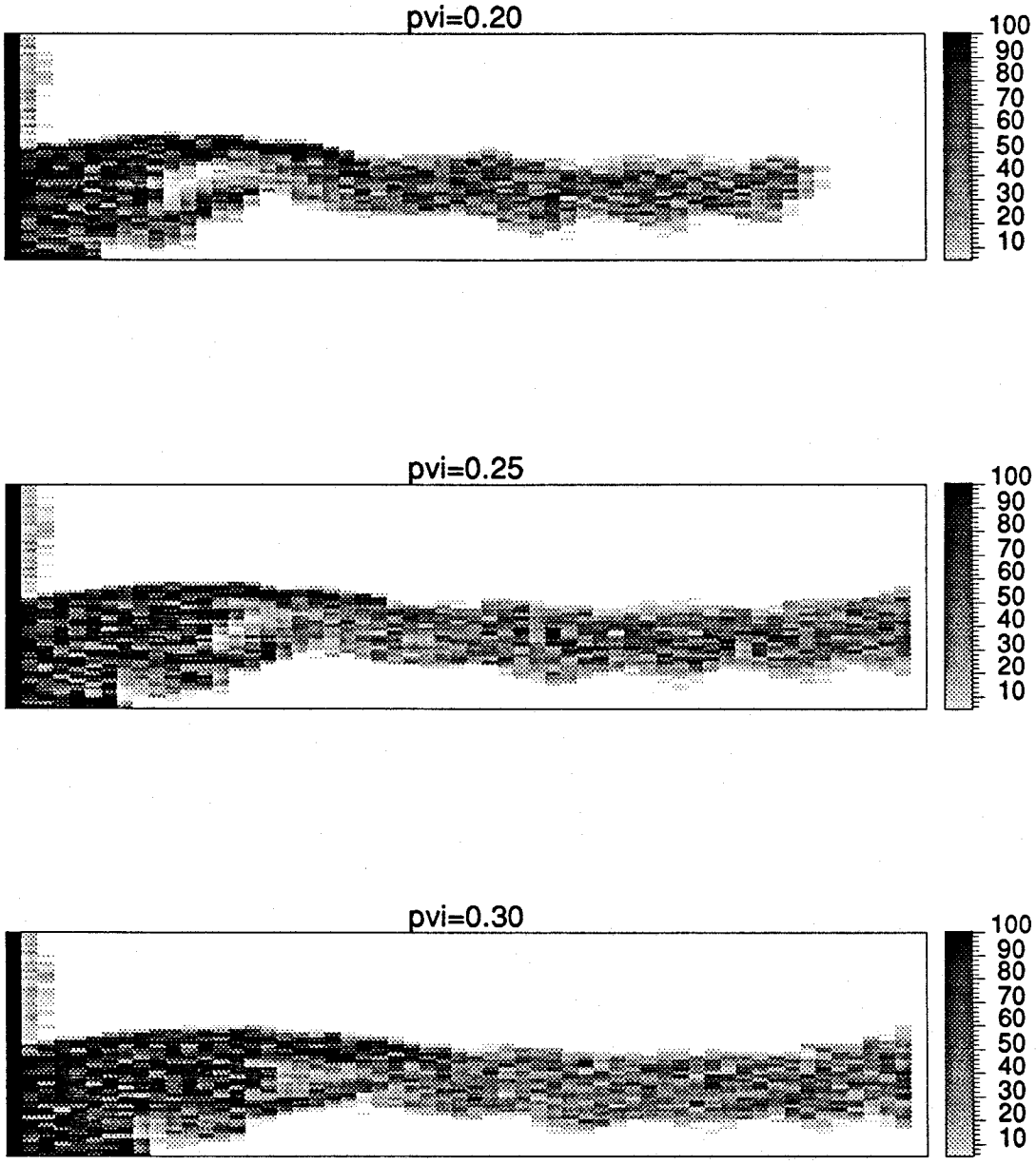

Figure 4.1-13(d-f). Simulated concentration distributions for displacement at M=40 in the two-layer model.

same as in the previous model, the high permeability streak is thin, with width approximately 0.1 of the total width. Fig. 4.1-14 shows results of a displacement at M = 40. Very quickly, at 0.025 PVI, flow began in the streak (Fig. 4.1-14a) as two fingers grew along the layer interfaces, presumably due to crossflow. Not much later in the experiment (0.05 PVI, Fig. 4.1-14b), more of the streak was flooded with the higher mobility fluid, and a single "finger" had spread and coalesced to occupy the entire streak. At 0.10 PVI (Fig. 4.1-14d), injected fluid broke through. Note also that crossflow had carried small amounts of injected fluid into the surrounding slow zone. Much later, at 0.50 PVI (Fig. 4.1-14f) displacement in the slow zones continued to be pulled slowly toward the high-permeability streak by crossflow.

Simulation results are shown in Fig. 4.1-15 for this model. As in previous cases, the permeability field estimated from the matched mobility displacement was used for the simulations. The simulation shown in Fig. 4.1-15 is nearly identical to the experiment. The main finger progressed quickly down the high permeability streak, while little flow occurred in the slow layer. Penetration rates in the simulation (Fig. 4.1-15b,c) were closer to those of the experiments, but the finger was still not as diffuse as the experimental finger. The simulator showed the same small amount of invasion into the slow layers.

Random Checkerboard Model

The previous heterogeneous models had layers extending completely from inlet to outlet, so that permeabilities in the flow direction were highly correlated at a scale of the total model length. To examine the effects of permeability heterogeneities that have shorter correlation lengths, a model consisting of blocks of different-sized beads (checkered model) was built.

First, a permeability field was created. The smallest feasible block sizes were 1-inch squares, leading to 36 blocks, 12 in the flow direction, but 3 in the transverse direction. A permeability field was created by generating a 12-by-3 pattern using the software of Mishra (1987). The program generates a log-normally distributed permeability field, then imposes spatial correlation using the moving circle averaging technique. For use in this system of only two bead sizes, blocks with permeability values higher than the mean were assigned high permeability, and those under the mean were assigned low permeability. The resulting ideal permeability field is shown in Fig. 4.1-5, where the light blocks represent high permeability and the dark blocks represent low permeability.

A matched mobility displacement was run in the model. The gray-scale visualization of the displacement is shown in Fig. 4.1-16. At 0.05 PVI (Fig. 4.1-16a), fast and slow stable fronts had begun in the first blocks. As flow continued, the front curved to follow the high permeability path, first upward at 0.10 PVI (Fig. 4.1-16b) and back downward at 0.15 PVI (Fig. 4.1-16c). Recall that the model was horizontal during the flow experiments, so "upward" and "downward" refer to the composition maps drawn, not the models themselves. At 0.20 PVI (Fig. 4.1-16d), the finger encountered the end of closely connected high permeabilities and began to move across the low permeability gap to meet the closest high permeability zone ahead of it. Note that a stable front continued to grow in the slow entry zone. This frontal profile is an example of a permeability induced instability. The fluids were of matched mobility, using the same fluid except for dye, so there was no tendency for viscous fingering. However, the heterogeneities caused a front which appeared fingered. After crossing the low permeability zone, the fastest finger followed the high permeability path (0.40 PVI, Fig. 4.1-16e; 0.60 PVI, Fig. 4.1-16f). Also at 0.60 PVI, other slow flow that started in the slow entry zone extended into a secondary finger. In contrast to the unstable displacements, the secondary finger did not coalesce because there was no mobility difference to cause viscous crossflow.

Results of the displacement with M = 40 and $q = 6\,cm^3/min$ are reported in Fig. 4.1-17. Initially, the flow was similar to the matched mobility case. It took only until 0.03 PVI (Fig. 4.1-17c), however, for the fast flow to move through the two high permeability entry blocks.

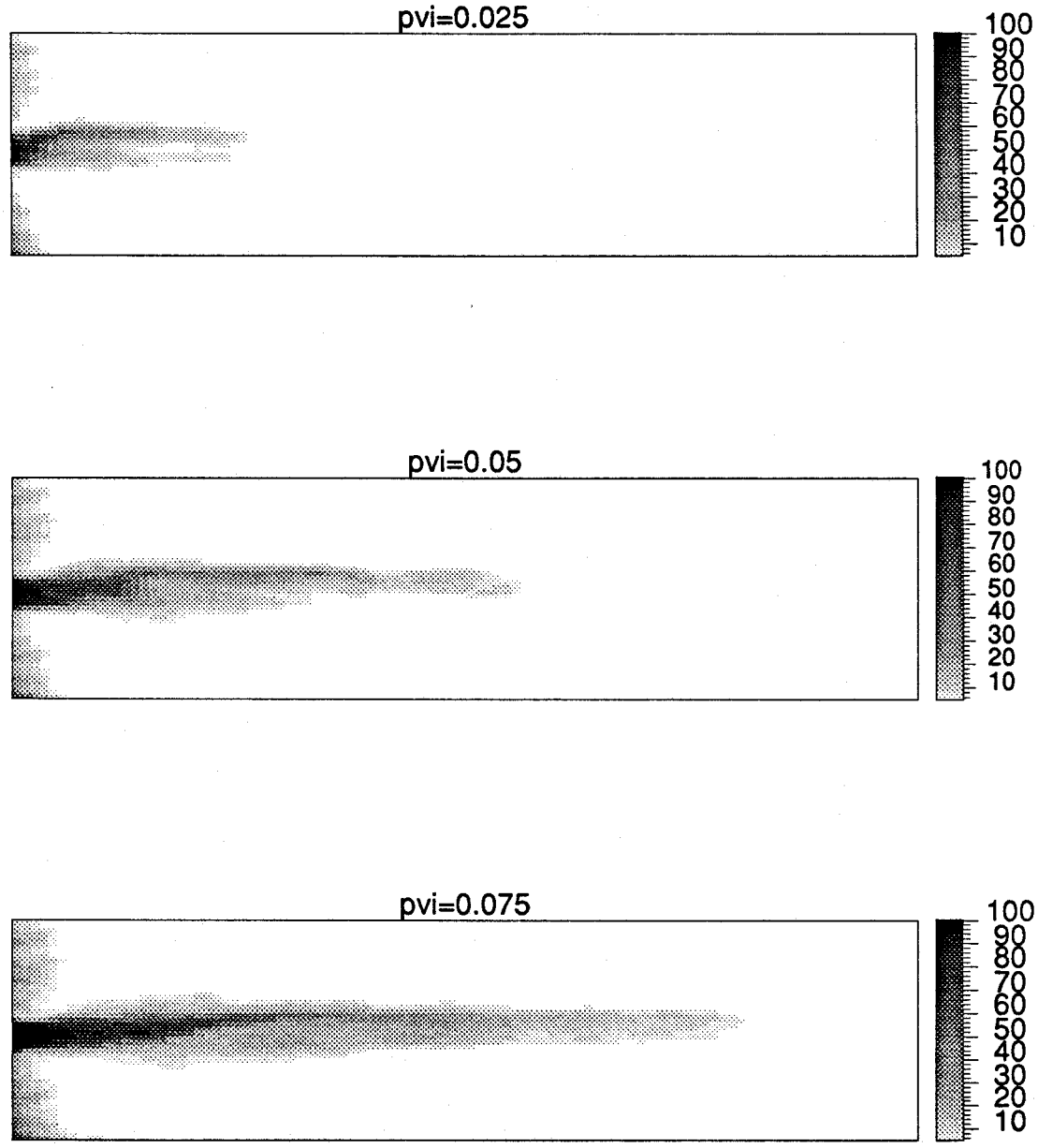

Figure 4.1-14(a-c). Injected fluid concentration in an experimental displacement at M=40 and q=6 ml/min in the streak model.

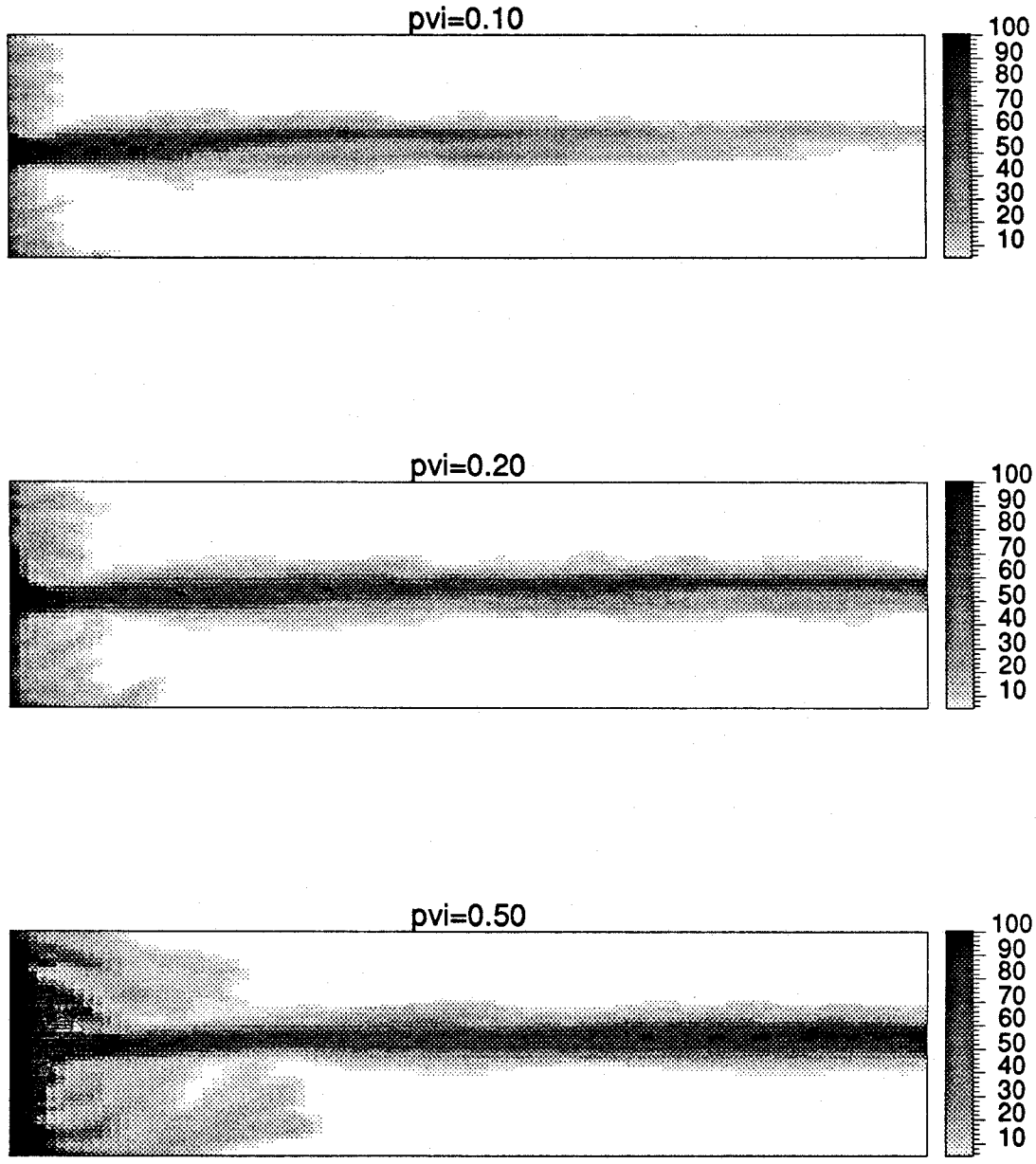

Figure 4.1-14(d-f). Injected fluid concentration in an experimental displacement at M=40 and q=6 ml/min in the streak model.

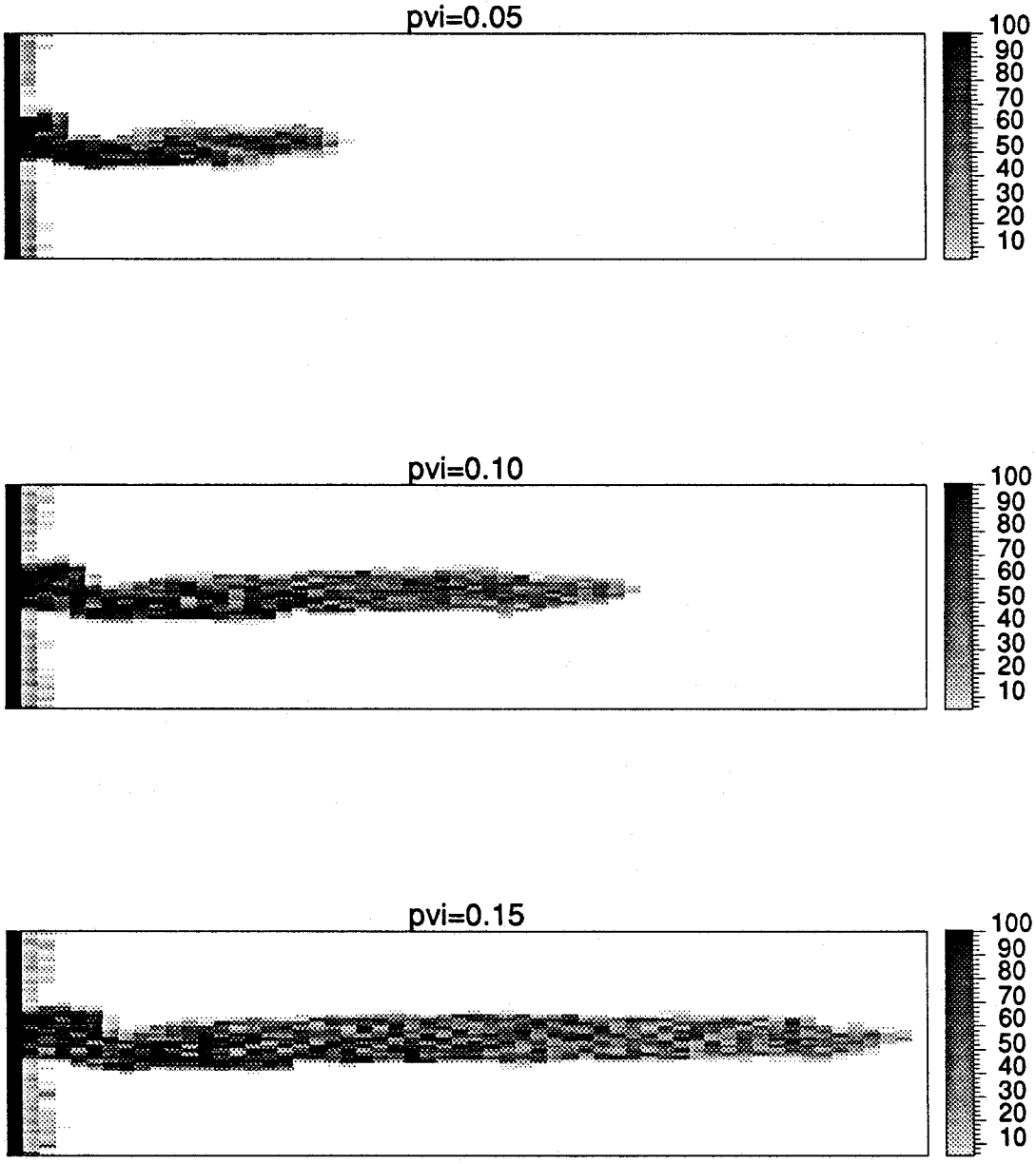

Figure 4.1-15(a-c). Simulated concentration distributions for displacement at M=40 in the streak model.

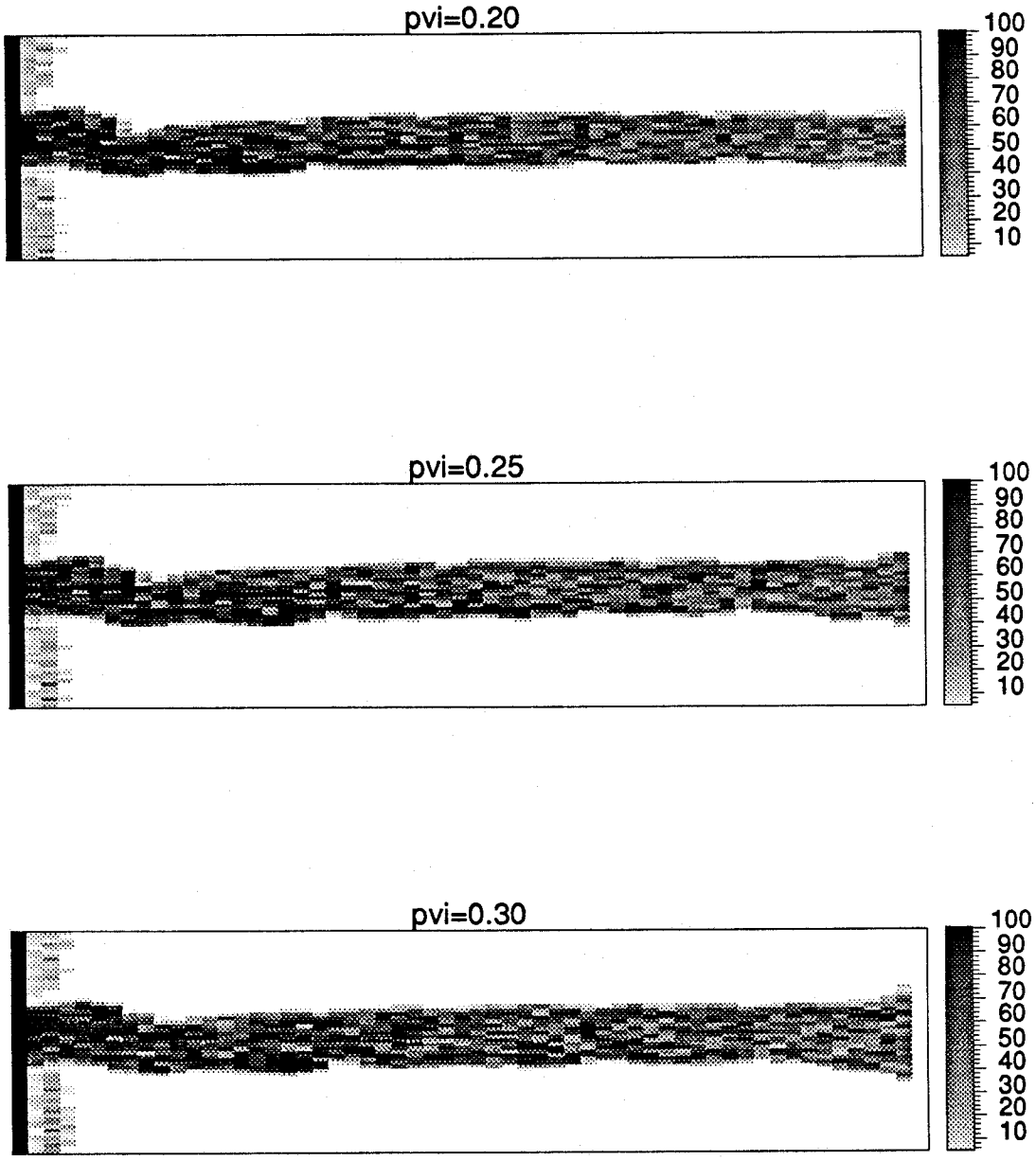

Figure 4.1-15(d-f). Simulated concentration distributions for displacement at M=40 in the streak model.

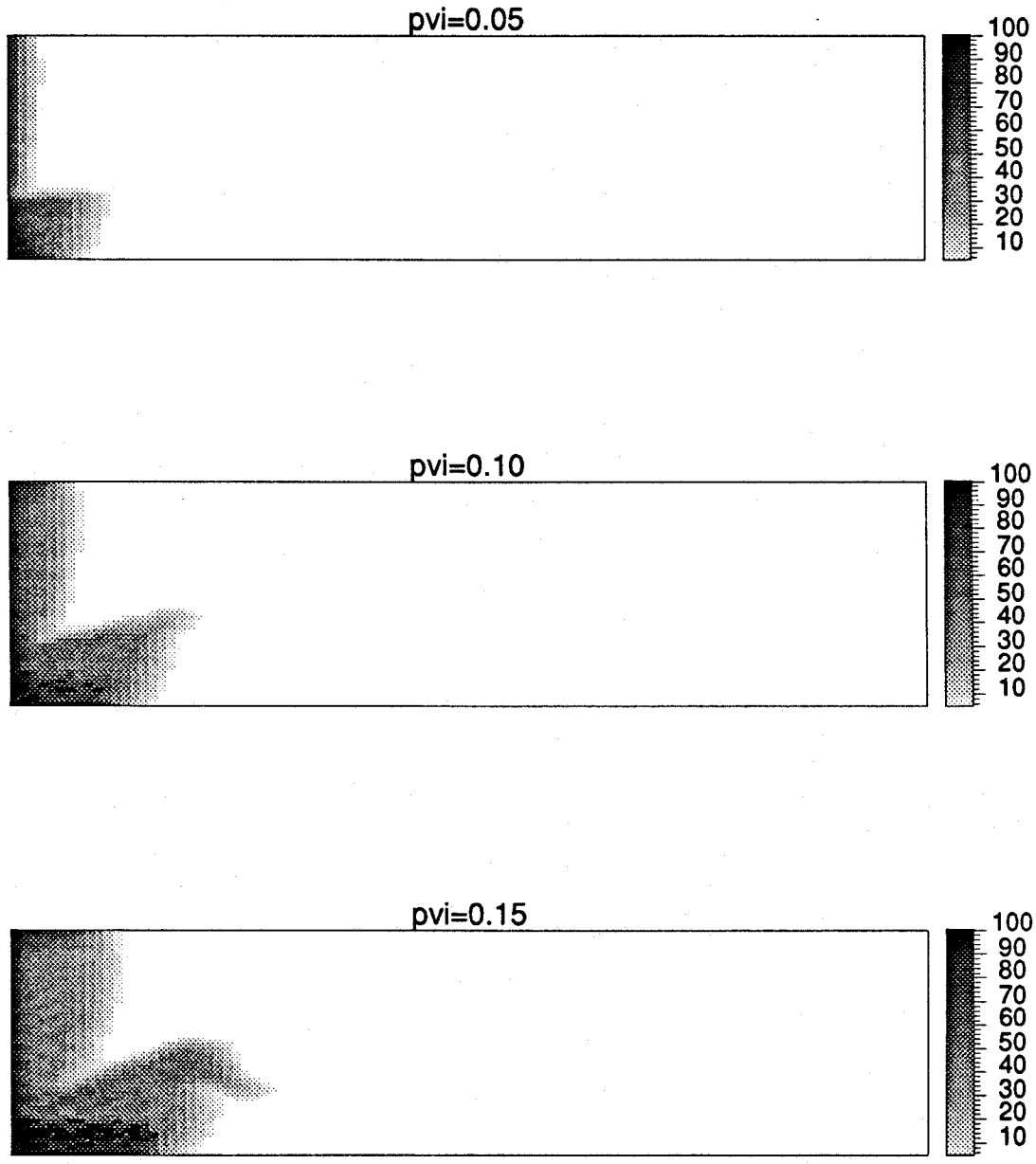

Figure 4.1-16(a-c). Injected fluid concentration in an experimental displacement at M=1 and q=6 ml/min in the checkered model.

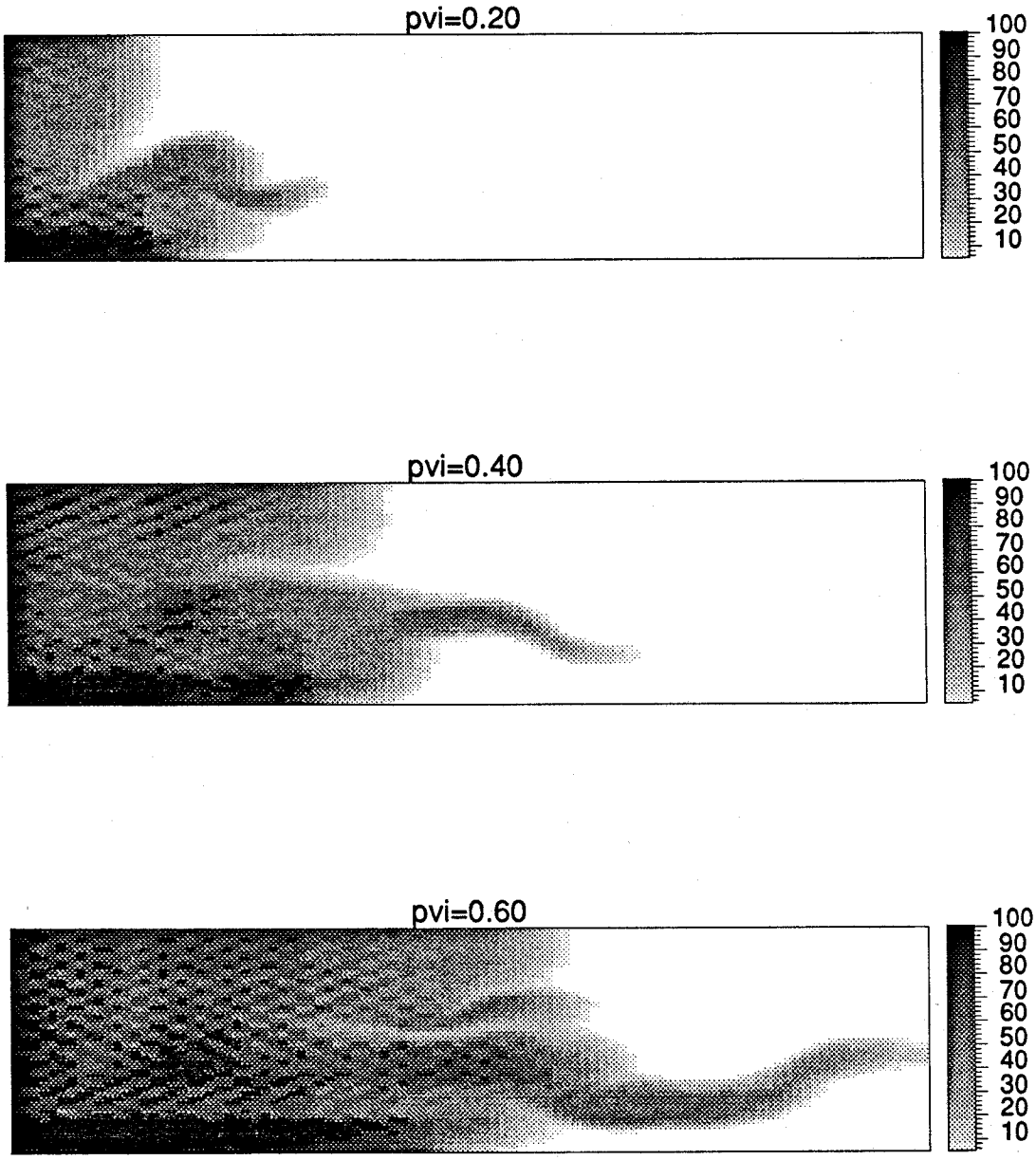

Figure 4.1-16(d-f). Injected fluid concentration in an experimental displacement at M=1 and q=6 ml/min in the checkered model.

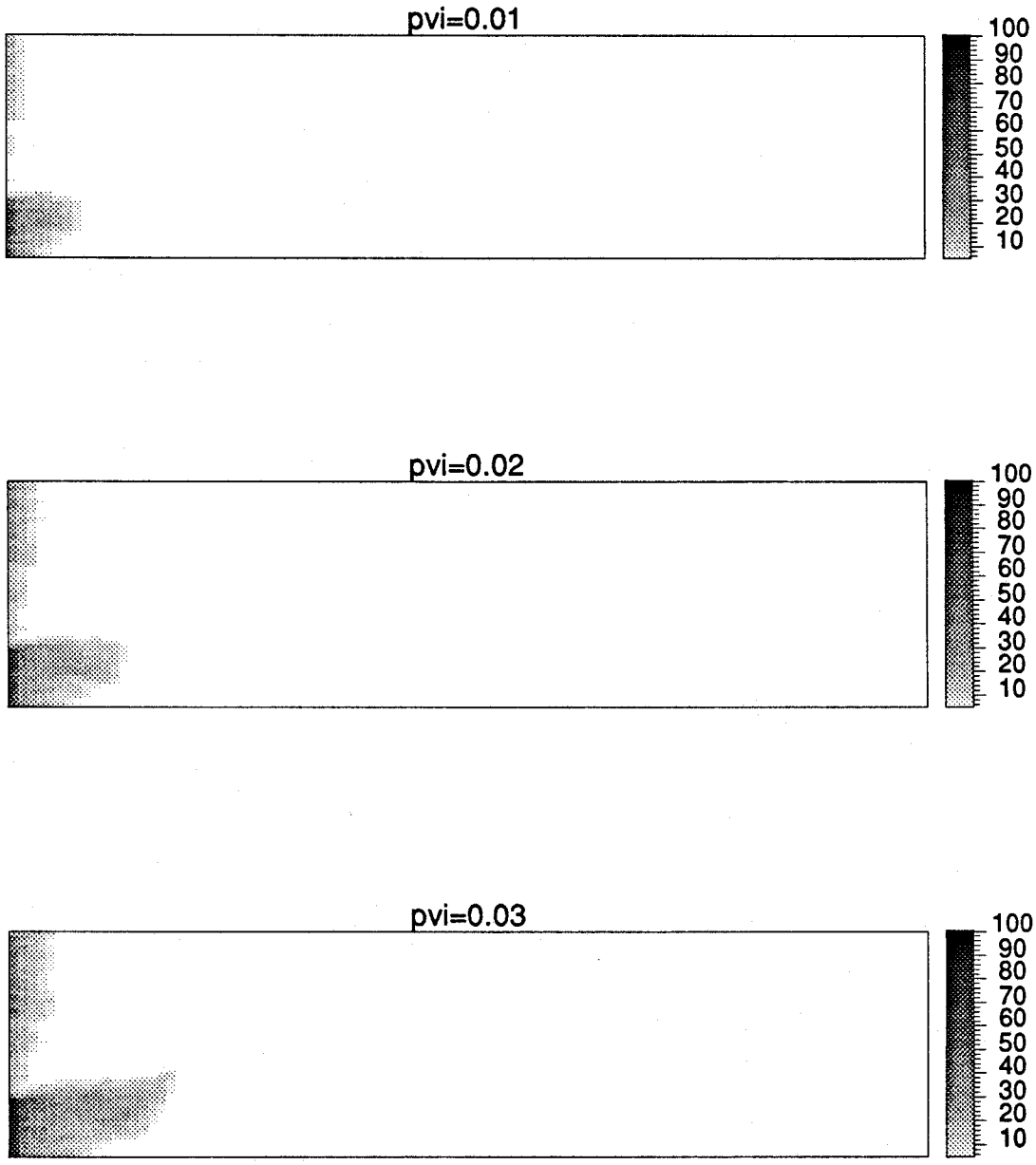

Figure 4.1-17(a-c). Injected fluid concentration in an experimental displacement at M=40 and q=6 ml/min in the checkered model.

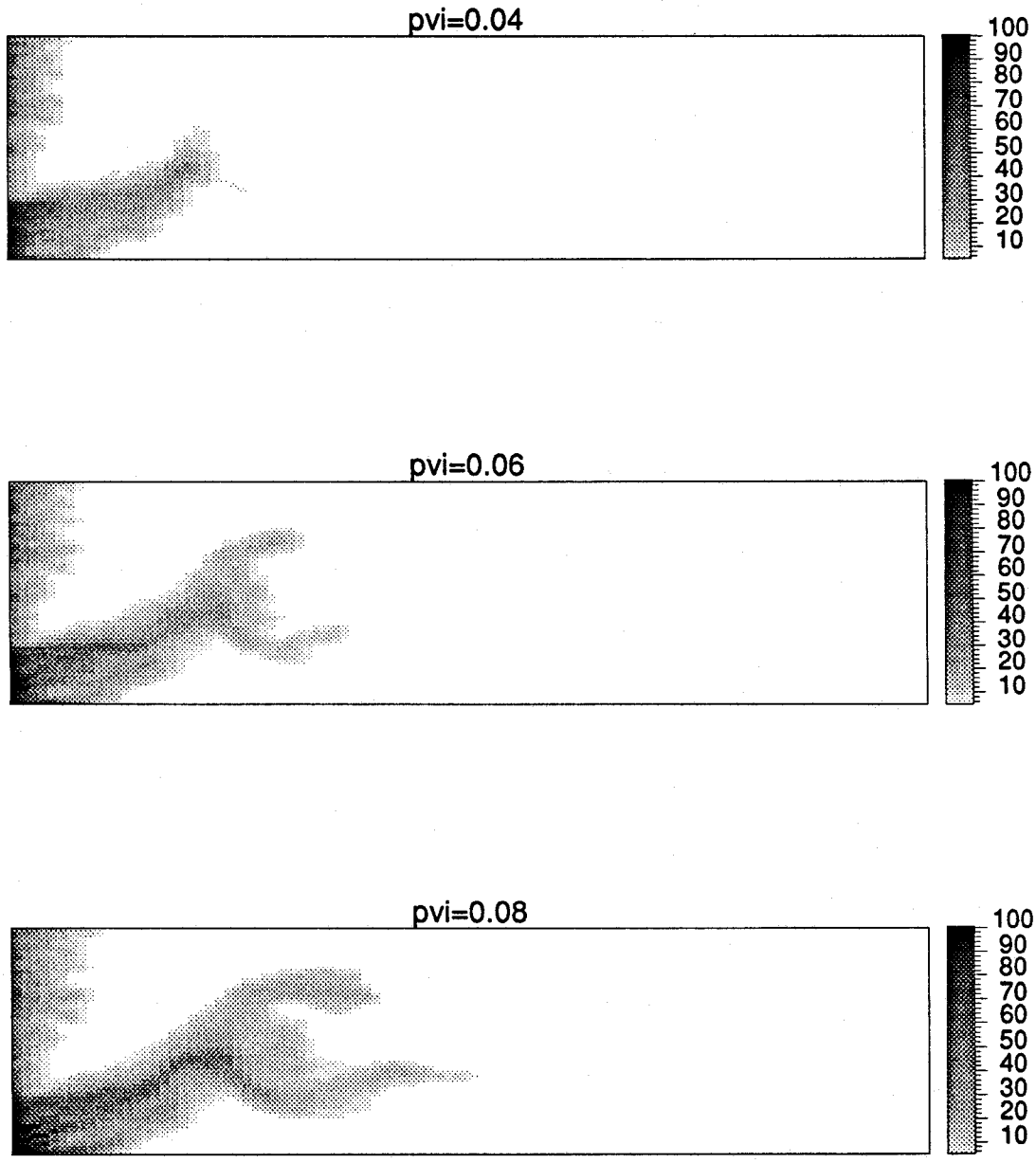

Figure 4.1-17(d-f). Injected fluid concentration in an experimental displacement at M=40 and q=6 ml/min in the checkered model.

Because of the small flow width, no distinct fingers formed. At 0.04 PVI, (Fig. 4.1-17d), the fast finger made the upward turn as did the finger in the stable case. Instead of simply turning back down to the closest high permeability block, as did the finger in the stable case, the tip split, with one finger following the lower path and one following the upper (Fig. 4.1-17e,f). As flow continued, some viscous fingers developed through tip splitting (Fig. 4.1-17g), but the dominant fingers clearly followed the same high permeability paths as did the flow in the stable case. Thus, in this case as well, the location and pattern of fingering was strongly influenced by the permeability distribution, though viscous instabilities also added an overlay of fingers on the flow pattern seen for M = 1.

Fig. 4.1-18 shows results of the numerical simulation of the flow in the random checkerboard model. In the simulation, the displacement front moved quickly in the fast inlet blocks (Fig. 4.1-18a). At 0.10 PVI (Fig. 4.1-18b), the finger followed the same path as the dominant finger in the experiments, but without the tip split seen there. As flow progressed, at 0.15 PVI (Fig. 4.1-18c) the main finger continued to follow the high permeability path, and some splitting was seen. By 0.25 PVI (Fig. 4.1-18e), despite the fact that the early tip split did not occur, the fingers look very similar to those in the experiment (Fig. 4.1-17h). Again, the experiment had diffuse fingers, while the simulator gave fingers with higher solvent concentrations. Thus, in this case as well, the simulations showed reasonable agreement with experimental observations.

4.1.4 Discussion

The three heterogeneous models were designed to examine the effects of three types of heterogeneity. Since all were created with only two sizes of beads, the permeability contrasts were the same in all models. Differences were in overall variance of the permeability field and geometry of heterogeneities. The two-layer and checkered models had roughly equal areas of high and low permeability, while the streak model had only a small amount of high permeability and therefore a smaller variance of permeabilities. Both the two-layer and streak models had permeability correlation lengths equal to the flow length. The checkered model had roughly a 3.8-cm correlation length, 1/8 of the flow length.

In the layer and streak models, the flow was virtually all in the high permeability layer. In the two-layer model, the layer was wide enough that viscous fingers could form. In the streak model, there was no room in the narrow high permeability layer for splitting to occur. Flow in both did not deviate greatly from the overall flow direction. In the checkered model, finger paths curved so fingers could follow high permeability paths. The permeability field in each case affected the fingering patterns. Specifically, the appearance of the displacements was dictated not only by the permeability contrast but by the way in which the high permeabilities were connected. Both the two-layer and checkered models were characterized by flow determined by the permeability field, with viscous fingering superimposed. Thus, these models should be categorized as in the transition between viscous-dominated and heterogeneity-dominated regimes. The flow in the streak model did not display viscous fingering within the high permeability streak, because the width of the streak was not large enough for viscous fingering to develop. In that case, the flow was dominated by the permeability distribution.

While the model displacements described here were not completely scaled to represent reservoir scale flows, some of the observations made above may have important ramifications for field-scale displacements. The experiments and simulations showed that a fairly mild, four-to-one permeability contrast was enough to have a significant impact on the form and location of fingers. Both the experiments and simulations indicate that, in addition to permeability contrast, the geometry and connectivity of high- and low-permeability zones will strongly influence unstable flow. Thus, an important question is: To what extent does permeability variation dominate unstable flow patterns in field-scale displacements? The answer to that question has important implications for simulation of large-scale flows. If a reservoir is like

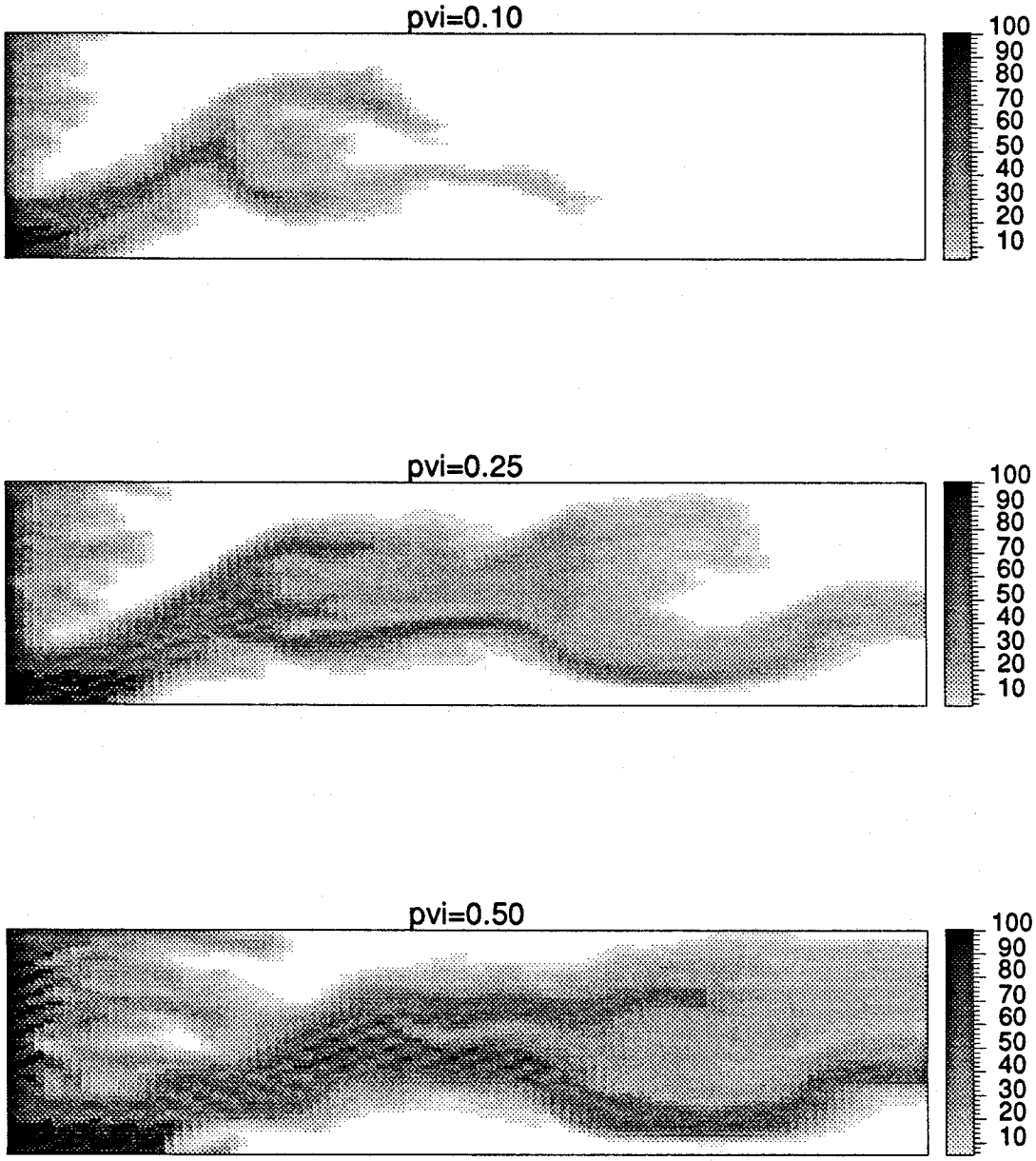

Figure 4.1-17(g-i). Injected fluid concentration in an experimental displacement at M=40 and q=6 ml/min in the checkered model.

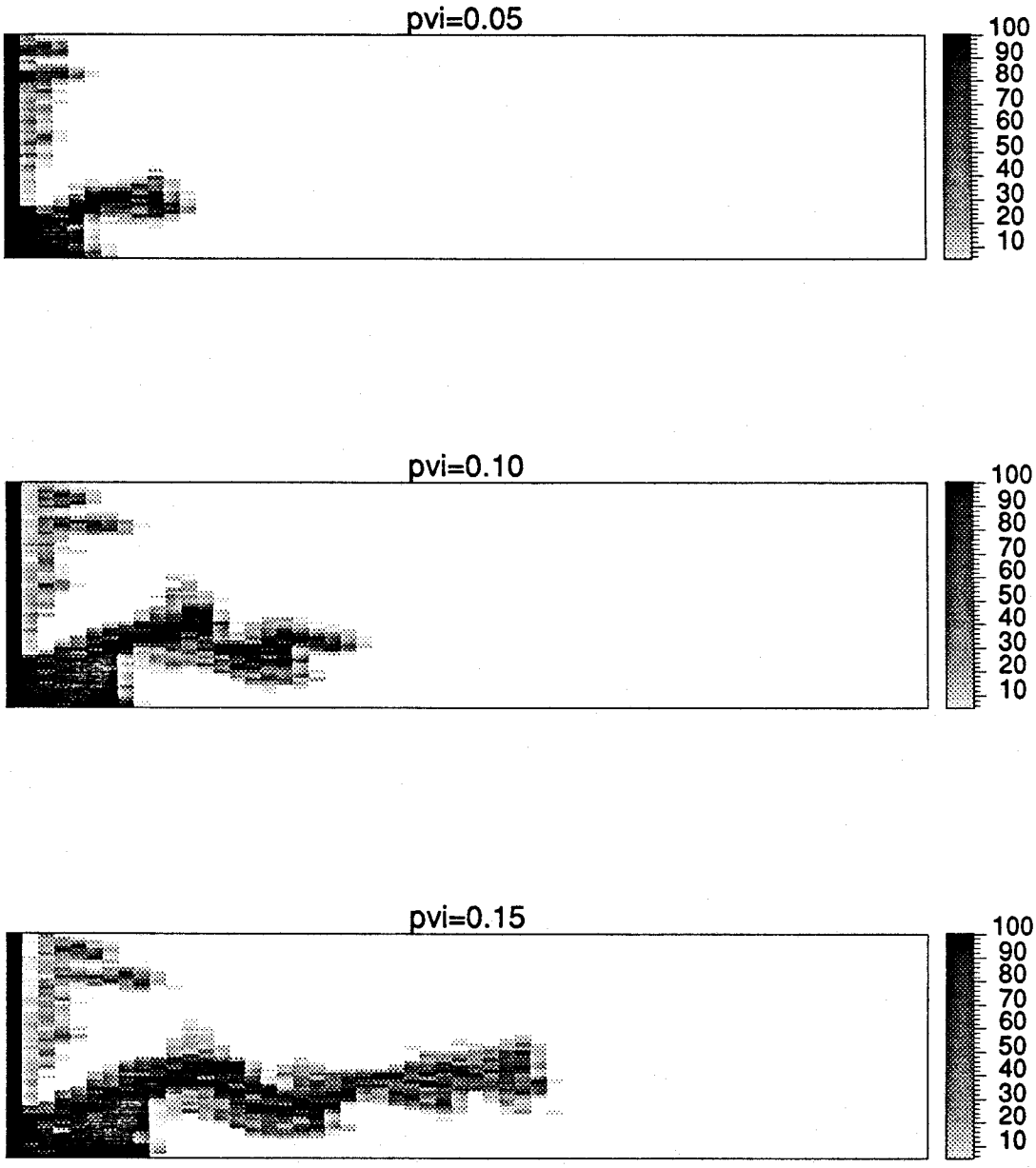

Figure 4.1-18(a-c). Simulated concentration distributions for displacement at M=40 in the checkered model.

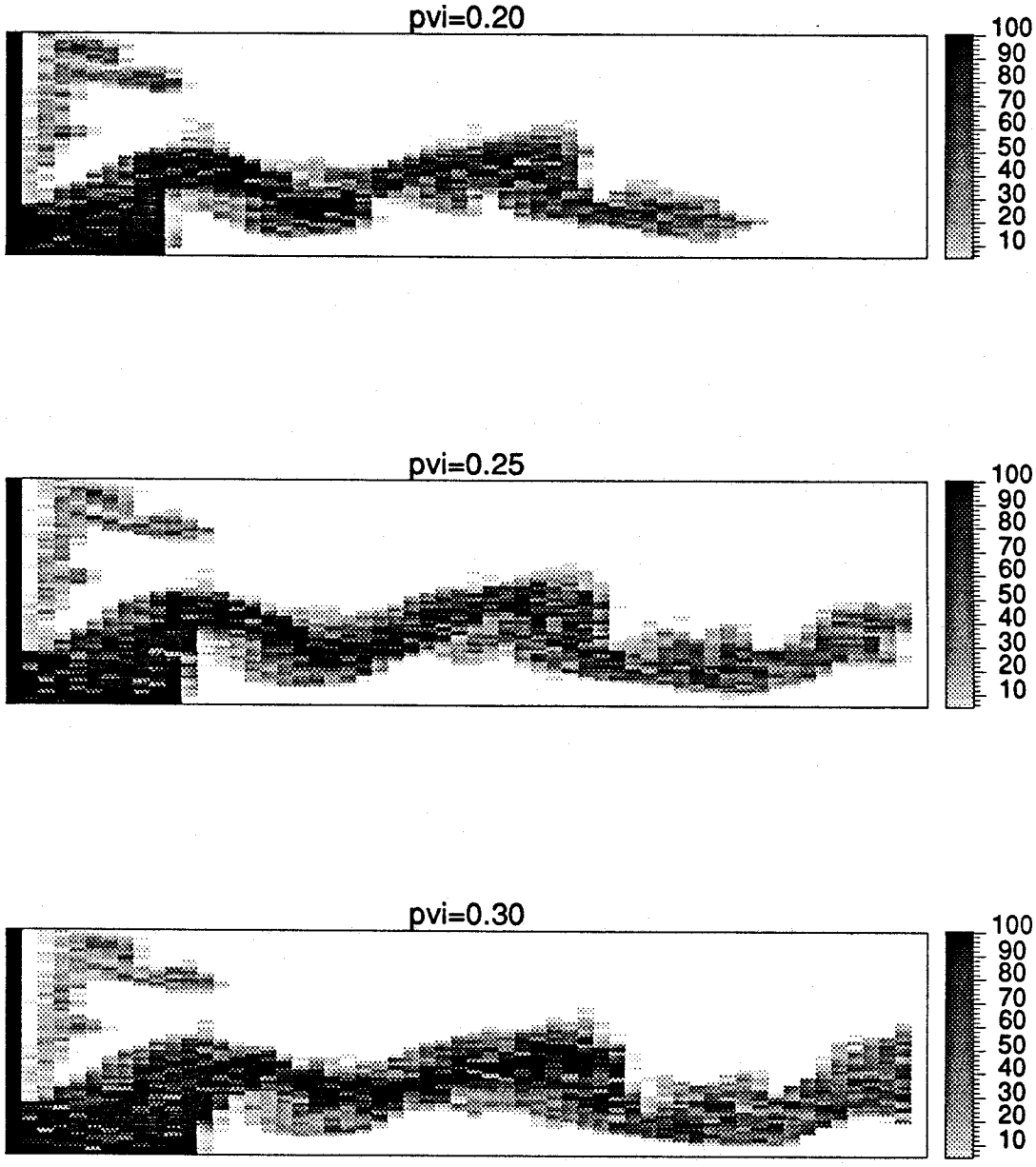

Figure 4.1-18(d-f). Simulated concentration distributions for displacement at M=40 in the checkered model.

the high permeability streak model with heterogeneity acting so strongly that it determines fingering, with only a faint overlay of viscous fingers, then a simulator would have to calculate only plug flow within a specific layer. If, however, the reservoir somewhere between that observed for the homogeneous and checkered models where heterogeneities affect finger locations and paths, but the flow is also influence by viscous fingers, accurate simulations of process performance might also require a more detailed representation of finger growth. Thus, it will be important to determine, probably by simulations, which length scales of heterogeneity and what levels of permeability contrast are most important to flow at reservoir scales. The results presented indicate that the simulation technique used here adequately models the transition from viscous-dominated to permeability-dominated unstable flow, and, therefore, it is a logical choice for such an investigation.

4.1.5 Conclusions

The experimental and numerical simulation results given here for stable and unstable displacements lead to the following conclusions:

(1) In homogeneous porous media, viscous fingers grow by spreading and splitting at their tips. Fingers that outpace others nearby shield them from further growth and some fingers are eliminated by coalescence into the wake of faster moving fingers. Hence, in rectilinear flow, at least, the number of fingers declines as the flow progresses. Numerical simulations show similar mechanisms and numbers of fingers.

(2) In heterogeneous porous media, fingering patterns develop along the same streamlines followed during flow at unit mobility in the same porous medium.

(3) Even a relatively modest permeability contrast of 4:1 is sufficient to dominate flow if the high permeability is arranged in long thin layers.

(4) Particle-tracking simulations of unstable flows reproduce with reasonable accuracy the transition from instability-dominated to permeability-dominated flow.

4.2 Simulation of Viscous Fingering in Heterogeneous Porous Media

Hamdi Tchelepi

In this section, we examine again the interaction between heterogeneity and viscous instability, this time with numerical simulations. This interaction dictates the number, size, shape and location of the dominant fingers in a miscible displacement. The ultimate goal is to delimit the regions of "viscous-dominated" and "heterogeneity-dominated" displacements. First, the particle-tracking numerical model is briefly described. Second, the influence of the inlet boundary condition on the resulting flow patterns is investigated. Third, the permeability data set of Giordano et al. (1985), as well as two data sets derived from it are used in simulations at various mobility ratios in order to study the combined effects of viscous instability and heterogeneity.

4.2.1 The Numerical Model

A random-walk technique is used to model dispersion in porous media (Araktingi 1988). The approach is based on the idea that dispersion is a random process at the microscopic level. Particles are used for a discrete representation of the displacing fluid. In a flow field, a particle experiences a net movement comprised of two components each corresponding to a certain type of motion. One component is the result of a deterministic convection motion along the local mean flow direction dictated by the pressure field. The other component is due to a

probabilistic random motion related to the flow length and the longitudinal and transverse dispersivities. It can be shown that the dispersion-convection equation governing miscible displacement can be written as a Fokker-Planck equation if terms containing spatial second-order derivatives of the dispersion coefficients are neglected. Solutions of the Fokker-Planck equation are represented in the form of a random walk experiencing the two types of motion described above. Due to the fact that dispersion is modeled as a random component, equiprobable realizations of the random dispersion component are possible through different sequences of random draws. Hence, the solutions obtained are probabilistic.

The mathematical model is based on the following assumptions:

(1) Two miscible components, flow in two dimensions.

(2) Fluids are incompressible and first-contact miscible, and may have differing densities and viscosities.

(3) There is no volume change on mixing, and the viscosity of mixtures is given by the quarter-power blending rule.

(4) The local flow velocity is given by Darcy's law, and harmonic weighting for the transmissibilities is applicable.

(5) Velocity variations at scales smaller than the grid block can be represented adequately by longitudinal and transverse dispersivities. And, if warranted, diffusion can be similarly included.

In two dimensions, the material balance equation for the injected solvent is the convection-dispersion equation.

$$\frac{\partial}{\partial x}\left[D_{xx}\frac{\partial C}{\partial x} + D_{xy}\frac{\partial C}{\partial y}\right] + \frac{\partial}{\partial y}\left[D_{yy}\frac{\partial C}{\partial y} + D_{yx}\frac{\partial C}{\partial x}\right] - u_x\frac{\partial C}{\partial x} - u_y\frac{\partial C}{\partial y} = q \tag{4.2-1}$$

The entries in the dispersion tensor are assumed to be related to the local flow velocity through the diffusion coefficient, D_m, and the longitudinal and transverse dispersivities, α_L and α_T,

$$D_{xx} = \alpha_L\frac{u_x^2}{u} + \alpha_T\frac{u_y^2}{u} + D_m \tag{4.2-2}$$

$$D_{yy} = \alpha_T\frac{u_x^2}{u} + \alpha_L\frac{u_y^2}{u} + D_m \tag{4.2-3}$$

$$D_{xy} = D_{yx} = (\alpha_L - \alpha_T)\frac{u_x u_y}{u} \tag{4.2-4}$$

The form used here is that described by Kinzelbach (1988). Eq. (4.2-1) can be rewritten in the following form

$$\frac{\partial^2}{\partial x^2}(D_{xx}C) + \frac{\partial^2}{\partial x\partial y}(D_{xy}C) + \frac{\partial^2}{\partial y\partial x}(D_{yx}C) + \frac{\partial^2}{\partial y^2}(D_{yy}C) - C\left[\frac{\partial^2 D_{xx}}{\partial x^2} + \frac{\partial^2 D_{xy}}{\partial x\partial y} + \frac{\partial^2 D_{yx}}{\partial y\partial x} + \frac{\partial^2 D_{yy}}{\partial y^2}\right] \tag{4.2-5}$$

$$- u_x^* \frac{\partial C}{\partial x} - u_y^* \frac{\partial C}{\partial y} = \frac{\partial C}{\partial t} + q$$

$$- u_x^* \frac{\partial C}{\partial x} \frac{\partial C}{\partial y}$$

u_x^* and u_y^* are corrected velocities given by

$$u_x^* = u_x + \frac{\partial D_{xx}}{\partial x} + \frac{\partial D_{xy}}{\partial y}$$

$$u_y^* = u_y + \frac{\partial D_{yx}}{\partial x} + \frac{\partial D_{yy}}{\partial y} \tag{4.2-6}$$

and the flow velocities, u_x and u_y are given by Darcy's law

$$u_x = - \frac{k}{\mu} \frac{\partial p}{\partial x}$$

$$u_y = - \frac{k}{\mu} \left[\frac{\partial p}{\partial y} - \rho g \right] \tag{4.2-7}$$

where x is horizontal, and y is aligned vertically and taken to be positive downward.

If the terms containing spatial second-order derivatives of the dispersion tensor components are neglected, then Eq. (4.2-5) is a version of the Fokker-Planck equation (Kinzelbach 1988). Solutions of the Fokker-Planck equation have been shown to result from a random walk of the type used here in the limit as the number of particles grows large (Ito 1951). The displacement of each particle in the random walk is given by

$$x_p(t + \Delta t) = x_p(t) + u_x^* \Delta t + Z_1 \sqrt{2\alpha_L u \Delta t} \frac{u_x}{u} + Z_2 \sqrt{2\alpha_T u \Delta t} \frac{u_y}{u}$$

$$y_p(t + \Delta t) = y_p(t) + u_y^* \Delta t + Z_1 \sqrt{2\alpha_L u \Delta t} \frac{u_y}{u} - Z_2 \sqrt{2\alpha_T u \Delta t} \frac{u_x}{u} \tag{4.2-8}$$

where Z_1 and Z_2 are normally distributed random variables with a mean of zero and standard deviation of one.

Corrections to the convective velocity components using the dispersion gradient terms shown in Eq. (4.2-6) are needed to write the material balance Eq. (4.2-1) as a Fokker-Planck equation. These corrections are usually small compared to the velocities u_x and u_y. They are of significance only when the velocities are small, as they are in the vicinity of a no-flow boundary or a nearly impermeable barrier. In such situations, the dispersion gradient terms of Eq. (4.2-6) generate velocities that keep the particles moving. Thus, the problem observed by Araktingi (1988) of high particle concentration buildup near the edges of the simulation field is alleviated. Another example of similar problems encountered in contaminant transport calculations is described by Kinzelbach (1988). Those problems were alleviated by the current formulation.

The mathematical model was implemented numerically using an explicit finite difference scheme on a point-distributed grid. The required input to the numerical model includes the following physical conditions: flow domain dimensions, dispersivities, flow rate, and the mobility ratio. The following information may be included, if needed: permeability distribution, porosity distribution, diffusion coefficient and densities. Requirements specific to the numerical

implementation include grid size and the number of particles taken to represent a unit concentration.

The algorithm that implements the model is

(1) Given the current location of fluids of high and low viscosity and the permeability distribution, the continuity equation is solved to obtain the current pressure distribution.

(2) From the pressure distribution, a local flow velocity is calculated for each particle using Darcy's law. Determine the time step subject to the current criterion due to the explicit scheme used. Generate the number of particles corresponding to the amount injected during the current time step.

(3) Each of the new and new particles is then moved to a new location in accordance with Eq. (4.2-8).

(4) Go back to step (1) until the desired displacement time is reached.

4.2.2 The Influence of Boundary Condition Formulation

The numerical model described above was used to simulate stable and unstable miscible displacements in a rectangular domain. The faces at $y = 0$ and $y = H$ were defined as no flow boundaries. At the outlet face ($x = L$) a constant potential condition was imposed. At the inlet face ($x = 0$), a constant total injection rate was specified. Thus, the pressure at the inlet face varied with time in such a way as to satisfy the rate constraint. A reference pressure in the first column, say $p(0,0)$, was treated as an unknown. The remaining pressures in the inlet column of blocks were taken to be related to $p(0,0)$ by the gravity head difference. This allowed for treating the individual block injection rates in the first column as unknowns. The rate constraint equation was added to the system of finite difference equations to complete the definition of the problem. At each time step, the number of particles introduced into a given entry block was dictated by the rate obtained for that particular block.

This implementation of the boundary condition differs from that used previously (Araktingi 1988, Araktingi and Orr 1988, Araktingi and Orr 1990). In those calculations, the inlet boundary condition was assumed to be that of a constant total rate that was introduced uniformly across the inlet face. This previous implementation of the inlet boundary condition will be referred to as the "old boundary condition", while the current implementation will be referred to as the "new boundary condition" in what follows. Note that the two implementations are identical for the case of a homogeneous porous medium flooded at unit mobility ratio.

Simulations of miscible displacements were performed to test the sensitivity of solutions to the formulation of the boundary conditions using the permeability field of Fig 4.2-1. The simulation grid was 58 x 60, and the mobility ratio was $M = 80$. Both implementations of the inlet boundary condition were used. Figs 4.2-2 to 4.2-5 are gray-scale representations of the concentration distribution in the flow domain at different times for the experiment and the old and new boundary conditions. The mechanisms of shielding, spreading, tip splitting and coalescence, which control the fingering behavior, are evident in the experiments (Brock 1990). It is important to note that differences in the absolute levels of concentration between experiment and simulations exist. This is due, at least partly, to the calibration of concentration derived from the video images in the experiment. No attempt was made here to normalize the concentrations in the simulations. Moreover, there are regions of low concentrations of injected fluid in the experiment that lead and surround the major flow regions. This may be the result of edge flow in the model (Brock 1990), preferential flow where the spherical beads meet the upper and lower glass plates. Such flow was not modeled in the simulations, of course.

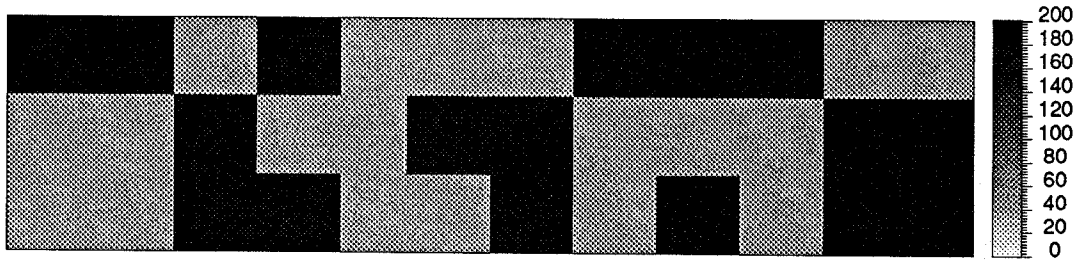

Figure 4.2-1. Permeability map for the checkerboard model.

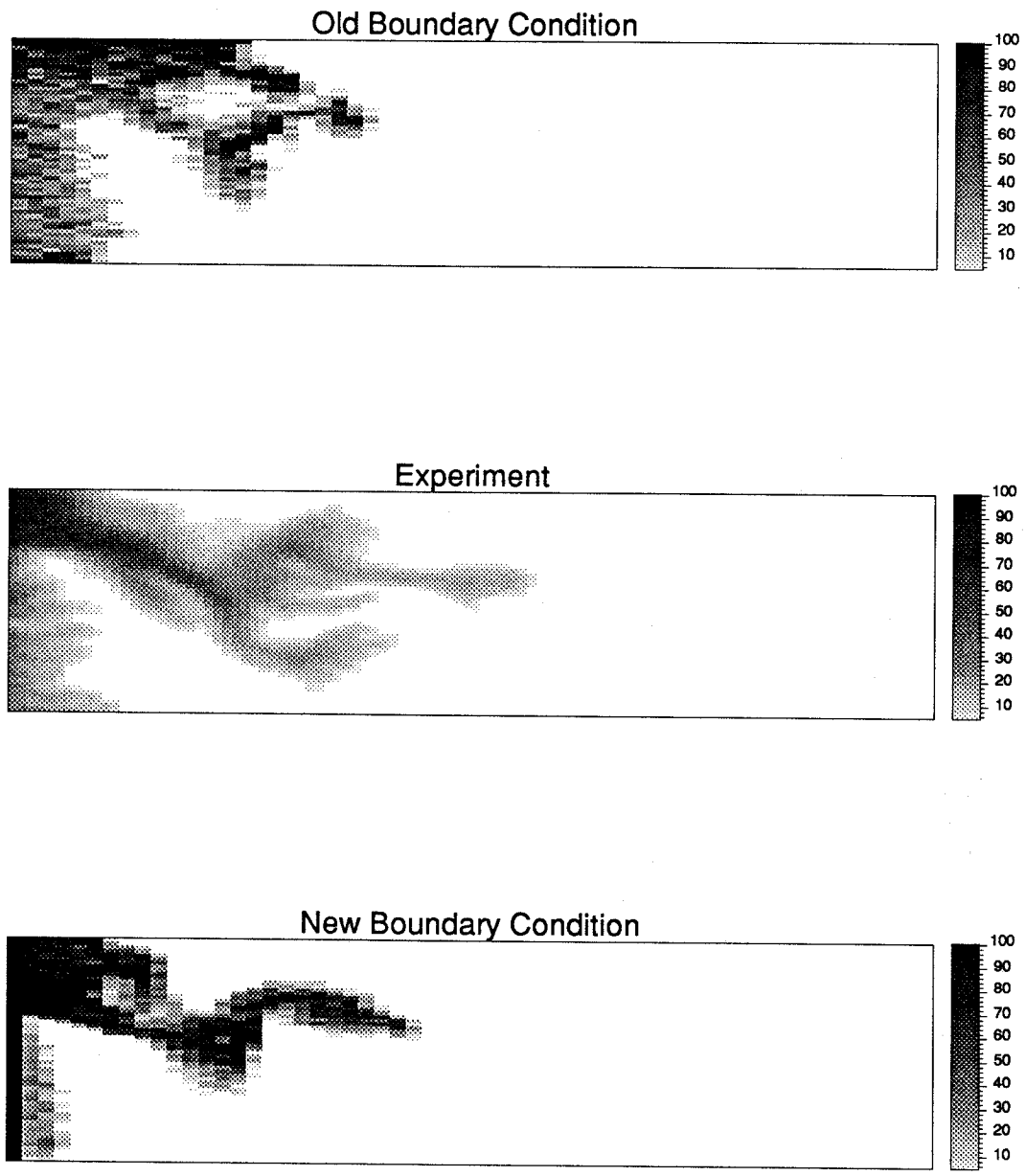

Figure 4.2-2. Concentration gray-scale maps for the experiment, new and old boundary condition at M = 80, PVI = 0.10.

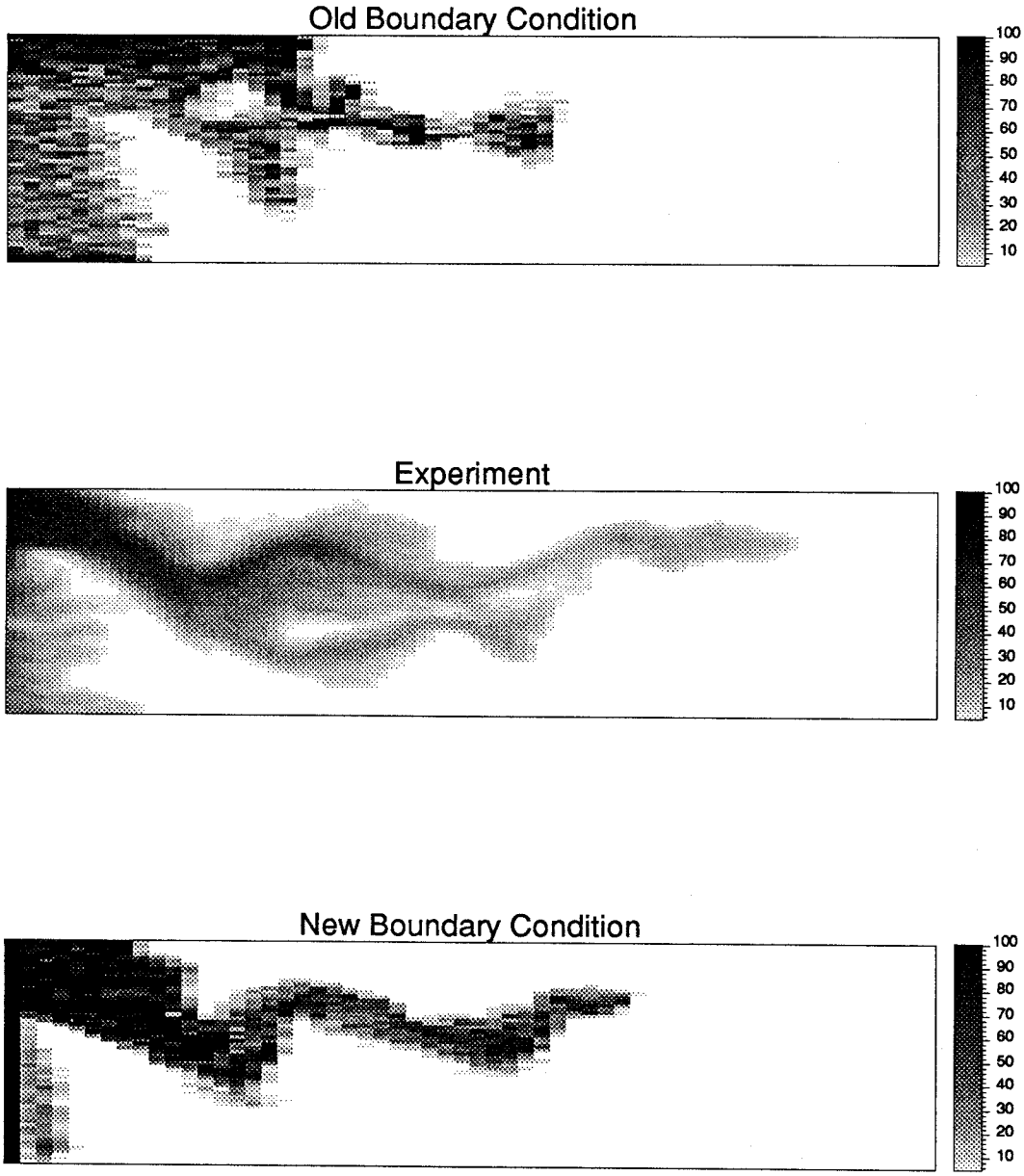

Figure 4.2-3. Concentration gray-scale maps for the experiment, new and old boundary condition at M = 80, PVI = 0.15.

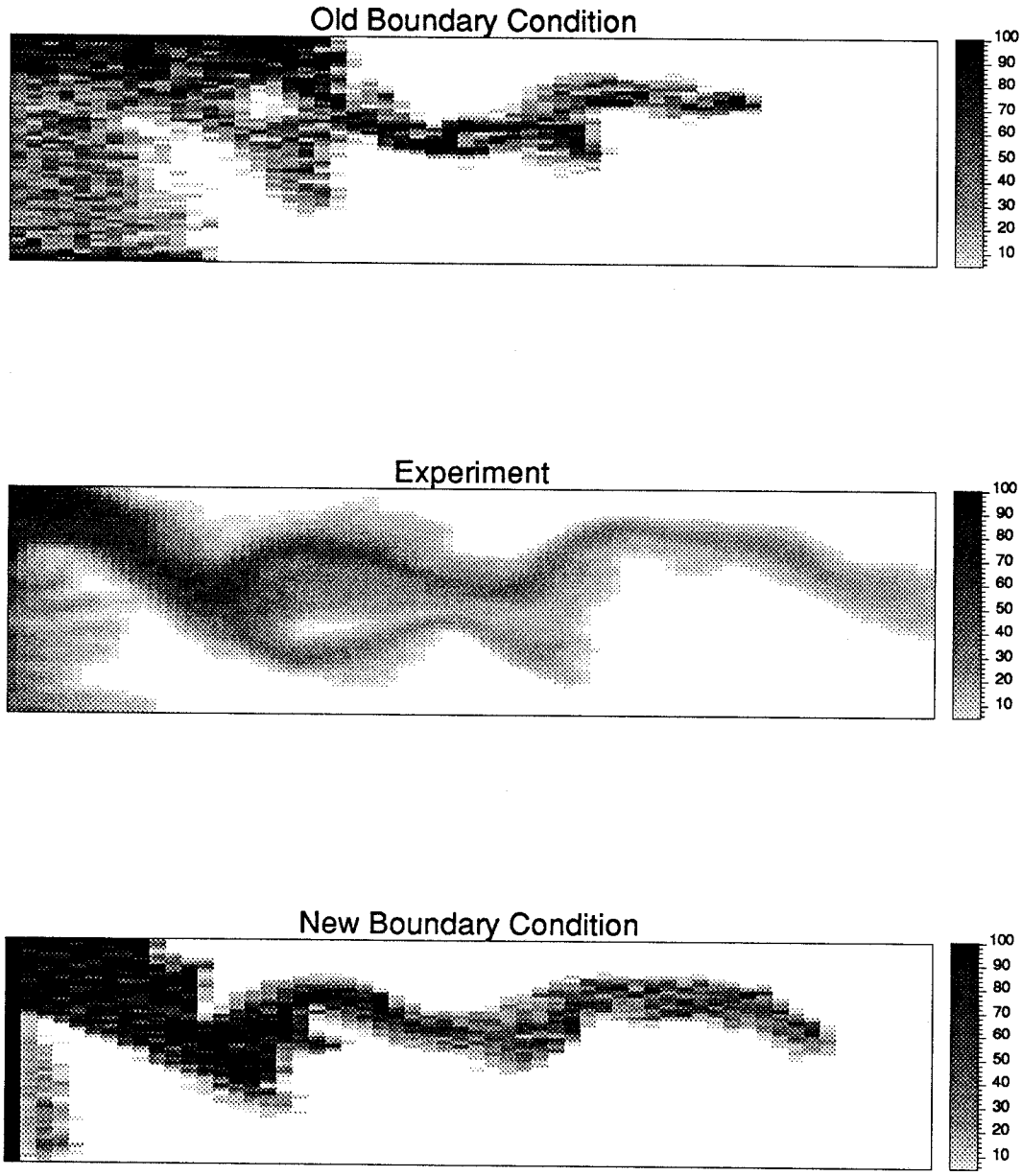

Figure 4.2-4. Concentration gray-scale maps for the experiment, new and old boundary condition at M = 80, PVI = 0.20.

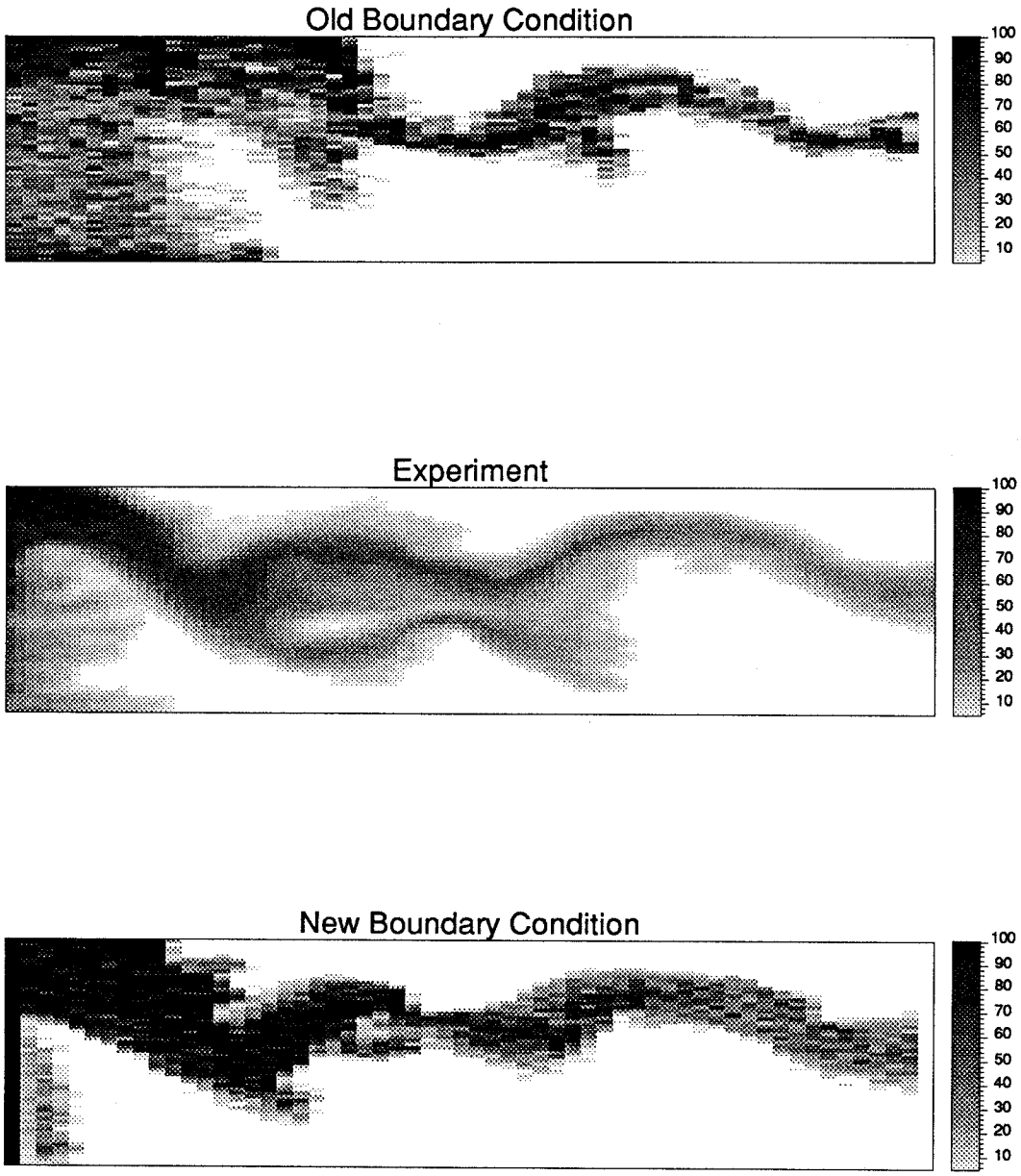

Figure 4.2-5. Concentration gray-scale maps for the experiment, new and old boundary condition at M = 80, PVI - 0.25.

Fig 4.2-2, at 0.10 PVI shows clearly that the old boundary condition introduces too much fluid into the lower section of the inlet face. However, the new boundary condition allocates the amounts of the injected fluid more appropriately as can be seen when contrasted with the experimental results. At later times (see for example Fig 4.2-5), that observation is still true; moreover, the flow configuration throughout the porous medium differs significantly for the two boundary condition implementations. This indicates that the pressure gradients in the mean flow direction are sufficient to cause additional flow of injected fluid once the total mobility has been increased by the presence of some low viscosity flow. The result is that crossflow in the inlet region cannot offset the effect of introducing the fluid uniformly across the inlet face. It is clear that the new boundary condition produces simulations that match more closely the experimental configuration than those implementing the old boundary condition.

The distribution of the injected fluid across the inlet face in the new boundary condition is sensitive to the mobility field in the flow domain while the old boundary condition is not. Mobility is a function of permeability and viscosity which in turn is determined by the local concentration. Consequently, the differences in the resulting flow patterns between the two implementations of the inlet boundary condition are expected to increase as the heterogeneity and mobility ratio increase.

It is not surprising that at early times, the new boundary condition produces flow configurations that are in closer agreement with the experiment. However, it is apparent that the impact is significant throughout the displacement history as can be seen from Figs. 4.2-2 to 4.2-5. In the limiting case of flow in long thin layers, of course, both forms of the boundary condition will reproduce the same solution. However, experiments usually utilize models of dimensions comparable to the model shown here. As a result, interpretation of laboratory displacement experiments requires careful implementation of the boundary conditions.

There are differences between the fingering patterns observed in the experiment and the simulations as can be seen in Figs. 4.2-2 to 4.2-5. The simulations are not aimed at a deterministic description of small scale behavior. After all, the solutions are probabilistic and cannot be expected to reproduce the exact locations of every small finger. However, understanding the small scale behavior and incorporating the proper physics underlying viscous instability is essential to the success in predicting behavior at larger scales. We are concerned here with the major features of fingering for a given set of conditions. These features include the number, size, location and configuration of the dominant fingers. The comparisons presented here and in Section 4.1 indicate that the numerical model used here captures these features successfully.

4.2.3 Interactions of Heterogeneity and Viscous Instability

To investigate the interaction between the heterogeneity (permeability distribution) and viscous instability, three data sets were used. Numerical particle tracking simulations for each of the three sets were performed for three different mobility ratios (viscosity ratios); namely, 1, 7.5 and 100.

The first data set used in this study is the 2nd Berea Data Set of Giordano et al. (1985). They took 40 x 40 surface permeability measurements of a 2 ft x 2 ft berea slab. This data set will be referred to as the original set. The overall variability of the permeability field for this set produced a coefficient of variation of 0.284. Since this coefficient of variation of the original set is low, two new sets were numerically derived from this original set by applying simple nonlinear transforms. Statistical measures for the three sets are shown in Table 4.2-1. The new data sets with coefficients of variation (C.V.) of 0.56 and 0.86 will be referred to as the first and second data sets, respectively. Gray scale maps for the three permeability fields studied are shown in Figs. 4.2-6 to 4.2-8. The banding structure is clear in the three sets.

Table 4.2-1. Data Sets Statistics.

Data Sets Statistics			
	mean	Std Dev.	C.V
Original Set	55.53	15.78	0.284
First Modified	333.22	188.01	0.564
Second Modified	2145.75	1854.46	0.866

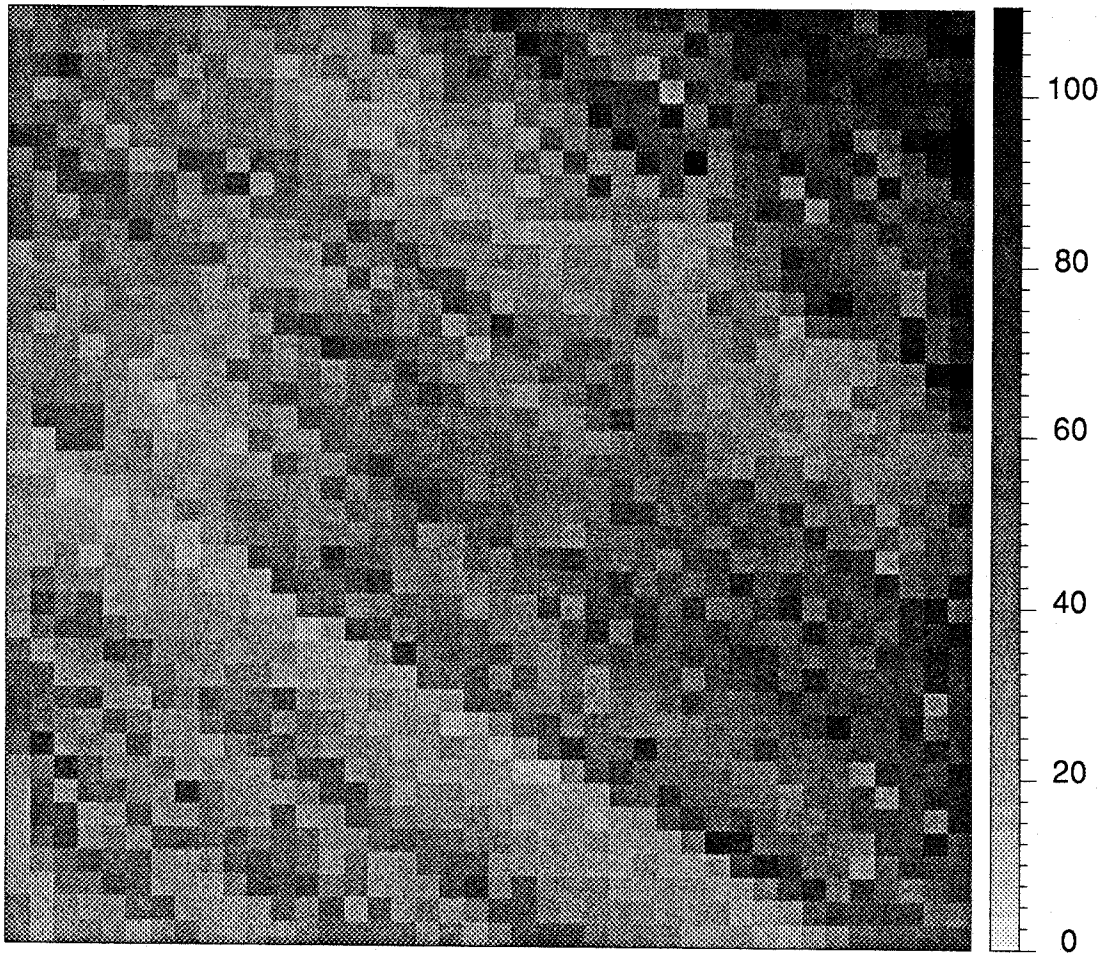

Figure 4.2-6. Gray-scale map of the permeability distribution for the original Berea data set (C.V. = 0.284).

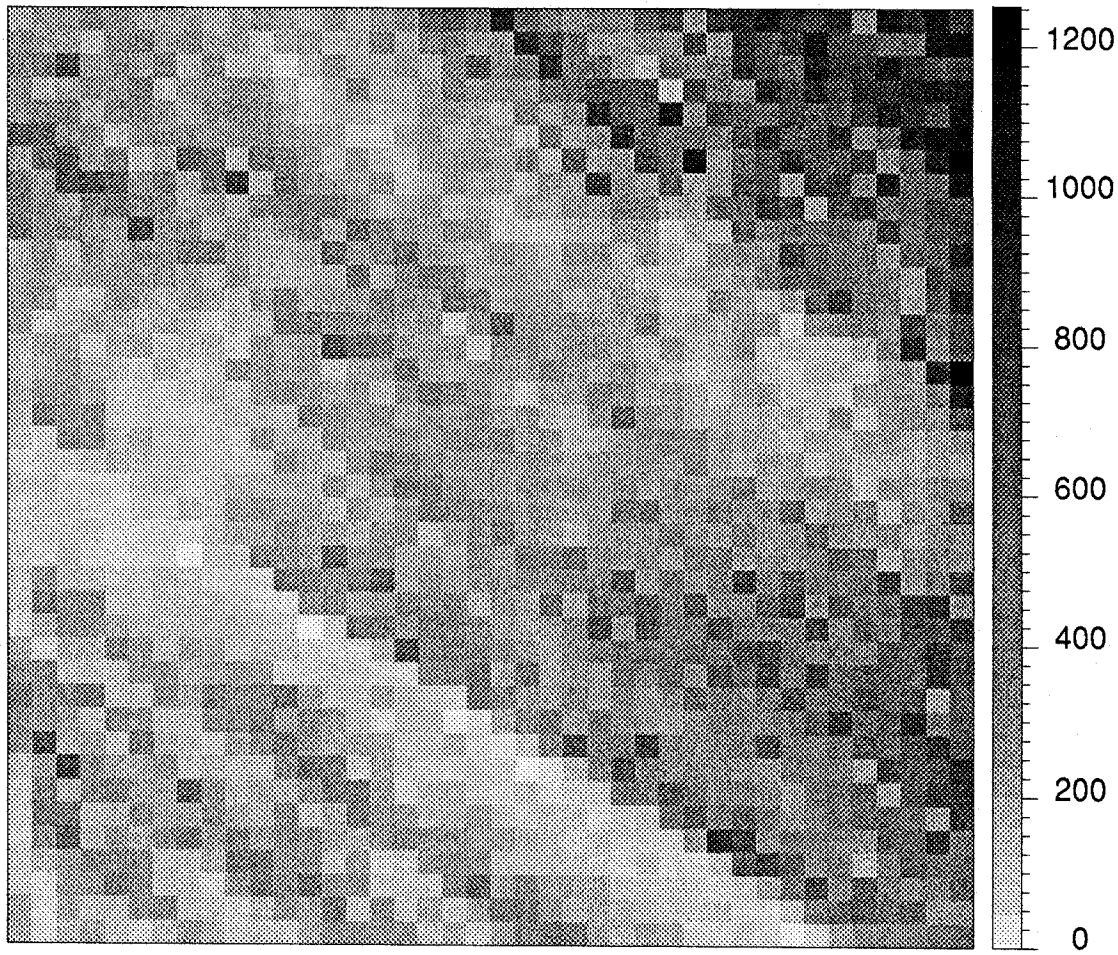

Figure 4.2-7. Gray-scale map of the permeability distribution for the first modified data set (C.V. = 0.56).

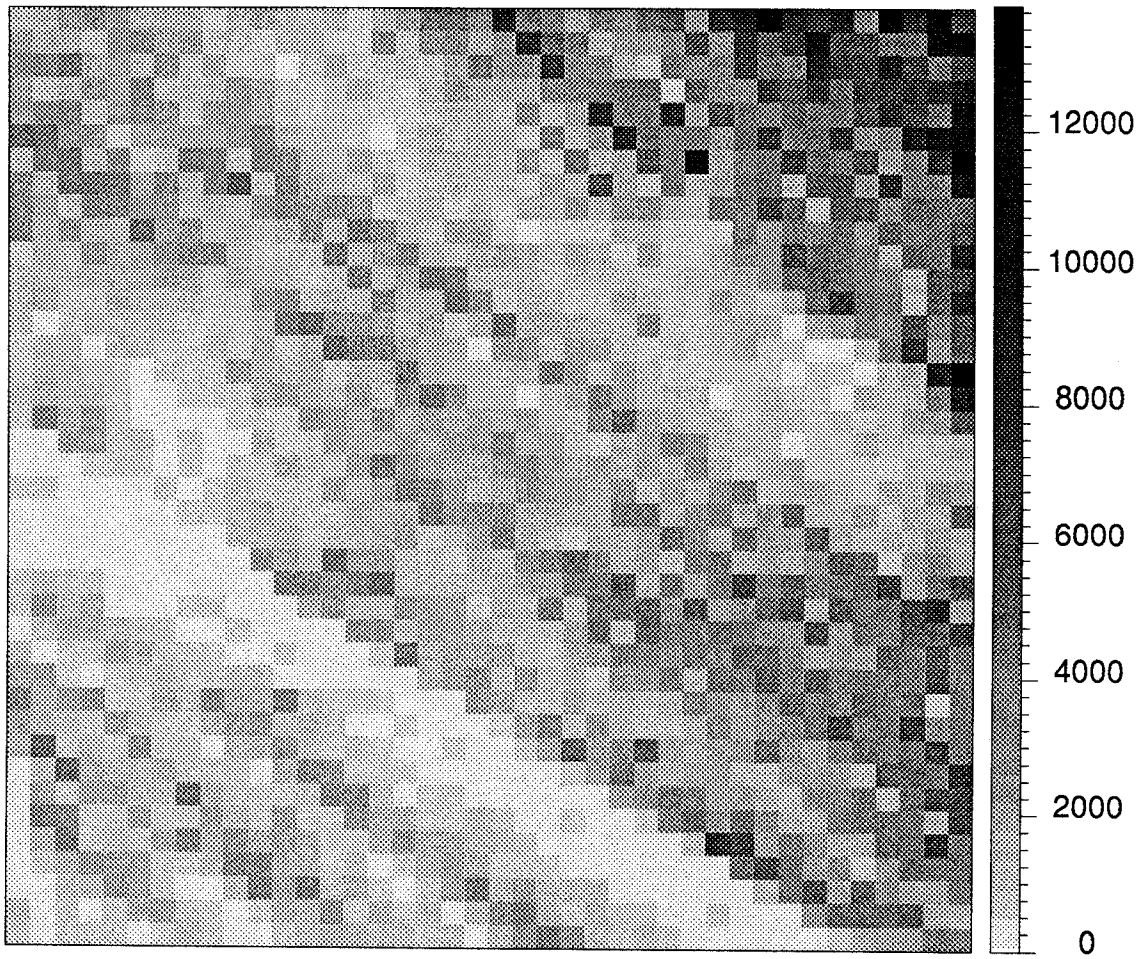

Figure 4.2-8. Gray-scale map of the permeability distribution for the second modified data set (C.V. = 0.86).

Maximum continuity is in the N. 57° W. direction and the minimum continuity is in the N. 33° E. direction. Two features of the permeability fields shown in Figs. 4.2-6 to 4.2-8 stand out. The first is a band of distinctively low permeability values that start from about the center of the left (west) face and extends in the N. 123° E. direction. The second feature is the concentration of high permeability values in the northeastern region of the permeability fields.

Figs. 4.2-9 and 4.2-10 are plots of the normalized variograms in the x (W-E) and y (N-S) directions, respectively. Note that these directional variograms do not correspond to the major and minor axes of the anisotropy. Rather, they are taken parallel and transverse to the mean flow direction of the numerically simulated displacements. There is no clear sill value for the variograms, an indication of space dependent correlation lengths and an anisotropy that is imperfect. Interestingly, the normalized variance at a given lag decreases as the overall variability, indicated by the coefficient of variation, increases for the three data sets subject to investigation here.

The following conditions apply to all of the simulation results presented here. Each permeability block was represented by one grid block. Thus the grid used in the numerical model was 40 x 40. The longitudinal and transverse dispersivities used were 0.075 cm and 0.0024 cm, respectively. These values are in accordance with those used by Giordano et al. (1985). A constant rate of injection corresponding to a displacement velocity of 2 ft/day was used. The injection fluid was introduced across the left (west) face of a given slab and produced across the right (east) face. The north and south faces were taken as no flow boundaries.

To isolate the influence of the permeability distribution on the flow behavior, simulations of displacements at unit mobility ratio were performed. Fig. 4.2-11 shows the position of the 50% concentration contour at PVI of 0.4, 0.5, 0.7 and 0.9 for unit mobility ratio displacements using the permeability field of the original data set. It is obvious that nonuniformities in the 50% concentration contour, which will be referred to as "the front" for convenience, do exist but are not very pronounced. This is in line with the fact that that the heterogeneity is mild. However, note the influence of the high permeability region in the northeastern section of the slab on the shape of the front. Figs. 4.2-12 and 4.2-13 are similar to Fig. 4.2-11, but are for the first (C.V. = 0.56) and second (C.V. = 0.86) data sets, respectively. The same observations hold here with a more pronounced influence of the high permeability region on pulling the front. Moreover, the streak of low permeability mentioned earlier has its signature on the unit mobility displacements of the first and second data sets.

Next, we consider what behavior might be expected in unstable displacements. If the displacement takes place in a porous medium with strong heterogeneity characteristics at mobility ratios greater than unity, the nonuniformities in the displacement front observed at unit mobility ratio will stretch and grow at rates that are dependent on the local viscosity contrast. As a result, the location and size of the fingers (channels) will be highly correlated with the permeability distribution. On the other hand, if the porous medium is homogeneous, then the random dispersion component controls the location and scales of the viscous fingers at inception and throughout the displacement. And different realizations will yield different spatial distributions of fingers. The differences increase as the mobility ratio (i.e viscous instability) increases. It is important to note, however, that the scales, numbers and sizes of the fingers will be similar across the realizations.

Figs. 4.2-12 to 4.2-16 show a series of snap shots of the 50% concentration contour at a mobility ratio of 7.5 for the original, first and second data sets, respectively. The viscous instability is clearly illustrated in these figures. For the three permeability fields investigated, the fastest finger is clearly influenced by the concentration of distinctively high permeabilities in the northeastern region. Comparison of the three figures indicates that this feature becomes increasingly prominent as the coefficient of variation increases from the original to the first and second sets, respectively. The flow behavior and distances of penetration close to the southern face for the first and second data sets exhibit a correlation with the band of low permeabilities described earlier.

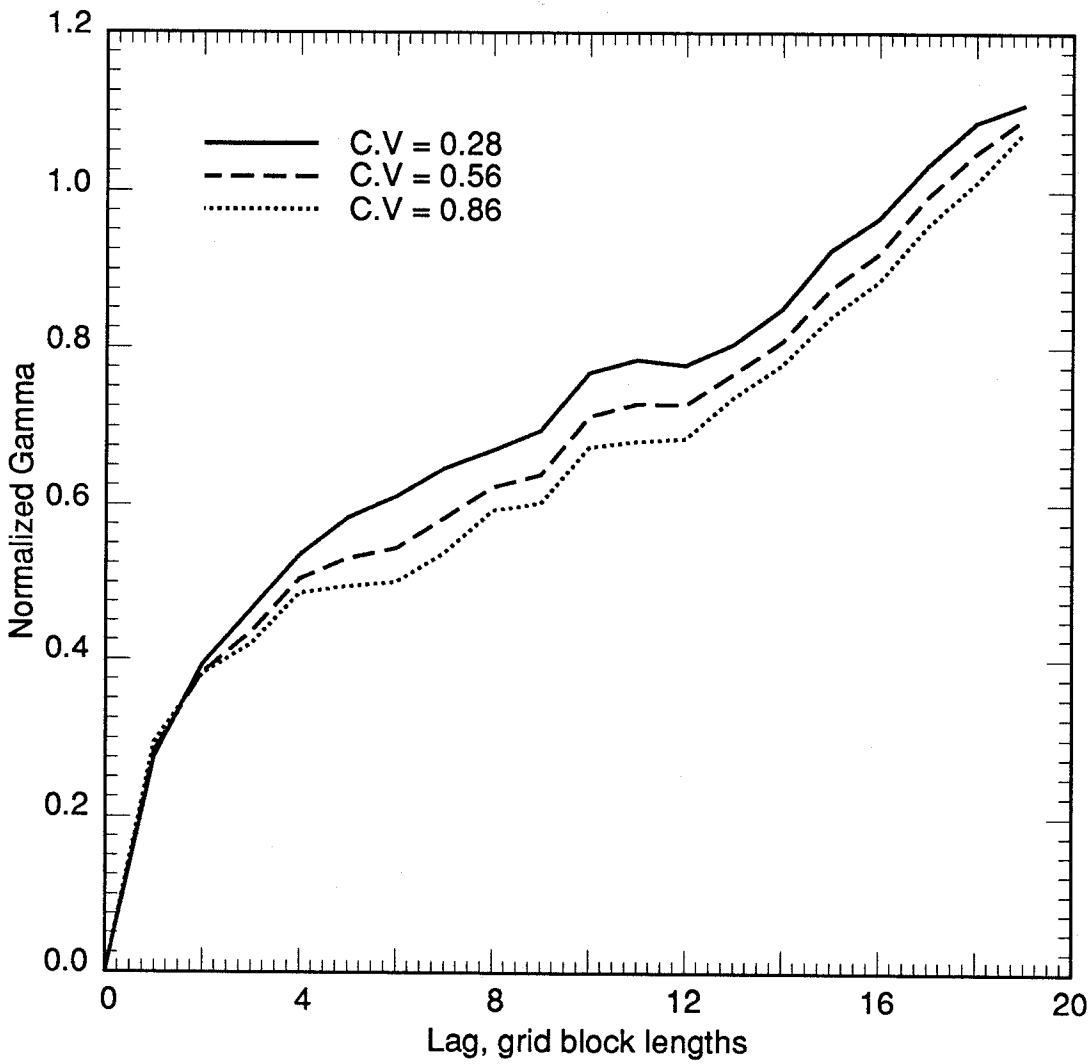

Figure 4.2-9. X-direction variograms for the three data sets.

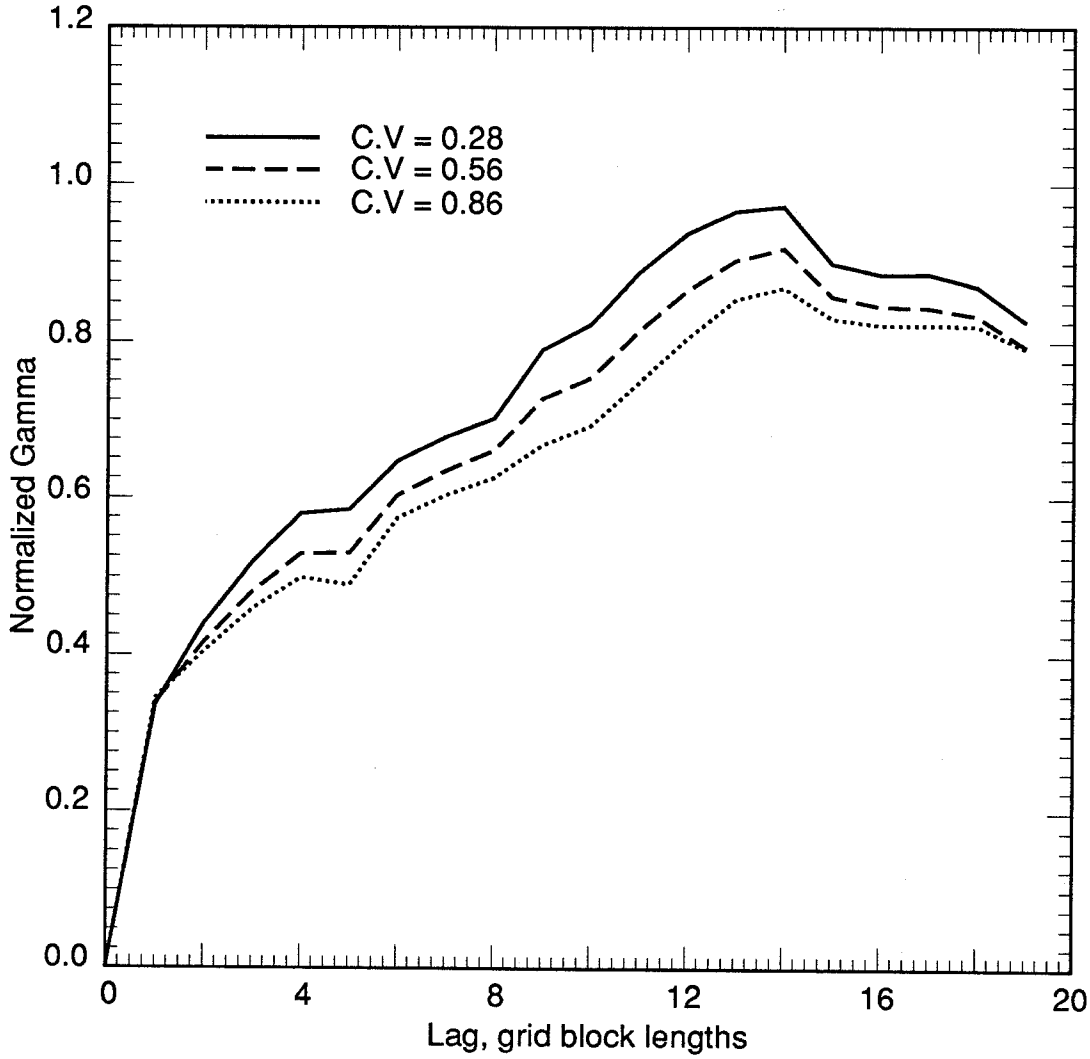

Figure 4.2-10. Y-direction variograms for the three data sets.

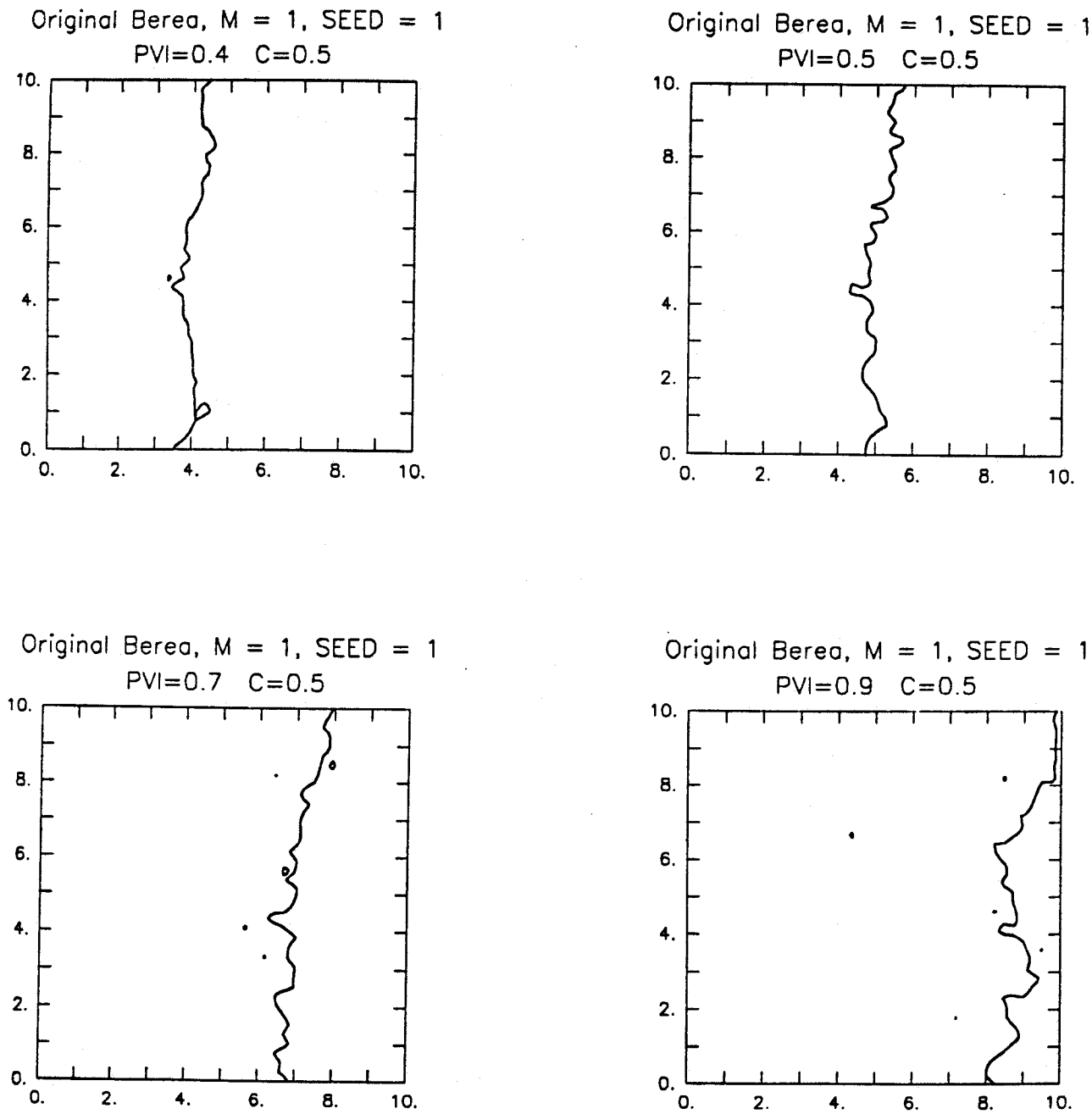

Figure 4.2-11. The 50% concentration contour at 0.4, 0.5, 0.7 and 0.9 PVI at M=1 for the original Berea data set.

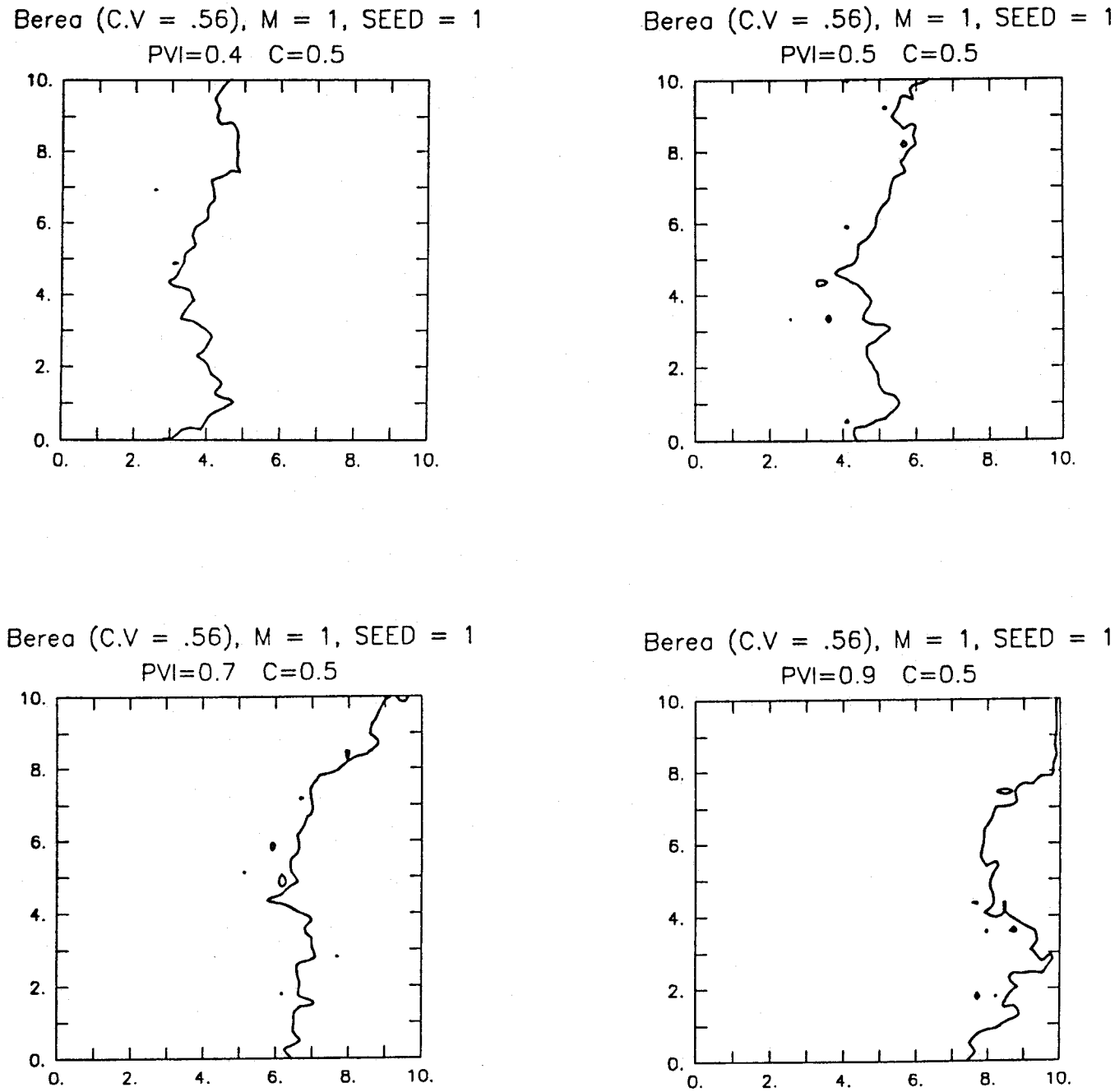

Figure 4.2-12. The 50% concentration contour at 0.4, 0.5, 0.7 and 0.9 PVI at M=1 for the first modified data set.

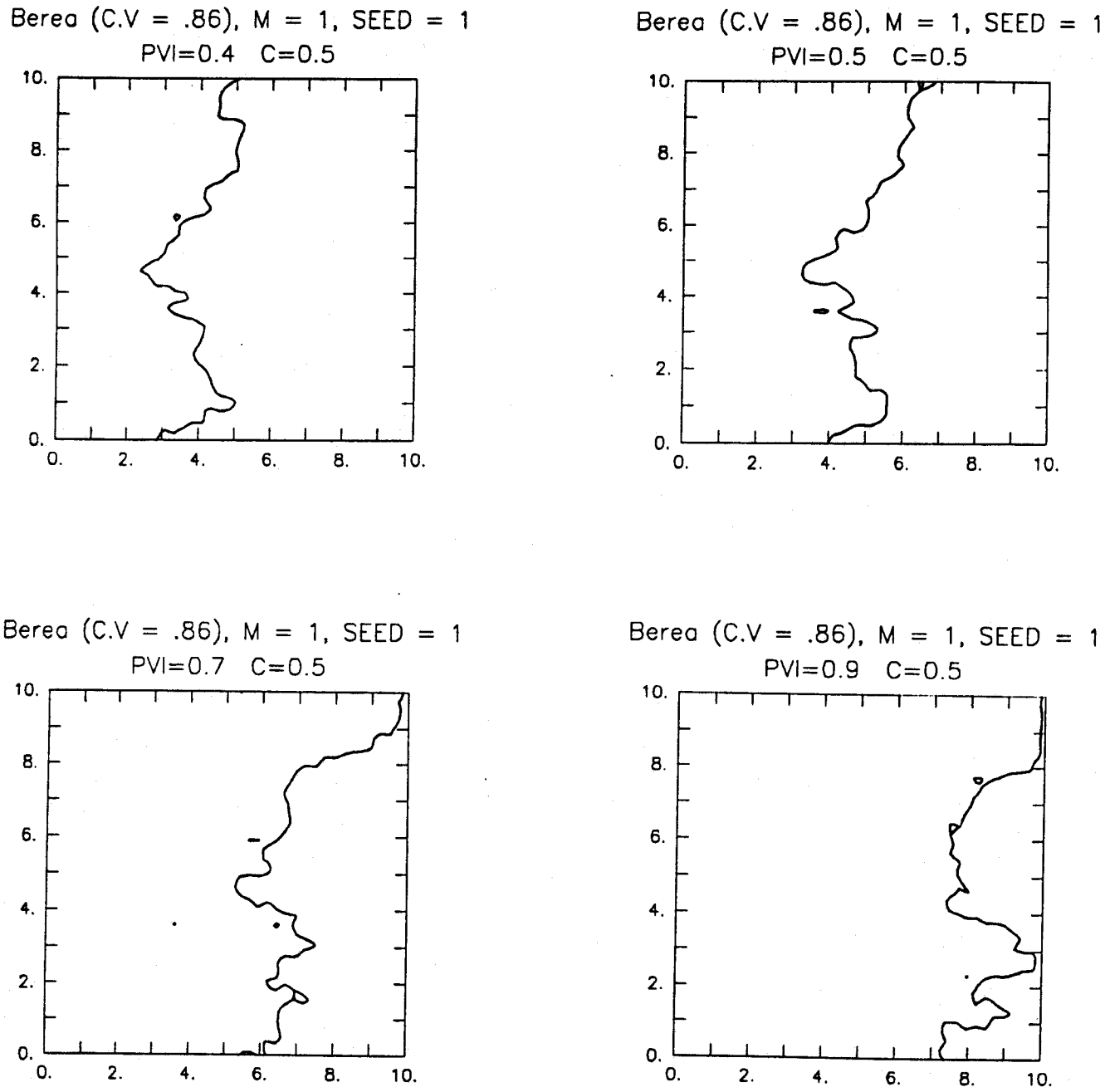

Figure 4.2-13. The 50% concentration contour at 0.4, 0.5, 0.7 and 0.9 PVI at M=1 for the second modified data set.

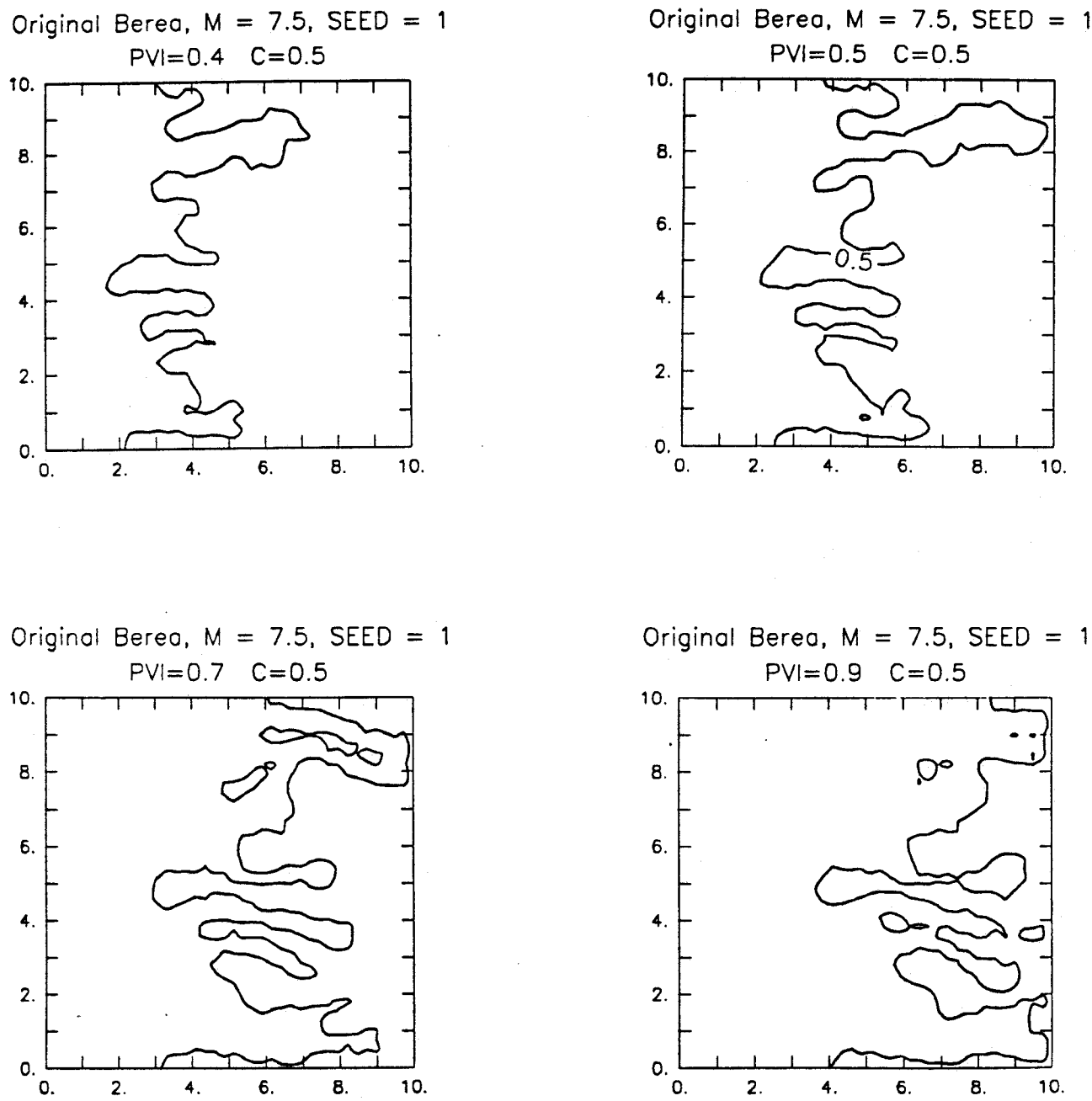

Figure 4.2-14. The 50% concentration contour at 0.4, 0.5, 0.7 and 0.9 PVI at M=7.5 for the original Berea data set.

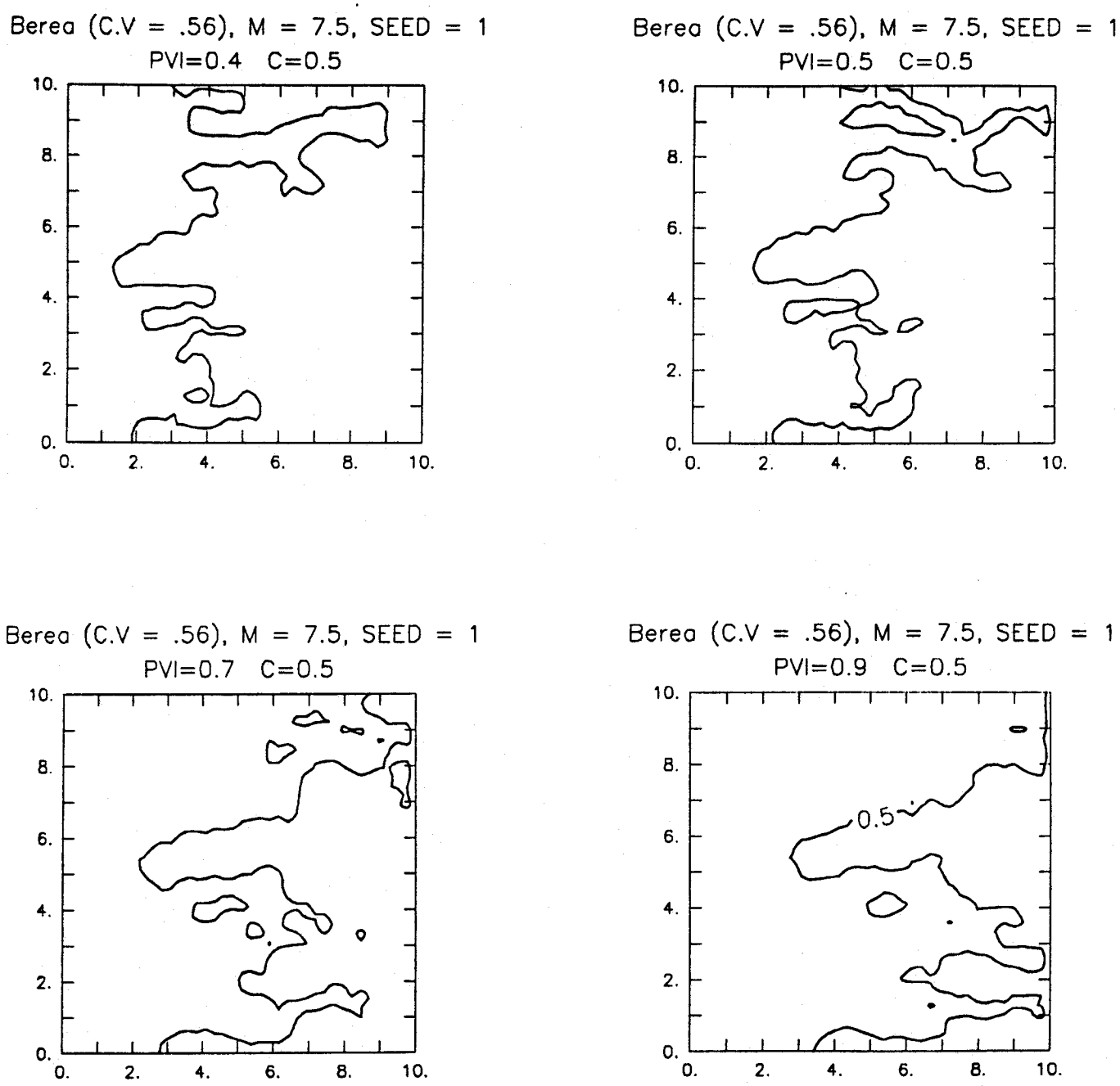

Figure 4.2-15. The 50% concentration contour at 0.4, 0.5, 0.7 and 0.9 PVI at M=7.5 for the first modified data set.

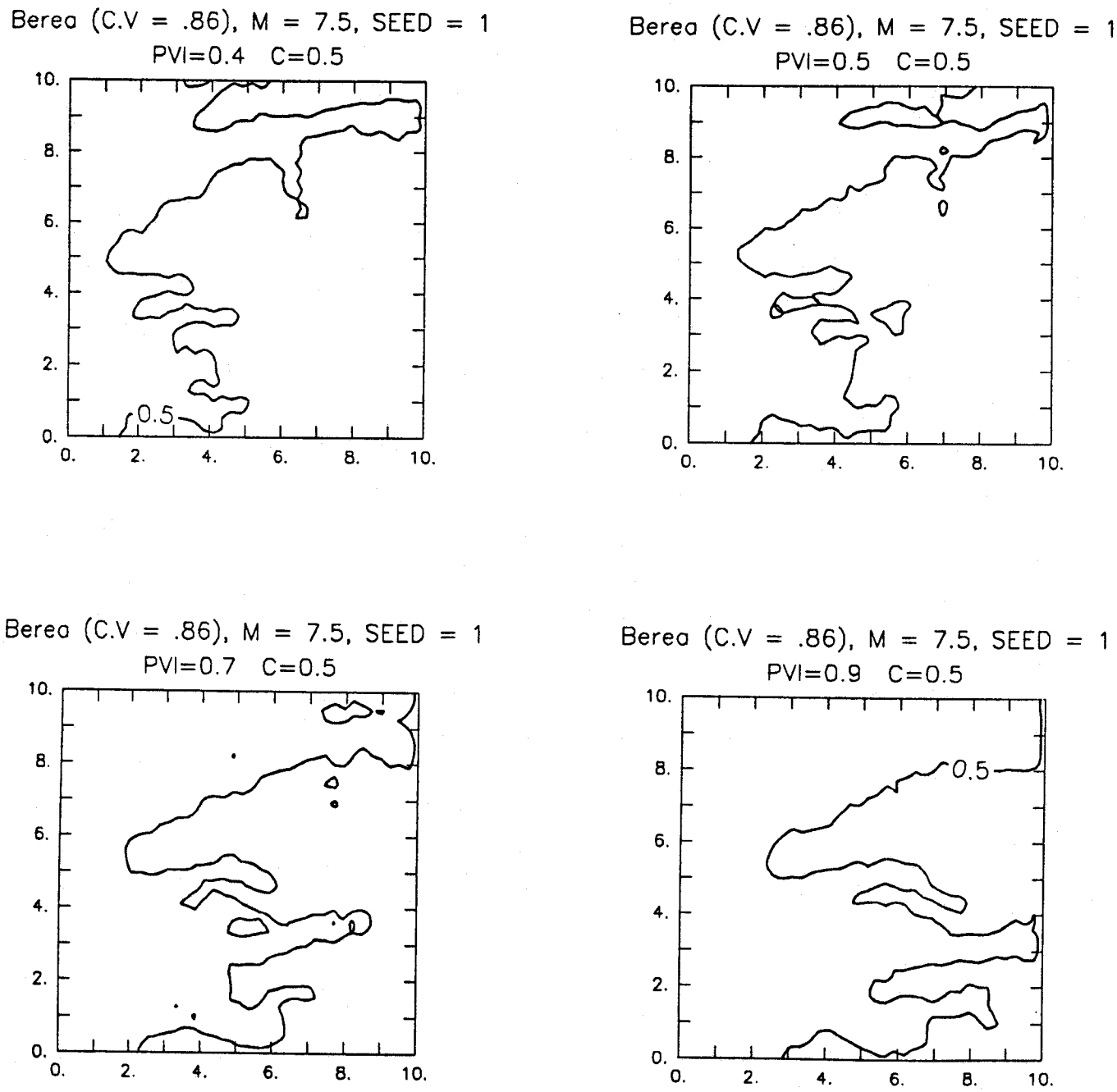

Figure 4.2-16. The 50% concentration contour at 0.4, 0.5, 0.7 and 0.9 PVI at M=7.5 for the second modified data set.

Similar plots for a mobility ratio of 100 for the original, first and second data sets are shown in Figs. 4.2-17 to 4.2-19. Fig. 4.2-17 indicates the severity of the viscous instability and the fact that the influence of the heterogeneity is small. The fingering patterns observed in Figs. 4.2-18 and 4.2-19, however, still show the influence of the major features of the permeability fields. In spite of the fact that the viscous instability is severe (M = 100), the major features of the spatial characteristics of the permeability field under consideration have a say in the location and spatial distribution of the fingers.

4.2.4 Conclusions

The simulation results presented in this section indicate that:

(1) The impact of the boundary conditions on the resulting flow configuration throughout the displacement history is significant. Thus, simulations of laboratory scale experiments must model the boundary conditions accurately.

(2) Simulations of stable and unstable miscible displacements in heterogeneous porous media indicate that there is a competition between heterogeneity and viscous instability to dominate the flow behavior. Although the heterogeneity was mild in the three data set investigated, the location and size of the dominant fingers was correlated with the spatial permeability distribution for a mobility ratio of 7.5. Viscous instability at the high mobility ratio of 100 dominated the displacements in the three data sets studied. However, the influence of the permeability distribution on the location and size of the dominant finger was apparent. Thus, the results suggest that at a given value of mobility ratio, there is some level of heterogeneity that is strong enough to dominate the flow, and at a given level of heterogeneity, there is some mobility ratio high enough to add significant viscosity instability to the flow patterns that arise from the permeability field alone.

4.3 Summary

The results presented in this chapter provide considerable evidence that the physics of unstable flows can be represented with reasonable accuracy by the particle-tracking simulation technique developed as part of previous research under this project. Furthermore, the combination of experimental work and numerical simulation indicates that the transition from flow dominated by viscous instability to flow dominated by the permeability distribution is also modeled accurately by the simulations. That result is a useful one, because it implies that the simulation technique can be used with reasonable confidence to explore the flow behavior of unstable displacements in field-scale permeability distributions. In the experiments described, a modest 4:1 permeability contrast was sufficient to dominate flow when the high permeability was arranged in long thin layers. Because much higher contrasts are common in reservoir rocks, we speculate, though we cannot yet prove, that many field-scale miscible floods will be dominated by permeability distributions. Work in progress now is aimed at quantifying the relative importance of instabilities and permeability distributions for realistic porous media.

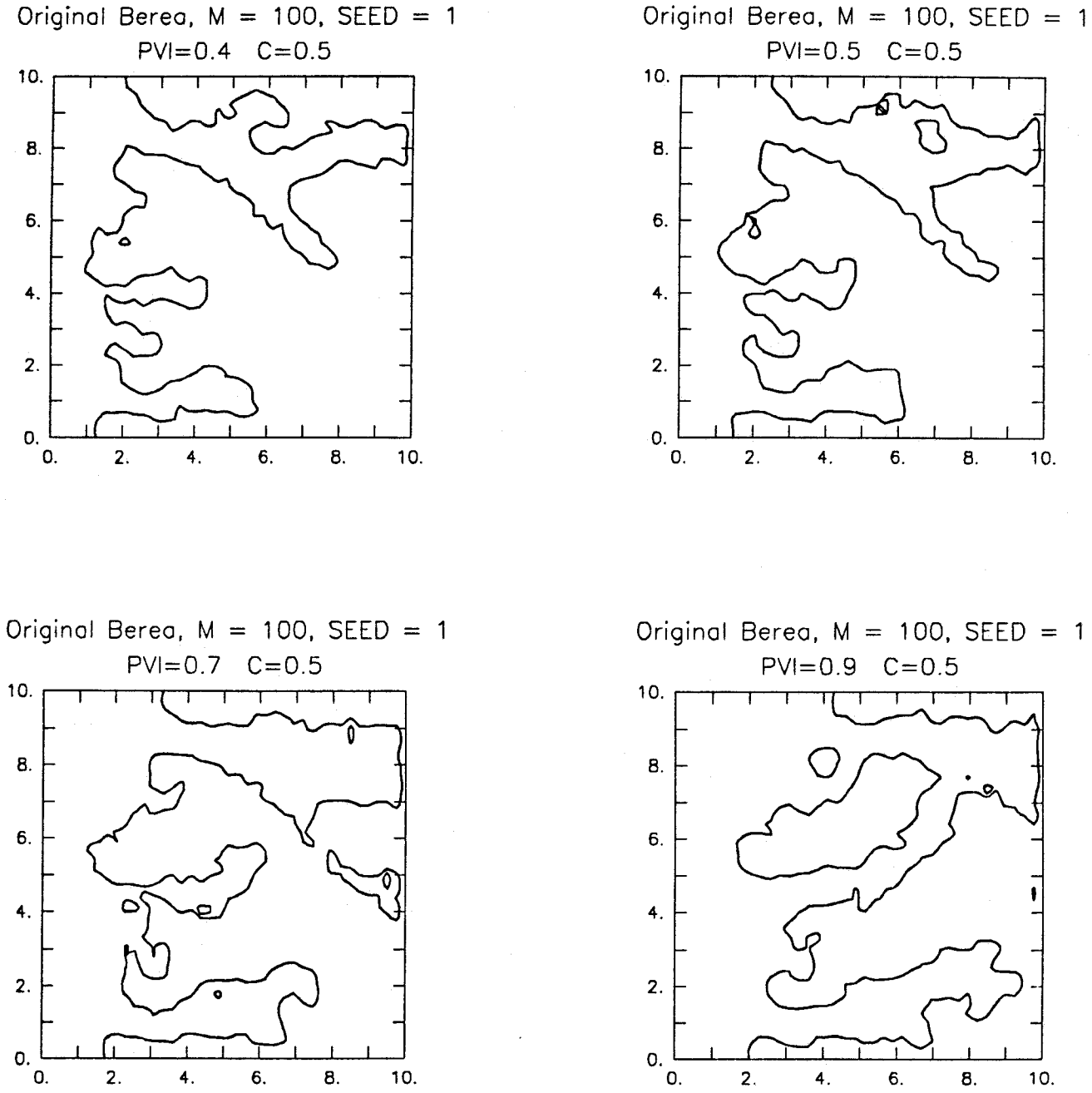

Figure 4.2-17. The 50% concentration contour at 0.4, 0.5, 0.7 and 0.9 PVI at M=100 for the original Berea data set.

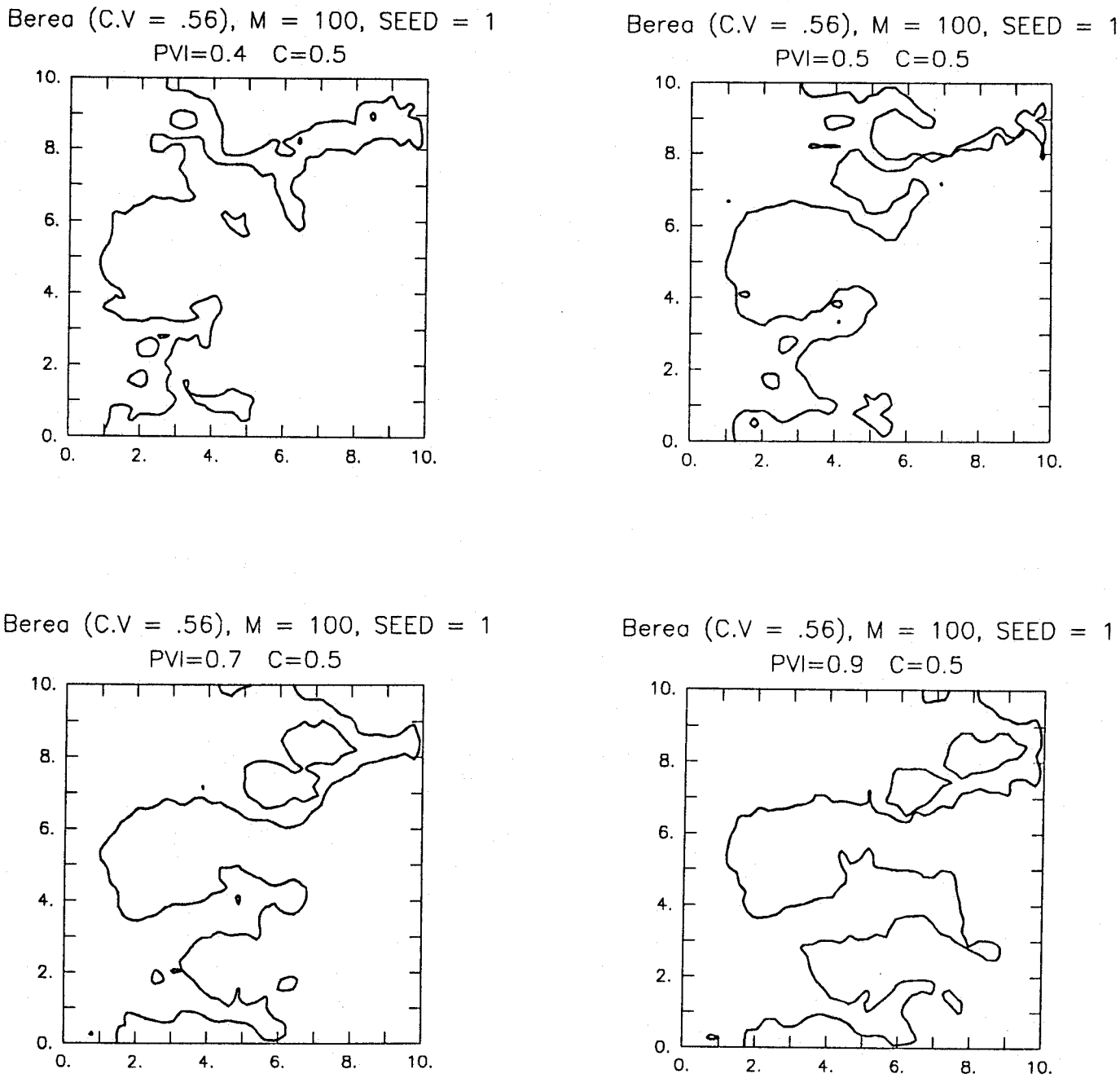

Figure 4.2-18. The 50% concentration contour at 0.4, 0.5, 0.7 and 0.9 PVI at M=100 for the first modified data set.

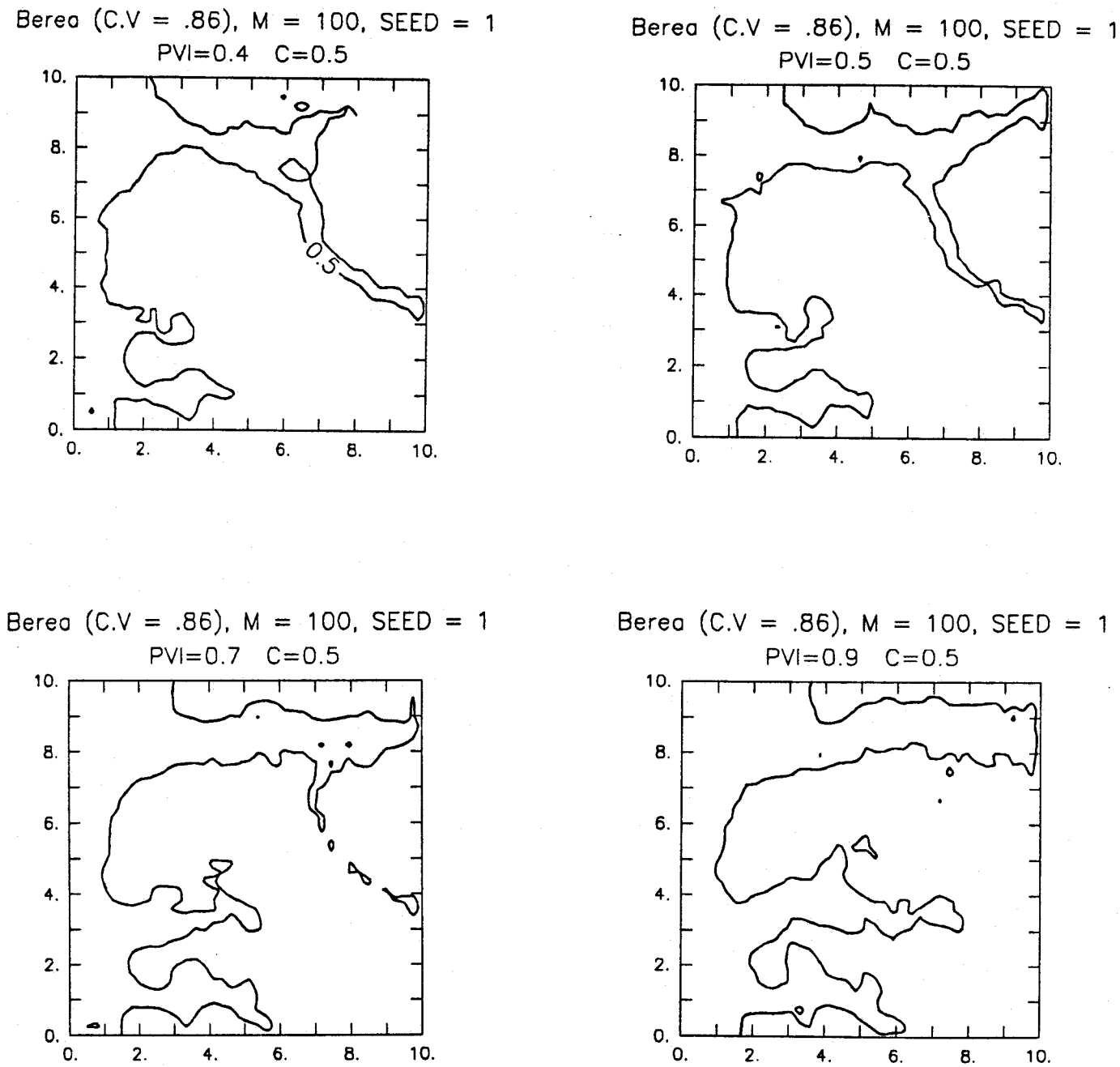

Figure 4.2-19. The 50% concentration contour at 0.4, 0.5, 0.7 and 0.9 PVI at M=100 for the second modified data set.

5. Summary

The range of physical mechanisms discussed in this report is the direct result of the complexity of miscible flood processes. It is well known by now that phase behavior, or more accurately, the transfer of components between phases, can produce very high local displacement efficiency, in one-dimensional flow at least. When flow is not one-dimensional, however, additional complexities play important roles. Viscous instability and local variations in permeability and porosity cause local variations in flow velocity. Those variations affect sweep efficiency, of course, but they also can interact with the component transfers that control local displacement efficiency. If crossflow occurs between zones of low and high flow velocity, the resulting mixing can induce two-phase flow, even though the displacement would have been miscible if the flow had been one-dimensional. If there is any difference in mobility, then viscous crossflow will inevitably occur, and if two or more phases coexist, then capillary forces will also contribute to crossflow. In addition, density differences can drive transport transverse to the average flow direction.

The goal of the work presented here is to develop accurate quantitative representations of all those physical mechanisms, so that a quantitative picture of the scaling of the interactions can be constructed. Because the full process is too complex for any one graduate student to attack, we have chosen to examine subsets of the overall problem. Throughout the research effort, we have made use of a combination of experiments and theory to tackle the scaling questions. We have chosen that approach because we believe that experimental verification of the mathematical representations is an essential part of the process.

The research presented is divided into three overlapping areas. In the first, phase equilibrium experiments combined with detailed chromatographic analyses of the hydrocarbon mixtures were used to study the effect of crude oil composition on the efficiency of extraction of hydrocarbons by dense supercritical CO_2. The experiments showed that hydrocarbons that contain multiple aromatic rings are extracted less efficiently than straight chain or branched chain alkanes with the same number of carbon atoms. Fortunately, such hydrocarbons also elute late in chromatographic analyses on nonpolar columns, so that a crude oil can be conveniently divided into pseudocomponents for equation of state calculations based on elution time. In other words, the experiments showed that components that elute together also partition approximately together, and hence grouping components by elution time makes sense.

Additional experiments to investigate the use of supercritical fluid chromatography for characterization of crude oils were performed. In those experiments, CO_2 was used as the carrier. A thermodynamic analysis of retention time behavior indicates that it may be possible to use chromatography data to obtain CO_2 binary interaction parameters for hydrocarbon fractions in crude oils. The technique was demonstrated for a pure hydrocarbon. The interaction parameter for CO_2 with dodecane (C_{12}) was determined from elution time data, and the phase behavior of binary mixtures of C_{12} with CO_2 was predicted with the Peng-Robinson equation of state. The agreement observed between predicted phase behavior and measured values was good enough to suggest that characterization of crude oils by supercritical fluid chromatography is feasible.

The second area of investigation is the interaction of phase behavior with flow. New analytical solutions by the method of characteristics were presented. The first set showed the sensitivity of calculated composition paths and oil recovery to the representation of phase densities. The comparison of solutions obtained based on the assumption of no volume change as components move between phases with similar solutions including the effects of volume change showed that the no volume change analysis produces optimistic predictions of oil recovery behavior. Thus, the more complex solution which includes volume change is preferred. In addition, a relatively simple manipulation was demonstrated by which solutions

obtained for flow in linear systems can be transformed to give solutions for flow in radial systems.

The theory of slug injection processes was also examined by the method of characteristics. Solutions for binary mixtures were presented that demonstrate how the effects of interfering shocks can be calculated. When the techniques are extended to systems with more components, the analysis will be the basis of a rational theory of slug sizes based on convective effects rather than dispersive phenomena.

The interplay of phase behavior, capillary forces, and gravity segregation was investigated in a series of core displacement experiments. The experiments showed that increased recovery results when the interfacial tension was lowered by the addition of alcohol to oil/water mixtures. In addition, the presence of interfacial tension gradients was shown to aid or impede recovery depending on the direction of the gradient. Those results suggest that crossflow due to the combined effects of gravity and capillary forces may be important in systems that show low interfacial tensions. Because successful miscible floods do generate low tensions over a portion of the transition zone, the transverse transport associated with low tension crossflow can evidently be important in flow systems with high enough permeability. The experimental results also suggest that it may be possible to design efficient recovery processes for fractured reservoirs based on the use of low interfacial tensions.

In the third area, the combined impact of reservoir heterogeneity and viscous instability was investigated experimentally and computationally. Displacement experiments performed in glass bead packs showed that even mild permeability contrasts can have a significant effect on the form and location of viscous fingers. If high permeability zones are long and relatively thin, then the permeability can dominate the flow completely. Numerical simulations with a particle tracking technique showed good agreement with the experimental observations, though careful attention to the details of the implementation of the inlet boundary condition was required. The simulations reproduced mechanisms observed in experiments in homogeneous media, and also represented well the transition from instability-dominated flow to permeability-dominated flow. The simulations and experiments suggest that in many field situations the distribution of low viscosity fluid will be controlled by the permeability distribution. Additional calculations to establish whether that conjecture is true are underway. The agreement observed between experiments and simulations indicates that such an investigation of scaling issues can be undertaken with confidence that the particle tracking simulations represent with reasonable accuracy the important physical mechanisms.

As with any research effort that investigates complex competing and interacting physical mechanisms, this one raises as many questions as it answers. While much remains to be done to develop a comprehensive analysis of scaling of miscible floods, the research effort described here represents significant progress toward a detailed description of the factors that control miscible flood performance at field scale.

REFERENCES

Araktingi, U.G., 1988, "Viscous Fingering in Heterogeneous Porous Media," PhD dissertation, Stanford University, Stanford, CA.

Araktingi, U.G. and Orr, F.M., Jr., 1988, "Viscous Fingering in Porous Media," paper SPE 18095 presented at the 1988 SPE Annual Technical Conference and Exhibition, Houston, October 2-5.

Araktingi, U.G. and Orr, F.M., Jr., 1990, "Viscous Fingering, Gravity Segregation and Reservoir Heterogeneity in Miscible Displacements in Vertical Cross Sections," paper SPE 20176 presented at the SPE/DOE Seventh Symposium on Enhanced Oil Recovery, Tulsa, Okllahoma, April 22-25.

Blackwell, R.J., Rayne, J.R., and Terry, W.M., 1959, "Factors Influencing the Efficiency of Miscible Displacement," *Trans.*,, AIME, **216**, 1-8.

Brock, David C., 1990, "An Experimental Investigation of Viscous Fingering in Heterogeneous Porous Media," PhD dissertation, Stanford U., Stanford, CA.

Buckley, S.E., and Leverett, M.C., 1942, "Mechanism of Fluid Displacement in Sands," *Trans.*, AIME, **146**, 107.

Campbell, B.T., and Orr, F.M., Jr., 1985, "Flow Visualization for CO_2-Crude Oil Displacements," *Soc. Pet. Eng. J.*, **25** , 665-678.

Christie, M.A. and Bond, D.J., 1987, "Detailed Simulation of Unstable Processes in Miscible Flooding," *SPE Reservoir Engineering J.*, 514-522, November. (Note: in Sec. 4, 2d para shows 1986)

Courant, R., and Hilbert, D., 1962, "Methods of Mathematical Physics: Vol. 2. Partial Differential Equations," Wiley-Interscience, New York.

Cuiec, E., Bourbiaux, B., and Kalaydjian, F., 1990, "Imbibition in Low-Permeability Porous Media: Understanding and Improvement of Oil Recovery," paper SPE/DOE 20259 presented at 7th Symposium on Enhanced Oil Recovery, Tulsa, April 22-25.

Deo, M.D., Nutakki, R., and Orr, F.M., Jr., 1989, "Schmidt-Wenzel and Peng-Robinson Equations of State for CO_2-Hydrocarbon Mixtures: Binary Interaction Parameters and Volume Translation Factors," paper SPE 18796 presented at the SPE California Regional Meeting, Bakersfield, April 5-7.

Dria, M., 1988, "Chemical and Thermochemical Wave Behavior in Multiphase Fluid Flow Through Permeable Media: Wave-Wave Interactions," PhD Dissertation, University of Texas, Austin, TX.

Dumoré, J.M., Hagoort, J., and Risseeuw, A.S., 1984, "An Analytical Model for One Dimensional Three Component and Vaporizing Gas Drives," *Soc. Pet. Eng. J* **24**, 169-179.

Giordano, R.M., Salter, S.J., and Mohanty, K.K., 1985, "the Effects of Permeability Variations on Flow in Porous Media," paper SPE 14365 presented at the SPE 60th Annual Technical Conference, Las Vegas, September 22-25.

Gorell, S.B., 1989, "Modeling the Effects of Trapping and Water Alternate Gas (WAG) Injection on Tertiary Miscible Displacements,"

Helfferich, F.G., 1981, "General Theory of Multicomponent, Multiphase Displacement in Porous Media," *Soc. Pet. Eng. J.* **21**, 51-62.

Hewett, T.A., and Behrens, R.A., 1989, "Scaling Laws in reservoir Simulation and their Use in a Hybrid Finite Difference/Streamtube Approach to Simulating ghe Effects of Permeability Heterogeneity," presented at the NIPER/DOE Second International Reservoir Characterization Technical Conference, Dallas, June 25-28.

Hirasaki, George J., 1981, "Application of the Theory of Multicomponent, Multiphase Displacement to Three-Component, Two-Phase Surfactant Flooding," *Soc. Pet. Eng. J.*, **21**, 191-204.

Ito, K., 1951, "On Stochastic Differential Equations," *Memoirs of the Am. Math. Soc.*, No. 4, 44-51.

Jossi, J.A., Stiel, L.I., and Thodos, G., 1962, "The Viscosity of Pure Substances in the Dense Gaseous and Liquid Phases," *A.I.Ch.E. J.*, **8**, No. 1, 59-62.

Kinzelbach, W., 1988, "The Random Walk Method in Pollutant Transport Simulation," *Groundwater Flow and Quality Monitoring*, NATO ASI Series C: Mathematical and Physical Sciences (1988) **224**, E. Custodio, A. Gurgin and J.P. Lobo Ferreira (eds.), D. Reidel Publishing, 227-245.

Kleppe, J., and Morse, R.A., 1974, "Oil Production from Fractured Reservoirs by Water Displacement," paper SPE 5084 presented at the 1974 SPE Annual Meeting, Houston, October 6-9.

Lake, L.W. 1989, *Enhanced Oil Recovery*, Prentice Hall, New Jersey.

Larsen, L.L., Silva, M.K., Taylor, M.A., 1989, "Temperature Dependence of $L_1/L_2/V$ Behavior in CO_2/Hydrocarbon systems," *SPE Reservoir Engineering J.*, February, 105-114.

Lax, P.D., 1957, "Hyperbolic Systems of Conservation Laws: Part 2," Communications in Pure and Applied Mathematics, **10**, 537-566.

Lohrenz, John, Bray, B.C., and Clark, C.R., 1964, "Calculation Viscosities of Reservoir Fluids from their Compositions," *J. Pet. Tech.*, **6**, 1171-1176.

Magruder, J.B., Stiles, L.H., Yelverton, T.D., 1990, "Review of the means San Andres Unit CO_2 Tertiary Project," *J. Pet. Tech.*, 638-644.

Mathias, P.M., Naheiri, T., and Oh, E.M., 1989, "A Density Correction for the Peng-Robinson Equation of State," *Fluid Phase Equilibria*, **47**, 77-87.

Mattax, C.C., 1962, "Imbibition Oil Recovery from Fractured, Water-Driven Reservoir," *Soc. Pet. Eng. J.*, **225**, 177-184.

Mishra, s., 1987, "On the Use of Pressure and Tracer Test Data for Reservoir Description," PhD dissertation, Stanford University, Stanford, CA.

Monroe, W.W., 1986, "The Effect of Dissolved Methane on Composition Paths in quaternary CO_2-Hydrocarbon Systems," Master's thesis, Stanford University, Stanford, CA.

Monroe, W.W., Silva, M.K., Larsen, L.L., and Orr, F.M., Jr., 1990, "Composition Paths in Four-Component Systems: Effect of Dissolved Methane on 1D CO_2 Flood Performance," *SPE Reservoir Engineering*, 423-432.

Morrow, N.R., Chatzis, I., and Taber, J.J., 1988, "Entrapment and Mobilization of Residual Oil in Bead Packs," *SPE Reservoir Engineering*, **3**, 927-935.

Morrow, N.R., and Songkran, B., 1982, Effect of Viscous and Buoyancy Forces on Nonwetting Phase Trapping in Porous Media," *Surface Phenomena in Enhanced Oil Recovery*, D.O. Shah (ed.), Plenum Press, New York City, 387-411.

Naar, J., Wygal, R.J., and Henderson, J.B., 1962, "Imbibition Relative Permeability in Unconsolidated Porous Media," *SPEJ*, **2**, 13-17.

Orr, F.M., Jr., 1989, "Reservoir Characterization for the CO_2 Enhanced Oil Recovery Process, Final Report," US DOE Rep. No. DOE/MC/22042-15.

Orr, F.M., Jr., and Jensen, C.M., 1984, "Interpretation of Pressure-Composition Phase Diagrams for CO_2-Crude Oil Systems," *Soc. Pet. Eng. J.*, October, 485-497.

Orr, F.M., Jr., and Taber, J.J., 1984, "Displacement of Oil by Carbon Dioxide," Final Report, Rep. No. DOE/BC/10331-12.

Orr, F.M., Jr., Yu, A.D., and Lien, C.L., 1981, "Phase Behavior of Carbon Dioxide and Crude Oil in Low Temperature Reservoirs," *Soc. Pet. Eng. J.*, **21**, 480-492.

Pande, K.K., 1989, "Interaction of Phase Behavior with Nonuniform Flow," PhD dissertation, Stanford U., Stanford, CA.

Pande, K.K., and Orr, F.M., Jr., 1989, "Interaction of Phase Behavior, Reservoir Heterogeneity and Crossflow in CO_2 Floods," paper SPE 19668 presented at the SPE Annual Technical Conference and Exhibition, San Antonio, Oct. 8-11.

Pande, K.K., and Orr, F.M., Jr., 1990a, "Analytical Computation of Breakthrough Recovery for CO_2 Floods in Layered Reservoirs," paper SPE 20177 to be presented at the SPE/DOE Seventh Symposium on Enhanced Oil Recovery, Tulsa, April 22-25.

Pande, K.K., and Orr, F.M., Jr., 1990b, "Composition Paths in Binary CO_2 -C_{10} Displacements: Effects of Reservoir Heterogeneity and Crossflow on Displacements with Limited Solubility," Proc. Second European Conference on the Mathematics of Oil Recovery, Arles, Sept. 11-14.

Peneloux, A., Rauzy, E., and Freze, R., 1982, "A Consistent Correction for Redlich-Kwong-Soave Volumes," *Fluid Phase Equilibria*, **2**, 7-23.

Peng, D-Y, and Robinson, D.B., 1976, "A New Two-Constant Equation of State," *Ind. Eng. Chem.*, **15**, 59-64.

Pope, G.A., Lake, L.W., and Helfferich, F.G., 1978, "Cation Exchange in Chemical Flooding: Part 1—Basic Theory Without Dispersion," *SPEJ,/F1* **18**, 418-434.

Pozzi, A.L. and Blackwell, R.J., 1963, "Design of Laboratory Models for Study of Miscible Displacement," *SPEJ*, 28-40.

Rhee, H., Aris, R., and Amundson, N.R., 1986, *First-Order Partial Differential Equations: Volume I*, Prentice-Hall, Englewood Cliffs, New Jersey.

Stewart, W.C. and Nielsen, R.F., 1954, "Phase Equilibria for Mixtures of Carbon Dioxide and Several Normal Saturated Hydrocarbons," *Producers Monthly*, 27-32, January.

Tan, C.T., and Homsy, G.M., 1986, "Stability of Miscible Displacements in Porous Media: Rectilinear Flow," *Phys. Fluids*, **29**, 3549-3569.

Tan, C.T. and Homsy, G.M., 1988, "Simulation of Nonlinear Viscous Fingering in Miscible Displacement," *Phys. Fluids*, **31**,, 1330-1338. (Note: in text shows 1986 and 1987)

van Wassen, U. and Schneider, G.M., 1975, "Pressure and Density Dependence of Capacity Ratios in Supercritical Fluid Chromatography (SFC) with Carbon Dioxide as Mobile Phase," *Chromatographia*, 274-276.

Welge, H.J., Johnson, E.F., Hicks, A.L., and Brinkman, F.H., 1962, "An Analysis for Predicting the Performance of Cone-Shaped Reservoirs Receiving Gas or Water Injection," *J. Pet. Tech.*, **14**, 894-898.

Yonker, C.R., Gale, R.W., and Smith, R.D., 1987, "Effects of Pressure on Retention in Supercritical Fluid Chromatography," *Journal of Physical Chemistry*, 3333-3336.